Dissertation
submitted to the
Combined Faculty of Mathematics, Engineering and Natural Sciences
of Heidelberg University, Germany
for the degree of
Doctor of Natural Sciences

Put forward by
Martin Jonák
born in Bratislava, Slovakia

Oral examination: 09 November 2022

Low-Energy Magnetic Excitations and Magnetisation in Magnetoelectric Antiferromagnets $MnTiO_3$ and $LiMnPO_4$ and in van-der-Waals Ferromagnet CrI_3

Referees: Prof. Dr. Rüdiger Klingeler
Prof. Dr. Maurits W. Haverkort

Low-Energy Magnetic Excitations and Magnetisation in Magnetoelectric Antiferromagnets $MnTiO_3$ and $LiMnPO_4$ and in van-der-Waals Ferromagnet CrI_3:

High-frequency electron spin resonance is utilised to study antiferromagnetic and ferromagnetic resonance in $MnTiO_3$, $LiMnPO_4$, and CrI_3. The main measurement technique is complemented by X-band electron spin resonance and by magnetisation measurements in static and oscillating magnetic fields. For each studied material, a resonance-frequency–magnetic-diagram of the magnon excitations is constructed and effective anisotropy and exchange constants derived. $MnTiO_3$ is found to be describable by a two-sublattice antiferromagnetic model with uniaxial anisotropy and with effective exchange field $B_\mathrm{E} = 107(6)\,\mathrm{T}$ and anisotropy field $B_\mathrm{A} = 0.17(1)\,\mathrm{T}$. The source of the anisotropy is argued to be magnetic dipole-dipole interactions. $LiMnPO_4$ is found to be a two-sublattice antiferromagnet with orthorhombic anisotropy and effective parameters $B_\mathrm{E} = 37.4(1)\,\mathrm{T}$, $B_\mathrm{A}^\mathrm{c} = 0.22(1)\,\mathrm{T}$, and $B_\mathrm{A}^\mathrm{b} = 0.55(1)\,\mathrm{T}$. An anomalous magnon branch is shown to be accountable for by rotation of the anisotropy axis at the spin-flop field by 6.5° towards the hard magnetisation axis. A spin-flip along the hard magnetisation axis is detected and suggested to indicate Dzyaloshinskii-Moriya-interaction-caused spin canting in the ground state. CrI_3 is shown to possess anisotropy gap $\Delta = 80(1)\,\mathrm{GHz}$ at $2\,\mathrm{K}$ and its closure is detected only at $\approx 1.3T_\mathrm{C}$, confirming the quintessential role of anisotropy in formation of long-range ferromagnetic order. Critical-scaling analysis yields $\beta = 0.21(4)$, $\gamma = 1.05(2)$, and $\delta = 6.05(1)$, which are interpreted as indicating a predominantly two-dimensional nature of magnetic interactions.

Niederenergetische magnetische Anregungen und Magnetisierung in den magnetoelektrischen Antiferromagneten $MnTiO_3$ und $LiMnPO_4$ und im van-der-Waals Ferromagneten CrI_3:

Mittels hochfrequenter Elektronenspinresonanz-Spektroskopie werden die magnetischen Anregungen in $MnTiO_3$, $LiMnPO_4$ und CrI_3 untersucht. Komplementiert werden diese Messungen durch Messungen im X-Band, sowie durch Magnetisierungsmessungen in statischen und oszillierenden magnetischen Feldern. Für die untersuchten Materialien wird jeweils ein magnetisches Resonanz-Frequenzdiagramm der Magnonanregungen erstellt und die effektiven Anisotropie- und Austauschkonstanten werden bestimmt. $MnTiO_3$ kann mithilfe eines antiferromagnetischen Zwei-Untergitter-Modells mit uniaxialer Ansiotropie, einem effektiven Austauschfeld $B_\mathrm{E} = 107(6)\,\mathrm{T}$ und einem Anisotropiefeld $B_\mathrm{A} = 0.17(1)\,\mathrm{T}$ beschrieben werden. Ursache der Anisotropie sind magnetische Dipol-Dipol-Wechselwirkungen. Auch $LiMnPO_4$ lässt sich im Modell eines Zwei-Untergitter-Antiferromagneten beschreiben, wobei eine orthorhombische Anisotropie und die effektiven Parametern $B_\mathrm{E} = 37.4(1)\,\mathrm{T}$, $B_\mathrm{A}^\mathrm{c} = 0.22(1)\,\mathrm{T}$ und $B_\mathrm{A}^\mathrm{b} = 0.55(1)\,\mathrm{T}$ betragen. Ein anomaler Resonanzzweig kann durch die Rotation der Anisotropieachse um 6.5° in Richtung der harten magnetischen Achse am Spinflopfeld erklärt werden. Entlang der harten magnetischen Achse wird ein Spinflip detektiert, welcher die Verkantung der Spins im Grundzustand aufgrund Dzyaloshinskii-Moriya-Wechselwirkungen zeigt. CrI_3 weist bei 2 K eine Anisotropielücke von $\Delta = 80(1)\,\mathrm{GHz}$ auf, die erst bei ca. $1.3T_\mathrm{C}$ vollständig geschlossen wird. Letzteres bestätigt die Bedeutung der Anisotropie für die Entstehung langreichweitiger ferromagnetischer Ordnung. Die Analyse der kritischen Exponenten ergibt $\beta = 0.21(4)$, $\gamma = 1.05(2)$, $\delta = 6.05(1)$, welche mit einer überwiegend zweidimensionalen Natur der magnetischen Wechselwirkungen im Einklang stehen.

Contents

1. Introduction **1**

2. Theory **5**

2.1. Isolated Magnetic Ions 5

2.1.1. Single-Atom Hamiltonian 5

2.1.2. Hund's Rules 6

2.1.3. Spin-Orbit Coupling 7

2.1.4. Zeeman Energy 7

2.1.5. Landé g-Factor 8

2.2. Magnetic Ions in Solids 8

2.2.1. Crystal Field Effects 8

2.2.2. Orbital Quenching 10

2.2.3. Fictitious Orbital Moment 10

2.2.4. g-Factor and Anisotropy Tensors 11

2.3. Magnetic Interactions 12

2.3.1. Magnetic Dipole-Dipole Interaction 12

2.3.2. Exchange Interaction 12

2.4. Sources of Anisotropy 16

2.4.1. Single-Ion Anisotropy 16

2.4.2. Interaction-Mediated Anisotropy 16

2.4.3. Shape Anisotropy 17

2.5. Long-Range-Ordered Magnets 17

2.5.1. Microscopic Spin Hamiltonian 17

2.5.2. Classical Solution to Long-Range-Ordered Magnets 18

2.5.3. Derivation of Effective Exchange and Anisotropy Fields 19

2.6. Electron Spin Resonance 20

2.6.1. Landau-Lifshitz-Gilbert Equation 20

2.6.2. Solutions of the Landau-Lifshitz-Gilbert Equation 21

3. Experimental Methods **27**

3.1. High-Frequency Electron Spin Resonance 27

3.2. X-Band Electron Spin Resonance 31

3.3. Magnetometry 32

3.3.1. DC-Field Magnetisation 32

3.3.2. AC-Field Magnetisation 34
3.4. Laue X-Ray Diffraction 34
3.5. Note on Usage of Symbols and Units 35

4. $MnTiO_3$ **37**
4.1. Material Background 37
4.2. Sample and Experimental Details 41
4.3. Experimental Results 41
4.3.1. Static Magnetic Susceptibility 41
4.3.2. Electron Spin Resonance 42
4.4. Discussion 54
4.5. Summary 57

5. $LiMnPO_4$ **59**
5.1. Material Background 59
5.2. Experimental Results 63
5.2.1. Magnetisation and Magnetic Phase Diagrams 64
5.2.2. High-Frequency Electron Spin Resonance 75
5.3. Discussion 90
5.4. Summary 96

6. CrI_3 **99**
6.1. Material Background 99
6.1.1. Crystallographic Information 99
6.1.2. Exchange Constants 100
6.1.3. Chromium Ion in CrI_3 100
6.1.4. Sources of Anisotropy in CrI_3 102
6.1.5. Long-Range Magnetic Order in Thin Layers of CrI_3 103
6.2. Sample and Experimental Details 104
6.3. Experimental Results 105
6.3.1. DC Magnetisation 105
6.3.2. High-Frequency Electron Spin Resonance 109
6.3.3. AC Susceptibility 124
6.3.4. High-Temperature Isothermal Magnetisation 132
6.4. Discussion and Summary 140

7. Overall Summary and Conclusion **143**

A. List of Publications **147**

B. Bibliography **149**

1. Introduction

One half of the 2021 Nobel Prize was awarded to Giorgio Parisi "for the discovery of the interplay of disorder and fluctuations in physical systems from atomic to planetary scales" [1]. Although Parisi's original work was concerned with providing a self-consistent mean-field theory of spin glasses [2, 3], Parisi's solution subsequently found utilisation in diverse areas of physics and beyond, ranging from solutions to optimisation problems [4] to applications in artificial neural networks [5].

Spin glasses – macroscopic solids in which spins freeze into one of a macroscopic number of energetically equivalent ground states of randomly oriented spins with no long-range magnetic order [6, 7] – are just one example of magnetic systems in which the interplay between structure, charge, and spin degrees of freedom lead to complex emergent phenomena. Other examples include (high-T_C) superconductivity and topological insulators, but also the insulating state of the antiferromagnet CoO. Whereas some of these effects (insulating CoO) are exhaustively understood (by means of an electron-correlation-driven metal-insulator transition [8]), others are still awaiting their comprehensive explanation (high-T_C superconductivity).

As Parisi's work demonstrates, research in complex spin-spin phenomena may bear fruits not only in understanding fundamental solid state magnetism – a motivation in and of itself –, but it may also shed light on other areas of the natural sciences and mathematics, and is hence of further considerable significance.

The present work too is concerned with the study of spin systems and it too uses mean-field theories at a number of places to gain insight into the effects of magnetic interactions and anisotropy. However, whereas spin glasses are inherently disordered, the materials studied here all exhibit long-range magnetic order – be it antiferromagnetic or ferromagnetic. Electron spin resonance (ESR) spectroscopy, which uses light in the microwave part of the electromagnetic spectrum ($10\,\mathrm{GHz} \lesssim \nu \lesssim 1000\,\mathrm{GHz}$, i.e. $0.04\,\mathrm{meV} \lesssim \nu \lesssim 4\,\mathrm{meV}$), is employed to study experimentally the low-energy excitations in long-range-ordered magnets.

A fundamental reason for studying excitations in an ordered system – be it, for instance, a crystal or a magnet – is the footprint of the system's ground state on the corresponding excitations. In other words, by investigating an ordered system's excitations, the system's ground state may be determined in qualitative and quantitative terms. A long-range-ordered magnet is capable of sustaining long-wavelength, low-energy magnetic

waves – in quantum-mechanical parlance called *magnons* and in classical terminology *spin waves*. The magnetic waves' energy dependence on external parameters, such as the k-vector, external magnetic field, or temperature, is determined by the microscopic interactions which give rise to the long-range order in the first place. And hence, from the experimentally-observed energy dependence of the magnetic excitations, the underlying magnetic properties of the ground state may be inferred. Further important insights may be obtained through analysis of the shape of the signal which the excitation produces: the detected signal's width contains information about relaxation processes, its amplitude about the number of spins.

In addition to gaining understanding of the fundamental principles governing long-range magnetic ordering, the second crucial aspect of studying low-energy magnetic excitations in long-range-ordered magnets is the systems' application potential and the unique capabilities which ESR can provide. On the one hand, a detailed characterisation of the various magnetic materials is required for spintronic applications: in bulk antiferromagnets, the knowledge of the number and precise size of the zero-field excitation gaps is crucial for efficient engineering [9]. In thin films and multilayered heterostructures, ESR provides unique characterisation on the exchange coupling between the multilayers [10–12]. On the other hand, the very spintronic technology relies on concepts and methods from ESR: spin transport through magnetic tunnel junctions is often found to be mediated by magnon modes [13, 14], while spin pumping into a magnetic tunnel junction may be driven by ferromagnetic resonance [15, 16].

Two magnetoelectric antiferromagnets – $MnTiO_3$ and $LiMnPO_4$ – and a van-der-Waals ferromagnet – CrI_3 – are studied by means of high-frequency ESR (HF-ESR) in this work. The main experimental method is complemented by low frequency ESR (in the X-band region of the spectrum) and by magnetisation measurements in static and oscillating magnetic fields. After these opening remarks, selected theoretical concepts which are essential for studying magnetically-ordered materials by means of HF-ESR are introduced in Chapter 2. The following chapter (Chapter 3) introduces the experimental methods employed in this work with special attention to the operation of the HF-ESR setup. The following three chapters – which form the main corpus of the text – present, analyse, and discuss the obtained experimental data on the materials: Chapter 4 is devoted to $MnTiO_3$, Chapter 5 to $LiMnPO_4$, and Chapter 6 to CrI_3. In each case, firstly, the available background information on the respective material is summarised. Secondly, magnetisation results in static magnetic fields are presented – in some cases ($MnTiO_3$ and CrI_3), they serve as a basic characterisation tool; in other cases ($LiMnPO_4$), they provide new observations and are duly discussed. Thirdly, resonance-frequency–magnetic-field diagrams of the magnon excitations are constructed, analysed, and the obtained parameters discussed. Fourthly, temperature-dependent resonance is presented and discussed. Penultimately, comple-

mentary measurements – X-band ESR on $MnTiO_3$ and $LiMnPO_4$, AC susceptibility on CrI_3 – are presented and analysed. Each results chapter concludes with a discussion and a summary. The entire text then closes with an overall conclusion, which comprises Chapter 7.

2. Theory

This chapter provides a basic theoretical framework for this study. The approach is highly selective but the generally followed path starts from a single isolated magnetic ion (Section 2.1) which is subsequently treated when incorporated in a non-magnetic crystalline environment (Section 2.2). Thereafter, the environment is assumed to be magnetic, and magnetic interactions and sources of anisotropy are discussed (Sections 2.3 and 2.4). Following from that, selected aspects of long-range-ordered magnets are discussed (Section 2.5). The chapter closes with introducing the magnetic resonance phenomenon in a paramagnet and in long-range-ordered magnets (Section 2.6). Sections 2.1–2.4 are based predominantly on the treatment by S. Blundell [6], D. Khomskii [17], A. Abragam and B. Bleaney [18], and P. Fazekas [8]. Sections 2.5–2.6 are derived predominantly from S. Rezende [19], S. Vonsovskii [20], G. Rado and H. Suhl [21], and E. Turov [22].

2.1. Isolated Magnetic Ions

2.1.1. Single-Atom Hamiltonian

The Hamiltonian of an electron moving in the electrostatic potential of a stationary massive point-like nucleus is given by:

$$\mathcal{H} = \frac{\boldsymbol{p}^2}{2m_\mathrm{e}} - \frac{Ze^2}{r} \tag{2.1}$$

where Z is the atomic number and r the electron's distance from the nucleus. For N electrons moving around the nucleus, the above Hamiltonian can be expanded to read:

$$\mathcal{H} = \sum_{i=1}^{N} \left(\frac{\boldsymbol{p}_i^2}{2m_\mathrm{e}} - \frac{Ze^2}{r_i} + V_i(r_i) \right) \tag{2.2}$$

Here, V_i is the electrostatic potential on the i^{th} electron due to the remaining electrons. The eigenstates of the Hamiltonian in Eq. 2.2 are given by the wave function:

$$\psi_{n,l,m_l,m_s}(r,\theta,\phi) = R_{n,l}(r) Y_l^{m_l}(\theta,\phi) \chi(m_s) \tag{2.3}$$

where $R_{n,l}(r)$ quantifies the radial, $Y_l^{m_l}(\theta,\phi)$ the angular, and $\chi(m_s)$ the spin part, respectively, whereby $Y_l^{m_l}(\theta,\phi)$ are known as spherical harmonics. For the various

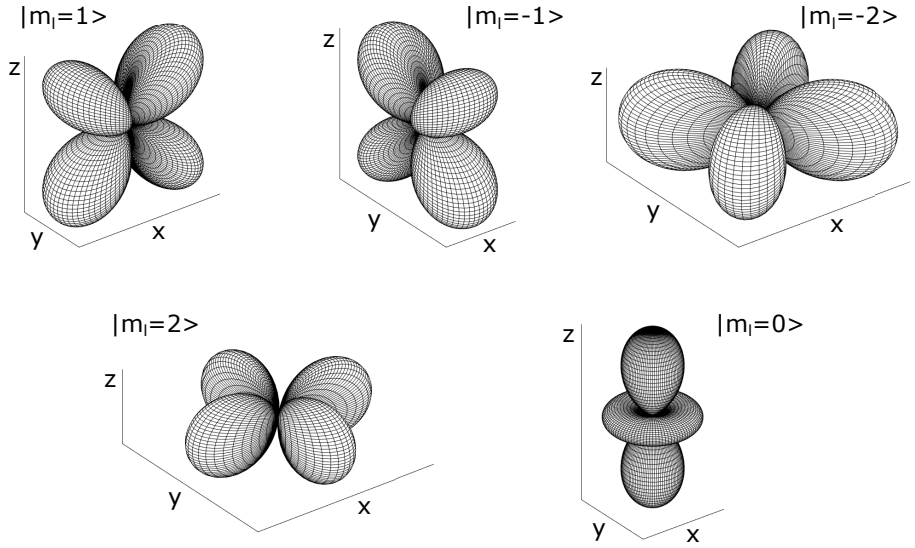

Figure 2.1.: Visualisation of the angular component of an electron's wave function for atomic 3d orbitals, given by the spherical harmonics $Y_{l=2}^{m_l}(\theta, \phi)$ from Eq. 2.3. The legend in each subfigure denotes the particular state $|m_l\rangle$. Visualisation performed by means of the Matlab library from [23].

quantum numbers, it holds: $n = 1, 2, ...$; $l = 0, 1, ..., n-1$; $m_l = -l, -l+1, ..., l-1, l$, and; $m_s = \pm s$, whereby for a single electron, $s = 1/2$. The analytical form of the radial and angular functions can be found, for instance, in [6, 8]. For illustrative purposes, the spherical harmonics which correspond to atomic 3d orbitals ($n = 3$, $l = 2$) are shown in Fig. 2.1. In this case m_l can take five values, $m_l = -2, -1, 0, 1, 2$, and so there are five distinct solutions to the angular part of Eq. 2.2. Due to the Pauli exclusion principle, each of the orbitals can be occupied at most by one spin-up and one spin-down electron.

2.1.2. Hund's Rules

The ground state electronic configuration of an atom or an isolated ion is given by Hund's rules. These state that:

1. the total spin quantum number S is maximised;
2. the total orbital quantum number L is maximised while respecting the first rule;
3. the total angular momentum quantum number J is given by:
    - $J = |L - S|$ if the corresponding shell is less than half-filled;
    - $J = |L + S|$ if the corresponding shell is more than half-filled;
    - $J = S$ if the corresponding shell is half-filled.

In addition, for completely empty or fully-filled shells, $S = L = J = 0$.

Hund's first two rules have their origin in the Pauli exclusion principle and in the minimisation of the Coulomb electrostatic repulsion energy: electrons with identical

spin orientation and with identical orbital parity can avoid each other more efficiently due to the exchange hole effect, which leads to the decrease in the Coulomb energy [8]. The energy saving associated with obeying the first rule is about 1 eV and the second rule about 0.1 eV–0.3 eV [8].

2.1.3. Spin-Orbit Coupling

Hund's third rule, which governs the ground state total angular momentum J, is a consequence of the relativistic spin-orbit coupling interaction. For an individual electron i, this is given by:

$$\mathcal{H}_{\mathrm{SO}}^{i} = \zeta_i \boldsymbol{l}_i \cdot \boldsymbol{s}_i \tag{2.4}$$

where ζ_i is a shell-dependent spin-orbit coupling constant. In order to obtain the total spin-orbit coupling of an atom, the contributions from individual electrons must be added up. Depending on the concrete atom at hand, the addition is more appropriately performed within the so-called LS-coupling (or Russell-Saunders) scheme or within the so-called jj-coupling scheme. In the LS-coupling scheme, the individual electrons' orbital moments and spins are first added up as $\boldsymbol{L} = \sum_i \boldsymbol{l}_i$ and $\boldsymbol{S} = \sum_i \boldsymbol{s}_i$ to give the total spin-orbit coupling of:

$$\mathcal{H}_{\mathrm{SO}} = \lambda \boldsymbol{L} \cdot \boldsymbol{S} \tag{2.5}$$

where $\lambda = \pm\zeta/(2S)$, whereby $\zeta = \zeta_i$ for electrons belonging to the same orbital shell. and whereby λ is positive for less-than-half-filled shell and negative for more-than-half-filled shell.

The LS-coupling scheme is appropriate for all $3d$ elements, as here the spin-orbit coupling is much smaller than the crystal-field energy ($\lambda_{3\mathrm{d}} \approx 10\,\mathrm{meV}$–$90\,\mathrm{meV}$ [24]). In the jj-coupling scheme, angular momenta of individual electrons are built first as $\boldsymbol{j}_i = \boldsymbol{l}_i + \boldsymbol{s}_i$, and these are then added up to give the total angular momentum of the atom as $\boldsymbol{J} = \sum_i \boldsymbol{j}_i$. The jj-coupling scheme is appropriate for elements whose spin-orbit coupling energy is much greater than the crystal-field energy, namely the $4f$ and $5f$ elements ($\lambda_{4\mathrm{f}} \approx 90\,\mathrm{meV}$–$360\,\mathrm{meV}$ [24]).

2.1.4. Zeeman Energy

The energy of a magnetic moment in an external magnetic field $\boldsymbol{B}$ is referred to as the Zeeman energy. It can be calculated by means of the following Hamiltonian:

$$\mathcal{H}_{\mathrm{Zeeman}} = \mu_{\mathrm{B}} (g_{\mathrm{L}} \boldsymbol{L} + g_{\mathrm{S}} \boldsymbol{S}) \cdot \boldsymbol{B} \tag{2.6}$$

where $g_{\mathrm{L}} = 1$ and $g_{\mathrm{S}} = 2$ are the g-factors associated with the orbital moment and spin, respectively, and where μ_{B} is the Bohr magneton.

2.1.5. Landé g-Factor

It can be shown (see, e.g., [6]) that the Landé g-factor of an isolated magnetic ion with spin S, orbital moment L, and total moment J is given by:

$$g_J = \frac{3}{2} + \frac{S(S+1) - L(L+1)}{2J(J+1)} \tag{2.7}$$

Consequently, the saturated magnetic moment of the ion is given by $\mu_{\mathrm{sat}} = \mu_{\mathrm{B}} g_J J$ and the effective moment as featuring, e.g., in the Curie-Weiss law, by $\mu_{\mathrm{eff}} = \mu_{\mathrm{B}} g_J \sqrt{J(J+1)}$.

2.2. Magnetic Ions in Solids

2.2.1. Crystal Field Effects

The inclusion of a magnetic ion in a crystalline solid has a profound effect on its magnetic properties. The potential which determines the energy of a particular electron on the ion is no longer given solely by the ion's nucleus and by the remaining electrons on the magnetic ion, but now also by electrons from neighbouring ligands. Through electrostatic interactions the orbitals may be increased or decreased in energy with respect to their free-ion values. While microscopic calculations may be very involved, if at all possible, symmetry-based arguments allow for qualitative and partially quantitative predictions of the energy changes. These are elaborated next.

Fig. 2.2 illustrates the changes to the 3d-orbitals energy for a particular set of crystal-field effects. When isolated, the five 3d orbitals are energetically fully degenerate (Fig. 2.2a). This remains the case also when they are placed in a spherically-symmetric crystal field, albeit the electrostatic interaction between the spherical crystal field and the orbitals raises the orbitals' energy (Fig. 2.2b). An octahedral crystal field produced by six ions located along the x-, y-, and z-axes results in a splitting of the orbital energies, with reduction of the t_{2g}-orbitals energy by $2\Delta_{\mathrm{CF}}/5$ and elevation of the e_g orbitals energy by $3\Delta_{\mathrm{CF}}/5$ (Fig. 2.2c). Here, Δ_{CF} is the crystal-field-splitting constant which is a function of the particular magnetic ion and of the particular ligand acting on the ion. For example, in a hydrate solution, Ni^{2+} exhibits $\Delta_{\mathrm{CF}} \approx 1.1\,\mathrm{eV}$, whereas Cu^{2+} $\Delta_{\mathrm{CF}} \approx 1.6\,\mathrm{eV}$ [18]. On the other hand, Cr^{3+} in an octahedral environment of Cl^- exhibits $\Delta_{\mathrm{CF}} \approx 1.7\,\mathrm{eV}$, whereas it shows $\Delta_{\mathrm{CF}} \approx 2.7\,\mathrm{eV}$ in an octahedral environment of NH_3 [17].

If the octahedron is slightly distorted, further energy splitting of the orbitals occurs.

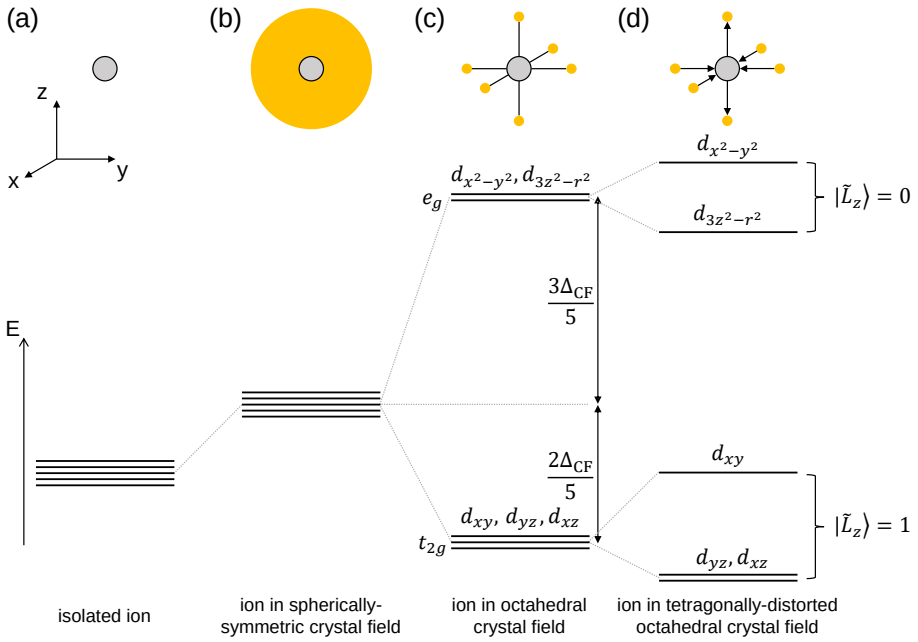

Figure 2.2.: Crystal-field-splitting scheme appropriate for 3d elements in (a) isolated environment, (b) spherically symmetric coordination, (c) octahedral coordination, (d) tetragonally-distorted octahedral coordination. Grey spheres depict the magnetic ion, yellow spheres the ligands. The 3d orbitals in (a) and (b) are degenerate, degeneracy is partially (or completely) lifted in (c) and (d). The energy scales in (a)–(d) are not to scale with each other. After [17, 25].

In Fig. 2.2d, a tetragonal distortion with an elongation of the bonds oriented along the z-axis and contraction of the bonds oriented in the xy-plane is envisaged. This partially lifts the degeneracy of the t_{2g} orbitals, while completely lifting the degeneracy of the e_g orbitals. If the contraction appears rather along the z-axis and the expansion in the xy-plane, the order of the split orbitals within the respective orbital manifold is reversed.

The incorporation of an isolated ion into a crystalline lattice which breaks the spherical symmetry of the ion's environment impacts, among others, the solution to Eq. 2.2. Consequently, the wave functions of the five 3d orbitals consist of linear superposition of the five atomic basis functions. In case of a dominant octahedral crystal field, as is the case for the three materials studied in this work, the angular part of the orbitals is given by [17]:

$$t_{2g}\begin{cases} d_{xy} = -\frac{i}{\sqrt{2}}(|2\rangle - |-2\rangle) \\ d_{yz} = \frac{i}{\sqrt{2}}(|1\rangle + |-1\rangle) \\ d_{xz} = -\frac{1}{\sqrt{2}}(|1\rangle - |-1\rangle) \end{cases} \qquad e_g\begin{cases} d_{x^2-y^2} = \frac{1}{\sqrt{2}}(|2\rangle + |-2\rangle) \\ d_{3z^2-r^2} = |0\rangle \end{cases} \tag{2.8}$$

where $|m_l\rangle$ are the atomic basis functions displayed in Fig. 2.1. The upper three orbitals form the t_{2g} orbitals manifold, the lower two the e_g orbitals manifold [6, 8]. The energy

dependence of these orbitals is illustrated for the case of a perfect octahedral crystal field in Fig. 2.2c and of a weakly tetragonally-distorted octahedral crystal field in Fig. 2.2d.

2.2.2. Orbital Quenching

The phenomenon of orbital quenching refers to the realisation of a spuriously low value of the orbital moment given the predictions from Hund's second rule, in extremal cases $\langle \boldsymbol{L} \rangle = 0$. Orbital quenching comes about due to the electrostatic interaction of the crystal field with the 3d orbitals. The orbital momentum operator is given by $\boldsymbol{L} = -i\hbar \boldsymbol{r} \times \vec{\nabla}$, i.e. is purely imaginary. At the same time, a physical observable, such as orbital momentum, must have real expectation values. It follows that if the wave function $|\Psi\rangle$ of a particular orbital state is purely real, the expectation value of the state when acted on by the orbital momentum operator must vanish: $\langle \Psi | \boldsymbol{L} | \Psi \rangle = 0$.

Inspecting the crystalline 3d orbitals in Eq. 2.8, it may be seen that the wave functions of the e_g orbitals are purely real. Based on the arguments in the preceding paragraph, it follows that the orbital moment associated with the e_g orbitals is quenched. Ni^{2+} and Cu^{2+} in an octahedral environment are good examples of ions with orbitally-quenched e_g orbitals [8].

2.2.3. Fictitious Orbital Moment

The situation on the t_{2g} orbitals is even more subtle. It may be observed in Eq. 2.8 that their wave functions consist of real and imaginary parts, so that a straightforward argument to show that orbital moment is fully quenched is not possible. However, experimental evidence suggests that even these orbitals undergo at least partial quenching [18]. This may be explained as follows: due to the large energetic separation Δ_{CF} of the t_{2g} from the e_g orbitals, it is possible to treat the t_{2g} orbitals as forming a closed pseudo shell and to assign to them a fictitious, pseudo orbital moment $\tilde{L} = 1$, with three possible values $m_{\tilde{l}} = -1, 0, 1$.

Considering now a magnetic ion with the electronic configuration $3d^{3+}$ (such as Cr^{3+}), its ground state under the supposition of an isolated ion (or a perfectly spherically-symmetric crystal field) is predicted to be: $S = 1/2 + 1/2 + 1/2 = 3/2$ (Hund's first rule); $L = 2 + 1 + 0 = 3$ (Hund's second rule), and; $J = |3 - 3/2| = 3/2$ (Hund's third rule). Based on Eq. 2.7, the Landé g-factor is calculated as $g_{\mathrm{J}} = 0.4$. This results in the saturated moment of $\mu_{\mathrm{sat}} = \mu_{\mathrm{B}} g_{\mathrm{J}} J = 0.6\,\mu_{\mathrm{B}}$ and in the effective moment of $\mu_{\mathrm{eff}} = \mu_{\mathrm{B}} g_{\mathrm{J}} \sqrt{J(J+1)} = 0.77\,\mu_{\mathrm{B}}$, contrary to experimental observations [18].

In an octahedral environment (as is the case for Cr^{3+} in, e.g., CrI_3, see Chapter 6), the crystal field lifts the five-fold degeneracy of the 3d orbitals, rendering the t_{2g} orbitals lowest in energy, while they remain energetically three-fold degenerate. Assigning

the fictitious orbital moment $\tilde{l} = 1$ to them and following Hund's rules, the ground state may be ascertained to be: $S = \sum_i s_i = 1/2 + 1/2 + 1/2 = 3/2$; $\tilde{L} = \sum_i \tilde{l} = 1 + 0 + (-1) = 0$, and; $\tilde{J} = S = 3/2$. This gives the Landé g-factor $g_{\tilde{\mathrm{J}}} = 2$. And hence, the saturated moment is given by $\mu_{\mathrm{sat}} = \mu_{\mathrm{B}} g_{\tilde{\mathrm{J}}} \tilde{J} = 3\,\mu_{\mathrm{B}}$ and the effective moment by $\mu_{\mathrm{eff}} = \mu_{\mathrm{B}} g_{\tilde{\mathrm{J}}} \sqrt{\tilde{J}(\tilde{J}+1)} = 3.87\,\mu_{\mathrm{B}}$, in line with experimental observations [18].

2.2.4. g-Factor and Anisotropy Tensors

By its nature, the spin-orbit coupling interaction ties the spin degree of freedom through its coupling with the orbital degree of freedom to the crystalline lattice. Although spin-coupling energy in 3d transition metal ions is much weaker than the crystal-field energy, it can still bring about macroscopically measurable effects. These are, on the one hand, a partial restoration of the quenched orbital moment and, on the other hand, the introduction of anisotropy in magnetic properties.

It may be shown that in second-order perturbation theory, the spin-orbit coupling term of Eq. 2.5 and the Zeeman term of Eq. 2.6 become [18]:

$$\begin{aligned} \mathcal{H}_{\mathrm{SO}} + \mathcal{H}_{\mathrm{Zeeman}} &= \lambda \boldsymbol{L} \cdot \boldsymbol{S} + \mu_{\mathrm{B}} (g_{\mathrm{L}} \boldsymbol{L} + g_{\mathrm{S}} \boldsymbol{S}) \cdot \boldsymbol{B} \\ &\overset{\text{2nd order}}{\underset{\text{pert. theory}}{\longrightarrow}} \\ &= -\lambda^2 \boldsymbol{S} \cdot \boldsymbol{\Lambda} \cdot \boldsymbol{S} + \mu_{\mathrm{B}} \boldsymbol{S} \cdot \boldsymbol{g} \cdot \boldsymbol{B} \end{aligned} \tag{2.9}$$

where the free-ion g-factors g_{L} and g_{S} are replaced by a g-factor tensor $\boldsymbol{g}$. In addition, Eq. 2.9 introduces an anisotropy tensor $\boldsymbol{\Lambda}$. The two tensors are given by [18]:

$$\boldsymbol{g}_{ij} = 2(\delta_{ij} - \lambda \Lambda_{ij}) \tag{2.10}$$

and

$$\boldsymbol{\Lambda}_{ij} = \sum_{n \neq 0} \frac{\langle 0|L_i|n\rangle \ \langle n|L_j|0\rangle}{E_n - E_0} \tag{2.11}$$

Here, δ_{ij} is the Kronecker delta, and L_i and L_j are components of the orbital angular momentum $\boldsymbol{L}$, such that the matrix elements connect the orbital ground state $|0\rangle$ of energy E_0 with the n^{th} orbital excited state $|n\rangle$ of energy E_n.

The crucial observation from the effective spin Hamiltonian in Eq. 2.9 is that the orbital momentum operator $\boldsymbol{L}$ has been consumed by the remaining terms while its effects, originating in spin-orbit coupling, are transmitted through the anisotropic g-tensor and the anisotropy constant.

2.3. Magnetic Interactions

In this section, the most important spin-spin interactions which are realised in long-range-ordered magnets are discussed. It is thanks to these magnetic interactions that correlation effects and ultimately long-range magnetic order evolves in crystalline solids.

2.3.1. Magnetic Dipole-Dipole Interaction

Magnetic dipole-dipole interaction is the magnetic equivalent of the electric dipole-dipole interaction and is given by [26]:

$$\mathcal{H}_{\text{dipole}} = \frac{\mu_0 \mu_{\text{B}}^2 g_1 g_2}{4\pi |\boldsymbol{r}|^3} [3(\boldsymbol{S}_1 \cdot \hat{\boldsymbol{r}})(\boldsymbol{S}_2 \cdot \hat{\boldsymbol{r}}) - \boldsymbol{S}_1 \cdot \boldsymbol{S}_2] \tag{2.12}$$

where the spins $\boldsymbol{S}_1$ and $\boldsymbol{S}_2$ are connected by the position vector $\boldsymbol{r}$, and where $\hat{\boldsymbol{r}}$ is the unit vector in the direction of $\boldsymbol{r}$. g_1 and g_2 are the isotropic g-factors associated with $\boldsymbol{S}_1$ and $\boldsymbol{S}_2$, respectively.

2.3.2. Exchange Interaction

The exchange interaction is determined by the fermionic nature of the electrons. Writing the spatial component of the i^{th} electron's wave function located at position $\boldsymbol{r}_j$ as $\phi_i(\boldsymbol{r}_j)$ and its spin component as χ_i, the respective symmetric and antisymmetric components are given by:

$$\begin{aligned} \psi^{\text{sym}} &= \frac{\phi_1(\boldsymbol{r}_1)\phi_2(\boldsymbol{r}_2) + \phi_1(\boldsymbol{r}_2)\phi_2(\boldsymbol{r}_1)}{\sqrt{2}} \\ \psi^{\text{antisym}} &= \frac{\phi_1(\boldsymbol{r}_1)\phi_2(\boldsymbol{r}_2) - \phi_1(\boldsymbol{r}_2)\phi_2(\boldsymbol{r}_1)}{\sqrt{2}} \end{aligned} \tag{2.13}$$

and

$$\chi^{\text{sym}} = \begin{cases} |\uparrow\uparrow\rangle \\ |\downarrow\downarrow\rangle \\ \frac{|\uparrow\downarrow\rangle + |\downarrow\uparrow\rangle}{\sqrt{2}} \end{cases} \qquad \chi^{\text{antisym}} = \frac{|\uparrow\downarrow\rangle - |\downarrow\uparrow\rangle}{\sqrt{2}} \tag{2.14}$$

where the ket notation in Eq. 2.14 follows the nomenclature that the first arrow refers to the spin orientation of the electron at $\boldsymbol{r}_1$ and the second arrow to the spin orientation of the electron at $\boldsymbol{r}_2$. In order to ensure that the total two-electron wave function be antisymmetric, two ways of combining the spatial and spin components are possible:

$$\Psi^{\text{antisym}} = \begin{cases} \Psi^{\text{S}} = \psi^{\text{sym}} \cdot \chi^{\text{antisym}} \\ \Psi^{\text{T}} = \psi^{\text{antisym}} \cdot \chi^{\text{sym}} \end{cases} \tag{2.15}$$

where the superscripts S and T refer to the singlet and triplet state, respectively. In the spatially antisymmetric state, the spin component is symmetric; the state is triplet. This forbids the two electrons from occupying the same space due to the Pauli exclusion principle. On the other hand, in the spatially symmetric state, the spin component is antisymmetric, allowing greater proximity of the two electrons to each other; the state is a singlet. In this way, the Coulomb electrostatic repulsion is lowered in the triplet with respect to the singlet. The energy difference between the triplet and the singlet state can be expressed as [6]:

$$E_{\mathrm{T}} - E_{\mathrm{S}} = \int_V \phi_1^*(\boldsymbol{r}_1)\phi_2^*(\boldsymbol{r}_2)\mathcal{H}\phi_1(\boldsymbol{r}_2)\phi_2(\boldsymbol{r}_1)d\boldsymbol{r}_1 d\boldsymbol{r}_2 \equiv 2J \tag{2.16}$$

where the integral is performed over the volume V and J is the exchange constant. A corresponding effective spin Hamiltonian may be written as:

$$\mathcal{H}_{\mathrm{spin}} = 2J\boldsymbol{S}_1 \cdot \boldsymbol{S}_2 \tag{2.17}$$

In case of a many-body system, the Hamiltonian is expanded to read:

$$\mathcal{H}_{\mathrm{Heisenberg}} = \sum_{<i,j>} J_{ij}\boldsymbol{S}_i \cdot \boldsymbol{S}_j \tag{2.18}$$

where the sum runs over all pairs of neighbouring spins i and j which are coupled by the neighbour-specific exchange constant J_{ij}. If J_{ij} is positive (negative), the singlet (triplet) state between the two neighbouring spins is energetically lower and antiferromagnetic (ferromagnetic) arrangement results. Eq. 2.18 is known as the Heisenberg Hamiltonian.

2.3.2.1. Direct Exchange

Direct exchange refers to the mechanism of a proxy-free exchange interaction between two neighbouring electrons. It lies at the heart of Hund's first rule but also, for instance, of the bonding effect in an H_2 molecule. In long-ranged magnetic systems it is a rather weak effect, since direct spatial wave function overlap is a precondition for it to be operative (c.f. Eq. 2.16). Typical spatial extensions of 3d orbitals (in neutral atoms) amount to $\approx 0.3\,\text{Å}$–$0.5\,\text{Å}$ [17], while nearest magnetic-neighbour distances amount to $\approx 2.5\,\text{Å}$–$4\,\text{Å}$, implying the limited strength of the direct exchange.

2.3.2.2. Superexchange

Superexchange interaction refers to an exchange process which takes places between two magnetic ions via one or more mediating proxy ions. In the core of the superexchange interaction is the possibility of electrons' reduction in kinetic energy if they are able to delocalise from their ionic position. The delocalisation occurs via a virtual hopping

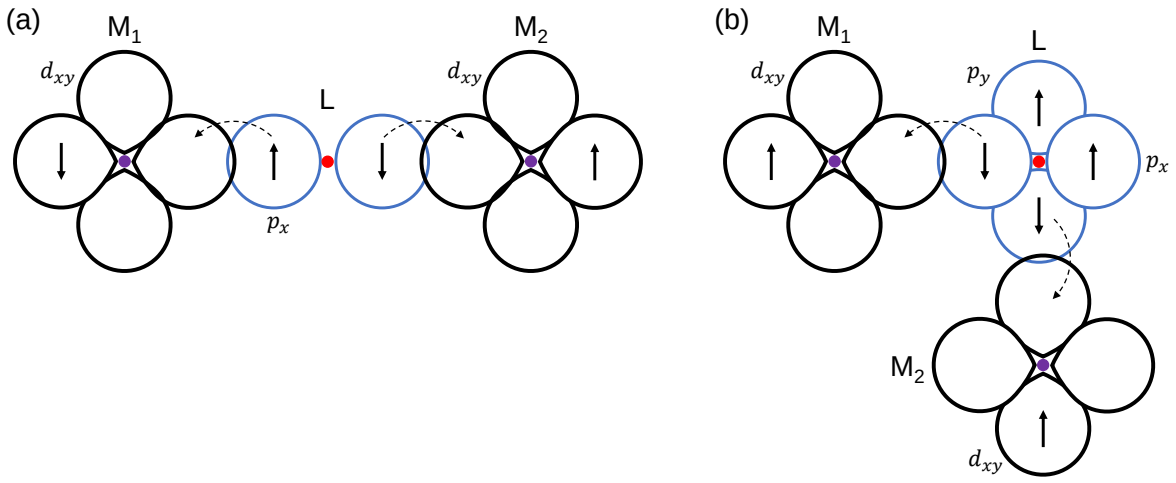

Figure 2.3.: Visualisation of a virtual hopping process of electrons from p orbitals (blue) of a ligand (L) to half-occupied d orbitals of a magnetic ion M_i (black) in a scenario of (a) 180°-bonding angle, and (b) 90°-bonding angle along the exchange path M_1–L–M_2. Purple (red) spheres depict the magnetic ions (ligands). After [25, 27].

process between overlapping orbitals of neighbouring ions.

Fig. 2.3 illustrates such a virtual hopping process for two different bonding angles along the exchange path of magnetic-ion–ligand–magnetic-ion, M_1–L–M_2. It is assumed that the bonding is perfectly ionic and that the respective d orbitals are singly occupied while the p orbitals are fully occupied. The Pauli exclusion principle implies that the two spins on the fully-occupied p orbitals are arranged in an antiferromagnetic fashion. When the bonding angle is 180° (Fig. 2.3a) and the spins on the magnetic ions arranged antiferromagnetically, both electrons can virtually hop from L, one to M_1, the other to M_2. On the other hand, if the spins on the magnetic ions were arranged ferromagnetically, only one such virtual hopping process would be permitted. Therefore, greater kinetic-energy saving is possible in the former case than in the latter case, favouring antiferromagnetic arrangement of the spins on the magnetic ions.

When the bonding angle is 90° (Fig. 2.3b), two p orbitals on the mediating ligand are involved in the superexchange process. If the spins on the magnetic ions are arranged ferromagnetically, two electrons of equal spin orientation undergo virtually hopping – one from the p_x orbital to M_1, one from the p_y orbital to M_2. This leaves behind two electrons of the same spin orientation on the ligand. If the spins on M_1 and M_2 were arranged antiferromagnetically, two electrons with opposite spin orientations can virtually hop from p_x and p_y orbital, respectively, leaving two electrons of opposite spin orientation behind on the ligand. Based on Hund's first rule, the scenario of two equally oriented spins on the ligand after the virtual hopping processes is energetically favourable, hence favouring the ferromagnetic arrangement of the spins on the magnetic

ions.

A number of orbital occupations and exchange paths are possible. The semi-empirical Goodenough-Kanamori-Anderson rules predict the sign of the resulting exchange interaction. A good overview of the rules may be found in [17].

2.3.2.3. Anisotropic Exchange

Through spin-orbit coupling, the isotropic exchange interaction (Eq. 2.18) becomes anisotropic. Consequently, the scalar quantity J_{ij} assumes a tensorial character [21]:

$$\begin{aligned}\mathcal{H} &= \sum_{<i,j>} J_{ij}\boldsymbol{S}_i \cdot \boldsymbol{S}_j \\ &\xrightarrow[\text{coupling}]{\text{spin-orbit}} \\ &= \sum_{<i,j>} \boldsymbol{S}_i \cdot J_{ij} \cdot \boldsymbol{S}_j \\ &= \underbrace{\sum_{<i,j>} J_{ij}\boldsymbol{S}_i \cdot \boldsymbol{S}_j}_{\text{isotropic}} + \underbrace{\sum_{<i,j>} \boldsymbol{S}_i \cdot \boldsymbol{K}_{ij}^{\text{sym}} \cdot \boldsymbol{S}_j}_{\text{anisotropic symmetric}} + \underbrace{\sum_{<i,j>} \boldsymbol{S}_i \cdot \boldsymbol{K}_{ij}^{\text{antisym}} \cdot \boldsymbol{S}_j}_{\text{anisotropic antisymmetric}}\end{aligned} \tag{2.19}$$

Here the first term is the isotropic component of the exchange Hamiltonian. The second term quantifies the anisotropic symmetric exchange, and the third term the anisotropic antisymmetric exchange interaction, where $\boldsymbol{K}_{ij}^{\text{sym}}$ and $\boldsymbol{K}_{ij}^{\text{antisym}}$ are the corresponding tensors. The symmetric part is invariant under the exchange of $\boldsymbol{S}_1$ and $\boldsymbol{S}_2$, whereas the antisymmetric changes sign under the exchange of $\boldsymbol{S}_1$ and $\boldsymbol{S}_2$. Moreover, perturbation theory reveals that the symmetric component of the anisotropic interaction scales linearly, while the antisymmetric component quadratically, with the spin-orbit-coupling constant [21]:

$$\begin{aligned}\boldsymbol{K}_{ij}^{\text{sym}} &\sim \left(\frac{\lambda}{\Delta E}\right)^2 J_{ij} \sim \left(\frac{\Delta g}{g}\right)^2 J_{ij} \\ \boldsymbol{K}_{ij}^{\text{antisym}} &\sim \left(\frac{\lambda}{\Delta E}\right) J_{ij} \sim \left(\frac{\Delta g}{g}\right) J_{ij}\end{aligned} \tag{2.20}$$

The anisotropic symmetric interaction is also known as the pseudo dipolar interaction, while the anisotropic antisymmetric interaction as the Dzyaloshinskii-Moriya interaction. It is the latter which shall be of interest in Chapter 5 of the present work. It is typically expressed as [17]:

$$\mathcal{H}_{\text{DM}} = \boldsymbol{d}_{ij} \cdot (\boldsymbol{S}_i \times \boldsymbol{S}_j) \tag{2.21}$$

where $\boldsymbol{d}_{ij}$ is a bond-dependent Dzyaloshinskii-Moriya vector. In order to obtain the total effect of the Dzyaloshinskii-Moriya interaction in a crystal, a sum of the individual

Dzyaloshinskii-Moriya vectors $\boldsymbol{d}_{ij}$ must be performed. Due to the cross product in Eq. 2.21, the Dzyaloshinskii-Moriya interaction acts against the collinearity of the isotropic and anisotropic symmetric interactions, favouring instead canting of the spins. As such, it may produce spiral and helical magnetic order.

2.4. Sources of Anisotropy

It may be observed that whenever the spin-orbit coupling constant is finite, it transmits the symmetry of the crystalline environment onto the spins, whence the spins become anisotropic. In this section, different anisotropy sources are briefly summarised.

2.4.1. Single-Ion Anisotropy

The single-ion (or single-site) anisotropy refers, as the name suggests, to the anisotropy effect which a magnetic ion acquires in isolation from other magnetic neighbours. Naturally, the presence of a ligand-caused crystal field which lifts the five-fold 3d-orbital degeneracy is necessary, for otherwise the spin-orbit coupling would vanish. The single-ion anisotropy was already encountered in Eq. 2.11. It takes the simplest form when all the elements of the anisotropy-constant tensor are zero with the exception Λ_{zz}. Then, $\mathcal{H}_{\mathrm{single-ion}} = -\lambda^2 \Lambda_{\mathrm{zz}} (S_{\mathrm{z}})^2$. It leads to zero-field splitting between states with different value of $|m_{\mathrm{S}}\rangle$, and in long-range-ordered magnets, it induces a finite zero-field excitation gap in the magnon energy spectrum (see the ensuing exposition in Section 2.6.1).

2.4.2. Interaction-Mediated Anisotropy

Apart from the anisotropy due to a single-site effect, the spin may acquire anisotropy also as a result of its interaction with spins on neighbouring magnetic sites. This effect has already been alluded to when discussing anisotropic exchange above.

2.4.2.1. Exchange-Mediated Anisotropy

Considering the anisotropic symmetric part of the Hamiltonian in Eq. 2.19 and taking $\boldsymbol{K}_{ij}^{\mathrm{sym}} = \mathrm{diag}(J_\perp, J_\perp\ J_\parallel)$, the exchange interaction becomes:

$$\sum_{<i,j>} \boldsymbol{S}_i \cdot \boldsymbol{K}_{ij}^{\mathrm{sym}} \cdot \boldsymbol{S}_j = \sum_{<i,j>} J_\parallel S_i^z S_j^z + J_\perp (S_i^x S_j^x + S_i^y S_j^y) \tag{2.22}$$

As can be readily observed in Eq. 2.22, the spins acquire an anisotropic character. If $J_\parallel > J_\perp$, the spins become Ising-like; if $J_\parallel < J_\perp$ they become XY-like. For $J_\parallel = J_\perp$, the isotropic symmetric Heisenberg exchange is recovered.

Moreover, the Dzyaloshinskii-Moriya interaction can too lead to anisotropic effects. This is owing to the presence of the Dzyaloshinskii-Moriya vector in Eq. 2.21.

2.4.2.2. Dipole-Dipole-Interaction-Mediated Anisotropy

The vectorial character of Eq. 2.12 indicates that the shear crystallographic arrangement of the magnetic moments in a solid with fixed mean distances and angular orientation of the lattice sites brings about preferential orientation of the magnetic moments. This effect is small on an absolute energy scale but it becomes important when spin-orbit coupling vanishes.

2.4.3. Shape Anisotropy

Another source of anisotropy which is not mediated by spin-orbit coupling and which can be understood in (semi-)classical sense is the shape anisotropy. It occurs whenever a surface forms in a magnetic medium. Additional energy is involved when magnetisation attempts to transgress a surface from a high-permeability medium to a low-permeability medium. A demagnetising field develops at the surface which acts against the magnetisation. Correspondingly, in the vicinity of the surface, the magnetic moments preferentially align parallel to the surface, hence following the shape of the sample. Shape anisotropy becomes appreciable when at least one of the sample's dimensions is significantly smaller than the remaining directions, such as in thin films.

2.5. Long-Range-Ordered Magnets

The aim of this section is to derive several important equations pertaining to the analysis of long-range-ordered magnetic systems undertaken in this study. More concretely, effective mean fields as well as the spin-flop field in an antiferromagnet are derived in terms of experimentally accessible quantities.

2.5.1. Microscopic Spin Hamiltonian

A minimal Hamiltonian required for describing magnetic systems with a large number of interacting spins at zero temperature is the following microscopic spin Hamiltonian [19]:

$$\mathcal{H} = \underbrace{\sum_{<i,j>} J_{ij} \boldsymbol{S}_i \cdot \boldsymbol{S}_j}_{\text{exchange}} \underbrace{- D_\mathrm{z} \sum_i (S_i^\mathrm{z})^2}_{\text{anisotropy}} \underbrace{- g\mu_\mathrm{B} \sum_i (\boldsymbol{S}_i \cdot \boldsymbol{B})}_{\text{Zeeman}} \tag{2.23}$$

The first term quantifies the Heisenberg exchange energy, the second term the anisotropy energy along the z-axis, and the third term the Zeeman energy. J_{ij} is the magnetic exchange constant between two magnetic neighbours, occupying the sites i and j, and D_z is the uniaxial anisotropy constant. The signs before the various terms imply that a positive value of J_{ij} minimises the system's energy for antiferromagnetic

arrangements of the spins, and a positive value of D_z selects out the z-axis as the easy magnetisation axis.

Refinement of the above terms in the Hamiltonian or addition of further terms may be required, depending on the system at hand. In particular, the Hamiltonian uses a generic uniaxial constant D_z without providing any indication as to what its origin may be. Moreover, additional interactions may be crucial for a particular system at hand. The sources of anisotropy and the different types of magnetic interactions were already addressed in Sections 2.4 and 2.3, respectively. Despite the present simplifications and omissions, the Hamiltonian is rich enough to enable the derivation of several important ground-state and low-energy excitation properties of long-range-ordered ferromagnets and antiferromagnets.

The derivations of these may follow one of at least two available routes: a quantum mechanical solution which involves the techniques of second quantisation in which the above spin operators $S_{i,j}$ are expressed in terms of S^z and of raising and lowering operators S^+ and S^-, and; a classical solution in which the on-site spin operators are replaced by magnetisation – a macroscopic, continuous quantity. The former received a detailed treatment, for example, in [19, 21, 28, 29]; the latter in [19, 21, 30, 31]. In the present case, the classical theory, which is in the literature also referred to as the phenomenological [21], molecular-field [32], mean-field [7], or effective-field [19] theory, shall be pursued, following mostly its exposition in [19].[1]

It ought to be remarked at this stage that an altogether different approach to deriving the ground-state and low-energy excitation properties is based on principles of Lagrangian mechanics with the corresponding solution formulated in terms of the symmetry of the exchange interactions [33, 34]. Although no further exposition of this approach shall be given in the present work, it may be noted that it predicts the same low-energy excitations as the other approaches, as long as the external field remains considerably smaller than the energy of the exchange interaction [34].

2.5.2. Classical Solution to Long-Range-Ordered Magnets

As already indicated above, the signature feature of the classical, mean-field theory in approaching the Hamiltonian in Eq. 2.23 is to consider the magnetic system at hand to be sufficiently large such that a definitive value of the magnetisation vector can be given at every spatial and temporal coordinate [21]. A further ingredient employed by the mean-field solution is to keep dividing up the ground state configuration into a finite number of interpenetrating sublattices until each sublattice consists only of spins which mutually stand in a ferromagnetic arrangement. Trivially, a ferromagnet consists

[1] As the quantities which are of interest in the present work are the effective, mean fields, the terminology of *(effective) mean fields* shall be adapted.

of only one sublattice. While this procedure may require a large number of divisions for antiferromagnets, the ensuing derivation shall be restricted to antiferromagnets with two sublattices.[2]

Mathematically, the move from the spin Hamiltonian to the continuous magnetic medium made up of up to two sublattices amounts to treating the spin operators $\boldsymbol{S}_{i,j}$ in the Hamiltonian in Eq. 2.23 as classical vectors which give rise to the macroscopic magnetisation on the two sublattices: $\boldsymbol{M}_{1,2} = g\mu_\mathrm{B} N \boldsymbol{S}_{i,j}$ where N is the number of magnetic moments per unit volume of the sublattice [19]. Moreover, the constants D_z and $J_{i,j}$ in Eq. 2.23 are replaced by the effective anisotropy field B_A, and by the effective exchange field B_E, respectively [19]:

$$\begin{aligned} B_\mathrm{A} &= (2SD_\mathrm{z})/(g\mu_\mathrm{B}) \\ B_\mathrm{E} &= (2SzJ_\mathrm{eff})/(g\mu_\mathrm{B}) \end{aligned} \tag{2.24}$$

Here, J_eff is the effective exchange constant which couples the two sublattices with one another, replacing all the individual exchange couplings J_{ij} between any two magnetic sites i and j. Note that the inclusion of the factor 2 and of the number of nearest neighbours z in the above definitions is not prescribed by theoretical considerations and is, instead, a matter of convention. Due care must be taken when comparing results from different studies, as the present convention is not followed universally.

Equipped with the transformation of the spin operators to sublattice magnetisations and with the definitions of the effective fields, the Hamiltonian in Eq. 2.23 can be expressed in mean-field terms as [19]:

$$E = \frac{B_\mathrm{E}}{M}\left(\boldsymbol{M}_1 \cdot \boldsymbol{M}_2\right) - \frac{B_\mathrm{A}}{2M}\left((M_1^z)^2 + (M_2^z)^2\right) - \boldsymbol{M}_1 \cdot \boldsymbol{B} - \boldsymbol{M}_2 \cdot \boldsymbol{B} \tag{2.25}$$

2.5.3. Derivation of Effective Exchange and Anisotropy Fields

Since the magnetisation in Eq. 2.25 is a classical vector, it can be decomposed into its orthogonal components or, alternatively, associated with polar angles. When the external magnetic field is applied along the easy magnetisation axis (i.e. the z-axis based on Eqs. 2.23 and 2.25), the easy-axis component can be expressed as $M_1^\mathrm{z} = |\boldsymbol{M}|\cos(\theta)$ and $M_2^\mathrm{z} = |\boldsymbol{M}|\cos(\phi)$. Here, θ and ϕ are polar angles which the sublattice magnetisation encloses with the external magnetic field. Eq. 2.25 can be now expressed as [19]:

$$\frac{E(\theta,\phi)}{M} = B_\mathrm{E}\left(\cos(\theta+\phi)\right) - \frac{B_\mathrm{A}}{2}\left(\cos^2(\theta) + \cos^2(\phi)\right) - B_\mathrm{z}\left(\cos(\theta) + \cos(\phi)\right) \tag{2.26}$$

[2] The derivations for n-sublattice systems with $n > 2$ are performed in the same spirit as their simpler two-sublattice counterpart; however, the mathematical complexity increases rapidly as n is increased above two (see, e.g., the treatment of a six-sublattice antiferromagnet in [35]).

To find the expression for the effective exchange and anisotropy fields in terms of the experimentally-accessible spin-flop field B_{SF} and saturation field B_{sat}, the configuration of the sublattice magnetisation is obtained by deriving $\partial E(\theta,\phi)/\partial\theta \stackrel{!}{=} 0$ and $\partial E(\theta,\phi)/\partial\phi \stackrel{!}{=} 0$. Recognising that for $B_{\mathrm{z}} < B_{\mathrm{SF}}$, $\theta = 0$ and $\phi = \pi$; for $B_{\mathrm{SF}} \leq B_{\mathrm{z}} < B_{\mathrm{sat}}$, $\theta = -\phi$, and; for $B_{\mathrm{sat}} \leq B_{\mathrm{z}}$, $\theta = \phi = 0$, the effective exchange and anisotropy fields are found to be given by:

$$\begin{aligned} B_{\mathrm{A}} &= \frac{B_{\mathrm{SF}}^2}{B_{\mathrm{sat}}} \\ B_{\mathrm{E}} &= \frac{B_{\mathrm{sat}}}{2} + \frac{B_{\mathrm{SF}}^2}{2B_{\mathrm{sat}}} \end{aligned} \tag{2.27}$$

The above derivation also finds that the angle between the sublattice magnetisation and the external magnetic field in the spin-flop phase is given by $\theta(B_{\mathrm{SF}} \leq B_{\mathrm{z}} < B_{\mathrm{sat}}) = \cos^{-1}(B_{\mathrm{z}}/(2B_{\mathrm{E}} - B_{\mathrm{A}}))$. In addition, from Eq. 2.27 it follows that the spin-flop field is given by:

$$B_{\mathrm{SF}} = \sqrt{2B_{\mathrm{E}}B_{\mathrm{A}} - B_{\mathrm{A}}^2} \tag{2.28}$$

2.6. Electron Spin Resonance

Electron spin resonance is the phenomenon of resonant absorption of light by an electron.[3] The energy of the absorbed light depends, among others, on the total magnetic field which the electron experiences. The latter, in turn, may be a complicated function of the internal fields acting on the electron, such as the exchange interaction and various anisotropy effects, and the external, applied magnetic field.

2.6.1. Landau-Lifshitz-Gilbert Equation

The dynamics of the electron's spin in a magnetic field is described by the Landau-Lifshitz-Gilbert (LLG) equation [19, 21][4]:

$$\frac{\partial \boldsymbol{S}}{\partial t} = -\gamma \boldsymbol{S} \times \boldsymbol{B} + \gamma \frac{\lambda}{|\boldsymbol{S}|} \boldsymbol{S} \times (\boldsymbol{S} \times \boldsymbol{B}) \tag{2.29}$$

Here, $\gamma = (g\mu_{\mathrm{B}}/\hbar)$ is the gyromagnetic ratio, whereby $\hbar$ is the reduced Planck constant, $\boldsymbol{S}$ is the spin vector $\boldsymbol{S} = (S^x\ S^y\ S^z)^{\mathrm{T}}$, $\boldsymbol{B}$ the applied magnetic field, and λ a small unitless constant. The first term in Eq. 2.29 describes the torque exerted by the applied magnetic field on the spin and thus quantifies the driving aspect of the dynamics, whereas the second term describes the restoring of the equilibrium state and thus

[3] The phenomenon goes also by name of electron *paramagnetic* resonance. In the present work, the nomenclature of *spin* resonance is adopted in order to avoid the misunderstanding that the investigated resonant behaviour might be associated exclusively with paramagnetic electrons.

[4] A comprehensive mathematical overview of the LLG equation may be found in [36].

quantifies the damping aspect of the dynamics. After a suitable rescaling, Eq. 2.29 can be cast into the compact form [36]:

$$\frac{\partial \boldsymbol{S}}{\partial t} = \gamma \boldsymbol{S} \times \boldsymbol{B}_{\text{eff}} \tag{2.30}$$

where $\boldsymbol{B}_{\text{eff}}$ now denotes the effective field acting on the electron. The LLG equation can be extended to systems with a macroscopic number of electrons. To do so, the same reformulation in terms of macroscopic mean-field quantities is undertaken as in Section 2.5.2, i.e. individual spin operators are replaced by the magnetisation vector $\boldsymbol{M} = g\mu_{\text{B}} N \boldsymbol{S}_i$. Then, Eq. 2.30 takes the form [36]:

$$\frac{\partial \boldsymbol{M}}{\partial t} = \gamma \boldsymbol{M} \times \boldsymbol{B}_{\text{eff}} \tag{2.31}$$

Qualitatively, Eq. 2.31 implies that a magnetisation vector $\boldsymbol{M}$ placed in an effective field $\boldsymbol{B}_{\text{eff}}$ will experience a torque perpendicular to the magnetisation orientation. The torque will induce a precession of the magnetisation around its equilibrium orientation. Hence, the magnetisation vector can be expressed as $\boldsymbol{M} = (M_{\text{x}} e^{i(2\pi\nu)t}\ M_{\text{y}} e^{i(2\pi\nu)t}\ M_{\text{z}})^{\text{T}}$, where ν is the precession frequency [19].

Due to the non-linearity of the LLG equation, its solutions can be highly complex. Nevertheless, approximate analytical solutions can be derived under suitable approximations which linearise the dependencies. One such approximation is to treat the magnetisation precession as being limited to very small angles, such that the component of the magnetisation along the easy magnetisation (z-)axis remains constant, $M_{\text{z}} = |\boldsymbol{M}|$. Correspondingly, for the components of the magnetisation vector perpendicular to the easy axis, it holds $M_{\text{x}}, M_{\text{y}} \ll M_{\text{z}}$.

2.6.2. Solutions of the Landau-Lifshitz-Gilbert Equation

In order to find the solution of the LLG equation for a concrete magnetic system, an expression for the effective field $\boldsymbol{B}_{\text{eff}}$ is required. This may be obtained from the thermodynamic relation [19]:

$$\boldsymbol{B}_{\text{eff}} = -\vec{\nabla}_{\text{M}}[E(\boldsymbol{M})] \tag{2.32}$$

where the nabla operator performs a vector differentiation of the free energy E with respect to the three orthogonal components of the magnetisation.[5] That is, if the system's free energy is known in terms of the magnetisation, the magnetisation dynamics can be calculated. For example, $\boldsymbol{B}_{\text{eff}}$ of an antiferromagnet with a uniaxial anisotropy

[5] The non-linearity of the LLG equation can be seen by observing that the effective field $\boldsymbol{B}_{\text{eff}}$ featuring in Eq. 2.32 and being substituted into Eq. 2.31 is itself via its dependence on the free-energy derivative a function of the magnetisation.

is calculated by substituting Eq. 2.25 into Eq. 2.32.

2.6.2.1. Paramagnetic Resonance

The most elementary mode of magnetic excitation is that of a paramagnet. As paramagnet is, by definition, not long-range-ordered, no collective excitations are possible.[6] In such a case, the free energy contains only the contribution from the Zeeman term, while all other internal fields vanish (in particular, $B_\mathrm{E} = B_\mathrm{A} = 0$). The solution of the LLG equation yields:

$$\nu = \frac{g\mu_\mathrm{B}B}{h} \tag{2.33}$$

That is, linear field dependence of the resonance frequency with no zero-field excitation gap is predicted (see Fig. 2.4a). The lack of zero-field excitation gap implies that the magnetic moments have no preferred orientation, i.e. are isotropic.

2.6.2.2. Ferromagnetic and Antiferromagnetic Resonance

For long-range-ordered magnetic systems, the low-energy solutions of the LLG equation represent collective excitations of all the spins in the system. These are known in classical terms as *spin waves* and in quantum-mechanical terms as *magnons*. The resonant behaviour of the system is typically referred to as *ferromagnetic resonance* (FMR) or *antiferromagnetic resonance* (AFMR). The analytical solutions of the LLG equation may be found, for instance, in [19, 20, 22, 37] for ferromagnets, and in [19, 21, 22, 30, 31] for antiferromagnets. The appropriate solutions shall also be stated in full when discussing a concrete material's results in the respective chapters. In the present case, solutions to selected magnetic systems are discussed in qualitative terms, so as to demonstrate FMR's and AFMR's general features. The assumption is made that the respective magnetic system is made up of one magnetic domain and is at $T = 0\,\mathrm{K}$.

Resonance-Frequency–Magnetic-Field Diagram of a Mean-Field Ferromagnet

An isotropic mean-field ferromagnet of a spherical shape exhibits qualitatively and quantitatively the same field dependence of the resonance frequency as a paramagnet (black solid line, Fig. 2.4b). The ferromagnetic arrangement of the moments ensures that all the magnetic moments precess in unison, forming, as it were, a single paramagnetic spin.

However, once the shape of a ferromagnet departs from a perfect sphere, demagnetisation fields change the internal field experienced by the magnetic moments, resulting in altered field dependence of the resonance modes. Orange solid lines in Fig. 2.4b show the qualitative behaviour of an isotropic ferromagnet in shape of an infinitely thin disc. It may be seen that when the external field is applied parallel to the disc's plane, the

[6] Here, the denotation "EPR", that is, *electron paramagnetic resonance*, is often used in the literature.

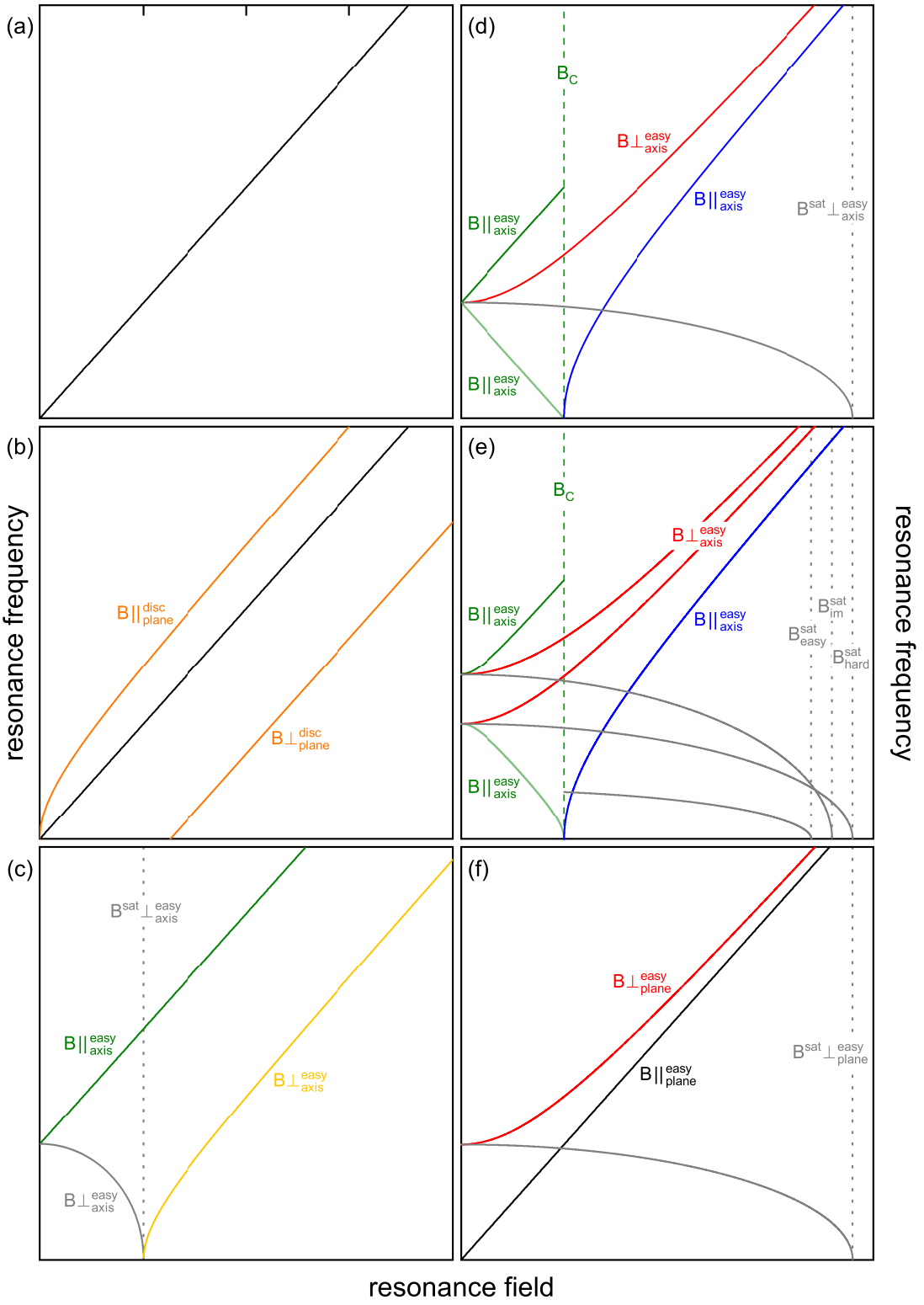

Figure 2.4.: Simulated mean-field-theory-based field dependence of resonance modes in: (a) paramagnet; (b) ferromagnet (FM) of spherical shape (black solid line), of thin-disc shape (orange solid lines); (c) FM of spherical shape with easy-axis anisotropy; and in antiferromagnets with (d) easy-axis, (e) orthorhombic, and (f) easy-plane anisotropy. Where appropriate, B_{SF} marks the spin-flop field and various B^{sat} the saturation fields.

resonance frequency is enhanced with respect to the spherical sample, whereas when the field is applied orthogonally to the disc's plane, considerable reduction of the resonance frequency is expected. Due to the assumed isotropy, no zero-field splitting is predicted.

On the other hand, if the ferromagnet is taken to be anisotropic, a zero-field excitation gap opens up (Fig. 2.4c). In fact, the size of the gap in ferromagnets is linearly dependent on the effective anisotropy field, $\Delta_{\mathrm{FM}} \propto B_{\mathrm{A}}$ [37]. When the external magnetic field is applied perpendicularly to the anisotropy axis, square-root-dependent reduction of the resonance frequency is predicted up to the saturation field, above which the frequency increases in an approximately linear fashion.

Interestingly, because the magnetisation is always parallel to the effective exchange field in a ferromagnet, the torque exerted by the exchange field onto the magnetisation is zero [37]. This implies that the ferromagnetic resonance frequency remains always independent of the ferromagnetic exchange field, irrespective of the ferromagnet's shape or the presence of anisotropy.

Resonance-Frequency–Magnetic-Field Diagram of a Mean-Field Antiferromagnet

The magnetic resonance phenomena in antiferromagnets depend on both, the effective anisotropy field and the effective exchange field. Unlike for the ferromagnets, it is the interplay between the anisotropy and exchange which gives rise to the zero-field excitation gap in long-range-ordered antiferromagnets. The analytical expression for the excitation gap is $\Delta_{\mathrm{AFM}} = \gamma\sqrt{2B_{\mathrm{E}}B_{\mathrm{A}} + B_{\mathrm{A}}^2}$ [38]. Consequently, the resonance frequency in mean-field antiferromagnets is a function of both, the anisotropy field and the exchange field, and, due to the typically large values of B_{E}, considerably higher than in ferromagnets [19]. On the other hand, due to the antiferromagnetic arrangement of the magnetic moments, the total demagnetisation field vanishes.

Figs. 2.4d–f depicts the simulated magnon branches for three types of mean-field antiferromagnets: with uniaxial anisotropy (Fig. 2.4d); with orthorhombic anisotropy (Fig. 2.4e), and; with easy-plane anisotropy (Fig. 2.4f). Several features which all the three system have in common can be observed in the figures. Firstly, antiferromagnets with a unique easy axis – i.e. systems with uniaxial or orthorhombic anisotropy – exhibit two magnon modes of opposite field dependence when the field is applied along the easy axis (solid green lines in Figs. 2.4d and 2.4e). One of the branches decreases in frequency until it reaches the critical field B_{C}, above which the spin-flop mode appears (solid blue lines in Figs. 2.4d and 2.4e). The critical field itself is given by $B_{\mathrm{C}} = \sqrt{2B_{\mathrm{E}}B_{\mathrm{A}} + B_{\mathrm{A}}^2}$ and is thus intrinsically related to the excitation gap Δ_{AFM} [38]. Secondly, whenever the field is applied orthogonally to an anisotropy axis in whichever of the three antiferromagnetic systems, a finite gap has to be overcome and the corre-

sponding resonance branch shows left-bending in the low-field regime, assuming ever greater linear character as the field is increased (solid red lines in Figs. 2.4d–f). Thirdly, each of the systems exhibits at least one magnon mode for which the resonance frequency decreases with increasing field, before completely vanishing at the saturation field (solid grey lines in Figs. 2.4d–f).[7]

A mean-field antiferromagnet with orthorhombic anisotropy is the only two-sublattice antiferromagnet with two zero-field excitations gaps, corresponding to two easy axes. When the anisotropy of one of easy axes is removed, the two gaps and the two branches associated with $B \perp$ easy axis merge into one and a mean-field antiferromagnetic with uniaxial anisotropy is recovered (c.f. Fig. 2.4d).

A special feature of the mean-field antiferromagnet with easy-plane anisotropy is its exhibition of a gapless magnon mode, the field dependence of which is identical to that of a regular paramagnet. This magnon mode is excited when the field is applied within the easy plane, whereby the magnetic moments undergo a spin flop within the plane at zero field.

[7] These modes are usually not observable in a field-swept experiment, as they remain almost field-independent at typically-accessible static fields. For illustration purposes, the saturation fields in Figs. 2.4d–f were chosen to lie at unreasonably low values given the choice of the other simulation parameters.

3. Experimental Methods

This chapter provides an overview of the experimental techniques employed in course of the present work. The intention is to provide a general operation principle and measurement recipes of the various techniques. Peculiarities, if any, pertaining to the individual measurements are addressed in the respective results chapters (see especially Chapter 6).

3.1. High-Frequency Electron Spin Resonance

The basic operational scheme of the high-frequency electron spin resonance (HF-ESR) experiment utilised in this work is as follows (see Fig. 3.1):

1. Electromagnetic waves in a tunable continuous microwave range of base frequency $8\,\mathrm{GHz} \lesssim \nu \lesssim 18\,\mathrm{GHz}$ are generated by a pair of YIG oscillators within a Millimeter Vector Network Analyzer (MVNA), from AB Millimetre [39];
2. the frequency of the generated microwaves is fixed by a frequency counter (EIP 575B Source Locking Microwave Counter, produced by Phase Matrix);
3. the microwaves (red lines in the figure) are guided via coaxial cables (blue lines) into a harmonic generator (HG) which multiplies the microwaves' base frequency;
4. the microwaves are subsequently guided via feed horns (not shown) into an oversized waveguide which is installed in a vacuum-sealing sample rod;
5. the sample of interest (dark blue square) is mounted in the way of the propagating microwaves on the bottom of the sample rod;
6. the transmitted microwaves are guided through a second waveguide to the top of the sample rod and into a harmonic mixer (HM), whereby all the steering of the microwaves is carried out by gold-coated mirrors (dark yellow lines in the figure);
7. the frequency of the microwaves is scaled down in the HM to the original base frequency and transmitted to the MVNA via another coaxial cable;
8. to improve detection sensitivity, the transmitted microwave signal received by the MVNA is sent to a lock-in amplifier (Model SR830 DSP, produced by Stanford Research Systems) together with a reference signal of $\nu = 10.488\,\mathrm{kHz}$ (green line);
9. the lock-in amplifier decomposes the received signal into its amplitude and phase components, amplifying the amplitude in the process;
10. the signal read-out from the lock-in amplifier is facilitated by a LabView programme on a PC.

The harmonic generator and the harmonic mixer consist of a series of Schottky diodes

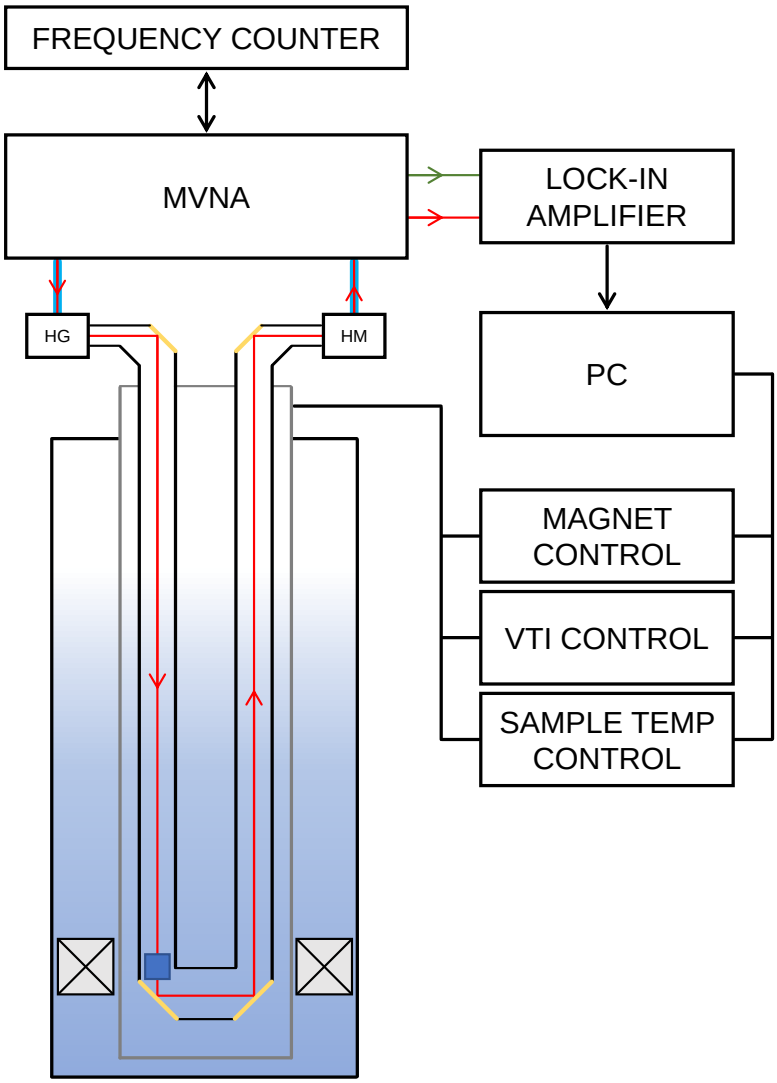

Figure 3.1.: Schematic visualisation of the high-frequency electron spin resonance experimental setup, see text for details of operation. After [25].

and are also produced by AB Millimetre. These are classified by their harmonic number N which specifies the multiplication of the base frequency. Harmonic generators and mixers are available with harmonic numbers sufficient to provide a (quasi-)continuous frequency coverage in the range $30\,\mathrm{GHz} \lesssim \nu \lesssim 1000\,\mathrm{GHz}$. Depending on the desired frequency, additional amplifiers, attenuators, or filters are installed on the harmonic generator and mixer. For $\nu \lesssim 30\,\mathrm{GHz}$ no propagation of the microwaves is possible through the waveguides due to the waveguides' cut-off frequency [40], while for increasing frequency, the observed dynamic range decreases.

As depicted in Fig. 3.1, for measurements, the sample rod is inserted into a liquid-helium cryostat with a superconducting magnet (grey squares with a cross). The superconducting coil is made of Nb_3Sn and generates magnetic fields up to $B_{\mathrm{ext}} =$

$\pm 18\,\mathrm{T}$. The liquid-helium reservoir serves for cooling of the superconducting magnet as well as of the sample. The latter is facilitated by a variable temperature insert (VTI) and allows to reach stable sample temperature down to $\approx 1.8\,\mathrm{K}$. Sample heating is provided by two separate resistive heaters: one located at the needle valve of the VTI, another directly at the sample. Sample temperature is measured by Cernox thermometer, model CX-1040, produced by Lake Shore. The magnet is controlled by Intelligent Power Supply (Mercury iPS), the VTI by Intelligent Temperature Controller (Mercury iTC), and the sample heater by 340 Temperature Controller. The cryostat, the superconducting magnet, the VTI, the iPS, and the iTC are products of Oxford Instruments. The temperature controller, which also reads the sample temperature, is a product of Lake Shore.

The magnetic field in the experiment is oriented vertically, the electric and magnetic components of the microwave radiation along the waveguide inside the sample rod horizontally. Hence, the experiments are performed in the Faraday configuration ($B_{\mathrm{ext}} \perp k_{\mathrm{MW}}$, where k_{MW} is the microwave wavevector). The microwave radiation remains unpolarised throughout the experiment. Due to the technical complexity of sustaining constant microwave intensity with varying microwave frequency, the experiments are performed in a field-swept mode. That is, the desired frequency ν is selected and locked by the frequency counter, B_{ext} from the superconducting magnet swept at a rate $1\,\mathrm{T/min}$, while the sample temperature is held constant. Owing to the utilisation of the lock-in amplifier for detection, the absolute values of the transmitted microwave amplitude cannot be conveyed. Instead, microwave transmitted amplitude and microwave phase as modulated by the lock-in amplification are recorded as a function of the swept field and constitute the acquired spectra.

A pure, undistorted transmitted amplitude, A_{pure}, is expected to assume a Lorentzian shape. However, owing to a number of intrinsic and extrinsic parameters, the detected amplitude, A_{det}, may become distorted by way of mixing-in of the microwave phase, that is of wave dispersion, D_{det}. Not only does such a distortion change the shape of the true resonance signal but it also masks the true resonance-field position. Throughout this work, this effect is referred to as wave-phase mixing. An important intrinsic parameter which affects the detected lineshape is the penetration depth of the microwaves into the sample, which itself is a function of the microwave frequency, and of the sample's conductivity and relative permeability [41]. The extrinsic parameters are given by the efficiency of microwave propagation through the waveguides and of microwave coupling to the sample. These in turn are a function, among others, of the sample shape and of the sample and waveguides temperature. To reconstruct the true lineshape of the resonance signal, $A_{\mathrm{pure}}(B) = \pm(1+\epsilon)^{-1}[A_{\mathrm{det}}(B) + \epsilon D_{\mathrm{det}}(B)]$ is calculated, where $\epsilon \leq 1$ is a parameter which quantifies the fractional admixture of the dispersion relative to the amplitude [42]. Under the assumption that A_{det} and D_{det} have been nor-

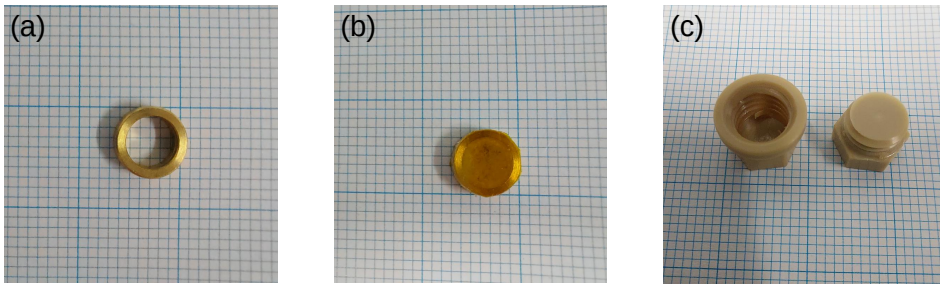

Figure 3.2.: (a) Empty brass ring used as a sample holder for HF-ESR measurements; (b) brass ring filled with an eicosane-fixed sample and covered by a layer of Kapton tape; (c) empty PEEK sample holder used for air- or light-sensitive samples.

malised with respect to each other appropriately, i.e. according to the Kramers-Kronig relations, the absolute value of the amplitude may too be recovered [40, 43].

A standard sample holder consists of a home-made brass ring, the top and bottom of which is sealed by a layer of Kapton tape. Single-crystal samples are fixed within the brass-ring-Kapton-tape structure by another layer of Kapton tape. Polycrystalline powders can be measured in the so-called "loose-powder" or "fixed-powder" arrangement, whereby the present work employed only the latter arrangement. This comprises a preparation of a mixture of the desired polycrystalline material with eicosane powder within the brass-ring-Kapton-tape structure, approximately in 1-to-1 volume ratio. Sealing both ends of the brass ring with Kapton tape, the structure is heated up by a heat gun up to $\approx 40\,^{\circ}\mathrm{C}$, upon which the eicosane powder melts and flows through the powder of interest. When the heat source is removed, the eicosane powder solidifies, fixing the polycrystalline powder of interest in its random orientation in the process. For air- or light-sensitive samples (c.f. Chapter 6), a home-made sample holder manufactured from PEEK material is utilised. This features a screwing lid, the windings of which may be wrapped in several layers of teflon tape to enhance the sealing capabilities.

For illustration purposes, an empty brass ring is depicted in Fig. 3.2a, a brass ring filled with a fixed-powder sample and covered by a layer of Kapton tape in Fig. 3.2b. Fig. 3.2c shows the PEEK sample holder.

The prepared sample is fixed into a home-made sample holder and attached to the sample rod. Prior to installing the sample rod into the cryostat, three cycles of vacuum-pumping–helium-gas-purging are performed. Subsequently, helium exchange gas of $p \approx 250\,\mathrm{mbar}$ (at room temperature) is introduced into the sample rod. The exchange gas enables good temperature control of the sample during measurements.

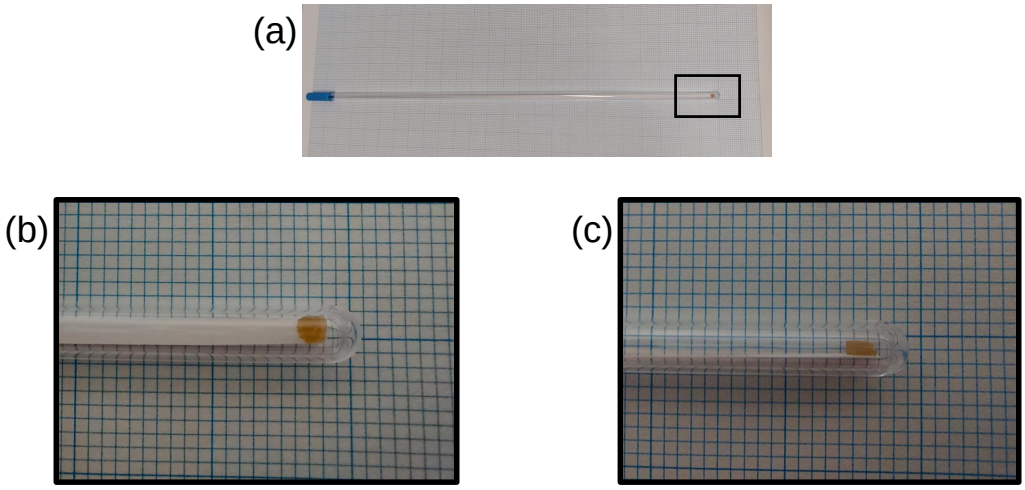

Figure 3.3.: (a) EPR quartz tube used as a sample holder for X-band electron spin resonance. A single-crystal sample is attached to a paper strip on the bottom of the tube, marked by a black rectangle; (b)–(c) magnification of the sample along two different orientations.

3.2. X-Band Electron Spin Resonance

Electron spin resonance in the X-band frequency range was performed in the research group of Prof. Dr. Peter Comba at the Institute of Inorganic Chemistry, Heidelberg University. The employed measurement setup consists of a commercial Elexsys E500 CW-EPR spectrometer, produced by Bruker, which delivers a continuous-wave signal. The setup utilises a rectangular resonator cavity, model ER 4122SHQE, which possesses two resonance modes: $\nu \approx 9.6\,\mathrm{GHz}$ with $B_{\mathrm{ext}} \perp k_{\mathrm{MW}}$ (Faraday configuration), and; $\nu \approx 9.4\,\mathrm{GHz}$ with $B_{\mathrm{ext}} \parallel k_{\mathrm{MW}}$ (Voigt configuration). Tuning of the incident microwave frequency enables access to either of the modes, whereby the precise resonance frequency depends on the concrete geometry of the measurement, in particular, on the shape of the sample and of the sample holder. The Q-factor of the cavity, defined as $Q = \nu/(\Delta\nu)$ is typically $Q \approx 4000$–5000 for the Faraday, and $Q \approx 3000$–4000 for the Voigt configuration.

External magnetic field accessible in the range $0\,\mathrm{T} \leq B_{\mathrm{ext}} \lesssim 1.2\,\mathrm{T}$ is provided by an electromagnet. The detection sensitivity is enhanced by applying a small oscillating magnetic field which modulates the main external magnetic field B_{ext}. The amplitude of the modulation field may be adjusted and lies typically in the range $1\,\mathrm{G}$–$10\,\mathrm{G}$. By applying the modulation field, the detected signal assumes a character of a derivative of a Lorentzian function.

Sample cooling down to $\approx 5\,\mathrm{K}$ is provided by a Cryo Edge cryostat. This utilises gaseous helium which is cooled by a compressor. The sample is heated by a resistive heater, and the heating as well as the temperature reading are facilitated by an Mercury iTC, produced by Oxford Instruments. Note that the spectra presented in the frame

	MPMS 3	PPMS
sample temperature range	1.8 K – 400 K	1.8 K – 400 K
DC magnetic field range	−7 T – 7 T	−14 T – 14 T
DC-mode measurement	yes	no
VSM-mode measurement	yes	yes
SQUID detection	yes	no
AC-field amplitude	0.1 Oe – 10 Oe	0.1 Oe – 17 Oe
AC-field frequency	0.1 Hz – 1 kHz	10 Hz – 10 kHz

Table 3.1.: Selected capabilities of the MPMS 3 and the PPMS used in magnetisation measurements.

of this work were recorded solely at room temperature.

Single-crystal samples are attached by a small amount of GE varnish to the bottom of a long paper strip which is inserted into an EPR quartz tube, produced by Sigma-Aldrich. For low-temperature measurements, the quartz tube is filled with argon and sealed. Fig. 3.3 depicts a single-crystal sample prepared for a measurement in the EPR quartz tube.

3.3. Magnetometry

Magnetisation measurements were performed in a DC-field as well as in an AC-field mode. For each of the options, two separate commercial devices were available: Magnetic Property Measurement System, MPMS 3, and; Physical Property Measurement System, PPMS; both of which are products of Quantum Design. Selected capabilities of each device are listed in Table 3.1. The choice of device for a particular measurement depended on concrete requirements, such as preference for signal detection by means of a SQUID (MPMS) or requirement of large AC-field excitation frequencies (PPMS), see Table 3.1.

3.3.1. DC-Field Magnetisation

DC-field magnetisation measurements involve measuring the DC magnetic moment of a sample, μ_{DC}, at particular sample temperature upon the application of a DC magnetic field.

In the course of this work, field-swept and temperature-swept measurements of the DC-field magnetisation were performed. Field-swept measurements involve measuring the magnetic moment as a function of applied magnetic field while the sample temperature is held constant. These shall be henceforth designated as isothermal magnetisation measurements. To perform them, the desired sample temperature was held constant

for 120 s prior to the start of the field sweep. Typical field sweep rates were 30–50 Oe/s. The magnetic moment was recorded upon ramping-up and ramping-down of the field, with a short pause in between (≈ 10 s).

Temperature-swept measurements involve measuring the magnetic moment as a function of temperature in a constant applied field. In the present work, the magnetic moment was recorded upon heating with typical sweep rates of 1 K/min. When recording the moment upon heating, an important defining parameter of the measurement is whether the applied magnetic field is present already during the cooling (field-cooled measurement) or whether the cooling takes place with no applied field and the field is applied only once the starting measurement temperature has been reached (zero-field-cooled measurement). The particular measurement mode in the present work is specified when introducing the experimental data for each respective material and concrete measurement. A typical quantity of interest resulting from temperature-swept measurements of μ_{DC} is the static magnetic susceptibility, χ. This is defined as $\chi = M/B$, where M is the sample magnetisation and B the applied magnetic field. Hence, the temperature-swept measurements of the DC magnetic moment shall be designated as static magnetic susceptibility measurements in the ensuing.

The measurement of the magnetic moment is realised by moving the sample through a set of pick-up coils, either singularly with a large scan length (DC mode) or in a vibrating fashion with a small vibration amplitude (VSM[1] mode). The moving sample induces a potential difference in the coils which is detected. The MPMS is capable of performing both measurement modes, employing a detection by a SQUID[2] which is built incorporated in the pick-up coil circuit while fully isolated from the sample space. The PPMS utilises only the VSM mode, whereby the detection of the potential difference induced in the pick-up coils is read-out directly, i.e. without a SQUID. Operation overview of a SQUID magnetometer may be found, for instance, in [44–46], that of a VSM, for instance, in [47]. When employing the SQUID magnetometer of the MPMS, a typical scan length through the pick-up coils of 30 mm with a scan time of 4 s was used. A typical peak amplitude of vibration in the VSM-mode measurements was 4 mm with averaging time of 2 s. In the MPMS, the VSM mode is operated at a pre-set frequency of 14 Hz–16 Hz, while in the PPMS, a choice of vibration frequency is possible; typically 40 Hz was used.

For DC-magnetisation measurements on powder samples, a sufficient amount ($m \approx$ 5 mg–10 mg) of the desired material was transferred by a spatula into a polypropylene capsule. To ascertain the mass of the powder, the capsule was weighed first without the sample and subsequently with the sample. In case of DC-magnetisation measurements on single crystals, thick enough samples were mechanically fixed between two quartz

[1] Vibrating-Sample Magnetometer
[2] Superconducting Quantum Interference Device

spacers within a brass holder; thin samples were fixed by Kapton tape onto a quartz sample holder. The polypropylene capsules as well as the brass and quartz sample holders are products of Quantum Design.

3.3.2. AC-Field Magnetisation

AC-field magnetisation measurements are based on the application of a small oscillating magnetic field, B_{AC}, on the background of a larger, DC magnetic field, B_{DC}, and the detection of the sample's magnetic moment. The oscillatory nature of B_{AC} induces a time-dependent moment in the sample. The AC susceptibility is given by $\chi_{\mathrm{AC}} = \chi' + i\chi''$, where χ' is the real, in-phase component, and χ'' the imaginary, out-of-phase component. The two components are given by:

$$\begin{aligned} \chi' &= \left(\frac{\partial M}{\partial B_{\mathrm{DC}}}\right)\cos\phi \\ \chi'' &= \left(\frac{\partial M}{\partial B_{\mathrm{DC}}}\right)\sin\phi \end{aligned} \tag{3.1}$$

where $\partial M/\partial B_{\mathrm{DC}}$ is the slope of the isothermal magnetisation curve.

The present work utilised the AC-susceptibility option of both of the available devices. In the MPMS, the three-point-measurement cycle was employed in which the sample's AC susceptibility is measured in a sequence at three spatial points within the detection coils: at the central point of the gradiometer; followed by the point of the gradiometer's maximum response; followed again by the central point of the gradiometer. Such a measurement cycle enhances the measurement sensitivity. The PPMS does not allow for the choice of the measurement cycle. Instead, a pre-set cycle is utilised by the device which involves measurements of the AC susceptibility in two separate counter-wound coils and in a compensation coil. The measurements details of the AC-susceptibility measurements on the two devices may be found in the respective manuals [48, 49].

Samples were either fixed by Kapton tape onto a quartz sample holder, akin to the DC-magnetisation measurements, or fixed by Kapton tape to a small teflon platform which was slid into a plastic straw.

3.4. Laue X-Ray Diffraction

Laue X-ray diffraction was utilised in the present study to verify the quality of single crystal samples and to obtain information on their crystallographic orientation. Back-scattering geometry in which the X-ray source and detector are located in the same plane was employed. The home-made setup consists of an X-ray tube in which electrons are accelerated towards a tungsten anode. The deceleration of the electrons upon interaction with the anode generates *Bremsstrahlung*, braking radiation. The detector

comprises a combination of a scintillating layer of Tb-doped Gd_2O_2S and two CCD cameras. Tube current $I = 20\,\mathrm{mA}$ and acceleration voltage $V = 35\,\mathrm{kV}$ with image exposure time $t = 300\,\mathrm{s}$ were typically used. During image acquisition, the sample was fixed on a goniometer which enabled the sample's orientation. The image analysis was performed by freely-accessible software CLIP [50].[3]

3.5. Note on Usage of Symbols and Units

Throughout this work and following the English-language-literature nomenclature, the distinction between the magnetic field strength $H = [\mathrm{Oe}]$ and the magnetic flux density $B = [\mathrm{G}]$ is not followed. All designations of magnetic field (strengths), may they be referring to internal fields, such as the exchange field, or to external applied fields, are made by B. Moreover, the cgs unit system is followed in which the numerical values of magnetic field strength and magnetic flux density are identical: $1\,\mathrm{Oe} = 1\,\mathrm{G}$, whereby $10\,000\,\mathrm{G} = 1\,\mathrm{T}$. This usage follows the standard English-language textbook on solid-state magnetism [6]. Additionally, references to "applied magnetic field" refer to DC magnetic field. When discussing AC susceptibility, designations of the field as "DC" or "AC" are made whenever ambiguity could arise.

Furthermore, the following shorthand is employed for statements pertaining to the magnetisation, M, and to the static magnetic susceptibility $\chi = M/B$:

- "M_i", or "M for $B||i$" refer to the magnetisation along a sample's i-axis when the external magnetic field is applied along the i-axis;
- "χ_i", or "χ for $B||i$" refer to the static magnetic susceptibility $\chi_{ii} = M_i/B_i$, i.e. to the diagonal element of the static magnetic susceptibility tensor.

The employed unit of magnetisation is $M = [\mu_\mathrm{B}/\mathrm{f.u.}]$, that is, magnetisation quantities are normalised to the number of Bohr magnetons per formula unit of the compound. Static magnetic susceptibility is given in the unit $\chi = [\mathrm{erg\,G^{-2}\,mol^{-1}}]$, whereby $[\mathrm{erg\,G^{-2}}] \equiv [\mathrm{emu}]$.

[3] Cologne Laue Indexation Program

4. $MnTiO_3$

A portion of the following chapter forms the basis of a recently submitted article to Physical Review B and is also available on the open-access repository arXiv under the title *The role of magnetoelastic coupling and magnetic anisotropy in $MnTiO_3$* [51]. The author of the present text features as one of two first co-authors of the submitted article. Unless stated otherwise, all data, analysis, and discussion presented here are sole work of the present author.

4.1. Material Background

$MnTiO_3$ belongs to the ilmenite family of titanates with the general formula $MTiO_3$ where M is a cation with oxidation state 2+, such as Mg^{2+}, Cd^{2+}, Mn^{2+}, Fe^{2+}, Co^{2+}, or Ni^{2+} [52]. Whereas the first two members of the above series are non-magnetic [52], the remaining compounds all display long-range antiferromagnetic order at low temperatures [53, 54]. At least two different stable polymorphs of $MnTiO_3$ have been identified, successfully synthesised, and characterised: a low-pressure polymorph, denoted $MnTiO_3$-I, and a high-pressure polymorph, denoted $MnTiO_3$-II [52]. By far the more investigated of the two is $MnTiO_3$-I which also exhibits higher crystallographic symmetry. The low-pressure phase (henceforth denoted simply as $MnTiO_3$) is also the subject of the present work.

$MnTiO_3$, together with all other titanates, crystallises in the so-called ilmenite structure which exhibits the crystallographic symmetry $R\bar{3}$ [57, 58]. Fig. 4.1 depicts the crystal structure of $MnTiO_3$ which consists of alternating planes of manganese and titanium cations, whereby the stacking direction of the planes defines the crystallographic c-axis. Within the individual crystallographic ab-planes, both cation species are displaced due to electrostatic forces from their high-symmetry position in an alternating fashion, reducing the local point group symmetry and leading to buckling of the basal planes (c.f. Fig. 4.1a) [59]. Within their respective plane, each cation species is coordinated in weakly-distorted oxygen octahedra (distortion parameter amounts to $c/a \approx 0.04$ at 100 K [55]). Neighbouring octahedra of the same species share a common edge within the ab-planes, and neighbouring octahedra of differing species share a common face along the c-axis. Lastly and as demonstrated in Fig. 4.1b, the manganese ions lie in an hexagonal arrangement within the basal planes.

The 2+ oxidation state of the manganese ions results in an electronic configuration

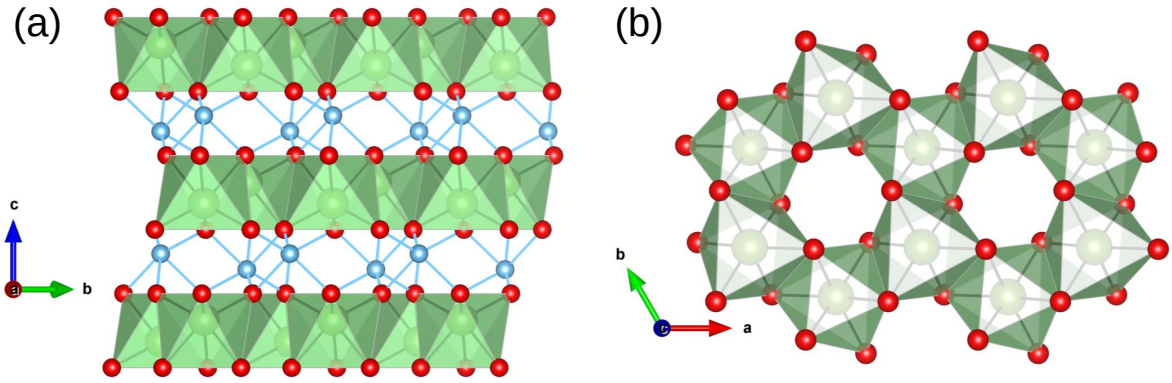

Figure 4.1.: Crystal structure of $MnTiO_3$ (a) in the *bc*-plane, and; (b) in the *ab*-plane, consisting of Mn^{2+} cations (green) embedded in octahedrally-coordinated O^{2-} anions (red). In between the individual manganese layers are sandwiched layers of Ti^{4+} cations (blue). For clarity, titanium octahedra have been omitted from (a), and titanium cations have been omitted in (b) altogether. Crystallographic data taken from [55], visualisation performed in VESTA [56].

$[Ar]3d^5$ with spin momentum $S = 5/2$ and vanishing orbital momentum $L = 0$. The long-range antiferromagnetic order in $MnTiO_3$ is of the G-type [62], contrasting with the other magnetic titanates which display A-type AFM order [62–64]. The long-range ordering temperature of $MnTiO_3$ has been found to vary between $T_N = 62.3\,K$ in a powder sample [65] and $T_N = 64.5(5)\,K$ in a single crystal [66].

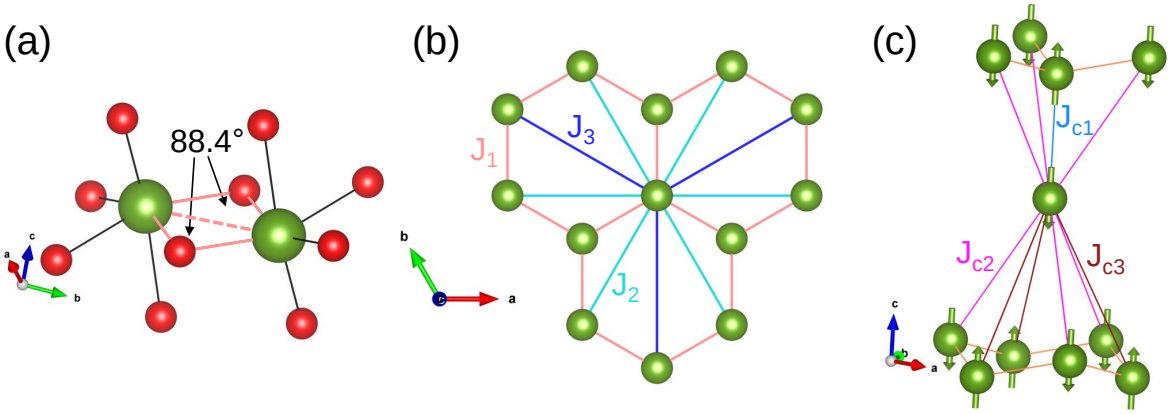

Figure 4.2.: (a) Manganese ions (green) coordinated octahedrally by six oxygen ions (red) with a bonding angle of 88.4° along the exchange path Mn–O–Mn. Exchange constants between various nearest manganese neighbours (b) within the *ab*-plane (J_1–J_3), and; (c) perpendicular to the *ab*-plane (J_{c1}–J_{c3}). The arrows in (c) depict the ground state spin structure as determined from inelastic neutron scattering [60, 61]. Crystallographic data taken from [55], visualisation performed in VESTA [56].

The difference in the types of antiferromagnetic order may be understood by considering the dominant exchange interaction in the titanates, J_1, which is realised between

M	configuration	S	AFM order	anisotropy type	T_N (K)
Mn^{2+}	$3d^5$	5/2	G-type [62]	uniaxial [62]	63.6 [67]
Fe^{2+}	$3d^6$	2	A-type [63]	uniaxial [68]	58.0 [68]
Co^{2+}	$3d^7$	3/2	A-type [64]	planar [64]	35.6 [69]
Ni^{2+}	$3d^8$	1	A-type [62]	planar [62]	23.2 [69]

Table 4.1.: An overview of the basic magnetic properties of the various magnetic titanates with the general formula $M\mathrm{TiO_3}$. Numbers in square brackets indicate the corresponding reference.

nearest in-plane magnetic neighbours M. With the help of Fig. 4.2a, it may be seen that J_1 comes about as a cooperative effect between, on the one hand, direct exchange between the two neighbours M–M (dashed salmon-coloured line) and, on the other hand, superexchange mediated by an oxygen anion which is bonded under 88.4° to the M ions via two equal paths (solid salmon-coloured lines). Whereas the direct exchange path favours antiferromagnetic spin arrangement, the sign of the superexchange path is dependent on the concrete electronic configuration: right-angled bonding between half-filled e_g and half-filled t_{2g} shells (as approximately realised in $\mathrm{MnTiO_3}$) favours antiferromagnetic spin arrangement; right-angled bonding between half-filled e_g and more-than-half-filled t_{2g} shells (as approximately realised in the other magnetic titanates) favours ferromagnetic spin arrangement [17]. Consequently, in-plane antiferromagnetic arrangement of the spins is realised in $\mathrm{MnTiO_3}$ [62], ferromagnetic in the other titanates [62–64]. The basic magnetic properties of the various magnetic titanates are summarised in Table 4.1.

Another intriguing difference between $\mathrm{MnTiO_3}$ and the other magnetic titanates concerns the temperature evolution of the static magnetic susceptibility. $\mathrm{FeTiO_3}$, $\mathrm{CoTiO_3}$, and $\mathrm{NiTiO_3}$ exhibit upon cooling a monotonic increase of χ all the way down to T_N with a sharp peak at T_N and a subsequent decrease towards the lowest temperatures [68, 69]. In contrast, the static magnetic susceptibility of $\mathrm{MnTiO_3}$ displays upon cooling a monotonic increase only down to about 100 K, at which point a broad maximum χ_m evolves, extending down to the antiferromagnetic ordering temperature $T_N \approx 64\,\mathrm{K}$ [67, 70].

Such a broad maximum in static magnetic susceptibility is a sign of reduced dimensionality of the magnetic interactions [71]. In the case of $\mathrm{MnTiO_3}$ the reduced dimensionality is suspected to originate from an accidental cancellation of otherwise sizeable interplanar exchange constants [61, 72]. Table 4.2 lists the first six nearest-neighbour exchange constants as determined from the most recent inelastic neutron scattering on $\mathrm{MnTiO_3}$ [61], and Figs. 4.2b,c visualise the various exchange constants. It may be observed that all interplanar exchange constants are antiferromagnetic in nature. However, due to the dominant intraplanar exchange constant J_1 which

forces all in-plane nearest neighbours into an antiferromagnetic arrangement, the interplanar constant J_{c2} is not realised. Consequently, the system has to pay energy $2n \cdot J_{c2}$, where n is the number of neighbours coupled via J_{c2}, in order to support the ground state spin arrangement (see also the ground-state spin configuration depicted in Fig. 4.2c). That is, the effective out-of-plane exchange constant equals to $J_c^{\text{eff}} = \sum_i n_i \cdot J_i = 1 \cdot J_{c1} - 6 \cdot J_{c2} + 3 \cdot J_{c3} = 0.102\,\text{meV}$, whereas the effective in-plane exchange constant to $J_{ab}^{\text{eff}} = 3 \cdot J_1 - 6 \cdot J_2 + 3 \cdot J_3 = 4.629\,\text{meV}$ (whereby the minus signs in the two sums indicate that the corresponding interaction is not satisfied in the ground state). This results in the ratio $J_c^{\text{eff}}/J_{ab}^{\text{eff}} \approx 0.022$ [61], highlighting the dominance of the intraplanar over the interplanar coupling.

intralayer coupling				interlayer coupling			
	(meV)	n	bond length (Å)		(meV)	n	bond length (Å)
J_1	1.833	3	3.057	J_{c1}	0.507	1	4.008
J_2	0.139	6	5.134	J_{c2}	0.131	6	5.604
J_3	−0.012	3	5.975	J_{c3}	0.127	3	6.252
J_{ab}^{eff}	4.629			J_c^{eff}	0.102		

Table 4.2.: Intra- and interlayer exchange coupling constants, the number of neighbours n connected via the respective coupling, and the corresponding bond lengths in $MnTiO_3$. J_{ab}^{eff} (J_c^{eff}) corresponds to the effective intraplanar (interplanar) exchange constant. Positive sign of the exchange constant corresponds to antiferromagnetic coupling. Exchange constants taken from [61], crystallographic information from [55].

Although the basic magnetic properties of $MnTiO_3$, such as the thermodynamic response functions or the magnetic ground state, had been long understood, the recent observation of the magnetoelectric effect in $MnTiO_3$ [73] has reawakened interest in the fundamental properties of the material, not least with a view on potential technological applications, harvesting the linear coupling between electric and magnetic fields (see e.g. [74] and the references therein). In spite of not showing spontaneous coexistence of ordered magnetic and electric dipole moments, characteristic for multiferroics [17], $MnTiO_3$ exhibits magnetic-field-induced electric polarisation within the antiferromagnetically-ordered phase [73]. Moreover, based on group-theoretical considerations the spin-flop phase of $MnTiO_3$ has been predicted to support the evolution of a ferrotoroidal structure [75, 76]. Measurements of the *d-d* transitions by means of second harmonic generation have provided experimental evidence that toroidal moments may indeed evolve in the spin-flop phase [76].

Another fascinating area of research on the titanates concerns the doping series $Ni_xMn_{1-x}TiO_3$. Since $MnTiO_3$ is a G-type antiferromagnet with an easy-axis anisotropy [62] and $NiTiO_3$ is an A-type antiferromagnet with an easy-plane anisotropy [62], competing interactions and anisotropies in the doped compounds lead

to exotic and novel phenomena [77]. For instance, $Ni_xMn_{1-x}TiO_3$ has been observed to exhibit an *ab*-plane-confined spin-glass state for $x = 0.40$–0.48 [78]. Moreover, the frozen disordered regime of the spin-glass behaviour is accompanied by a magnetoelectric effect which is thought to be induced by alignment of toroidal moments [78, 79].

The recent observations on $MnTiO_3$ and on the doping series $Ni_xMn_{1-x}TiO_3$ make the magnetic titanates an exciting material group to study. However, in order qualitatively and quantitatively to understand the ground-state properties of the Mn–Ni doping series, a detailed understanding of the end compounds is required. While the low-energy excitations of $NiTiO_3$ have already been investigated in the frame of another study [25], a comparable investigation of $MnTiO_3$ is still missing. Small parts of $MnTiO_3$'s resonance-frequency–magnetic-field diagram [54, 80] as well as the temperature evolution of the linewidth [81] have been studied before. However, the present work covers for the first time the low-temperature magnon excitations in a broad excitation-energy spectrum $30\,\mathrm{GHz} \leq \nu \leq 420\,\mathrm{GHz}$ in a large range of applied magnetic fields $0\,\mathrm{T} \leq B \leq 16\,\mathrm{T}$. Furthermore, profiting from a high-quality single-crystal sample, the parameters of the two-sublattice model of antiferromagnetic resonance (AFMR) with uniaxial anisotropy are derived with previously unattainable precision and the physical origin of the parameters is discussed in detail.

4.2. Sample and Experimental Details

The sample utilised in the present study was synthesised by Kaustav Dey by means of optical floating-zone technique in argon-filled atmosphere of 5 bar [55]. It was previously characterised by magnetisation [55], and thermal expansion and magnetostriction [66]. To perform high-frequency electron spin resonance (HF-ESR), a small sample in a wedge form was cut out with approximate dimensions $2\,\mathrm{mm} \times 1\,\mathrm{mm} \times 0.3\,\mathrm{mm}$–$0.6\,\mathrm{mm}$, where the *c*-axis dimension reflected the varying height of the wedge. This was necessary in order to minimise the effect of the so-called Walker modes [82–84]. Auxiliary HF-ESR measurements were conducted on a finely-ground polycrystalline sample fixed by means of eicosane (see Section 3.1 for more details on preparing fixed-powder samples).

4.3. Experimental Results

4.3.1. Static Magnetic Susceptibility

Fig. 4.3a depicts the axis-dependent static magnetic susceptibility, $\chi = M/B$, of $MnTiO_3$ at $B = 1\,\mathrm{T}$, measured by Kaustav Dey [85] and analysed by the present author. Coming from high temperatures, an approximately isotropic increase of χ may

be observed down to about 100 K. At that point, a broad maximum χ_m evolves along both crystallographic orientations which is indicative of reduced dimensionality of the magnetic interactions, as already discussed in the introductory remarks in Section 4.1. Long-range antiferromagnetic order sets in at $T_N = 64.0(5)$ K, as testified by a jump in the temperature derivative of the susceptibility $d\chi/dT$ (data not shown). The value of T_N corresponds well with its earlier determination [65–67]. Below T_N, the susceptibility curves assume an anisotropic character, with χ_c undergoing a sharp decrease almost to zero value while χ_b slightly increases as $T \to 2$ K. This observation confirms the orientation of the easy magnetisation axis along the crystallographic c-direction.

To obtain an estimate of the Weiss temperature θ, Curie-Weiss-law fitting was performed on the axis-averaged value[1] of the susceptibility in the temperature region $200\,\mathrm{K} \leq T \leq 300\,\mathrm{K}$. In the fitting procedure, the effective magnetic moment was fixed to $\mu_{\mathrm{eff}} = g\sqrt{S(S+1)} = 5.92\,\mu_B$, as appropriate for Mn^{2+} ions. The optimised parameters were determined to be $\theta = -237(4)$ K, and $\chi_0 = 4.0(6) \times 10^{-4}\,\mathrm{ergG^{-2}mol^{-1}}$ for a constant background. Here, the error bars reflect the variation of the optimised parameters when the fitting region is reduced to $250\,\mathrm{K} \leq T \leq 300\,\mathrm{K}$. The fitted Curie-Weiss curve is depicted as a solid blue line in the inset of Fig. 4.3a. From θ and T_N, a moderate frustration parameter $f = |\theta/T_N| \approx 3.7$ is obtained. Previous fitting of the powder static magnetic susceptibility up to 600 K yielded the Weiss temperature $\theta = -219$ K [54].

From the axis-dependent static susceptibility data, the temperature-dependent ratio $\alpha = \chi_\parallel/\chi_\perp$ can be calculated [30, 86]. Depicted in Fig. 4.3b, it confirms the isotropy of the susceptibility above T_N and its highly-anisotropic, antiferromagnetic-like behaviour below T_N, whereby T_N serves as a sharp demarcation line. The evolution of α will be important in a later discussion when considering the temperature effects on the resonance phenomena.

4.3.2. Electron Spin Resonance

4.3.2.1. Low-Temperature Antiferromagnetic Resonance

Fig. 4.4 depicts a selection of the spectra obtained at 2 K (i.e. deep in the antiferromagnetically-long-range-ordered phase of $MnTiO_3$) at high frequencies. Resonance features obtained on the single-crystal sample with $B||c$-axis exhibit a typical Lorentzian-like transmission shape only for frequencies $\nu \lesssim 100$ GHz (see, e.g., the spectrum obtained at $\nu = 68.0$ GHz depicted in Fig. 4.4a). As may be seen in Fig. 4.4a, the resonance structure becomes more irregular and complex with increasing value of the resonance frequency. This is a typical sign of the Walker modes which may arise in regularly-shaped single-crystal samples when the wavelength of the exciting microwave

[1] $\chi_{\mathrm{ave}} = (\chi_{\parallel c} + 2\chi_{\perp c})/3$

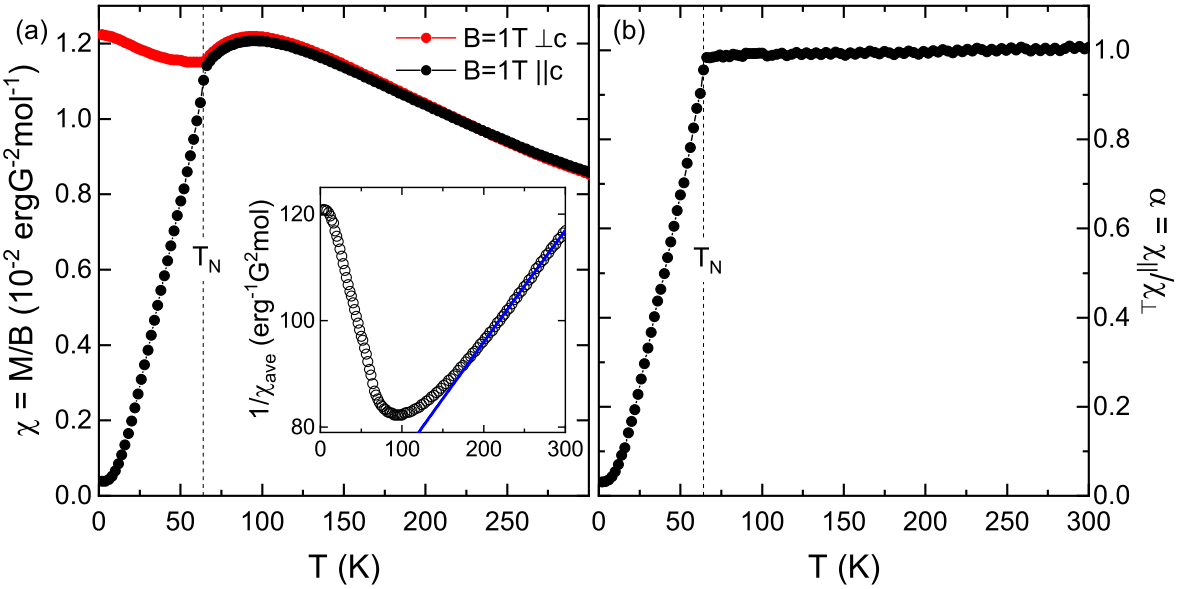

Figure 4.3.: (a) Static magnetic susceptibility $\chi = M/B$ obtained in a zero-field-cooled mode at $B = 1\,\mathrm{T}$ for the two main crystallographic orientations. The inset depicts the axis-averaged inverse static magnetic susceptibility (black data points) fitted by means of a Curie-Weiss law (blue solid line); (b) The temperature dependence of the ratio $\alpha = \chi_{\parallel}/\chi_{\perp}$ obtained from the susceptibility data in (a). Vertical dashed lines mark the antiferromagnetic phase transition. The data in (a) were obtained by Kaustav Dey [85].

field becomes comparable to the sample dimensions [82–84]. In order to extract the resonance fields from the spectra in Fig. 4.4a, the low extremal resonance field and the high extremal resonance field belonging to a particular group of Walker modes are noted and the resonance-field position assigned to the midpoint of the two extrema. The corresponding uncertainty is taken to extend from the low- to the high-field extrema. The assignment of the resonance fields together with their uncertainty is marked by coloured symbols in Fig. 4.4a.

Attempts were made also to measure antiferromagnetic resonance for $B \perp c$-axis on the same single-crystal piece of $MnTiO_3$. However, the measurements were distorted by the Walker modes to such an extent that an unambiguous assignment of the resonance fields was not possible (the width of the Walker modes amounted to 7 T or more). To circumvent the issue, resonance measurements were performed on a finely-ground powder stemming from the same synthesis batch as the single-crystal sample. The powder was fixed by eicosane in order to prevent reorientation in the magnetic field. The obtained spectra are depicted in Fig. 4.4b. As may be seen therein, well-defined resonance features are observed (marked by coloured symbols) which exhibit an increasing extent of wave-phase mixing with increasing frequency.

Following the colour-coding from Fig. 4.4, all the low-temperature resonance features are collected in the resonance-frequency–magnetic-field diagram depicted in Fig. 4.5.

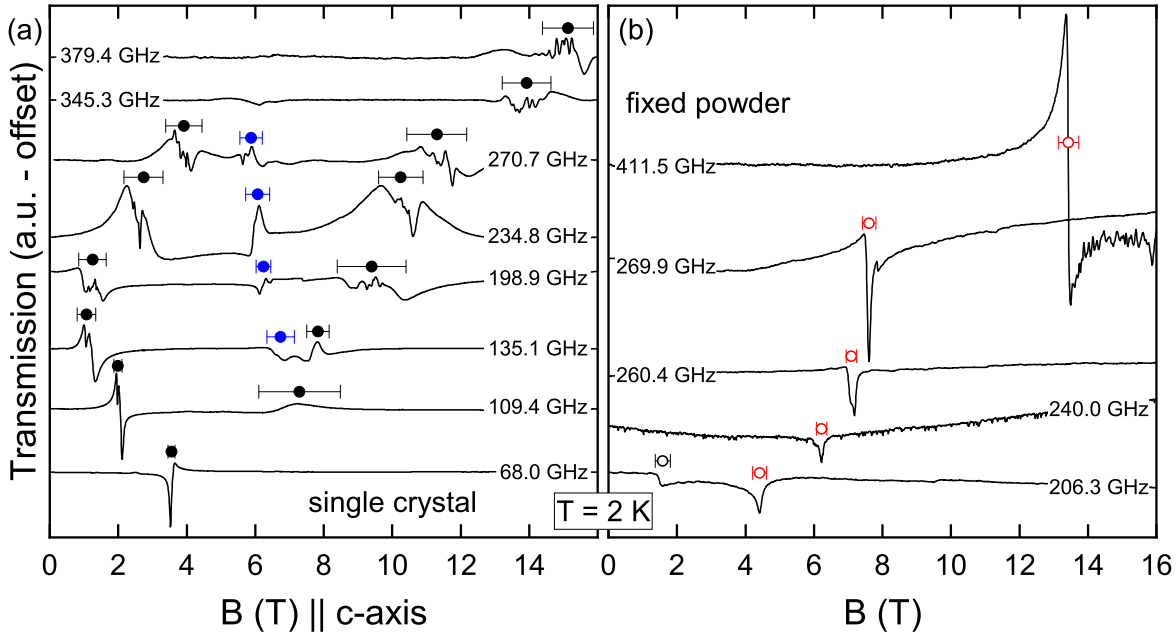

Figure 4.4.: Selected spectra at various frequencies at $T = 2\,\mathrm{K}$ for (a) $B||c$-axis on the single-crystal sample; and (b) on the powder sample. Coloured symbols mark the positions of the resonance features

In addition to the dominant resonance features (black and red data points in Fig. 4.5), a set of weak features has been observed which form a gapless branch with $g = 2.00$ and disappear for $\nu \geq 88.6\,\mathrm{GHz}$ (see grey data points in Fig. 4.5). These may be attributed to a small number of paramagnetic impurities and shall not be considered for further analysis.

The presence of four dominant resonance modes, three of which merge into a single zero-field excitation gap, suggests a two-sublattice AFMR model with axial-like anisotropy. At $T = 0\,\mathrm{K}$, the model's free parameters are given by the zero-field excitation gap Δ and by a pair of effective g-factors, $g_\parallel$ and $g_\perp$, for parallel and perpendicular orientation of the magnetic field with respect to the easy magnetisation axis. At finite temperatures, the temperature-dependent ratio of the parallel and perpendicular static magnetic susceptibilities $\alpha = \chi_\parallel/\chi_\perp$ features as the model's further parameter. For the field dependence of the resonance frequency, the model predicts [19, 21, 30]:

$$\nu_\parallel^{\mathrm{U,L}} = \sqrt{\Delta^2 + \left(\frac{\alpha}{2}\frac{g_\parallel \mu_\mathrm{B} B}{h}\right)^2} \pm \frac{g_\parallel \mu_\mathrm{B} B}{h}\left(1 - \frac{\alpha}{2}\right) \tag{4.1}$$

for $B||\mathrm{easy} \leq (h\Delta)/(g_\parallel \mu_\mathrm{B})$, and

$$\nu_\parallel^{\mathrm{SF}} = \sqrt{\left(\frac{g_\parallel \mu_\mathrm{B} B}{h}\right)^2 - \Delta^2} \tag{4.2}$$

for $B||\text{easy} \geq (h\Delta)/(g_{\parallel}\mu_{\mathrm{B}})$. For the magnetic field applied perpendicular to the easy magnetisation axis, the resonance frequency is given by:

$$\nu_{\perp} = \sqrt{\left(\frac{g_{\perp}\mu_{\mathrm{B}}B}{h}\right)^2 + \Delta^2} \tag{4.3}$$

In the above, $\nu_{\parallel}^{\mathrm{U}}$, $\nu_{\parallel}^{\mathrm{L}}$, $\nu_{\parallel}^{\mathrm{SF}}$, and $\nu_{\perp}$ denote the upper, lower, and spin-flop branch stemming from $B \parallel$ easy axis, and the perpendicular branch stemming from $B \perp$ easy axis, respectively. μ_{B} and h denote the Bohr magneton and the Planck constant, respectively. Note that for $\alpha = 0$, Eq. 4.1 assumes a simple form:

$$\nu_{\parallel}^{\mathrm{U,L}} = \Delta \pm \frac{g_{\parallel}\mu_{\mathrm{B}}}{h}B \tag{4.1b}$$

Since $\alpha \approx 0.03 \ll 1$ at $T = 2\,\mathrm{K}$ (c.f. Fig. 4.3b), i.e. the temperature at which the spectra were obtained, Eq. 4.1b, instead of Eq. 4.1, is used in the ensuing analysis of the field dependence of the AFMR modes in $MnTiO_3$. The error introduced by setting $\alpha = 0$ is expected to be smaller than the uncertainty associated with determination of the resonance-field positions. A least-squares fitting of the four magnon branches yields $\Delta = 166(1)\,\mathrm{GHz}$, $g_{\parallel} = 1.98(1)$, and $g_{\perp} = 2.00(1)$. The fitting results of the magnon branches are displayed in Fig. 4.5 as black and red solid lines. From the above Eq. 4.1b, the critical field at which $\nu_{\parallel}^{\mathrm{L}}$ reaches zero frequency can be calculated as $B_{\mathrm{C}} = (h\Delta)/(g_{\parallel}\mu_{\mathrm{B}})$. Using the optimised parameters, one finds $B_{\mathrm{C}} = 6.0(1)\,\mathrm{T}$ (marked by a dashed vertical line in Fig. 4.5).

The AFMR results confirm the orientation of the easy axis along the crystallographic c-axis, as the single-crystal measurements with $B||c$ contribute solely to the model's predictions for the easy-axis resonance features. The model's above-obtained parameters contrast with earlier observations from high-frequency ESR measurements in which the zero-field excitation gap was found to amount to $\Delta = 153\,\mathrm{GHz}$ and the low-temperature effective g-factor to 2.1 [80], and to $\Delta = 156\,\mathrm{GHz}$ [54], respectively; and from inelastic neutron scattering measurements which found $\Delta \approx 200\,\mathrm{GHz}$ [60], and $\Delta \approx 193\,\mathrm{GHz}$ [61], respectively. The limited accessible frequency in the earlier ESR reports and the superior energy resolution of ESR over neutron scattering spectroscopy lend support to the present values of Δ and the g-factors in $MnTiO_3$.

Further to the dominant strongly frequency-dependent features, almost frequency-independent resonance features around the position of the spin-flop field were detected in the single-crystal measurements for $B||c$ (blue data points in Fig. 4.5). For a perfect alignment of the external field with the easy axis of a two-sublattice antiferromagnet, a frequency-independent resonance branch is expected to occur at B_{C}, corresponding to the rotation of the spins about the easy axis at no cost of energy [19]. It may be speculated that the blue resonance features in Fig. 4.5 around B_{C} may be attributed

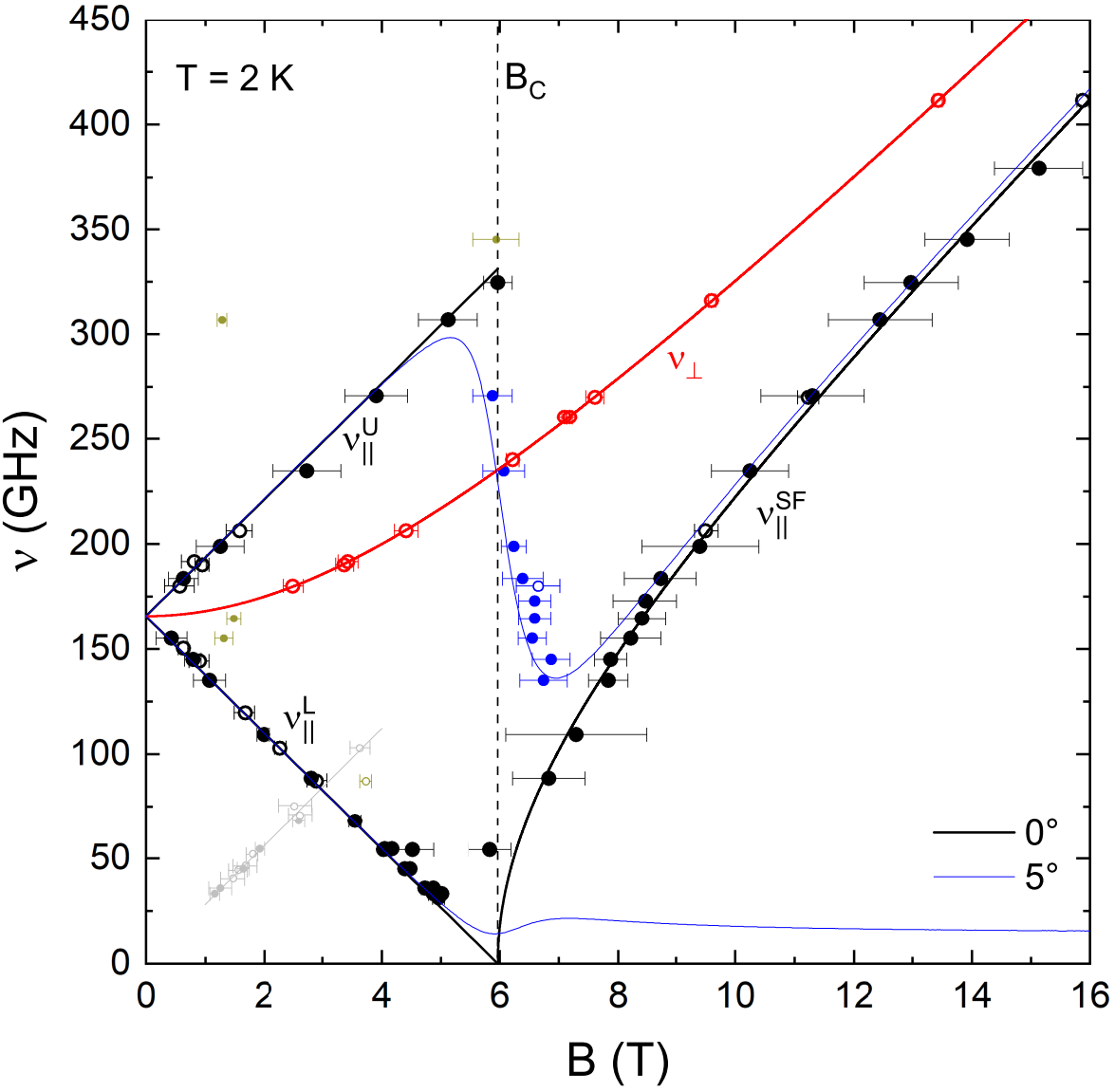

Figure 4.5.: Resonance-frequency–magnetic-field diagram at $T = 2\,\mathrm{K}$. Closed symbols depict data obtained on the single crystal with $B||c$-axis, open symbols on the polycrystal. Black and red lines show fitting results from a two-sublattice uniaxial AFMR model, defined in Eqs. 4.1b–4.3. Blue solid lines show a simulation based on the two-sublattice uniaxial AFMR model for the case of B applied 5° away from the easy axis (see text for details). Light grey line corresponds to a gapless $g = 2.00$ excitation branch. Vertical dashed line marks the critical field at which $\nu_{\parallel}^{\mathrm{L}}$ becomes zero (see text for a detailed discussion). Adapted from [51].

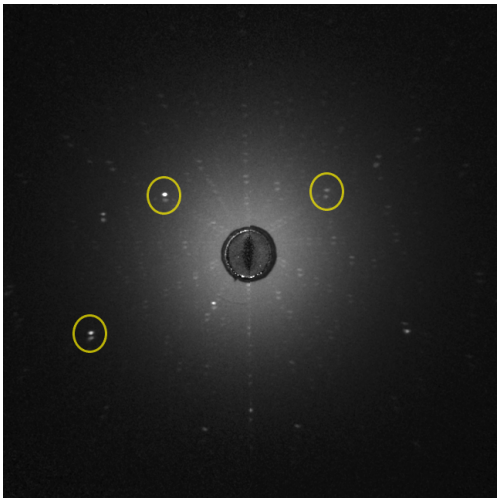

Figure 4.6.: Laue image taken in a back-scattering geometry on the single-crystal sample of $MnTiO_3$ utilised in the electron spin resonance measurements. Yellow circles mark areas where the doubling of diffraction spots is particularly noticeable.

precisely to this resonance branch, whereby at least a partial cause of their unexpected frequency dependence may be the finite temperature at which the measurements were performed. This speculation is corroborated by the observation of a finite width of the spin-flop transition seen in isothermal magnetisation measurements at 2 K [66, 76].

Another potential cause of the blue resonance features' unexpected frequency dependence is a possible deviation of the applied magnetic field from the easy axis, such as may occur due to a small sample misalignment. Using the above-obtained fitting parameters, the blue solid lines in Fig. 4.5 simulate the features' expected field dependence for B applied 5° away from the easy axis. As may be seen, the simulation captures the blue resonance features very well. Intriguingly, however, a number of the black resonance features are not correctly accounted for by the blue line and instead follow the fitting results for perfect alignment of $B||c$-axis (c.f. e.g. the features approximately at 5 T and 306 GHz or at 7 T and 90 GHz). Such doubling of the number of the resonance branches around B_{SF} indicates that a two-sublattice AFMR model is insufficient to explain the observed resonance-frequency–magnetic-field dependence. As the remainder of the phase diagram is satisfactorily captured by the two-sublattice model, this observation may indicate the presence of two grains within the single-crystal sample which are inclined by approximately 5° with respect to each other and which lead to the doubling of the resonance branches. Indeed, careful analysis of the single-crystal sample's Laue diffractogram, which is shown in Fig. 4.6, reveals doubling of the diffraction spots (most noticeable doubling of the diffraction spots is marked by yellow circles in Fig. 4.6). This observation confirms the hypothesis that the single-crystal sample of $MnTiO_3$ under investigation in the present study consists of two grains. Nevertheless, thanks to the unambiguous and high-precision determination of the resonance features

in the field regime up to 5 T, the reduced quality of the sample does not undermine the qualitative and quantitative results obtained from the present AFMR analysis.

Lastly, a small number of spectra exhibited additional resonance features (marked by dark yellow symbols in Fig. 4.5). Their lack of discernible resonant-frequency–magnetic-field dependence did not allow for their appropriate interpretation, and, as such, they shall not be considered for further discussion.

4.3.2.2. Temperature-Dependent High-Frequency Electron Spin Resonance

To measure the temperature evolution of the resonances, spectra were obtained at fixed resonance frequency $\nu = 54.2\,\mathrm{GHz}$ for $B||c$-axis at increasing temperature steps between $2\,\mathrm{K} \leq T \leq 200\,\mathrm{K}$. Measurements at this frequency allowed to track the temperature evolution of the AFMR modes $\nu_{\parallel}^{\mathrm{L}}$ and $\nu_{\parallel}^{\mathrm{SF}}$. As observed in Fig. 4.7, $\nu_{\parallel}^{\mathrm{L}}$ remains at approximately the same resonance field all the way up to 30 K. For $T \geq 40\,\mathrm{K}$, a significant shift of the resonance field to lower values is detected. Since in the two-sublattice AFMR model with uniaxial anisotropy, $\nu_{\parallel}^{\mathrm{L}}$ is directly related to the zero-field excitation gap, the branch's shift to lower fields signals reduction in Δ.

The resonance branch $\nu_{\parallel}^{\mathrm{SF}}$ is found to shift to higher resonance fields upon heating from the lowest measured temperatures, and, moreover, no resonance feature associated with $\nu_{\parallel}^{\mathrm{SF}}$ is observed for $T \geq 40\,\mathrm{K}$ in Fig. 4.7. A similar effect was observed in a number of long-range-ordered antiferromagnets, such as $CuCl_2 \cdot 2H_2O$ [87] or $LiFePO_4$ [88]. Note that a simple reduction of the internal fields with increasing temperature would lead to the resonance feature's shift to lower resonance fields [86, 87].

Quantitatively, use can be made of Eq. 4.1, which explicitly accounts for temperature effects through inclusion of the parameter α, to obtain the temperature dependence of Δ and of B_{C}. To do so, the position of the resonance field associated with $\nu_{\parallel}^{\mathrm{L}}$ at the various temperatures is extracted from Fig. 4.7 and the corresponding parameter α from Fig. 4.3b. By means of Eq. 4.1, the two values are used to simulate the branch $\nu_{\parallel}^{\mathrm{L}}$ at the various temperatures. The resulting simulated branches are depicted in Fig. 4.8 for selected temperatures. The temperature-dependent values of Δ and B_{C} are extracted directly from the figure as the zero-field crossing and zero-resonance-frequency crossing, respectively.

The obtained temperature dependencies are displayed in Fig. 4.9.[2] Starting from the lowest temperatures, Δ exhibits a gradual weakening with increasing temperature. For $T \geq 30\,\mathrm{K}$ the changes in Δ are drastic and as $T \to T_{\mathrm{N}}^{-}$ the data suggest a complete

[2] Note that the two-Kelvin values of Δ and B_{C} displayed in Fig. 4.9 differ by a small amount from the values calculated in the earlier analysis of the complete AFMR modes in Fig. 4.5. This is because in the earlier analysis of the complete AFMR modes, α was approximated to be zero, whereas in the present analysis, which leads to Fig. 4.9, the value of α is explicitly taken into account even at 2 K. Despite the different approaches, the thus-introduced difference in the parameters at 2 K is expected to be smaller than other errors contributing to the parameters' overall uncertainty.

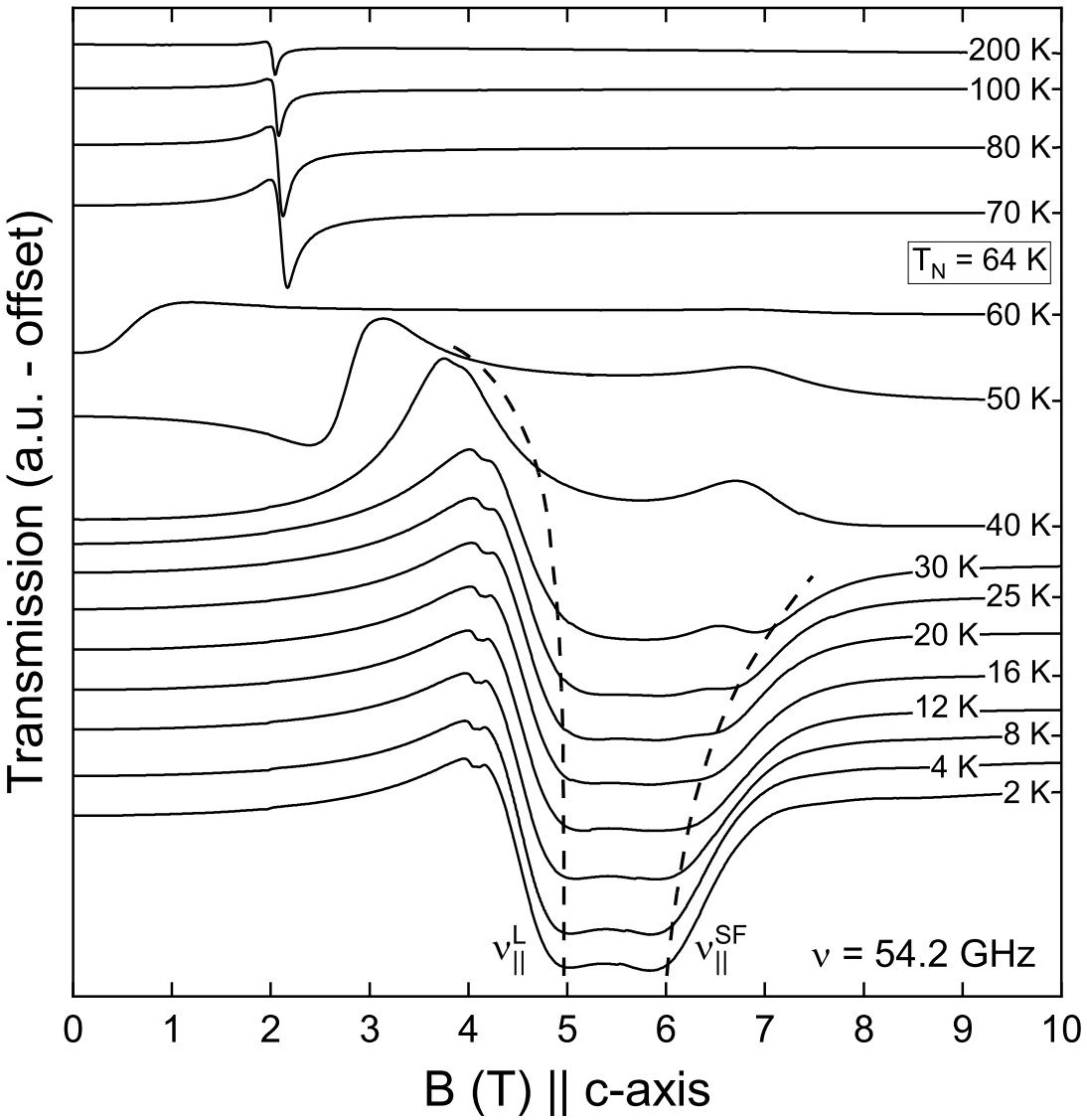

Figure 4.7.: Temperature evolution of the resonance spectra recorded at fixed frequency $\nu = 54.2\,\mathrm{GHz}$ for $B||c$-axis. Curved dashed lines are a guide to the eye to mark the evolution of the resonance features. Adapted from [51].

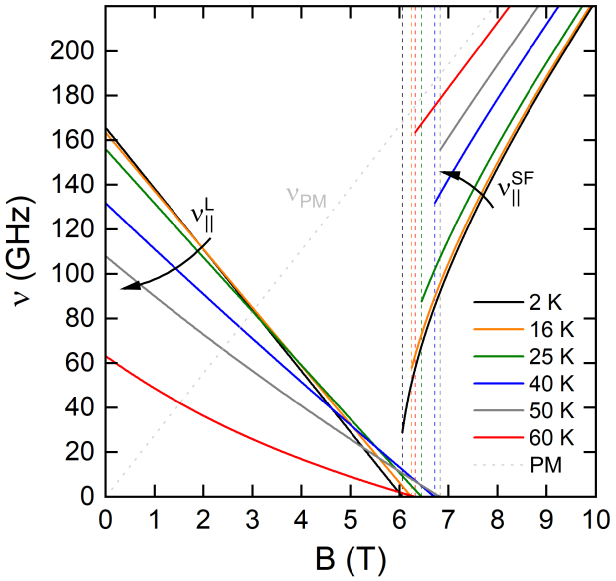

Figure 4.8.: Simulation of the resonance branch $\nu_{\parallel}^{\mathrm{L}}$ in $MnTiO_3$ at various temperatures based on Eq. 4.1, on the resonance field extracted from Fig. 4.7, and on the parameter α extracted from Fig. 4.3b. Additionally, simulation of the resonance branch $\nu_{\parallel}^{\mathrm{SF}}$ based on Eq. 4.2, whereby the values of the zero-field excitation gap at the various temperatures required to evaluate Eq. 4.2 are extracted from the corresponding simulation of $\nu_{\parallel}^{\mathrm{L}}$, see text for details. Grey dotted line, marked ν_{PM}, depicts a paramagnetic resonance branch with $g = 1.98$. Dashed vertical lines mark the critical field B_{C}, with colour-coding corresponding to the respective temperature. Arrows indicate the shift of the resonance fields for increasing temperature based on the simulated curves.

vanishing of the zero-field excitation gap. A qualitatively similar behaviour was also observed in previous HF-ESR studies on $MnTiO_3$ [54, 80]. The temperature dependence of B_{C} shall be addressed in the subsequent discussion.

By evaluating Eq. 4.2, the obtained temperature-dependent values of Δ can be used to simulate the branch $\nu_{\parallel}^{\mathrm{SF}}$ at the respective temperatures. The resulting simulated branches are also depicted in Fig. 4.8. It is evident that the simulation predicts a shift of the resonance features associated with $\nu_{\parallel}^{\mathrm{SF}}$ to lower resonance fields with increasing temperature, contrary to the observation in Fig. 4.7. Note that magnetostriction measurements revealed discontinuous length changes at the spin-flop transition for $B||c$, indicating the importance of orbital degree of freedom and hence of spin-orbit coupling in $MnTiO_3$ [66].[3] It may be speculated that concurring with the spin flop, structural changes take place which affect the temperature evolution of the internal fields and hence of the resonance field in the spin-flop mode.

Lastly, it may be seen in Fig. 4.7 that spectra obtained at $\nu = 54.2\,\mathrm{GHz}$ above T_{N} exhibit a single paramagnetic resonance absorption peak which assumes a Lorentzian

[3] Consequently, the field-induced transition does not constitute a proper spin flop. Bearing this in mind, it shall be referred to as such for the sake of brevity in the remainder of the present text.

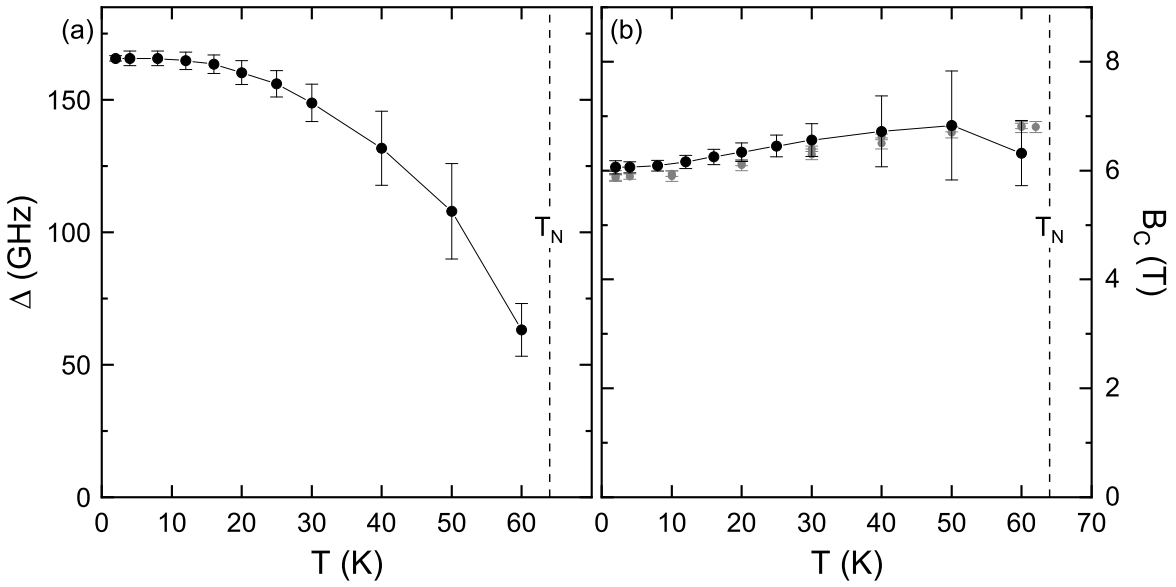

Figure 4.9.: Temperature dependence (a) of the zero-field excitation gap Δ, and; (b) of the critical field B_{C}, as obtained from the analysis of the temperature evolution of the resonance feature $\nu_{\parallel}^{\mathrm{L}}$ displayed in Fig. 4.7 by means of Eq. 4.1. Grey data points in (b) are the spin-flop-transition-indicating features from isothermal magnetisation and magnetostriction from [66]. Vertical dashed lines mark the antiferromagnetic ordering temperature. Adapted from [51].

character with a small amount of wave-phase mixing. The decreasing intensity of the resonance peak with increasing temperature corresponds well to Curie-Weiss-like behaviour. The spectroscopic g-factor can be estimated from the position of the resonance field by means of the relation $g = (h\nu)/(\mu_{\mathrm{B}} B_{\mathrm{res}})$. This yields $g(T = 100\,\mathrm{K}) = 1.91(3)$ and $g(T = 200\,\mathrm{K}) = 1.94(4)$. A deviation from the paramagnetic value $g = 2.00$ expected for Mn^{2+} with $S = 5/2$ and $L = 0$ [17] indicates that finite local internal fields are present in the compound at temperatures as high as $T \simeq 3T_{\mathrm{N}}$.

Evidence for short-range magnetic order may also be seen in thermodynamic measurements. In particular, a deviation from a Curie-Weiss-like behaviour may be observed to set in below approximately 180 K in static magnetic susceptibility (c.f. the inset of Fig.4.3a). In addition, finite magnetic entropy changes were observed in specific heat measurements up to about 130 K on a single-crystal sample [89], and up to about 170 K on a powder sample [65]. Furthermore, since inelastic neutron scattering observed a complete cessation of out-of-plane correlations at about 90 K, it was argued that the high-temperature short-range correlations are anisotropic in nature, extending only in the *ab*-planes [61]. This corresponds very well also with the observation of anisotropic length changes and especially with finite distortion parameter c/a up to 170 K derived from thermal expansion studies [66].

4.3.2.3. Room-Temperature X-Band Electron Paramagnetic Resonance

In addition to the high-frequency ESR measurements presented thus far, X-band ESR was also employed to study $MnTiO_3$. Fig. 4.10 presents room-temperature spectra obtained at $\nu \approx 9.4\,\mathrm{GHz}$ for two orientations of the external magnetic field, $B||c$ and $B \perp c$, respectively. Each spectrum can be successfully fitted by a single Lorentzian-derivative line (solid lines in Fig. 4.10). From the fitted resonance fields, the g-factors can be calculated as $g = (h\nu)/(\mu_\mathrm{B} B_\mathrm{res})$, yielding $g_{\parallel\mathrm{c}} = 2.004(6)$ and $g_{\perp\mathrm{c}} = 2.002(5)$, respectively. Both of the values align very well with the expectation for paramagnetic Mn^{2+} ions [90], indicating a complete cessation of short-range correlations at room temperature. In addition, the absorption's linewidth, defined as the full width of the field at half maximum of the intensity, amounts to $\Delta B_{\parallel\mathrm{c}} = 24.1(2)\,\mathrm{mT}$ and $\Delta B_{\perp\mathrm{c}} = 23.9(2)\,\mathrm{mT}$, respectively. The similarity in the linewidth values between the two orientations suggests that the room-temperature relaxation processes are isotropic and that no exchange narrowing effects occur [91]. An earlier study on the related titanate $NiTiO_3$ found $\Delta B_{\parallel\mathrm{c}} = 96.6(1)\,\mathrm{mT}$ and $\Delta B_{\perp\mathrm{c}} = 84.8(1)\,\mathrm{mT}$, respectively [25]. The approximately four times larger linewidth in case of $NiTiO_3$ relative to $MnTiO_3$ implies that the relaxation processes in $NiTiO_3$ are considerably faster than in $MnTiO_3$. Since the room-temperature relaxation is dominated by spin-phonon processes, it follows that $NiTiO_3$ possesses a considerably larger spin-lattice coupling constant than $MnTiO_3$ [25]. This can be qualitatively understood by considering the orbital angular momenta in the respective compounds. Although to first order orbital angular momentum is quenched in $NiTiO_3$, spin-orbit coupling partially restores it, thereby enhancing the interaction between the spin and lattice degrees of freedom. Since Mn^{2+} ions in $MnTiO_3$ exhibit a half-filled d-shell, the spin-lattice coupling in $MnTiO_3$ is correspondingly weaker.

As may be seen in Fig. 4.10, the detected X-band ESR signal for $B \parallel c$-axis exhibits greater intensity than the signal for $B \perp c$-axis. The detected intensity is proportional to the dynamical susceptibility χ_ESR which in turn is proportional to the static magnetic susceptibility χ_DC. As the measurements of the latter unequivocally showed that at room temperature $\chi_\mathrm{DC}(B \parallel c) = \chi_\mathrm{DC}(B \perp c)$ (see Fig. 4.3a), it is expected that χ_ESR assumes a constant value along both orientations of the applied magnetic field. The present observation can be understood if the varying dimensions of the single-crystal sample are considered. The dynamical susceptibility will be enhanced along longer sample edges, as the impinging microwave field will encounter a greater number of resonating magnetic moments along these edges than along shorter edges. Without appropriate normalisation of the detected signal (which has not been performed in the present case), this leads to different values of χ_ESR for different crystallographic orientations.

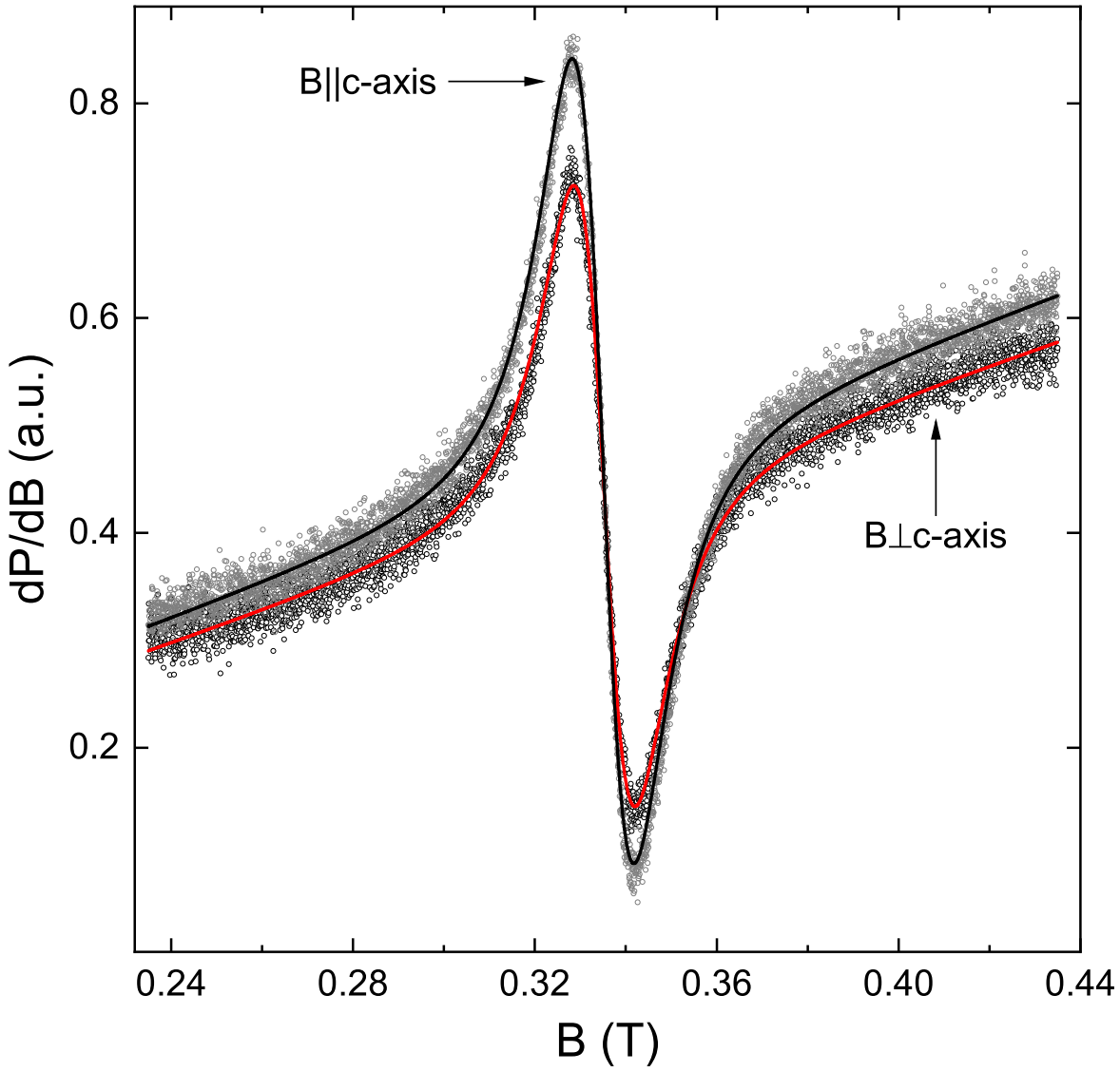

Figure 4.10.: Transmission derivative of paramagnetic resonance of $MnTiO_3$ at X-band frequency of $\nu = 9.395\,\mathrm{GHz}$ at room temperature with the external magnetic field applied parallel and perpendicular to the c-axis, obtained in a Voigt configuration ($B \parallel k_{\mathrm{MW}}$). Black and red solid lines are fitted Lorentzian-peak derivatives with a linear background. Adapted from [51].

4.4. Discussion

It can be shown that within the two-sublattice uniaxial AFMR model, the critical field at which $\nu_{\parallel}^{\mathrm{L}}$ reaches zero frequency at $T = 0\,\mathrm{K}$ is given by $B_{\mathrm{C}} = \sqrt{(2B_{\mathrm{E}}B_{\mathrm{A}} + B_{\mathrm{A}}^2)/(1-\alpha)}$ [19, 92], where B_{E} and B_{A} are the effective exchange and anisotropy fields defined in Eq. 2.24 in Chapter 2. The above analysis of the AFMR data yielded $B_{\mathrm{C}} = 6.0(1)\,\mathrm{T}$ at $2\,\mathrm{K}$. At the same time, a two-sublattice antiferromagnet with uniaxial anisotropy undergoes a spin-flop transition at $B_{\mathrm{SF}} = \sqrt{(2B_{\mathrm{E}}B_{\mathrm{A}} - B_{\mathrm{A}}^2)/(1-\alpha)}$ [30, 86]. In the case of $MnTiO_3$ previous magnetisation measurements found $B_{\mathrm{SF}}(T = 4.2\,\mathrm{K}) = 5.8\,\mathrm{T}$ [67, 93]; $B_{\mathrm{SF}}(T = 1.4\,\mathrm{K}) = 6.5\,\mathrm{T}$ [76], and; $B_{\mathrm{SF}}(T = 2\,\mathrm{K}) = 5.87(10)\,\mathrm{T}$ [66]. Such a good correspondence between B_{C} obtained from the present AFMR analysis and B_{SF} obtained from magnetisation measurements implies that $\sqrt{(2B_{\mathrm{E}}B_{\mathrm{A}} + B_{\mathrm{A}}^2)/(1-\alpha)} \simeq \sqrt{(2B_{\mathrm{E}}B_{\mathrm{A}} - B_{\mathrm{A}}^2)/(1-\alpha)}$, and consequently that $B_{\mathrm{A}} \ll B_{\mathrm{E}}$. This is typical for 3d-ion-containing long-range-ordered antiferromagnets, see, e.g., MnF_2 [92], Cr_2O_3 [86], or NiO [94]. A good correspondence between B_{C} and B_{SF} is also seen in Fig. 4.9b all the way up to $60\,\mathrm{K}$. Hence, in the ensuing calculation of the low-temperature values of the effective exchange and anisotropy fields, the critical field B_{C} obtained from the present AFMR analysis shall be taken as the spin-flop field.

Given the definition of B_{C} and B_{SF}, the observed increase in their values with increasing temperature implies that the $(1-\alpha)$ decreases more rapidly than $2B_{\mathrm{E}}B_{\mathrm{A}}$ as temperature increases. A gradual increase of B_{C} with increasing temperature at least up to $0.75T_{\mathrm{N}}$ was observed also in MnF_2, a related two-sublattice antiferromagnet with uniaxial anisotropy and manganese ions in $3d^5$ configuration [95]. A spin-wave solution to a Hamiltonian with exchange, single-ion, magnetic-dipole, and Zeeman contributions showed that exchange interaction in combination with anisotropy caused by magnetic dipole interactions could reproduce the temperature dependence of B_{C} in qualitative and, at sufficiently low temperatures, also quantitative terms [95]. It was also shown in the same work that exchange interaction alone would lead to the overestimation of the temperature dependence of B_{C}, whereas exchange interaction in combination with single-ion anisotropy would predict a decrease, rather than an increase, of B_{C} with increasing temperature [95]. Given the similarities between MnF_2 and $MnTiO_3$, especially in the success of the two-sublattice uniaxial AFMR model in describing the magnon branches (for HF-ESR on MnF_2 see, e.g., [96]) and in the same electronic configuration of the magnetic Mn^{2+} ions, it may be speculated that exchange energy in combination with dipole-dipole-driven anisotropy is responsible for the observed increase in B_{C} also in $MnTiO_3$.

As derived in Chapter 2, a mean-field approximation to a minimal Hamiltonian with the assumption of a two-sublattice system can be used to calculate the effective exchange

and anisotropy fields. To do so, the saturation field B_{sat} must be known in addition to the spin-flop field (see Eq. 2.27 in Chapter 2). Since no published isothermal magnetisation measurements extended to sufficiently large magnetic fields to induce magnetisation saturation, merely an estimate for the saturation field can be obtained. To do so, the linear part above the spin flop of the isothermal magnetisation at 2 K, measured in an earlier study by DC magnetometry up to 14 T [66], is extrapolated to the known value of the full ordered magnetic moment in $MnTiO_3$, $\mu = 4.55\,\mu_{\mathrm{B}}/\mathrm{Mn}^{2+}$ [62]. This procedure yields $B_{\mathrm{sat}} = 213(10)$ T (data not shown).

Substituting the values of B_{SF} and B_{sat} into Eq. 2.27, the effective exchange and anisotropy fields are obtained as $B_{\mathrm{E}} = 107(6)$ T and $B_{\mathrm{A}} = 0.17(1)$ T. Noting that in $MnTiO_3$ $z = 3$ for the number of nearest magnetic neighbours coupled by the dominant exchange constant J_1 (see Fig. 4.2 and Table 4.2), Eq. 2.24 given in Chapter 2 can be used to calculate the effective exchange coupling constant J_{eff} and the uniaxial anisotropy constant D. One finds $J_{\mathrm{eff}} = 0.82(4)$ meV and $D = 0.0038(3)$ meV.[4] Note that, per definition, the mean-field theory provides merely the effective exchange coupling constant. However, since the dominant exchange interaction in $MnTiO_3$ is J_1, it follows that the hereby-calculated value of J_{eff} is predominately an estimator of J_1.

Within the mean-field model at 0 K, the effective anisotropy field can be independently calculated as $B_{\mathrm{A}} = (B_{\mathrm{SF}}^2 \cdot \chi_\perp)/M_{\mathrm{sat}}$ [92]. Utilising $\chi_{\mathrm{b}}(T = 2\,\mathrm{K}) = 0.0122(2)\,\mathrm{erg G^{-2} mol^{-1}}$ as obtained from the static magnetic susceptibility measurements displayed in Fig. 4.3a, $B_{\mathrm{A}} = 0.17(1)$ T is found. This matches very well the value obtained based on Eq. 2.27.

The signs of the obtained parameters signal that the system's anisotropy assumes a uniaxial character and that the dominant intersublattice exchange interaction is antiferromagnetic. Moreover, the obtained values of D and J_{eff} quantitatively corroborate their determination by means of inelastic neutron scattering: $D = 0.0011$ meV and $J_1 = 0.63$ meV [60], and $D = 0.0045$ meV and $J_1 = 0.92$ meV [61], respectively. In addition, an earlier magnetisation study found the uniaxial anisotropy constant $D = 0.0039$ meV [67], which lies within the error bars of its present determination by means of AFMR analysis.[5]

The ratio of the anisotropy to exchange field amounts to $B_{\mathrm{A}}/B_{\mathrm{E}} \approx 1.6 \times 10^{-3}$, thereby confirming the weak effective anisotropy field relative to the effective exchange field, and matching well its previous estimate $B_{\mathrm{A}}/B_{\mathrm{E}} \approx 1.5 \times 10^{-3}$ [67]. Moreover, the several-

[4] Using another isothermal magnetisation dataset obtained in pulsed fields up to 35 T at 1.4 K [76], $B_{\mathrm{sat}} \approx 256(12)$ T is found by applying the same extrapolation procedure. This results in greater exchange field $B_{\mathrm{E}} \approx 128(6)$ T and smaller anisotropy field $B_{\mathrm{A}} \approx 0.14(1)$ T, corresponding to $J_{\mathrm{eff}} = 0.98(5)$ meV and $D = 0.0032(2)$ meV, respectively.

[5] Ref. [67] quotes the anisotropy constant $K_{\mathrm{eff}} = 5.7 \times 10^5\,\mathrm{erg/cm^3}$, whereby per definition, $K_{\mathrm{eff}} = 2SD$. Converting K_{eff} to SI units and utilising the unit cell volume $V_{\mathrm{u.c.}} = 325.7$ Å^3 (containing six manganese ions), $D = 0.0039$ meV is found.

orders-of-magnitude-larger value of B_E than B_A confirms the earlier observation that $B_A \ll B_E$ and justifies the utilisation of B_C as the spin-flop field. Such small values of the effective anisotropy field are expected for Mn^{2+} ions with negligible single-ion anisotropy due to vanishing orbital angular moment.

In searching for the origin of the anisotropy $MnTiO_3$, it may be observed that due to vanishing orbital moment of the Mn^{2+} magnetic ions, spin-orbit coupling is expected to act only in second order of perturbation theory [17]. In particular, only negligible contributions to the overall anisotropy are expected to arise from single-ion effects and from anisotropic exchange interaction. In principle, both symmetric and antisymmetric exchange may lead to macroscopic anisotropy effects [17] (see also Section 2.4). Based on symmetry considerations, however, the contribution from antisymmetric exchange in $MnTiO_3$ amounts to zero, $J_{\text{anis}}^{\text{antisym}} = 0$. The contribution due to symmetric exchange can be estimated as $J_{\text{anis}}^{\text{sym}} \sim J_{\text{eff}}(\frac{\Delta g}{g})^2$ [17]. With the room-temperature spectroscopic $g_{\parallel c} = 2.004(6)$ and $g_{\perp c} = 2.002(5)$ obtained in the X-Band measurement (c.f. Fig. 4.10), $\Delta g = 0.002$, resulting in the effective anisotropy energy on the order of $\sim S^2 J_{\text{anis}}^{\text{sym}} \approx 5 \times 10^{-6}\,\text{meV}$. This is almost three orders of magnitude smaller than the calculated anisotropy constant D and hence cannot account for its value.

On the other hand, the potential energy between two magnetic dipoles can be calculated by means of Eq. 2.12. Utilising the ordered moment of $4.55\,\mu_B/Mn^{2+}$ [62] and the crystallographic information from [55] (see also Table 4.2), the sum of the dipole-dipole energies $\sum_i n_i \cdot E_i^{\text{dipole}}$ is calculated up to first six nearest neighbours ($i = 6$), whereby n_i is the number of neighbours. $E^{\text{dipole}} = 0.0345\,\text{meV}$ is found, from which, based on $E \sim DS^2$, it follows that $D^{\text{dipole}} = 0.0055\,\text{meV}$. Although this value is almost 1.5 times larger than the above-obtained value of D, its proximity to the experimental observations indicates the significance of dipole-dipole interactions for the evolution of anisotropy in $MnTiO_3$. It may be speculated that a part of the discrepancy to the experimental observations is owing to possible admixing of Mn^{3+} ($3d^4$) ions, which reduces the actual dipole-dipole energy.

Furthermore, a superexchange mechanism involving a simultaneous transfer of an electron-hole pair between neighbouring ions was proposed to materialise along the Mn^{2+}–O^{2-}–Mn^{2+} exchange path in $MnTiO_3$ [59]. It was shown that such *exciton superexchange* may contribute to overall anisotropy energy if the octahedral symmetry of the crystal field acting on the Mn^{2+} ions is reduced [59]. As the exchange path Mn^{2+}–O^{2-}–Mn^{2+} lies in the *ab*-plane, the resulting anisotropy will too favour planar arrangement of the spins and hence act against the *c*-axis-oriented dipolar-interaction-caused anisotropy. The temperature evolution of the distortion parameter $(dL_{\parallel c}(T) - dL_{\perp c}(T))/(dL_{\parallel c}(T) + dL_{\perp c}(T))$, where $dL_{\parallel c}(T)$ and $dL_{\perp c}(T)$ is relative thermal expansion parallel and perpendicular to the *c*-axis, respectively, demonstrates that the high-temperature high-symmetry local environment of the Mn^{2+} ions is reduced

below $T \lesssim 150\,\mathrm{K}$ [66]. This suggests that exciton superexchange in $MnTiO_3$ may indeed act as another source of reduction of the dominant c-axis-oriented anisotropy due to dipole-dipole interactions.

4.5. Summary

The presented high-frequency electron spin resonance on $MnTiO_3$ has shown that the low-energy excitations in the antiferromagnetically-ordered phase can be successfully described by means of a two-sublattice model with uniaxial anisotropy. The least-square fitting of the antiferromagnetic resonance branches found $\Delta = 166(1)\,\mathrm{GHz}$, $g_\parallel = 1.98(1)$ and $g_\perp = 2.00(1)$. Correspondingly, the critical field at which the lower magnon branch $\nu_\parallel^\mathrm{L}$ reaches zero was determined as $B_\mathrm{C} = 6.0(1)\,\mathrm{T}$. It has been shown that this value lies very close to the spin-flop field obtained from magnetisation measurements, implying $B_\mathrm{A} \ll B_\mathrm{E}$. Utilising B_C obtained from the present AFMR analysis as the spin-flop field and the saturation field B_sat obtained by extrapolating isothermal magnetisation from available literature, the effective anisotropy and exchange fields were derived. The analysis has yielded $B_\mathrm{A} = 0.17(1)\,\mathrm{T}$ and $B_\mathrm{E} = 107(6)\,\mathrm{T}$ which lie close to their determination from inelastic neutron scattering experiments and confirm that the effective anisotropy field is almost three orders of magnitude smaller than the effective exchange field. These observations indicate that the low-temperature magnetic ground state of $MnTiO_3$ displays a mean-field-like behaviour.

On the other hand, a shift of the spin-flop branch towards higher resonance fields upon heating cannot be explained by means of the mean-field AFMR model. It may be speculated that the structural changes which accompany the spin-flop transition affect the temperature evolution of the internal fields and hence of the resonance field in the spin-flop mode. Moreover, magnetic properties also above T_N have been found intriguing, including short-range correlations up to at least $3T_\mathrm{N}$, as directly detected in the present study by following the temperature evolution of the resonance field above T_N, and a correlation maximum approximately at 100 K, as seen in static magnetic susceptibility.

Hence, the overall picture of magnetic interactions in $MnTiO_3$ indicates a robust long-range order with uniaxial anisotropy, as indicated by the excellent description of the AFMR by a mean-field model. With increasing temperature, the order assumes more complex and ever more anisotropic, two-dimensional character due to the weak effective interplanar exchange constant, resultant from the cancellation of otherwise strong exchange constants along various exchange paths.

5. $LiMnPO_4$

5.1. Material Background

$LiMnPO_4$ belongs to the material class of olivine-structured lithium orthophosphates with the general formula $LiMPO_4$, where M = Mn, Fe, Co, or Ni. These materials represent an attractive research field for both, addressing topics in fundamental solid-state magnetism and harvesting their technological applications. Technologically promising is the utilisation of the various lithium orthophosphates as cathode materials in batteries due to the materials' high capacity (predicted to be as high as $170\,\mathrm{mAhg^{-1}}$), good conductivity, and robust cycling stability [97–100]. Equally technologically attractive is the pronounced magnetoelectric coupling [101–103] which may be exploited in data-storage devices, spin field-effect transistors, or magnetic sensors [104–106].

At the same time, lithium orthophosphates display a number of intriguing magnetic properties at low temperatures. For example, $LiNiPO_4$ features short-range and long-range antiferromagnetic incommensurate phases below $T^{\mathrm{IC}}_{\mathrm{SRO}} = 36\,\mathrm{K}$ and $T^{\mathrm{IC}}_{\mathrm{LRO}} = 21.7\,\mathrm{K}$, respectively, followed by a first-order phase transition to an antiferromagnetically-ordered commensurate phase ($T^{\mathrm{C}}_{\mathrm{N}} = 20.8\,\mathrm{K}$) [102, 107]. In addition, a sequence of field-induced transitions was observed in $LiNiPO_4$ at the lowest temperatures [108], rendering the magnetic phase diagram of $LiNiPO_4$ highly complex. $LiCoPO_4$ possesses one of the highest thus-far measured components of the magnetoelectric tensor from all ferroelectrics with $\alpha_{\mathrm{yx}} = 30.6\,\mathrm{psm^{-1}}$ [101]. Moreover, ferrotoroidic domains – regions of spontaneously ordered toroidal moments [109] – were resolved by spatial second harmonic generation in $LiCoPO_4$ [110], a first ever observation of ferrotoroidic domains in an experiment. $LiFePO_4$ possesses the highest values of anisotropy constants from the four lithium orthophosphates, with $D_{\mathrm{a}} = 0.86(2)\,\mathrm{meV}$ and $D_{\mathrm{c}} = 2.23(2)\,\mathrm{meV}$ [111]. Moreover, D_{a} and the effective exchange constant J_{eff} show in $LiFePO_4$ complex, field-dependent behaviour [112] (see also Table 5.1 for an overview of the orthophosphates' selected magnetic properties).

Of all the orthophosphates, $LiMnPO_4$ displays the smallest components of the magnetoelectric tensor, amounting to no more than $\alpha = 0.8\,\mathrm{psm^{-1}}$ [119]. Moreover, the component of the magnetoelectric tensor for which the external magnetic field is parallel to the orientation of the spins, i.e. α_{aa}, vanishes as $T \to 0\,\mathrm{K}$, in line with *ab initio* calculations and in contrast to the remaining orthophosphates [119]. It is speculated that vanishing orbital momentum is responsible for both of the observations, the smallest

M	easy axis	T_N (K)	canted order	canting angle	anis. constants (meV)
Mn^{2+}	a	32.5 [113]	(undetected)	(undetected)	0.0069; 0.0089 [114]
Fe^{2+}	b	49.5 [113]	AFM	1.3° [103]	0.86; 2.23 [111]
Co^{2+}	b	21.9 [115]	AFM	4.6° [116]	0.718; 0.802 [117]
Ni^{2+}	c	20.8 [107]	WFM	7.8° [118]	0.413; 1.423 [108]

Table 5.1.: Overview of selected magnetic properties of the lithium orthophosphates with the general formula $LiMPO_4$ (where M = Mn, Fe, Co, Ni). AFM and WFM denote antiferromagnetism and weak ferromagnetism, respectively. Numbers in square brackets provide the corresponding reference.

magnetoelectric tensor components and for $\alpha_{aa} \to 0\,\mathrm{psm}^{-1}$ as $T \to 0\,\mathrm{K}$ [119]. Lastly, based on symmetry considerations of the magnetic point group, $LiMnPO_4$ is predicted to exhibit an antiferrotoroidic moment [120].

The orthophosphates crystallise in an orthorhombic crystal structure with space group *Pnma* [113, 121]. Focusing on $LiMnPO_4$ in more detail, its lattice constants amount to $a = 10.46\,\text{Å}$, $b = 6.1\,\text{Å}$, and $c = 4.75\,\text{Å}$ [122, 123]. The structure consists of lithium octahedra, manganese octahedra, and phosphorus tetrahedra, whereby oxygen ions are located at the vertices of the various polyhedra. For the present purposes, the most interesting are the manganese octahedra: sharing four vertices of oxygen ions with neighbouring manganese octahedra, they occupy the crystallographic *bc*-plane, as illustrated in Fig. 5.1a. It is also in the *bc*-plane, running along the [011] direction, that two neighbouring manganese-manganese ions are located at closest separation. The direct separation amounts to $d^{\text{nearest}}_{\text{Mn-Mn}} = 3.9203\,\text{Å}$ [123] and is marked by a solid purple line in Fig. 5.1a. The corresponding exchange path, denoted J_1 (see subsequent discussion), is mediated by a shared oxygen ion, with bonding angle Mn–O–Mn of 125.36° [123]. The individual planes of the manganese octahedra are stacked along the *a*-axis and are separated by lithium and phosphorus polyhedra, as may be seen in Fig. 5.1b.

In a picture of purely ionic bonding, the manganese ions exhibit oxidation state 2+, which results in a half-filled 3d shell ($3d^5$), giving rise to spin $S = 5/2$ and vanishing orbital momentum $L = 0$. As such, the single-ion magnetic properties of $LiMnPO_4$ are identical to those of $MnTiO_3$ (c.f. Section 4.1). Previous analysis of inelastic neutron scattering data determined the exchange interactions up to five nearest neighbours, labelled henceforth J_1–J_5 [114]. These are illustrated in Fig. 5.2a and are listed in Table 5.2. Interestingly, each of the five nearest-neighbour exchange constants is antiferromagnetic. However, due to the C-type antiferromagnetic long-range order [123], J_2, J_3, and J_5 are frustrated (c.f. Fig. 5.2a), and as such, the system has to pay the corresponding energy in order to support the ground state. The effective exchange coupling constant can be estimated as $J^{\text{eff}} = \sum_i n_i \cdot J_i = 4 \cdot J_1 - 2 \cdot J_2 - 2 \cdot J_3 + 2 \cdot J_4 - 4 \cdot J_5 = 1.192\,\text{meV}$.

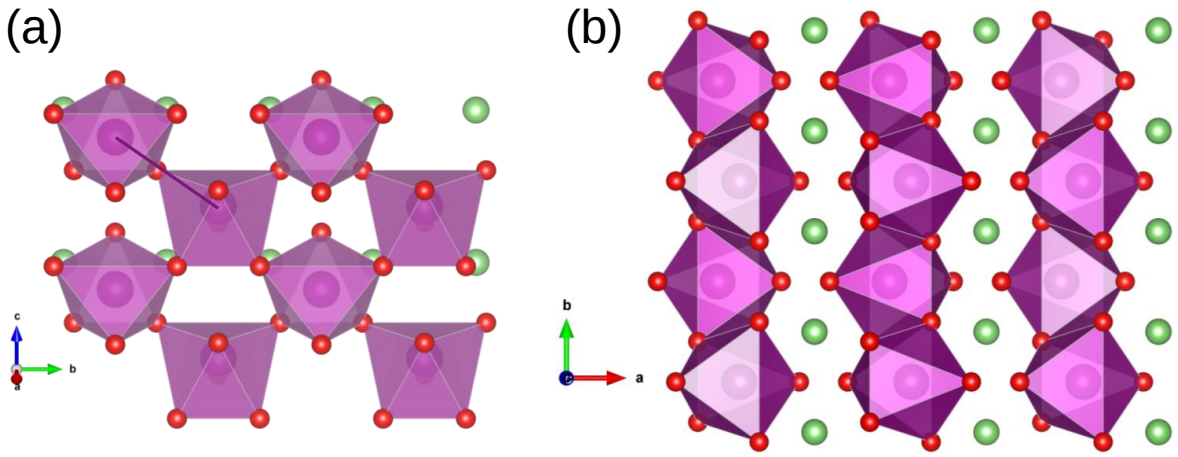

Figure 5.1.: (a) View of the *bc*-plane of $LiMnPO_4$ in which manganese ions (purple) are coordinated in distorted oxygen ion (red) octahedra. Solid purple line marks the shortest distance between two manganese ions. Lithium ions are depicted in green, while, for clarity, phosphorus ions have been omitted; (b) View of the *ab*-plane. Crystallographic data taken from [123], visualisation performed in VESTA [56].

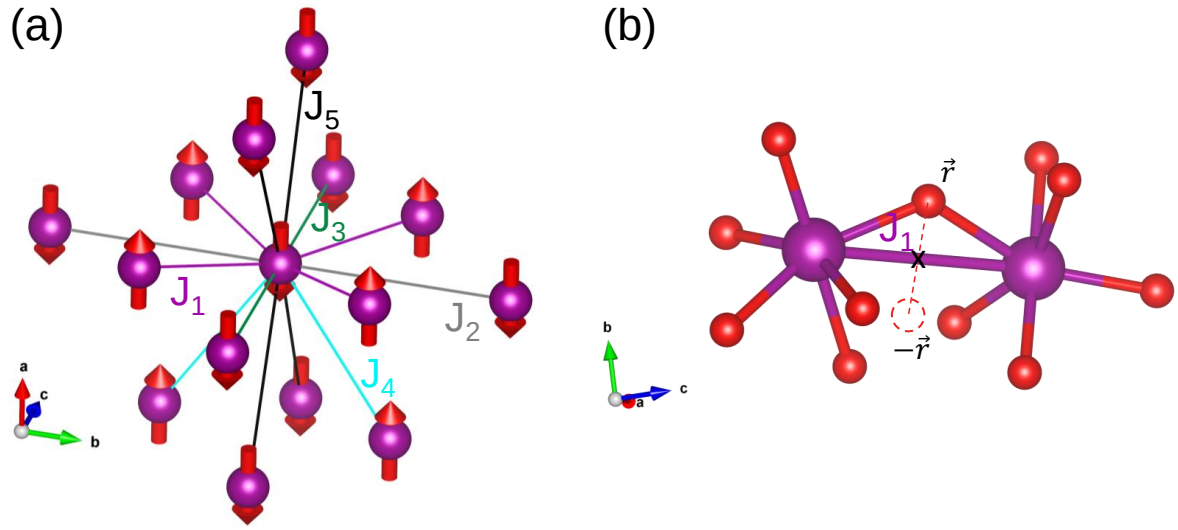

Figure 5.2.: (a) Exchange coupling constants J_1–J_5 between Mn^{2+} ions (purple spheres) up to five nearest neighbours in $LiMnPO_4$. Red arrows designate the ground-state spin configuration; (b) Two nearest Mn^{2+} neighbours, each coordinated in an octahedral environment of six oxygen ions (red spheres). Black cross marks the middle point of the exchange path J_1. Red dashed line originates in one of the oxygen ions and goes through the exchange path's middle, terminating in a mirror image (red dashed sphere) of the first oxygen ion (see text for details). Crystallographic data taken from [123], visualisation performed in VESTA [56].

	extension	(meV)	n		bond length (Å)
J_1	bc-plane	0.480	4	satisfied	3.9203
J_2	b-axis	0.200	2	frustrated	6.1000
J_3	c-axis	0.076	2	frustrated	4.7440
J_4	ab-plane	0.036	2	satisfied	5.4981
J_5'	ac-plane	0.062	2	frustrated	5.6379
J_5''	ac-plane	0.062	2	frustrated	5.8579
J^{eff}		1.192			

Table 5.2.: Nearest-neighbour exchange coupling constants, number of neighbours n connected via the respective coupling, status of the coupling constant in the ground state, and corresponding bond lengths in $LiMnPO_4$ (see also Fig. 5.2). J^{eff} refers to the effective exchange constant. Positive sign of the exchange constant corresponds to antiferromagnetic coupling. Coupling constants taken from [114], bond lengths from [123].

Upon inspection of the crystal structure of $LiMnPO_4$, it becomes evident that no inversion centre exists between the two nearest Mn^{2+} neighbours (see Fig. 5.2b). Based on geometrical considerations, an inversion centre is expected to lie in the middle of the corresponding bond, i.e. of J_1, marked by a black cross in the figure. However, if the cross did designate an inversion centre, then the oxygen ion located at $\vec{r}$ would have a counterpart at position $-\vec{r}$ (marked by red dashed sphere in the figure), such that a mirror plane containing the bond J_1 would exist between the two oxygen ions. As is evident from Fig. 5.2b, no oxygen ion is found at position $-\vec{r}$. A lack of inversion centre between two spins constitutes a necessary condition for the realisation of the antisymmetric, Dzyaloshinskii-Moriya interaction between the spins [17].

Long-range antiferromagnetic order in various single-crystalline $LiMnPO_4$ samples was found to develop at $T_N = 34.9(1)\,K$ by nuclear magnetic resonance [124], at $T_N = 35(2)\,K$ [125] and at $T_N = 32.5(5)\,K$ [113] by static magnetic susceptibility, and at $T_N = 33.0(1)\,K$ [126] by specific heat. Vanishing of the static magnetic susceptibility along the crystallographic a-axis as $T \to 0\,K$ [127] and the extremely small shift of the lithium resonance in nuclear magnetic resonance for $B||a$-axis [124] led to the conclusion that the spins in the ground state of $LiMnPO_4$ are oriented in a collinear fashion along the a-axis. Collinear spin arrangement along the a-axis was later confirmed by elastic neutron scattering experiments [123].

The observation of collinear spin configuration along the a-axis with no spin canting contrasts with spin structures determined for the related lithium orthophosphates: $LiFePO_4$ and $LiCoPO_4$ both exhibit collinear rotation of the spins away from their easy magnetisation axis, leading to antiferromagnetic ordering of the canted moments; the former by 1.3° [103], the latter by $\approx 4.6°$ [116]. $LiNiPO_4$, on the other hand,

displays spin canting of 7.8°, which is associated with weak ferromagnetism [118] (see also Table 5.1).

Similarly to the other lithium orthophosphates, $LiMnPO_4$ exhibits orthorhombic anisotropy, with two anisotropy constants determined by inelastic neutron scattering to be $D_c = 0.0069(10)\,\text{meV}$ and $D_b = 0.0089(10)\,\text{meV}$ [114]. Consequently, $D_a = 0\,\text{meV}$, demonstrating the crystallographic a-axis to be the easy magnetisation axis, while c-axis is the intermediate and b-axis the hard magnetisation axis, respectively.[1] The two anisotropy constants are about two orders of magnitude smaller than in the other orthophosphates (c.f. Table 5.1), a consequence of vanishing orbital angular momentum in first-order perturbation theory due to a half-filled 3d shell of the Mn^{2+} ion in $LiMnPO_4$. It was shown that about a half of the total anisotropy energy in $LiMnPO_4$ is due to dipole-dipole interactions and consequently argued that the remaining contributions are due to higher-order orbital modifications of the ground state [123]. The anisotropy constants give rise to energy gaps at $k = 0$ of $\Delta_1 = 148\,\text{GHz}$ and $\Delta_2 = 168\,\text{GHz}$ [114], which are accessible with the HF-ESR setup used in the present study.

The motivations to undertake the present investigation were twofold: firstly, the hitherto lack of observation of spin canting in the ground state of $LiMnPO_4$, despite good arguments from crystal-symmetry analysis for its existence and despite its unambiguous presence in the remaining lithium orthophosphates; secondly, the unique insight into the anomalous field dependence of the magnon branches in $LiFePO_4$ which HF-ESR was able to provide, encouraging the revisiting of the ground state Hamiltonian and the redefining of the exchange and anisotropy constants as explicitly field-dependent [112].

5.2. Experimental Results

The $LiMnPO_4$ samples utilised in the present study originate from two different batches synthesised by Christoph Neef [126]. In particular, a light-brown-coloured, rectangularly-shaped single-crystal sample with approximate dimensions 1.9 mm x 1.6 mm x 1.9 mm and mass $m = 8.38(3)\,\text{mg}$ stemming from one batch, and a polycrystalline powder sample stemming from a second batch. The single crystal was previously characterised by static magnetic susceptibility, isothermal magnetisation, and specific heat measurements [126]. Long-range antiferromagnetic order was found to evolve at $T_N = 32.5(5)\,\text{K}$ with an easy-axis orientation along the crystallographic a-axis [126], thereby matching well with earlier literature reports [114, 123].

[1] The anisotropy term in the Hamiltonian reads $\sum_{i,\xi} D_\xi (S_i^\xi)^2$ [114].

5.2.1. Magnetisation and Magnetic Phase Diagrams

5.2.1.1. Static Magnetic Susceptibility

To verify the quality of the powder sample required for subsequent HF-ESR studies, static magnetic susceptibility was measured in field of $B = 0.1\,\mathrm{T}$ in a zero-field-cooled mode. The resulting curve is depicted in Fig. 5.3a. Overlaying the powder data is an axis-averaged static magnetic susceptibility obtained on the single crystal, $\chi_{\mathrm{ave}} = (\chi_{\mathrm{a}} + \chi_{\mathrm{b}} + \chi_{\mathrm{c}})/3$. χ_{powder} was scaled to χ_{ave} at 320 K by a scaling factor 0.93 which may reflect a small error in determination of the mass of one or both of the samples. As may be seen in Fig. 5.3a, a very good correspondence exists between the two curves in a large temperature region extending from the highest measured temperatures all the way down to T_{N}. A small discrepancy may be observed only in the antiferromagnetically-ordered phase. This may be attributed to the presence of different amounts of paramagnetic impurities in the respective samples, with the powder exhibiting fewer paramagnetic defects than the single crystal. Calculating the Fisher's specific heat $d(\chi T)/dT$ (data not shown) determines the antiferromagnetic ordering temperature at $T_{\mathrm{N}} = 33.5(2)\,\mathrm{K}$. This matches well its earlier determination by nuclear magnetic resonance ($T_{\mathrm{N}} = 34.9(1)\,\mathrm{K}$) [124] and elastic neutron scattering ($T_{\mathrm{N}} = 33.9(1)\,\mathrm{K}$) [114]. Therefore, it follows that the polycrystalline sample may be used in electron spin resonance studies as a faithful representation of the single crystal and is expected to display the full resonance behaviour of the single crystal.

To provide a further characterisation of the powder sample, the susceptibility in the temperature region 220 K–355 K was fitted by a Curie-Weiss law. An effective moment of $\mu_{\mathrm{eff}} = 5.85(9)\,\mu_{\mathrm{B}}$ and Weiss temperature $\theta = -51(6)\,\mathrm{K}$ were found. Assuming a spin-only value of the total angular momentum $J = S = 5/2$, the g-factor $g = 1.98(3)$ is found, which lies within the expectation for a Mn^{2+} ion with a $3d^5$ orbital occupation. The negative sign of the Weiss temperature confirms the predominance of antiferromagnetic interactions in the compound, and its size implies an almost frustration-free ground state with the frustration ratio $\theta/T_{\mathrm{N}} \approx 1.5$. The three-dimensional nature of the magnetic interactions is also evidenced by a rather narrow correlation maximum which is observed at only a slightly higher temperature than the Néel temperature, $\chi_{\mathrm{max}} \approx 37\,\mathrm{K}$. On the other hand, a deviation from the Curie-Weiss behaviour may be seen for $T \lesssim 120\,\mathrm{K}$, which may indicate the evolution of three-dimensional short-range correlations.[2]

5.2.1.2. Isothermal Magnetisation

As part of the characterisation of the $LiMnPO_4$ powder sample an isothermal magnetisation measurement was performed at 1.8 K. This is displayed in Fig. 5.4. Continu-

[2] Specific heat reveals that short-range order exists only up about 60 K [128]. See the discussion on temperature-dependent paramagnetic resonance in Section 5.2.2.2.

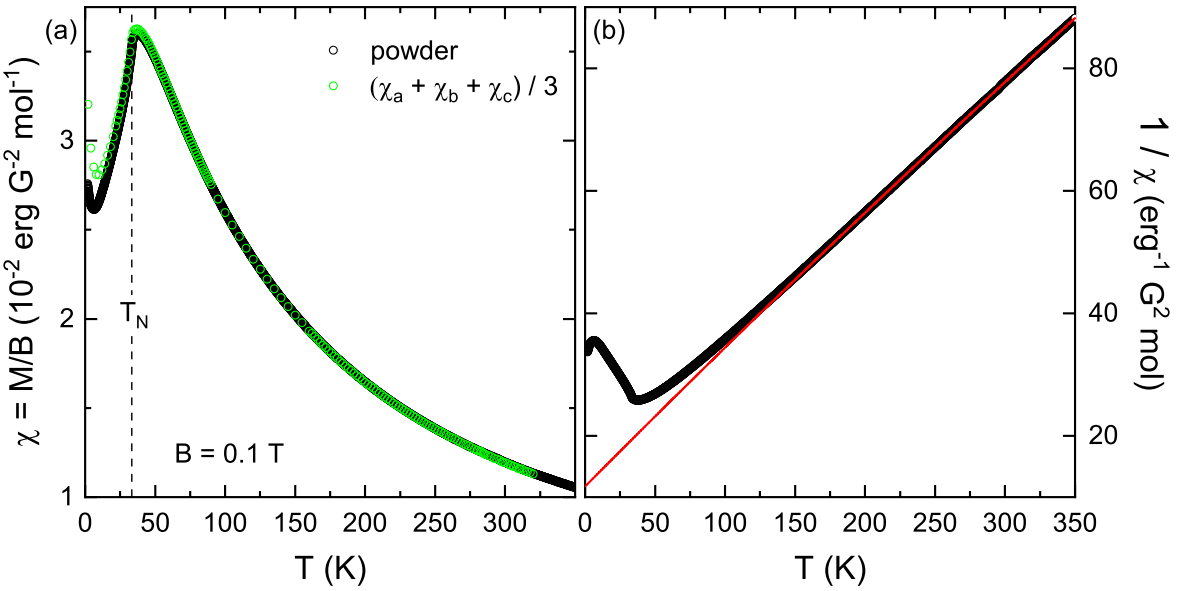

Figure 5.3.: (a) Static magnetic susceptibility of $LiMnPO_4$, obtained at $B = 0.1\,\mathrm{T}$, of a powder sample (black) scaled at $T = 320\,\mathrm{K}$ to axis-averaged susceptibility, $(\chi_a + \chi_b + \chi_c)/3$, of the single crystal (green). The data on the single crystal stem from an earlier work by Christoph Neef [126]. Vertical dashed line marks the antiferromagnetic ordering temperature; (b) inverse static susceptibility of the powder sample fitted by a Curie-Weiss law (solid red line).

ously increasing magnetisation all the way to the highest measured fields is observed. At around $B \approx 4\,\mathrm{T}$, a weak jump is detected. As shall become apparent in the ensuing discussion of the isothermal magnetisation of the single-crystal sample, the detected jump may be interpreted as a spin flop. The exact position of the jump may be ascertained from the corresponding peak in the field derivative of the magnetisation (right ordinate of Fig. 5.4): $B_{\mathrm{SF}} = 4.0(1)\,\mathrm{T}$. A small decrease of dM/dB as the field is ramped up from $0\,\mathrm{T}$ confirms the small but finite number of paramagnetic impurities in the sample.

Profiting from access to external magnetic fields up to $B = 14\,\mathrm{T}$, earlier isothermal magnetisation measurements on the single crystal of $LiMnPO_4$ reported elsewhere [126] could be extended to higher fields within the scope of the present work. The low-temperature axis-dependent data are displayed in Fig. 5.5. Isothermal magnetisation at $2\,\mathrm{K}$ along the a-axis (Fig. 5.5a) exhibits a small, approximately linear increase up to about $4\,\mathrm{T}$, at which point a jump is found, followed by a linear evolution towards the highest accessible fields. In contrast, no significant magnetisation jumps are found along the b- and c-axes. Much less visible is a small right bending of all three magnetisation curves in the low-field region. This indicates the alignment of a small number of paramagnetic impurities which are known to be distributed in the sample [126].

In order to prepare the isothermal magnetisation data for further quantitative analysis,

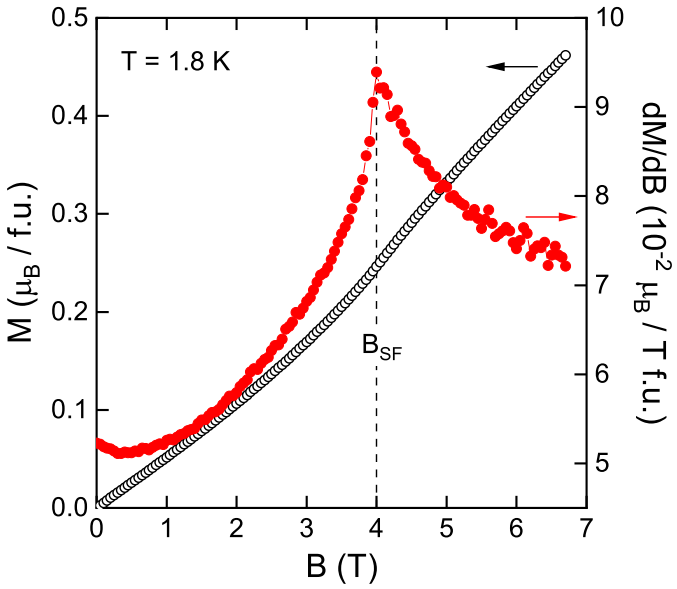

Figure 5.4.: Left ordinate: Isothermal magnetisation of powder sample of $LiMnPO_4$ at $T = 1.8\,\mathrm{K}$; right ordinate: corresponding field derivative. B_{SF} marks the spin-flop field.

the low-field regimes $0\,\mathrm{T} \leq B \leq 3.5\,\mathrm{T}$, i.e. field regimes sufficiently below B_{SF} and B_{C2} (see the ensuing discussion), are fitted by a function consisting of a Brillouin and linear part, namely $M = M_{\mathrm{Brillouin}} + \chi_0 B$. Here, the first term $M_{\mathrm{Brillouin}} = M_{\mathrm{PM}}^{\mathrm{sat}} B_{\mathrm{S}=5/2}(2\,\mathrm{K})$ accounts for the right bending of the low-field behaviour, whereby $B_{\mathrm{S}=5/2}(2\,\mathrm{K})$ is the Brillouin function with $S = 5/2$ as appropriate for Mn^{2+} paramagnetic moments and $M_{\mathrm{PM}}^{\mathrm{sat}}$ is the paramagnetic moments' saturation magnetisation. The second term in the above equation accounts for the linear regime associated with the magnetisation evolution of an antiferromagnet.

The resulting fits are displayed as solid green lines in Fig. 5.5. In the same figure, the solid blue lines depict the sole Brillouin component, $M_{\mathrm{Brillouin}}$, of the respective fitted function (this is further magnified in the respective insets in Fig. 5.5). It is apparent that the Brillouin component comprises only a very small part of the complete fitted function, indicating the low impurity content in the single-crystal sample. This may be estimated to amount to 0.1 %–0.3 %. Interestingly, and as evident from the insets in Fig. 5.5, the paramagnetic impurities exhibit anisotropic behaviour, with their detected saturation moment being approximately twice as large along the *c*-axis as along the *a*- or *b*-axes. This verifies earlier observations [126] and indicates that the impurities are not perfectly paramagnetic but merely quasi-free. A possible microscopic mechanism by which such quasi-free moments may be realised is provided by antisite disorder which has been postulated to affect compounds containing highly-diffusive lithium ions, such as $LiFePO_4$ [129].

In the next step of the isothermal magnetisation analysis, the thus-modelled Brillouin

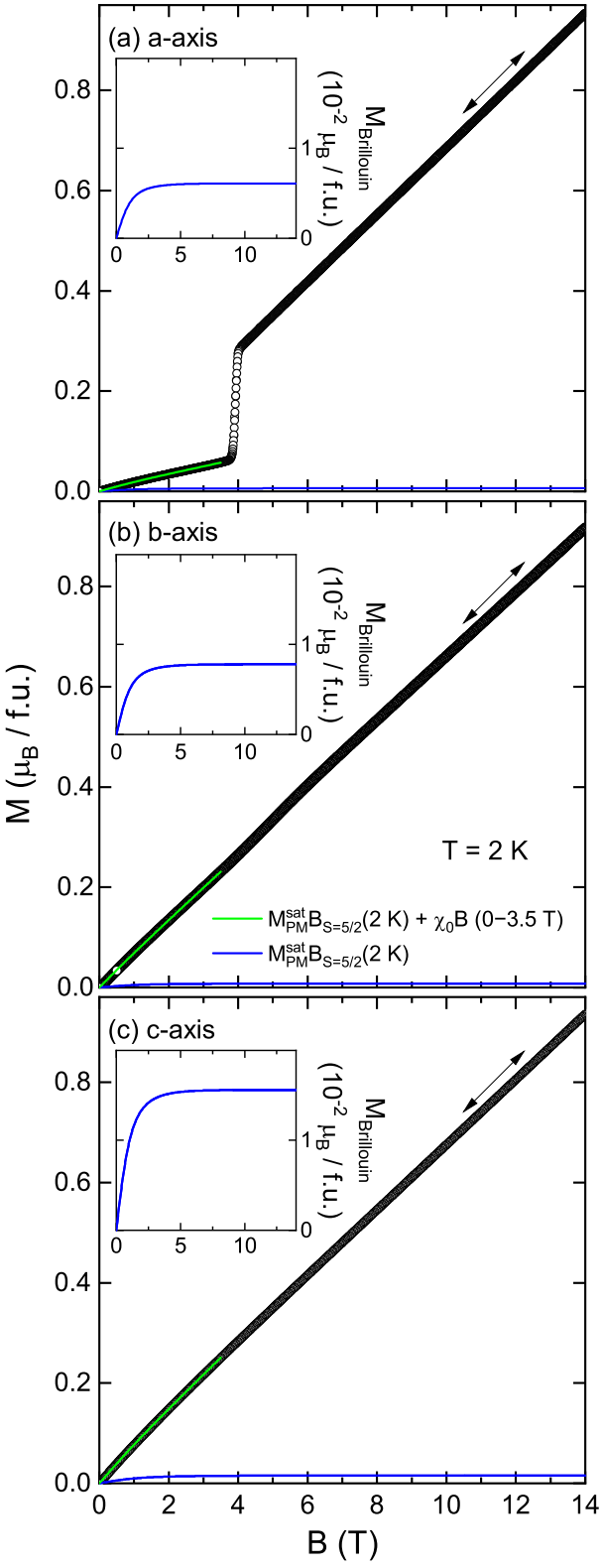

Figure 5.5.: Isothermal magnetisation of $LiMnPO_4$ at 2 K along the main crystallographic orientations (black), fitted by a function consisting of a Brillouin and a linear component in the region $0\,\mathrm{T} \leq B \leq 3.5\,\mathrm{T}$ (green) (see text for details). The obtained Brillouin component is shown in blue. The magnetisation curves depict a full measurement cycle $0\,\mathrm{T} \rightarrow 14\,\mathrm{T} \rightarrow 0\,\mathrm{T}$. Insets: magnification of the respective Brillouin components from the fits.

contributions are subtracted from the respective curves. Hence, the remaining magnetisation, $M - M_{\text{Brillouin}}$ (depicted in Figs. 5.6a,c,e), may be taken to be due to the antiferromagnetic ground state of $LiMnPO_4$. This is then fitted in the high-field region $10\,\text{T} \leq B \leq 14\,\text{T}$ by a linear function of the form $M_0 + \chi_0' B$ and the resulting fits are displayed in Figs. 5.6a,c,e as solid red lines.[3] Focusing first on the a-axis magnetisation, it is now possible to interpret the jump in M as a spin-flop transition, since the high-field fit extrapolates approximately to zero. This confirms that the spins in the ground state are aligned (predominantly) along the crystallographic a-axis. The exact spin-flop field, B_{SF}, can be determined as the peak in the field derivative of the magnetisation (see Fig. 5.6b). $B_{\text{SF}} = 3.92(6)\,\text{T}$ is found at $T = 2\,\text{K}$, confirming earlier work [126]. With increasing temperature, the spin-flop transition weakens and moves to slightly larger fields. Finally at 40 K, i.e. above T_{N}, no feature is found in the field derivative of the magnetisation. The size of the jump at the spin flop can be read off from Fig. 5.6a: $\Delta M_{\text{a}} = 0.276(5)\,\mu_{\text{B}}$/f.u. Assuming that the fully-saturated moment amounts to $\mu_{\text{sat}} = gS = 5\,\mu_{\text{B}}$/f.u., the angle between the sublattice magnetisation and the bc-plane, into which the spins flop, is found to be $\theta_{\text{SF}} = 3.2(2)^\circ$. That is, and as expected, the magnetic moments lie at the spin flop predominantly in the bc-plane, almost perpendicular to the easy axis.

The (Brillouin-component-accounted) isothermal magnetisation along the b-axis appears on the first look to be perfectly linear. However, upon closer inspection a small jump is found to occur at around 5 T, as demonstrated by a small but finite deviation from the high-field linear fit setting in for $B \lesssim 5\,\text{T}$ (c.f. Fig. 5.6c). The small jump becomes clearly visible when the high-field linear component is subtracted from the magnetisation curve. This is depicted in the inset of Fig. 5.6c, together with the low-field Brillouin component, previously seen already in Fig. 5.5b. Denoting the field at which the jump occurs as B_{C2}, its exact position may be determined – similarly to $B||a$-axis – as the maximum in the corresponding field derivative. At $T = 2\,\text{K}$, the maximum is found at $B_{\text{C2}} = 4.9(2)\,\text{T}$. As demonstrated in Fig. 5.6d, the maximum weakens and shifts somewhat to higher fields with increasing temperature, before it completely disappears at $T = 40\,\text{K}$. This provides a further strong indication that the jump is an inherent property of the antiferromagnetically-ordered ground state of $LiMnPO_4$. The origin of the is discussed in the following section (Section 5.2.1.3).

Lastly, as Figs. 5.6e,f demonstrate, no particular field-induced phase-transition-indicating features are detected in the isothermal magnetisation along the c-axis. Only a small decrease of the field derivative may be seen in the low-field regime in Fig. 5.6f. However, this is merely an artefact of the fitting of the original magnetisation curve by means of $M = M_{\text{Brillouin}} + \chi_0 B$ and may indicate the presence of other types of

[3] Note that χ_0' of the present fit of the high-field region $10\,\text{T} \leq B \leq 14\,\text{T}$ is distinct from χ_0 of the earlier fit of the low-field region $0\,\text{T} \leq B \leq 3.5\,\text{T}$ seen in Fig. 5.5.

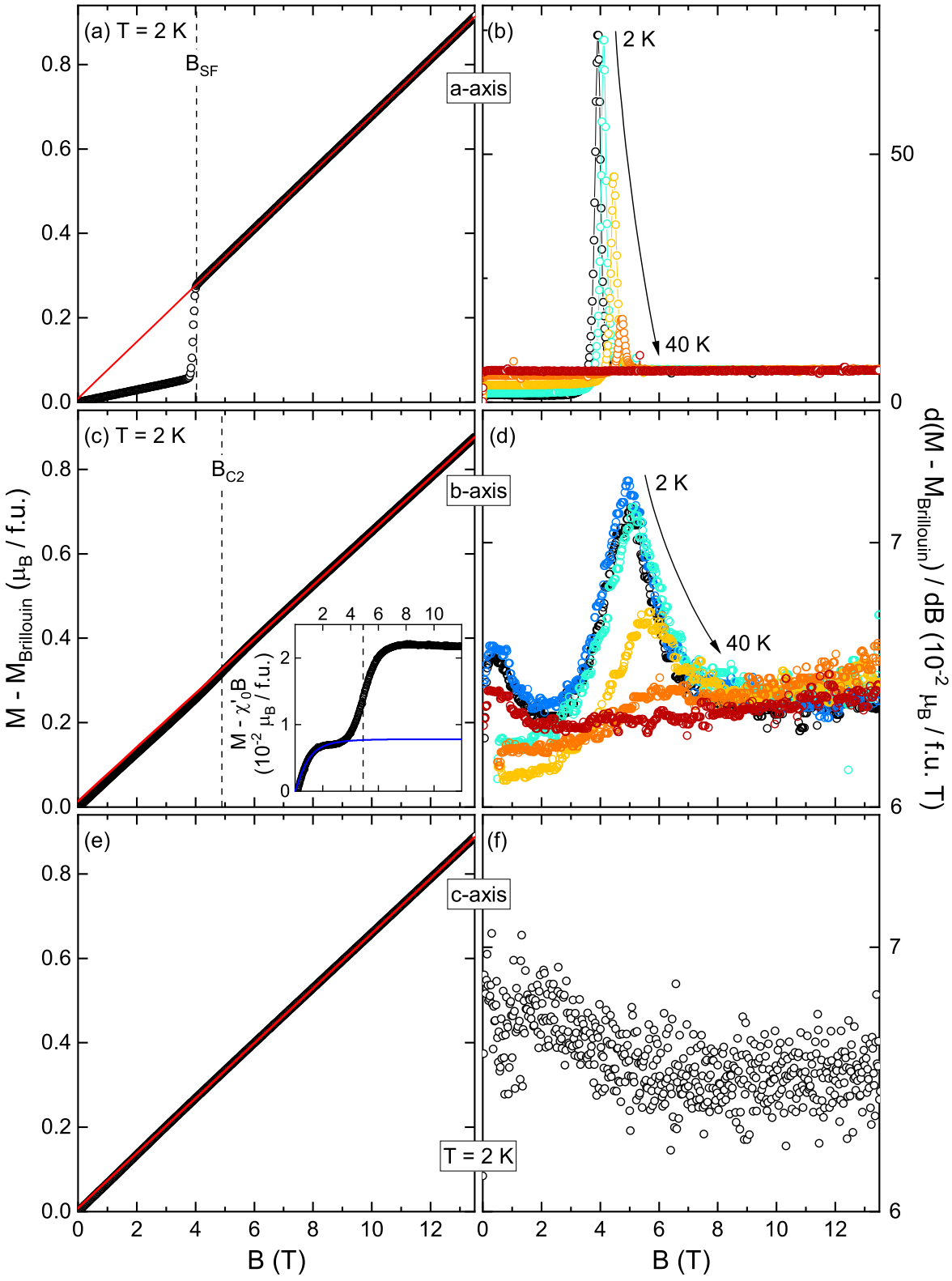

Figure 5.6.: Left: isothermal magnetisation of $LiMnPO_4$ at 2 K along the main axes accounted for the Brillouin component (see text for details). Right: corresponding field derivative. Solid red lines are straight-line fits in the region $10\,\mathrm{T} \leq B \leq 14\,\mathrm{T}$. The inset in (c) depicts the magnetisation for $B||b$ after subtraction of the high-field linear regime, whereby the solid blue line depicts the Brillouin component. Vertical dashed line marks the spin-flop field B_{SF} in (a) and the critical field B_{C2} in (c).

paramagnetic impurities beyond Mn^{2+} with $S = 5/2$ and $g = 2$.

The above straight-line fits may be used to estimate the saturation fields for the respective axes under the assumption that the ground state of $LiMnPO_4$ is characterised by unreduced size of the moment $\mu = gS = 5\,\mu_B$/f.u.. The saturation fields are thus found to be: $B_a^{sat} = 74.5(3)$ T; $B_b^{sat} = 78.0(20)$ T, and; $B_c^{sat} = 76.7(3)$ T. Such an order of saturation fields implies that the easy magnetisation axis lies along the crystallographic a-axis, the intermediate axis along c, and the hard axis along b, confirming the assignment of anisotropy values based on neutron scattering [114].

Previous, unpublished magnetostriction measurements at 2 K identified a jump in the relative length change of the a-axis at 4.0(3) T [128], hence corroborating the present observation of a spin flop at this field. Crucially, a counterpart to the much weaker magnetisation jump along the b-axis was also detected in magnetostriction at 2 K, albeit at slightly higher magnetic field of $\approx 5.6(4)$ T [128]. On the other hand, despite solving the spin structure in the ground state and in the spin-flop phase, previous elastic neutron scattering experiments gave no hints pertaining to the possible microscopic origin of the presently-observed b-axis feature [114].

5.2.1.3. Interpretation of the Isothermal Magnetisation

In the following, an attempt is made at providing a possible microscopic picture which could account for the observed magnetisation jump in $LiMnPO_4$ for $B||b$.[4] The attempt invokes small canting of the antiferromagnetically-ordered moments away from the easy a-axis in the ground state of $LiMnPO_4$. Since no magnetisation jump is observed when $B||c$ (at least up to 14 T), it may be assumed that the canting of the magnetic moments is solely towards the b-axis. In principle, the canting may be envisaged to occur in two different ways which are schematically depicted in Fig. 5.7. Therein, a projection of the nearest Mn^{2+} neighbours is made onto the ab-plane.[5] Without any canting, the individual magnetic moments would be aligned parallel or anti-parallel with respect to the a-axis. In Fig. 5.7a, a scenario is envisaged in which the canting on two nearest neighbours (i.e. canting along the b-axis) is realised in an opposite fashion, such that overall an antiferromagnetic arrangement of the canted components of the magnetic moments is realised along the b-axis. In contrast, Fig. 5.7b envisages a scenario in which the canting on nearest neighbours is realised in the same same fashion, such that overall a ferromagnetic arrangement of the canted components is realised (denoted by a thick red arrow in Fig. 5.7b). The latter scenario is typically referred to as weak ferromagnetism [17].

[4] It is to be stressed that without detailed information on the microscopic spin structure, the present attempt is merely a hypothesis the verification of which can be provided only by microscopic methods, such as elastic neutron scattering.

[5] The bond between the nearest Mn^{2+} neighbours is oriented predominantly along the [011] axis with a small component also along the a-axis.

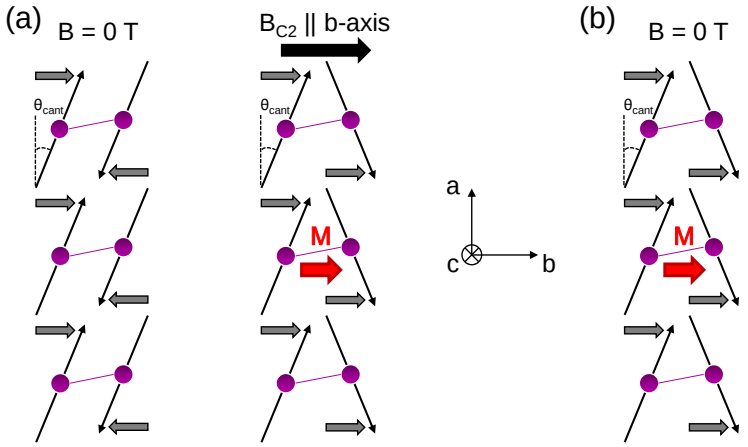

Figure 5.7.: A schematic depiction of two possible spin canting arrangements in $LiMnPO_4$: (a) with nearest-neighbour moments canting towards each other, resulting in zero net magnetisation when $B = 0\,\mathrm{T}$; (b) with nearest-neighbour moments canting in the same direction, resulting in finite net magnetisation M when $B = 0\,\mathrm{T}$ (thick red arrow). The right image in (a) visualises the spin canting just above the critical field B_{C2} applied along the b-axis. Thin black arrows represent the full magnetic moment of the Mn^{2+} ions (purple spheres), thick grey arrows the component of the magnetic moment along the b-axis, and purple lines the nearest-magnetic-neighbour interaction. θ_{cant} is the canting angle, which is greatly exaggerated for visualisation purposes.

Interestingly for the present purposes, the two envisaged scenarios make different predictions about the macroscopic magnetisation along the direction of the canted components of the total magnetic moments. Whereas weak ferromagnetism is characterised by spontaneous magnetisation at $B = 0\,\mathrm{T}$ and magnetisation hysteresis around $B = 0\,\mathrm{T}$, as is known for regular ferromagnets, the antiferromagnetic arrangement of the canted moments predicts a spin flip to occur in sufficiently large external field applied along the direction of the canted moments (i.e. along the b-axis in the present case). The spin flip of the antiferomagnetically-ordered canted components is illustrated in the right panel of Fig. 5.7a.

In the present case, no spontaneous magnetisation at $B = 0\,\mathrm{T}$ and only negligible hysteresis of approximately $0.01\,\mathrm{T}$ around $B = 0\,\mathrm{T}$ were observed, whereby the latter is on the order of typical hysteresis effects due to a superconducting magnet coil. On the other hand, the analysis of the isothermal magnetisation along the b-axis revealed that the linear regime above B_{C2} does not cross the abscissa at $M_0 = 0\,\mu_{\mathrm{B}}/\mathrm{f.u.}$, but rather a finite remnant moment is found (c.f. Fig. 5.6c). This indicates that the field-induced jump at B_{C2} is a spin-flip transition.

Therefore, it may be concluded that – should spin canting be responsible for the observed jump in the magnetisation along the b-axis – the spin canting must be of the type shown in Fig. 5.7a, i.e. of antiferromagnetically-arranged canted components of the

magnetic moments along the *b*-axis which undergo a spin-flip transition to full saturation at B_{C2}. Correspondingly, the size of the jump may be estimated by reading off the value of M_0 from the above fit, obtaining $M_0 = \Delta M_{\text{flip}}^{\text{spin}} = 0.014\,\mu_B$/f.u. The obtained value enables to estimate the canting angle as $\theta_{\text{cant}} = \sin^{-1}(\Delta M/(g\mu_B S)) \approx 0.16°$. Such a small value of the canting angle could have easily been missed by the reported neutron scattering experiments [123].

Note that earlier magnetisation measurements on a powder sample purported to have detected signatures of weak ferromagnetism in $LiMnPO_4$ [130, 131]. The basis for the conclusion was the observation of a hysteresis in the isothermal magnetisation with coercive fields on the order of 0.1 T, significant difference in the low-temperature static magnetic susceptibility between field-cooled and zero-field-cooled regimes, and a small value of the saturated magnetic moment at the lowest temperatures [130, 131]. Although clear left-bending of the isothermal magnetisation was observed for fields larger than approximately 1 T in the reported work [131], the limited available field range ($B \leq 5\,\text{T}$) and the unavailability of single-crystal samples would have rendered the present observation of the small jump at B_{C2} very unlikely. Indeed, isothermal magnetisation at $T = 1.8\,\text{K}$ up to $B = 7\,\text{T}$ of the powder sample of $LiMnPO_4$ in the present study reveals only the spin-flop-associated jump at $B_{SF} = 4.0\,\text{T}$ and no further features at higher fields (c.f. Fig. 5.4 and the corresponding discussion). Furthermore, it should be noted that the polycrystalline sample in the reported work was found to order at around 42 K [131]. This value is about 10 K higher than the ordering temperature in the present sample and in other, state-of-the-art literature reports [114, 124]. At the same time, ferrimagnetic compound Mn_3O_4 is known to order at $T_C = 39\,\text{K}$ and to show sizeable magnetisation hysteresis around $B = 0\,\text{T}$ [132]. It cannot be ruled out that such an impurity phase might have formed within the reported polycrystalline sample of $LiMnPO_4$ and distorted the reported results.

Given the arguments in the preceding paragraph, it is concluded that the weak ferromagnetic order proposed by earlier magnetisation studies on polycrystalline $LiMnPO_4$ is unjustified. Instead, the present analysis demonstrates that – if canting of the moments occurs – it leads to their antiferromagnetic arrangement.

The microscopic mechanism by which the spins may cant away from the easy magnetisation axis in the ground state of $LiMnPO_4$ may be provided by the antisymmetric, Dzyaloshinskii-Moriya (DM) interaction [17, 21] (see also Section 2.3). Inspection of the spin structure of $LiMnPO_4$ reveals that the bond between the nearest-neighbour magnetic ions, which lie in the *bc*-plane, does not contain an inversion centre (see Section 5.1 and especially the discussion pertaining to Fig. 5.2b) and, as such, supplies the necessary condition for the occurrence of the DM interaction. Not only is the DM interaction in $LiMnPO_4$ permitted on symmetry grounds, it was also invoked to explain several phenomena in other, structurally-related lithium orthophosphates: in

$LiFePO_4$ to account for the occurrence of an additional, mean-field-theory-forbidden magnetic resonance mode [112]; in $LiNiPO_4$ to account for the evolution of zero-field spin canting components away from the easy (*b*-)axis [118]. Moreover, in spite of no explicit reference to the Dzyaloshinskii-Moriya interaction in the discussion of neutron scattering results on $LiCoPO_4$, the compound's ground state was shown to exhibit a collinear rotation of the spins by $\approx 4.6°$ away from the easy axis [116], much akin to the scenario hypothesised in the current work (see also Section 5.1, and especially Table 5.1).

5.2.1.4. Magnetic Phase Diagrams

In order to map out the axis-dependent magnetic phase diagrams of $LiMnPO_4$, static magnetic susceptibility on the single crystal was measured at various fields in addition to the already-presented and discussed isothermal magnetisation (Fig. 5.6). The obtained curves are presented in Figs. 5.8a,c,e for the three main crystallographic orientations. It may be seen that all the curves fall onto each other at high temperatures. Upon cooling, a kink which signifies the onset of long-range antiferromagnetic order, is visible. The kink is found to remain at approximately the same temperature as the external magnetic field increases, indicating that the antiferromagnetic phase transition is only very weakly field-dependent in fields up to 14 T. The low-temperature evolution of the static magnetic susceptibility confirms that the *a*-axis is the easy magnetisation axis, since the corresponding curve at $B = 1\,\mathrm{T}$ drops to the lowest values of χ upon cooling. The susceptibility at the lowest temperatures shows a Curie-like increase, confirming the presence of paramagnetic impurities. As expected, the Curie-like increase is suppressed in increasing magnetic field. The antiferromagnetic transition temperature for the various fields and crystallographic orientations is determined as the maximum in the curves' corresponding Fisher's specific heat $\partial(\chi T)/\partial T$ (data not shown).

All phase-transition-indicating features from the static magnetic susceptibility and the earlier-presented isothermal magnetisation are summarised in magnetic phase diagrams in Figs. 5.8b,d,f. Whereas the *a*-axis phase diagram is partially corroborated by an earlier report [126], the *b*- and *c*-axes phase diagrams have not yet been reported in literature. Considering the *a*-axis diagram in more detail, the above-presented magnetisation and the known neutron scattering results [123] revealed that the magnetic moments are oriented along the *a*-axis in the ground state of $LiMnPO_4$.[6] Hence, as magnetic field is applied along *a*, the moments remain oriented along the easy magnetisation axis, i.e. $\mathbf{M}||a$-axis, until they undergo a spin flop at B_{SF}. From the order of anisotropy constants and from solutions of the microscopic spin structure in the spin-flop phase, it is known that above B_{SF} the moments occupy the *ac*-plane [114, 123], presumably until their full saturation. This is denoted as $\mathbf{M}||ac$-plane in Fig. 5.8b.

[6] The hypothesised small canting of the moments in the ground state is omitted in the present discussion.

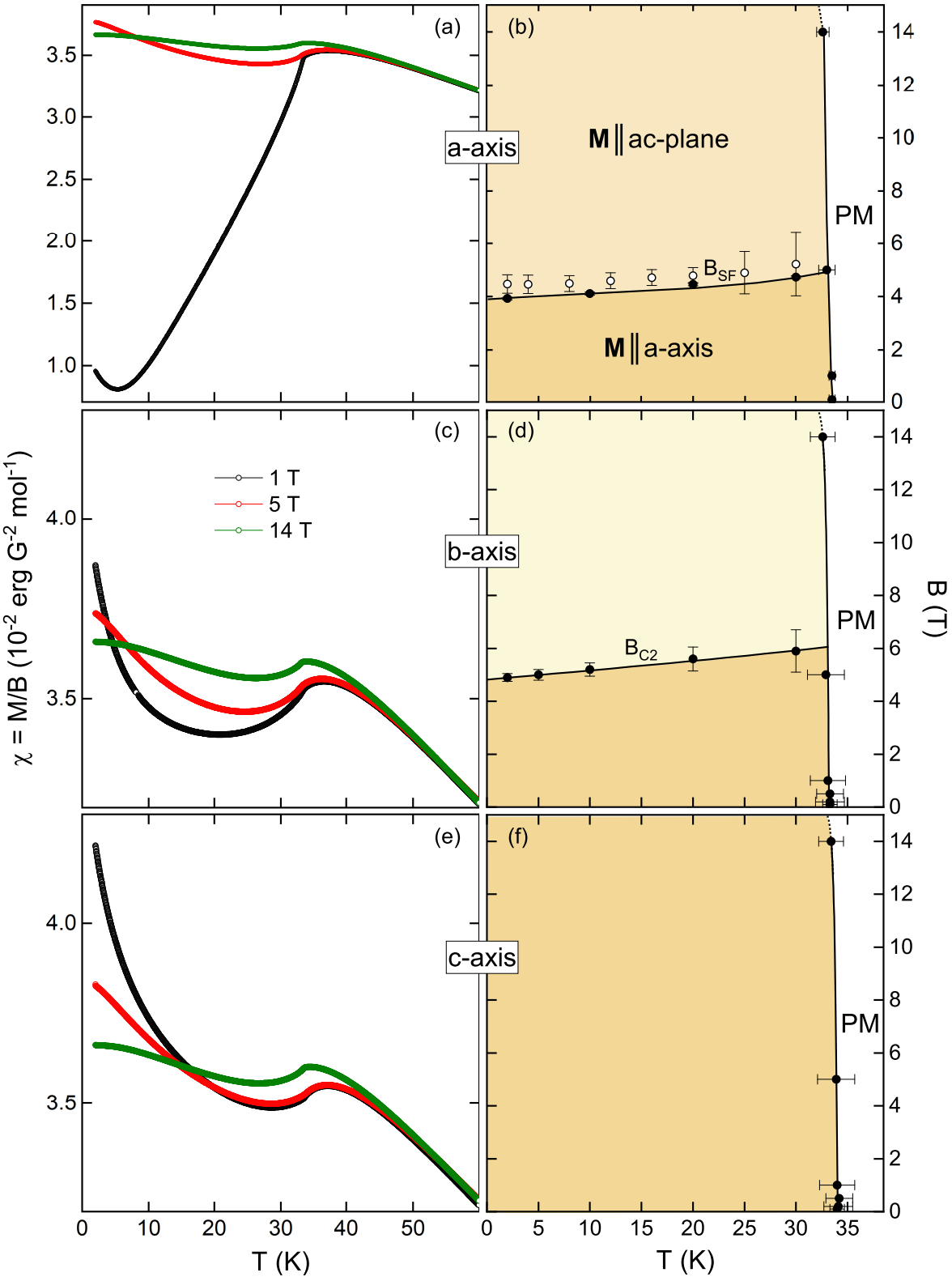

Figure 5.8.: Left: static magnetic susceptibility of $LiMnPO_4$ along the main crystallographic axes obtained in a zero-field-cooled mode; right: magnetic phase diagrams of $LiMnPO_4$ determined from anomalies in static magnetic susceptibility and isothermal magnetisation (closed black data points) and from temperature-dependent antiferromagnetic resonance (open black data points, see Section 5.2.2).

The a-axis magnetic phase diagram additionally includes data points from the analysis of temperature-dependent antiferromagnetic resonance (these are discussed in detail in Section 5.2.2.2). For $B||b$-axis, the magnetisation jump at B_{C2} has been hypothesised in the present work to mark the spin flip of the canted component of the magnetic moments. However, further microscopic studies are called for in order to verify this supposition and, moreover, to exclude any canting in the c-axis.

5.2.2. High-Frequency Electron Spin Resonance

5.2.2.1. Ground-State Antiferromagnetic Resonance

Profiting from the single-crystal sample, an attempt was made to obtain axis-dependent resonance spectra at $T = 2\,\mathrm{K}$, i.e. deep in the antiferromagnetically-ordered ground state of $LiMnPO_4$. For $B||a$-axis, these are displayed in Fig. 5.9a. It may be seen that at frequencies $\nu \leq 80\,\mathrm{GHz}$, up to four resonance features of varying shape are detected. Although the resonance features lack a Lorentzian character, the spectra's noise-free background allows for an unambiguous determination of the resonance-field positions (these are marked by the variously-coloured symbols in Fig. 5.9a). Especially noteworthy is the double-feature structure detected in the three spectrographs at 51.8 GHz, 57.0 GHz, and 62.3 GHz at $2.8\,\mathrm{T} \lesssim B \lesssim 4.0\,\mathrm{T}$, marked by black and orange symbols. For higher microwave frequencies, the double-feature structure disappears and a single resonance peak is observed at its position. At the same time, a different type of complexity of the resonance features evolves with increasing microwave frequency. Already at 102.0 GHz, the resonance feature at $\approx 6\,\mathrm{T}$ exhibits an intricate character, permitting a resonance-field assignment only with a large error bar. For still higher frequencies, no reliable assignment of any of the resonance features is possible, as illustrated in Fig. 5.9a for spectra recorded at high frequencies of $\nu = 306.1\,\mathrm{GHz}$ and $\nu = 331.1\,\mathrm{GHz}$. Therein, blue points mark the presumed resonance field but the number and exact position of the resonance features remain indeterminable. Such an evolution of the resonance peaks indicates Walker modes [82] which may result from the regularly-shaped sample or from a complex behaviour of the material's dielectric constant.

For this reason, electron spin resonance measurements were performed on an eicosane-fixed powder of $LiMnPO_4$. Although the powder sample did not stem from the same synthesis batch as the single-crystal sample, its magnetic properties were confirmed to be identical with the single crystal, as demonstrated and discussed in Section 5.2.1.1, especially with reference to Fig. 5.3. Spectra obtained on the powder and at frequencies comparable to those at which the single-crystal spectra were obtained are displayed in Fig. 5.9b (resonance features belonging to the same branch are marked by symbols of the same style and colour in both figures, (a) and (b)). As expected, single-crystal spectra exhibit more intense resonance features and more stable background than the powder spectra. The reduced quality of the powder spectra does not allow for the

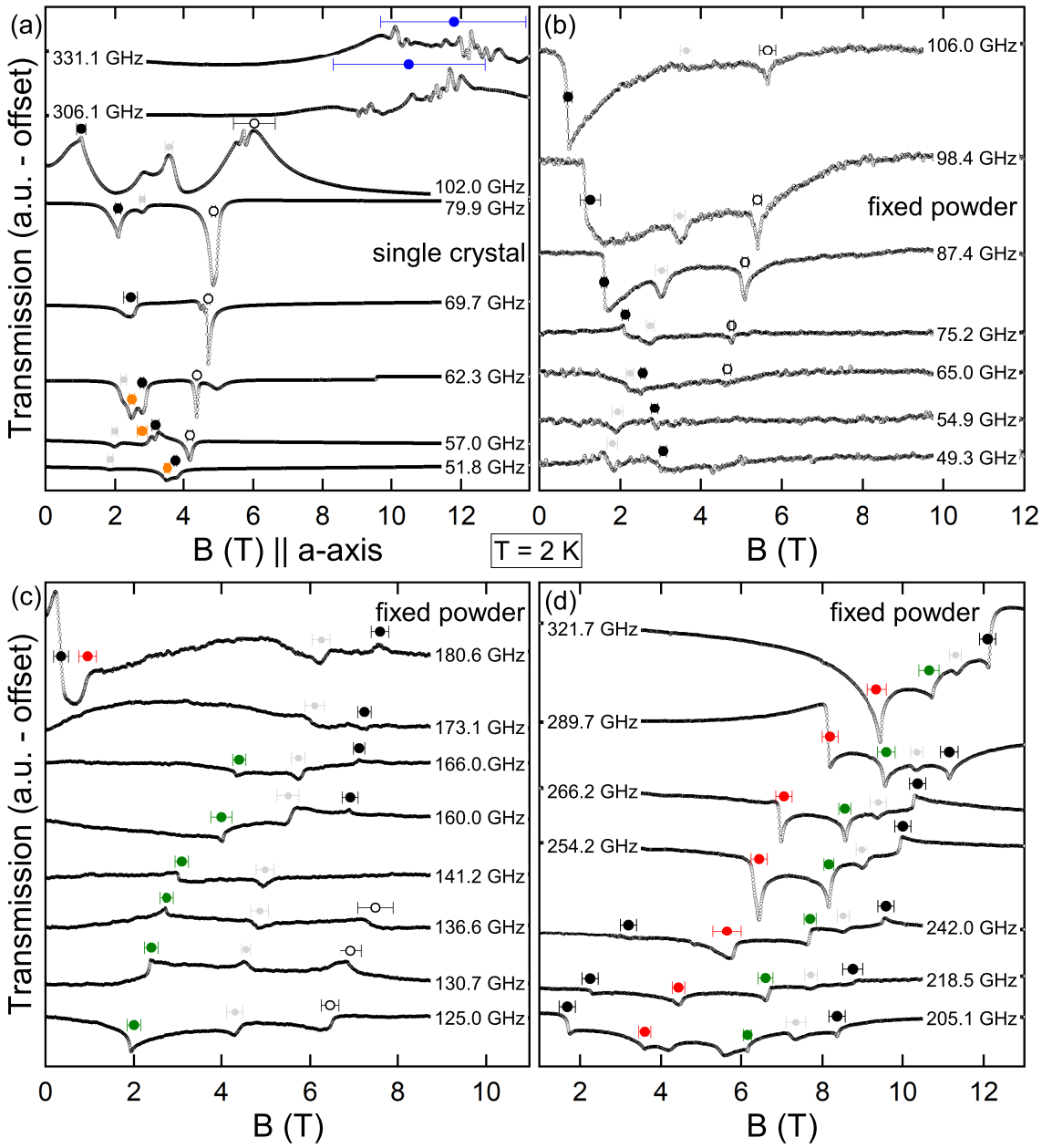

Figure 5.9.: Selected resonance spectra of $LiMnPO_4$ at $T = 2\,K$ obtained (a) on the single crystal sample with $B||a$-axis, and; (b)–(d) on the powder sample, fixed by eicosane. Variously-coloured symbols mark resonance feature positions.

detection of the double feature seen in the single-crystal spectra at low frequencies, and in place of the expected double feature, only a single absorption peak is observed.

Utilising the full available microwave frequency range, further spectra obtained on the powder sample at the lowest temperatures are displayed in Figs. 5.9c,d. While exhibiting a considerable amount of wave-phase mixing, these spectra possess a more stable background than their counterparts at lower frequencies, enabling an unambiguous assignment of the resonance-field positions.

Since it was not possible to obtain reliable resonance spectra on the single-crystal sample for frequencies $\nu \gtrsim 110\,\mathrm{GHz}$, resonance features stemming only from the powder measurement (Figs. 5.9b–d) are used in the next analysis step of constructing the resonance-frequency–magnetic-field diagram of $LiMnPO_4$. This is displayed in Fig. 5.10 and follows the colour coding introduced in Fig. 5.9. Altogether, the resonance features appear to fall onto six distinct magnon branches, labelled $\nu^{\mathrm{U}}_{\mathrm{easy}}$, $\nu^{\mathrm{L}}_{\mathrm{easy}}$, $\nu^{\mathrm{SF}}_{\mathrm{easy}}$, $\nu^{\mathrm{U}}_{\mathrm{im}}$, $\nu^{\mathrm{U}}_{\mathrm{hard}}$, and ν^{anom}, whereby the superscripts U, L, and SF refer to the *upper*, *lower*, and *spin-flop* branch, respectively, while the subscript "im" stands for *intermediate*. The branches $\nu^{\mathrm{U}}_{\mathrm{easy}}$ and $\nu^{\mathrm{U}}_{\mathrm{hard}}$, as well as the branches $\nu^{\mathrm{L}}_{\mathrm{easy}}$ and $\nu^{\mathrm{U}}_{\mathrm{im}}$ merge into two distinct excitation gaps for zero resonance field. The presence of two zero-field excitation gaps indicates two distinct anisotropy constants and hence an orthorhombic set of magnetisation axes with an easy, intermediate, and hard axis. Therefore, a minimal model required to describe the field dependence of the magnon branches of $LiMnPO_4$ is a two-sublattice antiferromagnetic resonance (AFMR) model with orthorhombic anisotropy. When the external magnetic field is applied along the easy magnetisation axis, the model predicts [31, 133–135]:

$$\nu^{\mathrm{U,L}}_{\mathrm{easy}} = \frac{1}{\sqrt{2}}\Bigg[(2-2\alpha+\alpha^2)\left(\frac{g_{\mathrm{easy}}\mu_{\mathrm{B}}B}{h}\right)^2 + (\Delta_2)^2 + (\Delta_1)^2 \pm \Bigg\{(2\alpha-\alpha^2)^2\left(\frac{g_{\mathrm{easy}}\mu_{\mathrm{B}}B}{h}\right)^4 + (8-8\alpha+2\alpha^2)\Big((\Delta_2)^2+(\Delta_1)^2\Big)\left(\frac{g_{\mathrm{easy}}\mu_{\mathrm{B}}B}{h}\right)^2 + \left((\Delta_2)^2-(\Delta_1)^2\right)^2\Bigg\}^{\frac{1}{2}}\Bigg]^{\frac{1}{2}} \tag{5.1}$$

for $B||\mathrm{easy} \leq (h\Delta_1)/(g_{\mathrm{easy}}\mu_{\mathrm{B}})$, and:

$$\nu^{\mathrm{SF}}_{\mathrm{easy}} = \sqrt{\left(\frac{g_{\mathrm{easy}}\mu_{\mathrm{B}}B}{h}\right)^2 - (\Delta_1)^2} \tag{5.2}$$

for $B||\mathrm{easy} \geq (h\Delta_1)/(g_{\mathrm{easy}}\mu_{\mathrm{B}})$. For the external magnetic field applied along the intermediate magnetisation axis, the field dependence of the magnon branch is given by:

$$\nu_{\mathrm{im}}^{\mathrm{U}} = \sqrt{\left(\frac{g_{\mathrm{im}}\mu_{\mathrm{B}}B}{h}\right)^2 + (\Delta_1)^2} \tag{5.3}$$

and for the field applied along the hard magnetisation axis by:

$$\nu_{\mathrm{hard}}^{\mathrm{U}} = \sqrt{\left(\frac{g_{\mathrm{hard}}\mu_{\mathrm{B}}B}{h}\right)^2 + (\Delta_2)^2} \tag{5.4}$$

In the above, α is a temperature-dependent ratio of the parallel and perpendicular static magnetic susceptibilities, $\alpha = \chi_{\parallel}/\chi_{\perp}$. μ_{B} and h refer to the Bohr magneton and the Planck constant, respectively, while g_{easy}, g_{im}, and g_{hard} refer to the effective g-factors associated with the easy, intermediate, and hard magnetisation axis, respectively. Lastly, Δ_1 and Δ_2 are the zero-field excitation gaps, whereby $\Delta_1 < \Delta_2$.

In addition to the dominant resonance features which can be associated with the AFMR model with orthorhombic anisotropy, a large number of spectra exhibit weak features which fall onto a gapless straight-line branch. Fitting the features by means of Eq. 2.33, $\Delta \approx 0\,\mathrm{GHz}$ and $g = 2.00(2)$ are found (the features and the fitted branch are displayed in grey colour in Fig. 5.10). This confirms that the features originate from the resonance behaviour of the paramagnetic impurities which were detected in DC magnetisation measurements and discussed above (see Section 5.2.1.1). Correspondingly, these resonance features shall not be considered for further analysis.

Similarly to the AFMR model with uniaxial anisotropy applied to $MnTiO_3$ (see Section 4.3.2), Eq. 5.1 can too be simplified if $\alpha = 0$:

$$\begin{aligned}\nu_{\mathrm{easy}}^{\mathrm{U,L}} = \frac{1}{\sqrt{2}}\Bigg[2\left(\frac{g_{\mathrm{easy}}\mu_{\mathrm{B}}B}{h}\right)^2 + (\Delta_2)^2 + (\Delta_1)^2 \pm \\ \left\{8\left((\Delta_2)^2 + (\Delta_1)^2\right)\left(\frac{g_{\mathrm{easy}}\mu_{\mathrm{B}}B}{h}\right)^2 + \left((\Delta_2)^2 - (\Delta_1)^2\right)^2\right\}^{\frac{1}{2}}\Bigg]^{\frac{1}{2}}\end{aligned} \tag{5.1b}$$

Accounting for the paramagnetic impurities in the sample, it is found that $\chi_{\mathrm{a}} \to 0$ as $T \to 0\,\mathrm{K}$ (c.f. Section 5.8), such that fixing $\alpha = 0$ is justified for the subsequent analysis of the low-temperature AFMR in $LiMnPO_4$. However, taking finite values of α into consideration shall be necessary in the later analysis of the temperature-dependent AFMR.

$\nu_{\mathrm{easy}}^{\mathrm{L}}$ is a magnon branch which can be excited when the external magnetic field is applied parallel to the easy magnetisation axis. The branch is associated with left-handed chirality of the processing sublattices [19] and softens with increasing external magnetic field. The softening becomes critical when the external magnetic field amounts

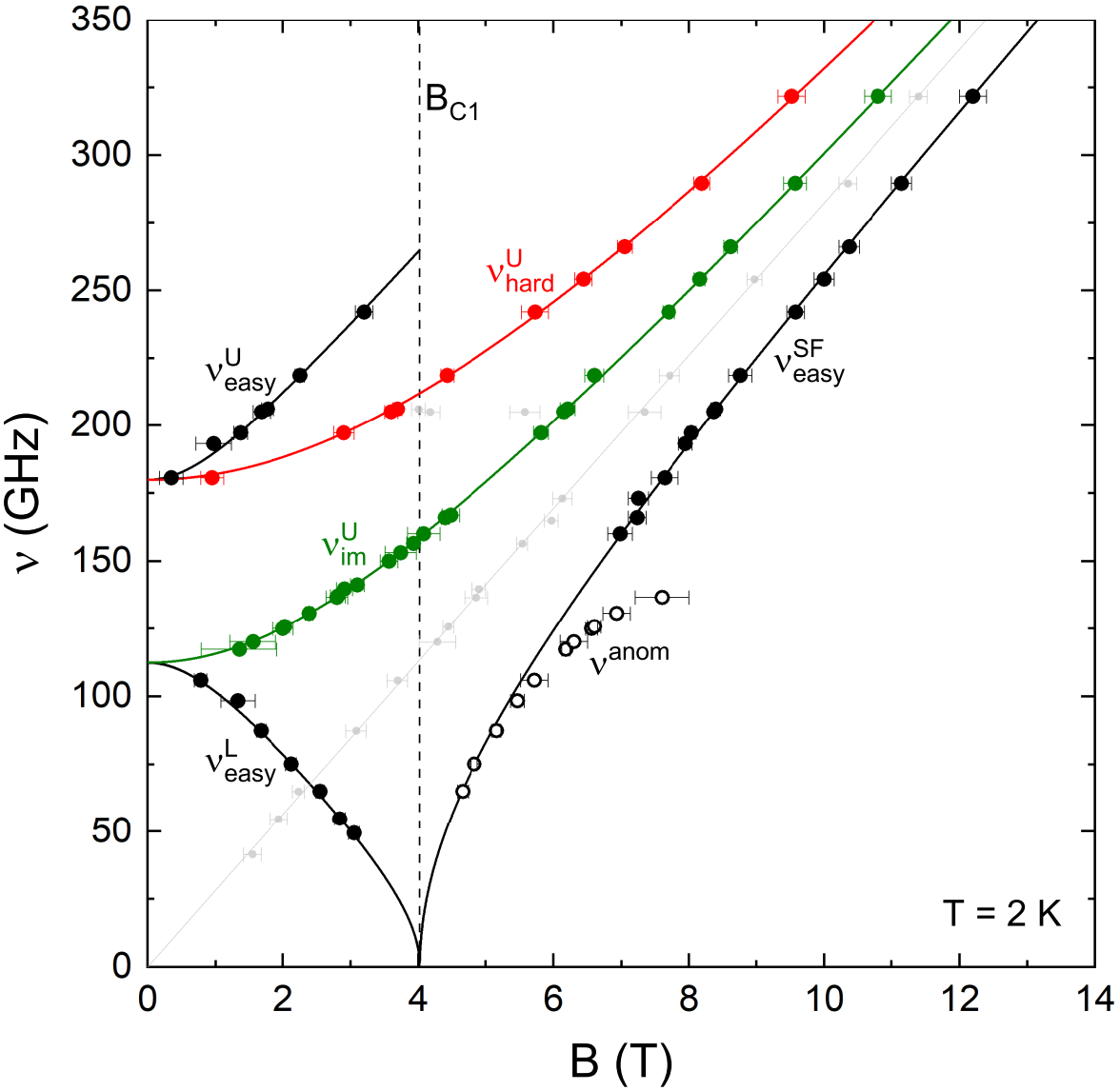

Figure 5.10.: Resonance-frequency–magnetic-field diagram of $LiMnPO_4$ obtained on a fixed powder at $T = 2\,\mathrm{K}$. Solid black, green, and red lines are fitting results based on Eqs. 5.1b–5.4. Solid grey line is a paramagnetic resonance branch, fitted by means of Eq. 2.33. Vertical dashed line marks the critical field B_{C1}.

to $B_{C1} = (h\Delta_1)/(g_{easy}\mu_B)$. At this point, the sublattice magnetisations jump and the system enters a spin-flop mode whose field dependence is given by Eq. 5.2. In spite of excluding the resonance features observed on the single-crystal sample with $B||a$ from the subsequent quantitative analysis, the single-crystal resonance features marked by solid black symbols in Fig. 5.9a do fall onto the same branch ν^{L}_{easy} as the features stemming from the powder measurement. This again confirms that a-axis is the easy magnetisation axis and that B_{C1} is related to the closing of the easy-axis-associated excitation gap.

Curiously, a region of anomalous behaviour is observed in the present case above the critical field B_{C1}. As may be seen in Fig. 5.10, two distinct branches, ν^{SF}_{easy} and ν^{anom}, are observed to lie below the paramagnetic resonance branch. As $B > B_{C1}$, ν^{anom} is observed (open black symbols). For increasing resonance field, ν^{anom} exhibits significant bending and, moreover, for $B \gtrsim 7.6\,T$ the branch either becomes field-independent or disappears completely. For $\nu \gtrsim 160\,GHz$, ν^{SF}_{easy} is observed (closed black symbols) which shows an almost perfectly linear field dependence. It is to be stressed that a systematic search for resonance features was conducted in the microwave frequency window $137.0\,GHz \leq \nu \leq 153\,GHz$, but only resonances associated with the green branch ν^{U}_{im} and grey paramagnetic branch were detected. The observation of two distinct branches above the spin-flop field but below the paramagnetic line is in stark contrast to the prediction of the two-sublattice AFMR model with orthorhombic anisotropy. This predicts a unique spin-flop mode given by Eq. 5.2.

Simulating all the observed resonance features by the two-sublattice orthorhombic AFMR model given in Eqs. 5.1b–5.4, it is found that ν^{U}_{easy}, ν^{L}_{easy}, ν^{SF}_{easy}, ν^{U}_{im}, and ν^{U}_{hard} – but not ν^{anom} – can be fitted by a unique set of parameters Δ_1, Δ_2, g_{easy}, g_{im}, and g_{hard} (simulation not shown). Therefore, resonance features belonging to ν^{anom} are excluded from the fitting and the remaining features fitted by the above model. The optimised parameters are found to be $\Delta_1 = 112.4(2)\,GHz$, $\Delta_2 = 179.9(2)\,GHz$, $g_{easy} = 2.00(1)$, $g_{im} = 2.00(1)$, and $g_{hard} = 2.00(1)$. The magnon branches obtained by means of the optimised parameters are displayed as solid black, green, and red lines in Fig. 5.10. It can be seen that all the resonance features are covered very well by the optimised curves with the exception of ν^{anom}. Possible origins of ν^{anom} are discussed in Section 5.3.

The presently-obtained excitation gaps contrast with their earlier determination by means of inelastic neutron studies which found $\Delta_1 = 148\,GHz$ and $\Delta = 168\,GHz$ [114]. The greater separation of the excitation gaps found in the present study indicates a greater difference in the axis-dependent anisotropy constants than suggested by the neutron study. The optimised effective g-factors associated with the AFMR model correspond very well to their paramagnetic counterparts for which, based on $3d^5$ shell occupation, $g = 2$ is expected. Using Eq. 5.1b, the critical field B_{C1} at which ν^{L}_{easy} reaches 0 GHz can be estimated as $B_{C1} = 4.02(2)\,T$. Since this value lies in the prox-

imity of the spin-flop field ($B_{\mathrm{SF}} = 3.92(6)\,\mathrm{T}$, see Section 5.2.1.2), such that $B_{\mathrm{C1}} \simeq B_{\mathrm{SF}}$, it follows that the effective exchange field in $LiMnPO_4$ is much larger than the effective anisotropy field along the easy axis.

The determined zero-field excitation gaps $\Delta_1 = 112.4(2)\,\mathrm{GHz}$ and $\Delta_2 = 179.9(2)\,\mathrm{GHz}$ can be used in combination with the spin-flop field $B_{\mathrm{SF}} = 3.92(6)\,\mathrm{T}$ and the estimated saturation field along the a-axis, $B_{\mathrm{a}}^{\mathrm{sat}} = 74.5(3)\,\mathrm{T}$, obtained from isothermal magnetisation (c.f. Section 5.2.1.2) to calculate the effective exchange and anisotropy fields. As already indicated above, besides the effective exchange field B_{E}, two effective anisotropy fields, $B_{\mathrm{A}}^{\mathrm{c}}$ and $B_{\mathrm{A}}^{\mathrm{b}}$, are expected, whereby the superscripts refer to the crystallographic axes. From the effective fields, the effective coupling and anisotropy constants, J_{eff}, D_{c}, and D_{b}, can be calculated. The strategy is similar to the analysis applied to $MnTiO_3$ (see Section 4.3.2), only made complicated by the presence of two energy gaps in the excitation spectrum, i.e. of two anisotropy constants.

In the first step, the spin-flop and saturation fields are evaluated by means of Eq. 2.27 (Chapter 2) to obtain the effective exchange field, finding $B_{\mathrm{E}} = 37.4(1)\,\mathrm{T}$.[7] In the second step, use is made of the relation $\Delta_i = \frac{g\mu_{\mathrm{B}}}{h}\sqrt{2B_{\mathrm{E}}B_{\mathrm{A}}^{i}}$ [133] to calculate the effective anisotropy fields, obtaining $B_{\mathrm{A}}^{\mathrm{c}} = 0.22(1)\,\mathrm{T}$ and $B_{\mathrm{A}}^{\mathrm{b}} = 0.55(1)\,\mathrm{T}$. In the third step, J_{eff}, D_{c}, and D_{b} are calculated with the help of Eq. 2.24. Taking into account that $z = 4$ for the number of Mn^{2+} nearest neighbours in $LiMnPO_4$ (see Table 5.2), $J_{\mathrm{eff}} = 0.43(1)\,\mathrm{meV}$ is found, as well as $D_{\mathrm{c}} = 0.005(1)\,\mathrm{meV}$ and $D_{\mathrm{b}} = 0.013(1)\,\mathrm{meV}$. From the above values, the ratios of the effective fields can be calculated: $B_{\mathrm{A}}^{\mathrm{c}}/B_{\mathrm{E}} \approx 6 \times 10^{-3}$ and $B_{\mathrm{A}}^{\mathrm{b}}/B_{\mathrm{E}} \approx 1.5 \times 10^{-2}$, confirming that $B_{\mathrm{A}}^{\mathrm{c}} \ll B_{\mathrm{E}}$ and $B_{\mathrm{A}}^{\mathrm{b}} \ll B_{\mathrm{E}}$.

Note that in order to facilitate comparison with literature data, the anisotropy constant along the easy-axis orientation was fixed to $D_{\mathrm{a}} = 0\,\mathrm{meV}$. Since no AFMR data were obtained on the single-crystal sample either with $B||b$ or $B||c$, the assignment of the anisotropy constants to the remaining two crystallographic orientations was informed by the above isothermal magnetisation. This showed that the intermediate magnetisation axis lies along the c-axis, whereas the hard magnetisation axis along the b-axis, such that D_{c} must be smaller than D_{b}.[8]

The anisotropy constants determined from the present AFMR analysis differ from those obtained from inelastic neutron scattering [114]. As noted above, the difference comes from the contrasting values of the zero-field excitation gaps, and from the quadratic dependence of the effective anisotropy field, and thus by extension of the anisotropy constant, on the excitation gap ($D_i \propto (\Delta_i)^2$). With energy resolution of HF-ESR of $\Delta\nu \lesssim 1\,\mathrm{GHz}$, as opposed to the moderate energy resolution in the cited inelastic

[7] Note that since $B_{\mathrm{C1}} \simeq B_{\mathrm{SF}}$, B_{C1} could also be used as the spin-flop field (see also the analysis of $MnTiO_3$ in Section 4.3.2).

[8] Here, the anisotropy term in the Hamiltonian reads $\sum_i D_{\mathrm{x}}(S_i^{\mathrm{x}})^2 + \sum_i D_{\mathrm{y}}(S_i^{\mathrm{y}})^2$ such that positive values of D_i render the orientation of the spin along the i-axis unfavourable by energy $\sim D_i S^2$.

neutron scattering of $\Delta\nu \approx 5\,\mathrm{GHz}$ [114], the present AFMR study is expected to yield more precise results.

On the other hand, the value of the effective exchange constant, $J_{\mathrm{eff}} = 0.43\,\mathrm{meV}$ corresponds well to the dominant exchange constant determined by means of inelastic neutron scattering, $J_1 = 0.48\,\mathrm{meV}$ [114]. This indicates that long-range antiferromagnetic order in $LiMnPO_4$ is predominately established through this nearest-neighbour interaction. This conclusion could have been anticipated directly from a careful inspection of the various exchange constants in Table 5.2. As may be observed, J_1 is more than two times larger than the next strongest constant, J_2, which is, moreover, frustrated.

Interestingly, the related orthophosphate $LiFePO_4$ exhibits a similarly strong effective exchange coupling as $LiMnPO_4$ but several orders of magnitude larger easy-axis anisotropy constant: $J_{\mathrm{eff}} = 0.67\,\mathrm{meV}$ and $D_{\mathrm{b}} = 0.53\,\mathrm{meV}$ in $LiFePO_4$ [136]; $J_{\mathrm{eff}} = 0.43\,\mathrm{meV}$ and $D_{\mathrm{c}} = 0.005\,\mathrm{meV}$ in $LiMnPO_4$ (present study). The significantly larger anisotropy constant increases the spin-flop field from the here-observed $B_{\mathrm{SF}} = 3.92\,\mathrm{T}$ in $LiMnPO_4$ to $B_{\mathrm{SF}} = 32\,\mathrm{T}$ in $LiFePO_4$ [136]. This is a direct consequence of the different orbital occupation in the two compounds: whereas $L = 0$ holds in $LiMnPO_4$, the nominal, Hund's-rules-predicted orbital moment in $LiFePO_4$ is $L = 2$ [111], although crystal-field effects likely introduce partial orbital quenching (see also the discussion on orbital quenching in Section 2.3). Furthermore, it may crudely be expected that the antiferromagnetic ordering temperature scales with the effective exchange constant, $T_{\mathrm{N}} \propto J_{\mathrm{eff}}$. Using the above values, $J_{\mathrm{eff}}(LiFePO_4)/J_{\mathrm{eff}}(LiMnPO_4) = 0.67\,\mathrm{meV}/0.43\,\mathrm{meV} \approx 1.56$ and $T_{\mathrm{N}}(LiFePO_4)/T_{\mathrm{N}}(LiMnPO_4) = 50.0\,\mathrm{K}/33.5\,\mathrm{K} \approx 1.49$ are found, whereby the Néel temperature of $LiFePO_4$ is taken from [125].

5.2.2.2. Temperature-Dependent Electron Spin Resonance Studies

Temperature evolution of the resonance behaviour was studied at three different frequencies $\nu = 79.9\,\mathrm{GHz}$ on the single-crystal sample, and $\nu = 125.0\,\mathrm{GHz}$ and $\nu = 197.3\,\mathrm{GHz}$ on the powder sample. Such frequency selection ensured that the temperature dependence of the resonance branches was covered in three distinct regimes: $\nu \leq \Delta_1$; $\Delta_1 \leq \nu \leq \Delta_2$, and; $\Delta_2 \leq \nu$. For clarity purposes, the presentation and discussion of the spectra is divided into two parts: in the first part, the temperature evolution of the AFMR, i.e. of spectra obtained at temperatures up to T_{N}, is in focus (Figs. 5.11, 5.12, and 5.13); in the second part, the temperature regime above T_{N} is discussed on the basis of spectra obtained in HF-ESR (Figs. 5.15 and 5.16), and in X-Band ESR (Fig. 5.17).

Temperature Dependence of the Antiferromagnetic Resonance Modes

In the antiferromagnetically-long-range-ordered phase, a pronounced shift of the resonance fields is found as temperature is increased from the lowest values up to T_N. In particular, ν^U_{easy}, ν^U_{hard}, and ν^U_{im} shift at $\nu = 197.3\,GHz$ to higher resonance fields upon heating (Fig. 5.11a), as does ν^U_{im} at $\nu = 125.0\,GHz$ (Fig. 5.11b). On the other hand, ν^{SF}_{easy} at $\nu = 197.3\,GHz$ shifts to lower resonance fields with increasing temperature (Fig. 5.11a), similarly to ν^L_{easy} at $\nu = 79.9\,GHz$ (Fig. 5.12). This way, the resonance branches ν^U_{easy}, ν^U_{hard}, ν^U_{im}, and ν^{SF}_{easy} shift towards the paramagnetic, $g = 2.00$ line as $T \to T_N^+$, thus approaching each other in the process. This behaviour is typical for a long-range-ordered antiferromagnet and signals the gradual closing of the zero-field excitation gaps as the Néel temperature is approached from below. In particular, at each of the three measured frequencies, the spectrum taken at 35 K, i.e. directly above T_N, exhibits a qualitatively different behaviour from the spectra taken below T_N (the paramagnetic spectrum at 35 K is included in the respective figure for comparative purposes together with the AFMR-bearing spectra). In each case, a pronounced feature is observed which can be associated with paramagnetic resonance. The resonance behaviour for $T > T_N$ is addressed in greater detail in the following section. Here, it is to be noted that the abrupt change of the resonant behaviour as the temperature is swept through T_N signals a complete closure of both excitation gaps at T_N.

Interestingly, the branch ν^{anom} exhibits an opposite trend to all the other AFMR branches in that it distances itself away from the paramagnetic line, shifting to higher resonance fields, with increasing temperature. This trend is observed in the temperature dependence of the powder spectra (Fig. 5.11b) as well as of the single-crystal spectra (Fig. 5.12). The observation of the same temperature trend in both sample types serves also as a good indication that the anomalous behaviour of ν^{anom} is not merely a property of the powder sample (or of the single-crystal sample) but rather that it is intrinsic to $LiMnPO_4$ itself. A further important observation from the temperature dependence of ν^{anom} is its disappearance for $T \to T_N^+$ (most clearly seen in Fig. 5.12), indicating that the branch is a property of the long-range-ordered $LiMnPO_4$. Lastly, upon careful inspection a shoulder to the right of the main resonance feature in ν^{anom} may be observed in the single-crystal spectra in Fig. 5.12. As the single-crystal spectra exhibited shoulders on varying sides of the main resonance features belonging to the branch ν^{anom} also at other frequencies and as the shoulders showed no univocal trend, they shall not be discussed in further detail. Although their nature as intrinsic resonant property of the ground state of $LiMnPO_4$ cannot be ruled out, it is also possible that they arose as a consequence of the developing Walker modes.

Quantitative analysis of the temperature-dependent spectra displayed in Figs 5.11 and 5.12 may be performed by means of Eqs. 5.1, 5.3, and 5.4.[9] This enables the

[9] The resonance features associated with the branches ν^{SF}_{easy} and ν^{anom} are excluded from the current

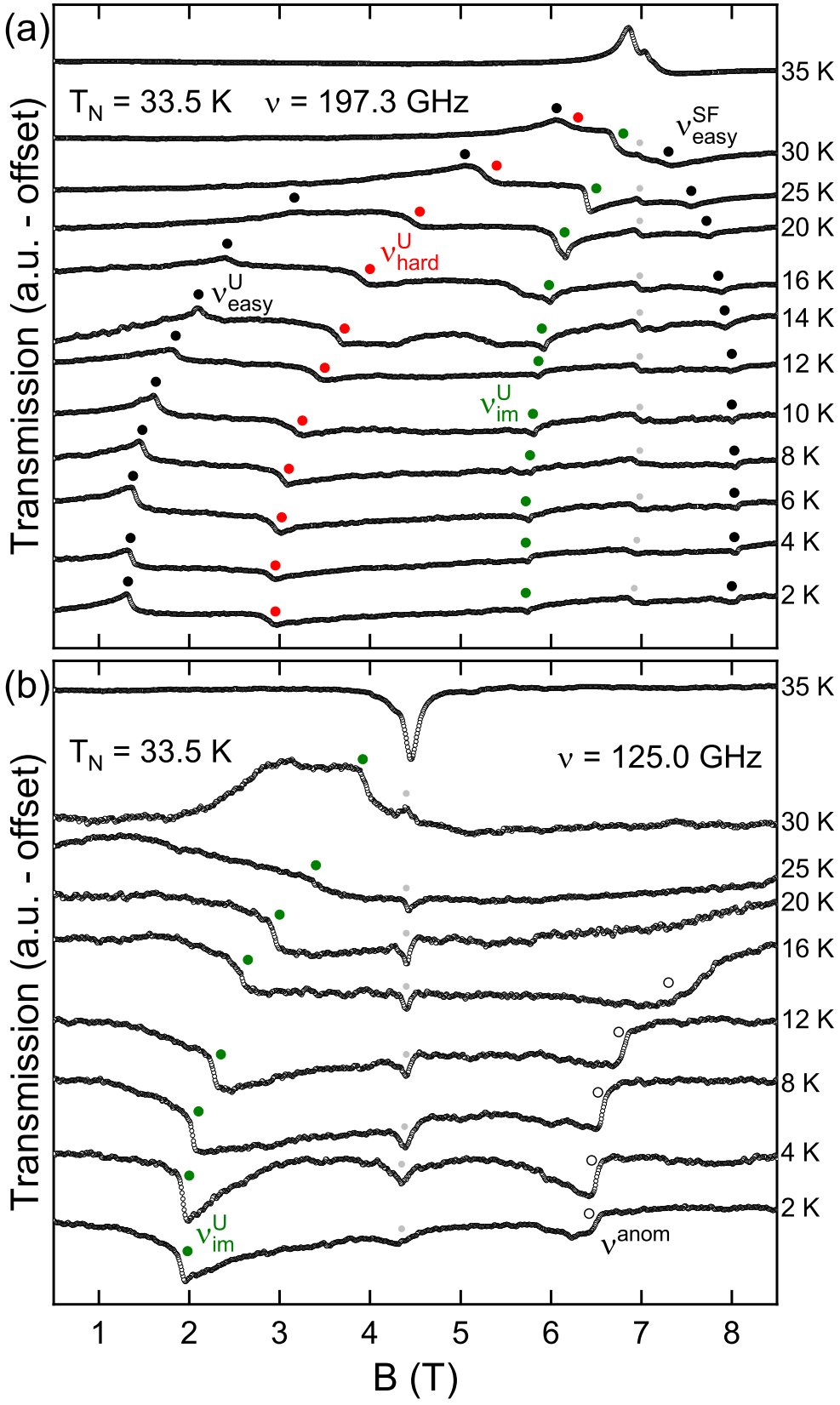

Figure 5.11.: Temperature evolution of resonance spectra obtained on the powder sample of $LiMnPO_4$ at fixed frequencies (a) $\nu = 197.3\,\mathrm{GHz}$, and (b) $\nu = 125.0\,\mathrm{GHz}$. Variously-coloured symbols mark the position of the resonance features, whereby the symbols' colour-coding follows Figs. 5.9 and 5.10.

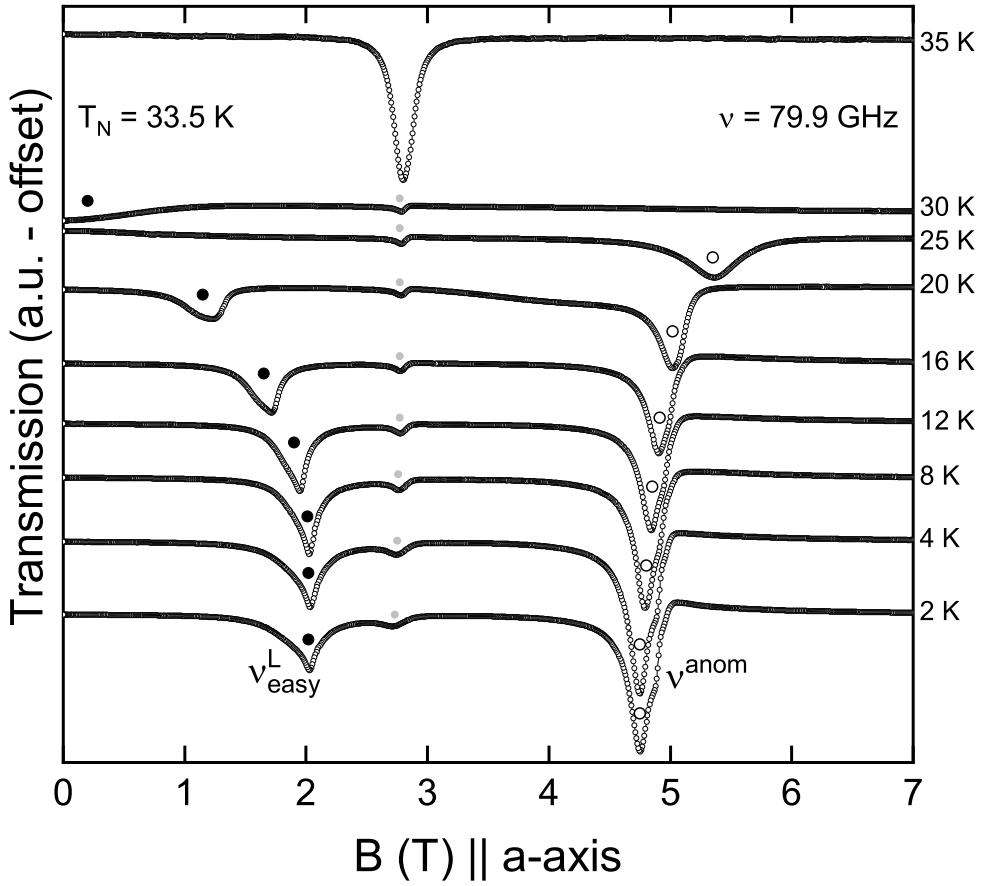

Figure 5.12.: Temperature evolution of resonance spectra obtained on the single-crystal sample of $LiMnPO_4$ for $B||a$-axis at fixed frequency $\nu = 79.9\,\mathrm{GHz}$. Variously-coloured symbols mark the position of the resonance features, whereby the symbols' colour-coding follows Figs. 5.9 and 5.10.

calculation of the temperature dependence of the excitation gaps Δ_1 and Δ_2, as well as of the critical field B_{C1}. To perform the analysis, the parameter $\alpha = \chi_{\mathrm{a}}/\chi_{\mathrm{c}}$ at a particular temperature is firstly obtained from the static magnetic susceptibilities at 1 T displayed in Figs. 5.8a and 5.8e.[10] Secondly, a simultaneous least-squares minimisation at each individual temperature is performed on Eqs. 5.1, 5.3, and 5.4 with the resonance fields given in Figs. 5.11 and 5.12. This mimics the procedure for analysing the full low-temperature frequency–resonance-field diagram with the exception that here only a small number of resonance frequencies and fields are available for the fitting. Moreover, the effective g-factors which enter Eqs. 5.1, 5.3, and 5.4 are taken to be temperature-independent in the present case and hence enter the minimisation routine as constant parameters. Their values are taken from the above two-Kelvin fitting, i.e. $g_{\mathrm{easy}}(T) = g_{\mathrm{im}}(T) = g_{\mathrm{hard}}(T) = 2.00(1) = \text{constant}$.

analysis, since ν^{anom} cannot be satisfactorily accounted for by the AFMR model at hand.

[10] In principle, α could also be defined as $\chi_{\mathrm{a}}/\chi_{\mathrm{b}}$. The choice of the definition affects the obtained value of the critical field B_{C1}, leaving the obtained values of Δ_1 and Δ_2 unaffected.

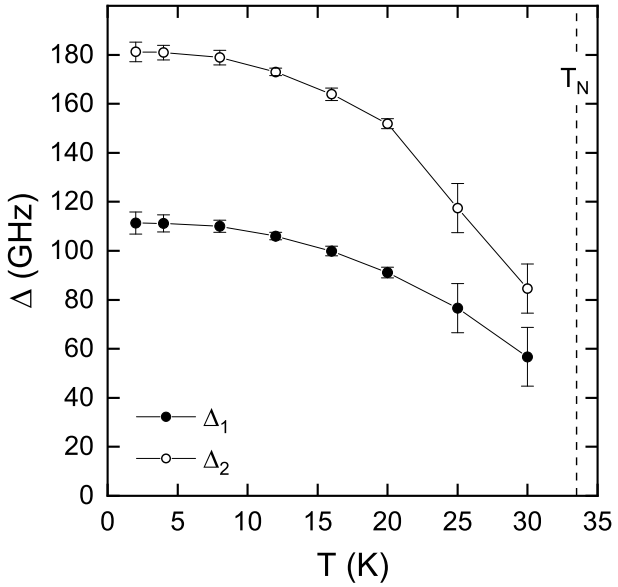

Figure 5.13.: Temperature dependence of the zero-field excitation gaps Δ_1 and Δ_2 of $LiMnPO_4$ as obtained from the analysis of the temperature-dependent spectra in Figs. 5.11 and 5.12 by means of Eqs. 5.1–5.4, see text for details. Vertical dashed line marks the antiferromagnetic ordering temperature.

The thus-obtained temperature dependence of the two excitation gaps is depicted in Fig. 5.13. As may be seen, both Δ_1 and Δ_2 decrease in size as the temperature increases. Interestingly, the two gaps remain distinct from each other in the entire temperature region of observation, indicating that the system preserves its orthorhombic anisotropy at least up to 30 K. A qualitatively similar but quantitatively different temperature evolution of the excitation gaps was recorded also by inelastic neutron scattering [114]. Although no spectra were obtained for $30\,\mathrm{K} \leq T \leq T_\mathrm{N}$ in the present study, it was already discussed above that the abrupt change of the spectra as temperature is swept through T_N indicates a complete vanishing of both gaps at T_N.

Also obtained from the quantitative analysis of the temperature-dependent AFMR spectra is the temperature dependence of the critical field B_{C1}. This is included in the a-axis magnetic phase diagram which is displayed above in Fig. 5.8b (open black data points). It may be seen therein that the temperature evolution of B_{C1} follows in general that of B_{SF} while lying consistently above it by $\approx$ 0.4–0.5 T. Such observation could indicate that the effective exchange field in $LiMnPO_4$ is not significantly larger than the effective anisotropy field, i.e. that $\sqrt{(2B_\mathrm{E}B_\mathrm{A} + B_\mathrm{A}^2)/(1-\alpha)} \not\approx \sqrt{(2B_\mathrm{E}B_\mathrm{A} - B_\mathrm{A}^2)/(1-\alpha)}$. However, the above low-temperature AFMR analysis found $B_\mathrm{A}^\mathrm{c}/B_\mathrm{E} \approx 6 \times 10^{-3}$ and $B_\mathrm{A}^\mathrm{b}/B_\mathrm{E} \approx 1.5 \times 10^{-2}$. The present observation that $B_{\mathrm{C1}} > B_{\mathrm{SF}}$ is a likely consequence of an overestimation of the parameter α, possibly owing to an incorrect accounting for the paramagnetic background in the static magnetic susceptibilities.

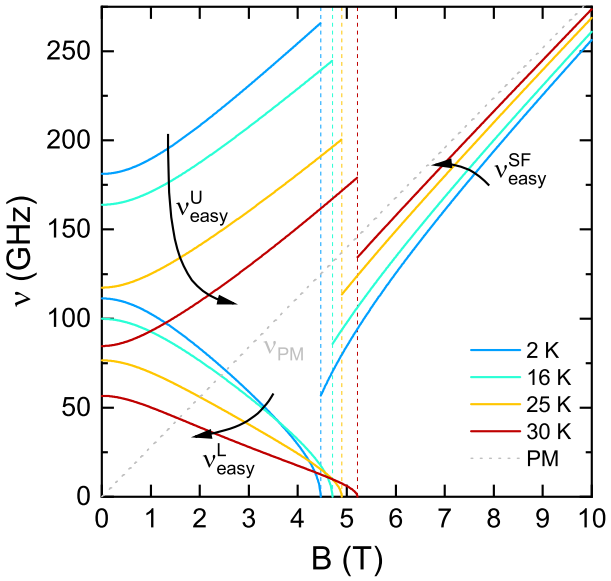

Figure 5.14.: Simulation of the resonance branches $\nu^{\mathrm{U}}_{\mathrm{easy}}$ and $\nu^{\mathrm{L}}_{\mathrm{easy}}$ in $LiMnPO_4$ at various temperatures based on Eq. 5.1, on the resonance fields extracted from Figs. 5.11 and 5.12, and on the parameter α. Additionally, simulation of the resonance branch $\nu^{\mathrm{SF}}_{\mathrm{easy}}$ based on Eq. 5.2, whereby the value of Δ_1 at the various temperatures required to evaluate Eq. 5.2 is extracted from the corresponding simulation of $\nu^{\mathrm{U}}_{\mathrm{easy}}$ and $\nu^{\mathrm{L}}_{\mathrm{easy}}$. Grey dotted line, marked ν_{PM}, depicts a paramagnetic resonance branch with $g = 2.00$. Dashed vertical lines mark the critical field B_{C1} with colour-coding corresponding to the respective temperature. Thick black arrows indicate the shift of the resonance fields for increasing temperature based on the simulated curves.

The AFMR branches simulated on the basis of the temperature-dependent resonance features in Figs. 5.11 and 5.12 are depicted for $B||a$-axis at selected temperatures in Fig. 5.14. The decreasing trend in the excitation gaps and the increasing trend in B_{C1} with increasing temperature are clearly visible. Although the resonance features belonging to $\nu^{\mathrm{SF}}_{\mathrm{easy}}$ were not included in the present fitting, the predicted trend of the resonance field's shift to lower values with increasing temperature matches the experimental observation at $\nu = 197.3\,\mathrm{GHz}$ seen in Fig. 5.11a. On the other hand, it clearly contradicts the observation made of ν^{anom} in Figs. 5.11b and 5.12.

Temperature Dependence of the Paramagnetic Resonance

The temperature evolution of the spectra obtained above T_{N} on the single-crystal sample at $\nu = 79.9\,\mathrm{GHz}$ and on the powder sample at $\nu = 125.0\,\mathrm{GHz}$ is displayed in Fig. 5.15 (note that the spectrographs at 35 K have already been included in Figs. 5.12 and 5.11a). A single Lorentzian-like resonance feature which may be assigned to a paramagnetic resonance of the Mn^{2+} ions is detected at 100 K and 80 K, respectively. Upon cooling, the resonance feature's linewidth increases while its position remains unchanged. The broadening of the linewidth as $T \to T_{\mathrm{N}}^{-}$ implies the reduction of the spin relaxation time and hence the growth of spin fluctuations. This likely occurs due

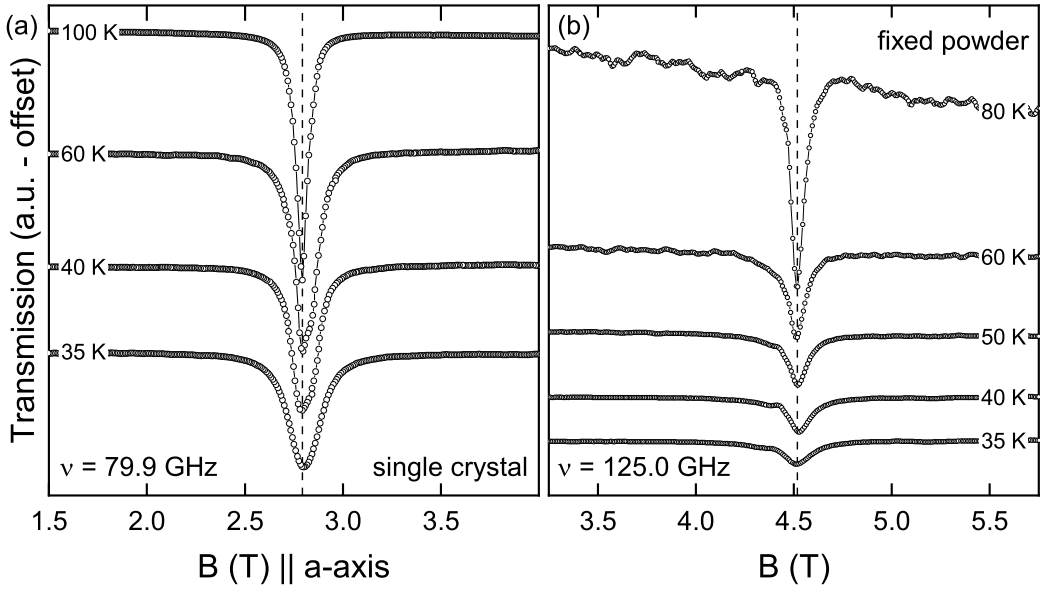

Figure 5.15.: Temperature evolution of resonance spectra above T_N of $LiMnPO_4$ obtained (a) on the single-crystal sample at $\nu = 79.9\,\mathrm{GHz}$, and (b) on the powder sample at $\nu = 125.0\,\mathrm{GHz}$. Vertical dashed lines serve as a guide for the eye.

to the opening of a spin-spin relaxation channel as an internal magnetic field evolves with the temperature's decrease towards T_N [18].

The lack of visible shift of the paramagnetic resonance with temperature may indicate that on the resolution scale of the presently-employed HF-ESR system, the local magnetic environment of the Mn^{2+} ions remains constant and, in particular, no short-range correlations are present in the temperature regime of study. This is partially corroborated by inelastic neutron scattering which detected finite correlation length in a modest temperature regime up to approximately 50 K [114]. Moreover, specific heat measurements showed that as much as 80% of the magnetic entropy in $LiMnPO_4$ is released upon heating up to T_N, whereby the small remaining entropy is completely released in the regime up to 60 K [137]. Furthermore, finite magnetostriction was detected up to about 65 K [128]. All these observations point to a weak short-range order in $LiMnPO_4$ above T_N which tends to complete melting within $1 \times T_N$ above the ordering temperature.

The spectra at 40 K and 60 K obtained on the single crystal exhibit an additional weak shoulder to the right of the dominant feature (c.f. Fig. 5.15a). If originating from the sample, it would indicate the presence of two distinct g-factors as may occur either in case of two crystallite grains which are rotated by a small angle with respect to each other, or in case of two distinct crystallographic sites with different crystal fields occupied by the Mn^{2+} ions. However, if the single-crystal sample did consist of two grains inclined at a small angle to each other, all the spectra would be expected to exhibit a double-feature behaviour, in particular, the spectra at 35 K and 100 K. But

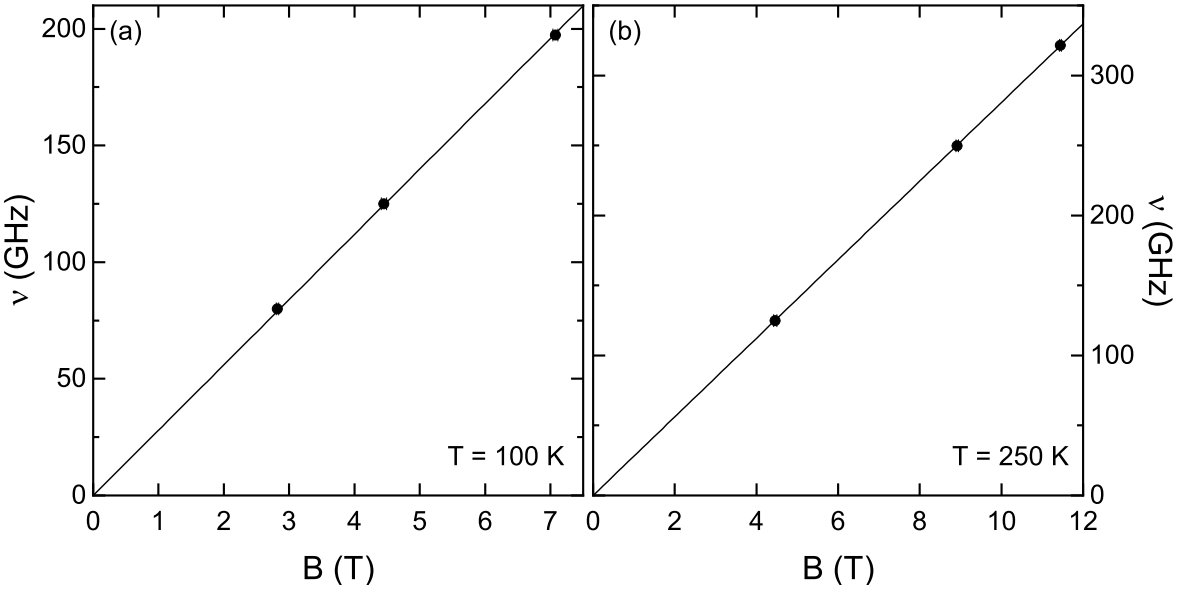

Figure 5.16.: Resonance-frequency–magnetic-field diagrams of $LiMnPO_4$ at (a) $T = 100\,\mathrm{K}$, and (b) $T = 250\,\mathrm{K}$. Solid lines are fit to the data by means of Eq. 2.33.

this is not the case. The second proposed scenario may be ruled out on the basis of the single-crystal refinement which detected only a single Mn^{2+} site [113].

The cessation of all short-range correlations and the realisation of a fully paramagnetic regime above $\approx 60\,\mathrm{K}$ is confirmed by the value of the corresponding g-factor. At selected temperatures – 60 K, 100 K, and 250 K – spectra at three different frequencies were obtained, the corresponding resonance field extracted, and the g-factor determined by fitting the resonance features' field dependence by means of Eq. 2.33. The optimised g-factors are found to be: $g(60\,\mathrm{K}) = 2.001(15)$; $g(100\,\mathrm{K}) = 1.999(8)$, and; $g(250\,\mathrm{K}) = 2.006(1)$. Within their respective error bars, the g-factors do not vary from each other and, moreover, lie in the region typical for paramagnetic Mn^{2+} ions [90]. The resulting frequency–resonance-field diagrams for $T = 100\,\mathrm{K}$ and $T = 250\,\mathrm{K}$ are displayed in Fig. 5.16 together with their respective fit.

In the last step, electron paramagnetic resonance was measured on the single-crystal sample of $LiMnPO_4$ at room temperature. This measurement was performed at X-Band frequency of $\nu = 9.632\,\mathrm{GHz}$, utilising a cavity (see Section 3.2). As may be seen in Fig. 5.17, the detected signal assumes a sharp Lorentzian-derivative form along all three main crystallographic orientations. Fitting the detected signal by a Lorentzian-peak derivative with a constant background, the resonance field and the linewidth are determined as: $B_\mathrm{a}^\mathrm{res} = 343.7(1)\,\mathrm{mT}$, $\Delta B_\mathrm{a} = 30.3(1)\,\mathrm{mT}$ for $B||a$; $B_\mathrm{b}^\mathrm{res} = 343.7(1)\,\mathrm{mT}$, $\Delta B_\mathrm{b} = 29.4(1)\,\mathrm{mT}$ for $B||b$, and; $B_\mathrm{c}^\mathrm{res} = 343.5(1)\,\mathrm{mT}$, $\Delta B_\mathrm{c} = 30.7(1)\,\mathrm{mT}$ for $B||c$. The corresponding g-factors amount to: $g_\mathrm{a} = 2.002(1)$; $g_\mathrm{b} = 2.002(1)$, and; $g_\mathrm{c} = 2.003(1)$. The g-factors reflect the behaviour present already at lower temperatures, namely that

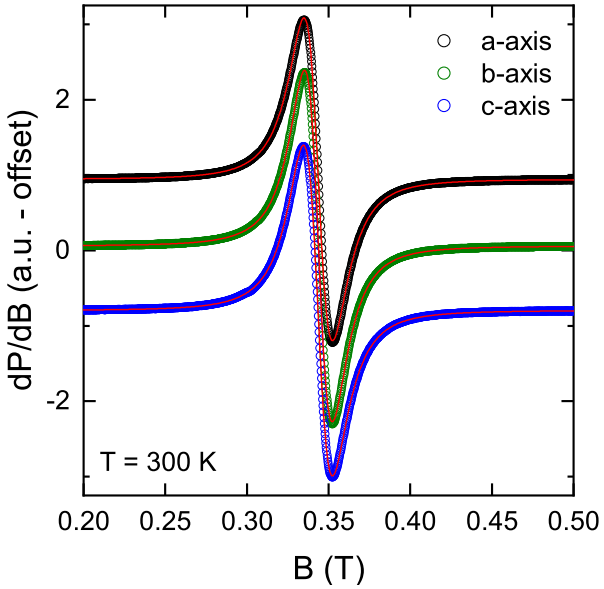

Figure 5.17.: Transmission derivative of room-temperature paramagnetic resonance of $LiMnPO_4$ at X-band frequency of $\nu = 9.632\,\mathrm{GHz}$ in a Faraday configuration ($B \perp k_{\mathrm{MW}}$) for the three main crystallographic orientations. Red solid lines are fitted Lorentzian-peak derivatives with a constant background. The spectrographs have been offset with respect to each other for clarity.

of typical paramagnetic Mn^{2+} ions [90]. The similar values of the linewidth for the different crystallographic orientations indicate that the room-temperature relaxation processes are isotropic. In particular, no signature of exchange narrowing, which would predict sharper resonance lines along directions with more dominant exchange interactions, is detected [91].

5.3. Discussion

Static magnetic susceptibility, specific heat, and magnetostriction reveal magnetism in $LiMnPO_4$ which in many respects provides a textbook-like example of a three-dimensional antiferromagnet: a sharp onset of long-range antiferromagnetic ordering with only a modest correlation maximum in susceptibility close above T_{N}, concomitant with a narrow window of short-range order as detected by specific heat and magnetostriction, as well as only a small frustration parameter derived from the Weiss and Néel temperatures. Even several aspects of the spectroscopic studies suggest behaviour of a three-dimensional mean-field antiferromagnet: X-Band- and HF-ESR above T_{N} indicate purely paramagnetic Mn^{2+} moments with $g = 2.00$ and no detectable evolution of short-range order down to T_{N}, while the ground-state properties as detected by HF-ESR point largely to a two-sublattice antiferromagnet with orthorhombic symmetry.

However, a more thorough look at the ground state has revealed at least two phenomena which cannot be explained by means of a simple two-sublattice AFMR model

and which make $LiMnPO_4$ an exciting material to investigate: a spin-flip transition along the hard magnetisation axis, and an additional, strongly field-dependent resonance branch ν^{anom}. Having already provided a possible account of the origin of the spin-flip transition by way of invoking small canting of the magnetic moments in the ground state of $LiMnPO_4$, and having argued that the origin of such canting may be Dzyaloshinskii-Moriya interactions, several models to account for the origin of ν^{anom} are to be considered next.

Firstly, without providing a microscopic underpinning, the right bending of ν^{anom} might suggest its phenomenological interpretation as a spin-flop branch, the dynamics of which is governed by Eq. 5.2. Performing the fitting under this hypothesis, the optimised parameters are found to be $g^{\text{anom}} = 1.53(9)$ and $\Delta^{\text{anom}} = 69(10)\,\text{GHz}$, and the optimised curve is displayed as a blue solid line in Fig. 5.18a. Not only is the determined g-factor unreasonably small for Mn^{2+} ions, but as evident from Fig. 5.18a, the fitted curve also fails to describe the resonance features satisfactorily. In particular, the resonance features appear to possess a considerably greater right bending than can be captured by Eq. 5.2. Moreover, the features seem to become field-independent or to vanish completely for $B \gtrsim 7.5\,\text{T}$, in contradiction to the expectation on the basis of Eq. 5.2.

Secondly, ν^{anom} might be associated with the canted component of the magnetisation and hence interpreted as a Dzyaloshinskii-Moriya mode. In the spin-flop phase, this is known to give rise to a modified frequency dependence of the usual spin-flop resonance branch and is given by [138–140]:

$$\nu_{\text{DM}}^{\text{SF}} = \sqrt{\left(\frac{g_{\text{easy}}\mu_{\text{B}}}{h}\right)^2 (B^2 + B_{\text{DM}}B) - (\Delta_{\text{DM}})^2} \tag{5.2b}$$

where B_{DM} is an effective Dzyaloshinskii-Moriya field and Δ_{DM} is a zero-field excitation gap, much akin to the usual excitation gap given, for instance, in Eqs. 5.1–5.4 but adjusted for Dzyaloshinskii-Moriya interactions. Although successful convergence of the fitting of ν^{anom} by Eq. 5.2b is possible (see Fig. 5.18b), the convergence can only be achieved at the expense of non-physical optimised parameters: $g_{\text{easy}} \approx 10^{-4}$; $B_{\text{DM}} \approx 7 \times 10^7\,\text{T}$, and; $\Delta_{\text{DM}} \approx 16\,\text{THz}$.

Having shown that ν^{anom} can be interpreted neither as a spin-flop mode nor as a Dzyaloshinskii-Moriya mode, it shall now be shown that the branch's unusual field dependence can be phenomenologically understood if the anisotropy axis is assumed to change its orientation above the spin-flop field (i.e. above B_{C1}). Fig. 5.18c depicts a simulation of $\nu_{\text{easy}}^{\text{SF}}$ and ν^{anom} using the earlier-optimised parameters of the AFMR model with orthorhombic anisotropy ($\Delta_1 = 112.4\,\text{GHz}$, $\Delta_2 = 179.9\,\text{GHz}$, and $g_{\text{easy}} = 2.00$, c.f. Section 5.2.2.1), but under the assumption that above B_{SF} the applied magnetic field has become inclined by 6.5° away from the easy a-axis towards the hard b-axis.

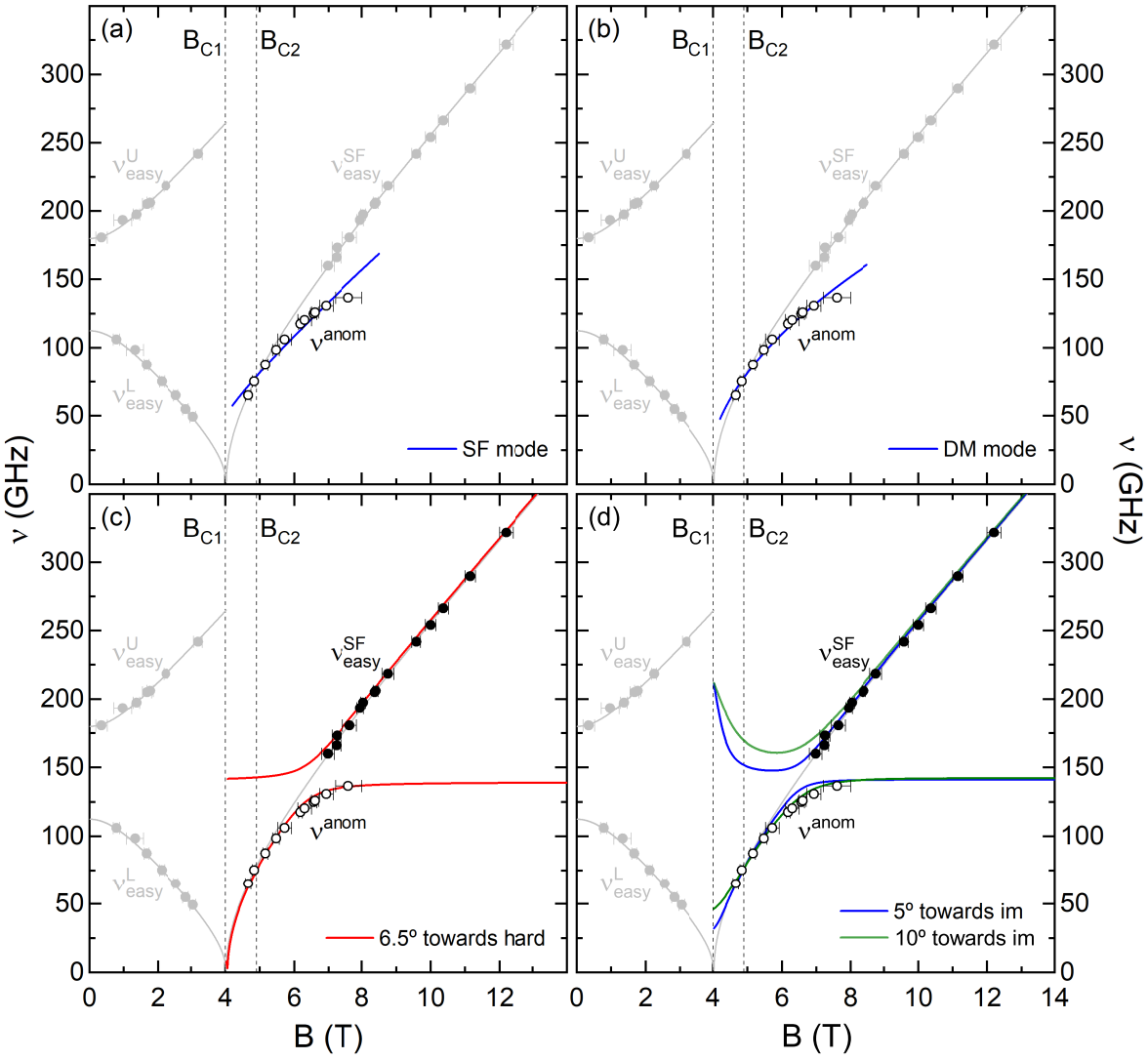

Figure 5.18.: Resonance-frequency–magnetic-field diagram of $LiMnPO_4$ displaying the fitting of ν^{anom} (a) as a spin-flop mode (Eq. 5.2, blue solid line), and (b) as a Dzyaloshinskii-Moriya mode (Eq. 5.2b, blue solid line). Further, the same diagram depicting a simulation of $\nu^{\mathrm{SF}}_{\mathrm{easy}}$ and ν^{anom} under the assumption that the anisotropy axis of the spin-flop phase is inclined (c) by 6.5° with respect to the axis' orientation in the ground state towards the hard magnetisation axis (red solid lines), and (d) by 5° and 10°, respectively, with respect to the axis' orientation in the ground state towards the intermediate (im) magnetisation axis, see text for details. For clarity, only resonance features associated with $B||$ easy axis are included (grey data points). Grey solid lines depict the fitting results of the non-inclined, ground-state antiferromagnetic resonance for $B||a$-axis, presented already in Fig. 5.10. Vertical dashed lines mark B_{C1} and B_{C2}, respectively.

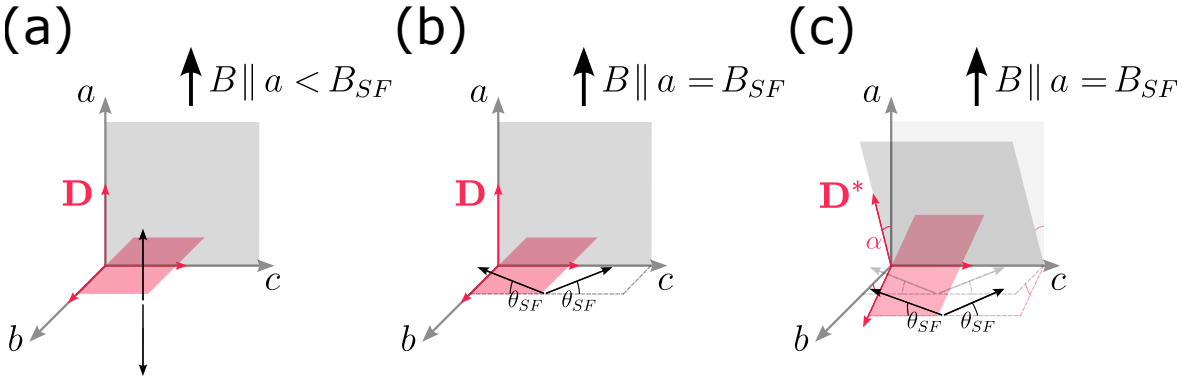

Figure 5.19.: Schematic visualisation of the orientation of the magnetic moments (black arrows) and anisotropy constant $\boldsymbol{D}$ (red arrows) in $LiMnPO_4$ with respect to the sample's crystallographic coordinate system (grey arrows) (a) in the ground state; (b) at a regular spin flop, and; (c) at a regular spin flop under the hypothesis of rotation of the anisotropy axis with respect to its ground-state orientation by angle α towards the b-axis. θ_{SF} denotes the spin-flop angle. The grey dotted arrows and lines in (c) depict the spin-flop scenario from (b) for comparative purposes.

But since it is assumed that for $B < B_{\mathrm{SF}}$, the magnetic field is applied perfectly along the easy magnetisation axis, this simulation procedure is equivalent to supposing that above B_{SF} the anisotropy axis itself deviates from its ground-state orientation by 6.5° towards the hard magnetisation axis.

Fig. 5.19 visualises the envisaged rotation of the anisotropy axis. In Fig. 5.19a, the collinear ground state arrangement of the magnetic moments along the a-axis is illustrated.[11] Fig. 5.19b illustrates the usual spin-flop scenario in which the magnetic moments flop from their ground-state arrangement along the a-axis into lying almost perpendicularly to the a-axis. The spin-flop angle which the moments enclose with the bc-plane was calculated earlier to amount to $\theta_{\mathrm{SF}} = 3.2(2)°$ (c.f. Section 5.2.1.2). The anisotropy vector $\boldsymbol{D}$ is identical in both cases and its direction given by $\boldsymbol{D} = (1\ 0\ 0)^{\mathrm{T}}$. In Fig. 5.19c, the spin flop is visualised under the assumption that the anisotropy vector has tilted with respect to its ground-state orientation by angle α towards the b-axis. That is, the direction of the anisotropy vector is now given by $\boldsymbol{D}^* = (\cos(\alpha)\ \sin(\alpha)\ 0)^{\mathrm{T}}$, where, based on the above simulation, it is argued that $\alpha = 6.5°$.

It may be seen in Fig. 5.18c that the simulation captures the right bending of the branch ν^{anom} very well while simultaneously successfully covering the resonance features associated with $\nu^{\mathrm{SF}}_{\mathrm{easy}}$. Moreover, the simulation correctly predicts the vanishing of the branch above $\approx 140\,\mathrm{GHz}$. As is evident from the figure, the vanishing is a consequence of an avoided crossing between the branches ν^{anom} and $\nu^{\mathrm{SF}}_{\mathrm{easy}}$. Importantly, the presumed change of the inclination of the anisotropy axis above B_{SF} has no impact on the field dependence of the remaining branches, $\nu^{\mathrm{U}}_{\mathrm{im}}$ and $\nu^{\mathrm{U}}_{\mathrm{hard}}$ (data not shown).

[11] The proposed Dzyaloshinskii-Moriya-caused small canting $\theta_{\mathrm{cant}} = 0.16°$ of the magnetic moments is omitted from the present discussion.

Note that a reasonable overlap between the resonance features and the simulated branches ν^{anom} and $\nu^{\mathrm{SF}}_{\mathrm{easy}}$ can also be achieved if a rotation of the anisotropy axis towards the intermediate c-axis above B_{SF} on the order of 5°–10° is assumed. This is illustrated in Fig. 5.18d. However, in such a case it is found that the frequency of several resonance features is overestimated: either those around $\approx 6.5\,\mathrm{T}$ belonging to ν^{anom} (for inclinations of $\approx 5°$, blue solid lines) or those around $\approx 7.5\,\mathrm{T}$ belonging to $\nu^{\mathrm{SF}}_{\mathrm{easy}}$ (for inclinations of $\approx 10°$, green solid lines). While the present analysis cannot definitively discriminate between the inclination towards the hard axis and the inclinations towards the intermediate axis, the apparent success of the former simulation in *simultaneously* describing all the resonance features provides a strong case for supposing its correctness.

It is important to stress that the argued-for misalignment between the anisotropy axis in the spin-flop phase and its ground-state orientation along the crystallographic a-axis cannot be understood by invoking a misalignment between the sample and the applied magnetic field during the measurement. It is true that HF-ESR on a single-crystal sample defined by the current optimised parameters of Δ_1, Δ_2, and g_{easy} but misaligned by 6.5° would produce an identical frequency–resonance-field diagram as presented in Fig. 5.18c. However, it is to be noted that the resonance data under the current discussion were obtained on a well-ground powder sample for which misalignments of the applied magnetic field are not possible.

The picture presented here contradicts the results obtained in elastic neutron scattering which found that the spin-flop phase in $LiMnPO_4$ retains its zero-field spin structure and, in particular, which observed no signature of change of anisotropy axis [123]. Speculatively, this may be owing to the fact that the elastic neutron scattering employed only a modest field above the spin-flop field, $B = 4.5\,\mathrm{T}$. The present data suggest that the resonance features for $B_{\mathrm{SF}} \leq B \lesssim 5.0\,\mathrm{T}$ may still be correctly described by the ground-state AFMR model (see the good overlap of $\nu^{\mathrm{SF}}_{\mathrm{easy}}$ with the two lowest lying resonance features of ν^{anom} in Fig. 5.10).

On the other hand, the hereby-developed account naturally incorporates magnetostriction measurements [128] and the above-presented isothermal magnetisation for $B||a$-axis (c.f. Fig. 5.6a), neither of which detected a field-induced phase transition above B_{SF}, and, in particular, in the region $B \approx 7.6\,\mathrm{T}$ where ν^{anom} disappears. The fact that the simulated branches ν^{anom} and $\nu^{\mathrm{SF}}_{\mathrm{easy}}$ are continuous at all fields above B_{SF} clearly demonstrates that no field-induced phase transitions are expected to occur. Additionally, the magnetostriction measurement at the lowest temperature detected a strong response of the lattice at B_{SF}, indicating that $LiMnPO_4$ cannot be understood as a pure spin magnet. Concretely, the lattice was found to contract below B_{SF}, undergoing an abrupt jump at B_{SF}, followed by positive lattice expansion for fields greater than B_{SF} [128]. From $\partial L_{\mathrm{a}}/\partial B_{\mathrm{a}} = -\partial M_{\mathrm{a}}/\partial p_{\mathrm{a}}$ it follows that the pressure dependence of the

magnetisation changes its character from being positive below B_{SF} to being negative above it.

Furthermore, pulsed-field isothermal magnetisation and HF-ESR on the related orthophosphate $LiFePO_4$ demonstrated that the zero-field values of the single-ion anisotropy (and of the exchange constants) cannot explain the high-field data, especially the low value of the spin-flop field given the size of the zero-field excitation gap and the strong bending of the corresponding resonance branch towards B_{SF} [112]. A detailed modelling showed that the anisotropy and exchange constants are field-dependent, with a proposed quadratic dependence [112]. Although the present study does not provide as detailed an account on $LiMnPO_4$ as the above-cited investigation on $LiFePO_4$, they both share one conclusion: that the HF-ESR data are compatible with a field-dependent anisotropy.

Notwithstanding the above-proposed phenomenological account of ν^{anom}, its success in explaining the branch's strong right bending and its plausibility based on other observations discussed in the previous paragraphs, it is stressed that without further detailed studies, the account remains a hypothesis. Moreover, the account provides no microscopic mechanism by which the proposed inclination of the anisotropy axis in the spin-flop phase takes place.

A further point worth discussing is the additional resonance feature seen in the single-crystal spectra (but not in the powder spectra) in a small frequency window $\nu \lesssim 65\,\mathrm{GHz}$, marked by orange data points in Fig. 5.9a. Since it possesses an approximately constant separation from the resonance feature associated with $\nu^{\mathrm{L}}_{\mathrm{easy}}$ and since it disappears for microwave frequencies greater than $\approx 65\,\mathrm{GHz}$, it is unlikely to originate from a second crystallite grain in the single-crystal sample. Should a second grain be present in the sample, other spectra would too be expected to exhibit such a doubling of the main resonance feature, and the additional feature's position would be expected to follow the bending of the corresponding resonance branch. Although no satisfactory theoretical underpinning of the observed feature can be currently provided, it may be noted that in $LiFePO_4$ an additional resonance feature for $B < B_{\mathrm{SF}}$, unaccountable by the employed AFMR model, was too detected along the easy magnetisation axis [112]. Simulations showed that the feature could be assigned to a Dzyaloshinskii-Moriya mode [112]. The present study has argued for the presence of small spin canting in the ground state of $LiMnPO_4$ as a mechanism to explain the observed spin flip for $B||b$-axis. Moreover, using symmetry arguments the appearance of Dzyaloshinskii-Moriya interactions has been made plausible. It may therefore be speculated that also in $LiMnPO_4$ the additional feature which appears below the spin flop is associated with a Dzyaloshinskii-Moriya mode.

5.4. Summary

$LiMnPO_4$ was previously known to be a three-dimensional long-range-ordered antiferromagnet with a collinear ground state spin structure and a simple spin flop along the easy magnetisation axis. In this respect, the material was at odds with its counterparts from the olivine group of lithium orthophosphates, such as $LiFePO_4$, $LiCoPO_4$, and $LiNiPO_4$, which show complex ground state properties, including exceptionally large magnetoelectric tensor, spin canting and incommensurate magnetic phases, or field dependence of the anisotropy and exchange constants.

Profiting from a high-quality single crystal sample, the present study revisited the low-temperature isothermal magnetisation, and, encouraged by non-trivial antiferromagnetic resonance in $LiFePO_4$, to study the low-energy magnon excitations in a broad range of frequencies and fields.

Isothermal magnetisation along the b-axis detected a hitherto unobserved small jump at $B_{C2} = 4.9(1)\,\mathrm{T}$ which could be interpreted as a spin flip. Spin canting of the magnetisation along the hard magnetisation b-axis with an antiferromagnetic arrangement was postulated to explain the observed spin-flip effect. From the size of the jump, the canting angle was estimated to be 0.16°. Despite its very small size, the canting's presence brings $LiMnPO_4$ in line with the other lithium orthophosphates, all of which display canting of the magnetic moments in the ground state. The lack of inversion centre along the bond between nearest-neighbour Mn^{2+} ions, lying in the bc-plane, was invoked as providing the necessary condition for occurrence of Dzyaloshinskii-Moriya interactions which were put forward as a candidate to explain the ground state's spin canting. Using the full available range of magnetic fields, the magnetic phase diagrams were constructed for the first time along all three main crystallographic directions.

Also constructed was the low-temperature resonance-frequency–magnetic-field diagram of the antiferromagnetic resonance in $LiMnPO_4$. While confirming the orthorhombic nature of the anisotropy in the system, the zero-field excitation gaps could be determined with superior resolution over inelastic neutron scattering. $\Delta_1 = 112.4(2)\,\mathrm{GHz}$, $\Delta_2 = 179.9(2)\,\mathrm{GHz}$, and $g_{\mathrm{easy}} = g_{\mathrm{im}} = g_{\mathrm{hard}} = 2.00(1)$ were determined directly from the fitting of the AFMR, while $J_{\mathrm{eff}} = 0.43\,\mathrm{meV}$, $D_{\mathrm{c}} = 0.005(1)\,\mathrm{meV}$, and $D_{\mathrm{b}} = 0.013(1)\,\mathrm{meV}$ were calculated from the subsequent analysis. Temperature evolution of Δ_1 and Δ_2 could be mapped thanks to the analysis of temperature-dependent AFMR, finding that at least up to $\approx 0.9T_{\mathrm{N}}$ the anisotropy preserves its orthorhombic nature while both excitations gaps vanish for $T \to T_{\mathrm{N}}^{+}$. HF-ESR above T_{N} detected a single paramagnetic line with no evolution of internal fields, indicative of negligible, if any, short-range order above T_{N}.

An anomalous AFMR mode was detected above the spin-flop field. It was shown that the branch could be interpreted neither as an additional spin-flop mode nor as a

Dzyaloshinskii-Moriya mode. Instead, it was shown that the mode is fully integrable into the rest of the resonance-frequency–field diagram if a rotation of the anisotropy axis above the spin-flop field is supposed. Computational results showed that a rotation of the anisotropy axis above the spin flop by 6.5° towards the hard axis could most comprehensively explain the field dependence of the AFMR modes.

6. CrI_3

6.1. Material Background

6.1.1. Crystallographic Information

CrI_3 belongs to the class of chromium trihalides with the general formula CrX_3, where X = Cl, Br, and I.[1] From a crystallographic point of view, CrI_3 consists of weakly, van-der-Waals-coupled two-dimensional layers spanning the *ab*-plane (see Fig. 6.1) [141]. Each chromium atom is embedded in edge-sharing octahedra of six I^- ions in such a way that nearest-neighbour chromium ions within the *ab*-plane form a hexagonal lattice (Fig. 6.1b).

At high temperatures, CrI_3 crystallises in a monoclinic $C2/m$ crystal structure with an imperfect ABC-like stacking of the hexagonal layers [141]. The interatomic Cr^{3+}–I^- separation within the individual octahedra at $T = 250\,\mathrm{K}$ amounts to 2.709 52 Å (2x), 2.709 43 Å (2x), and 2.702 35 Å (2x), respectively, leading to a small distortion of the regular octahedra of 0.27%. Upon cooling, the intralayer chromium–chromium and iodine–iodine separation increases, whereas the individual planes grow closer to each other, reducing the van-der-Waals gap [141]. A structural phase transition from the monoclinic $C2/m$ to rhombohedral $R\bar{3}$ crystal structure sets in at $T_\mathrm{S} = 212\,\mathrm{K}$ [141]. In contrast to the monoclinic structure, the rhombohedral crystal structure is characterised by almost perfectly regular chromium octahedra and an ideal ABC-like stacking of the hexagonal layers [141]. The Cr^{3+}–I^- separation in the $R\bar{3}$ phase (at $T = 90\,\mathrm{K}$) is 2.7271(15) Å (3x) and 2.7246(17) Å (3x), respectively, amounting to a minimal distortion of approximately 0.09%.

As is apparent from Fig. 6.1b, the intralayer nearest-magnetic-neighbour coupling is mediated by a single I^- ion. The bond angle at $T = 90\,\mathrm{K}$ along the exchange path Cr^{3+}–I^-–Cr^{3+} amounts to 93.31(6)° [141], favouring a ferromagnetic superexchange between the nearest neighbours [17, 142, 143] (see also Section 2.3.2). Indeed, CrI_3 undergoes a ferromagnetic phase transition at $T_\mathrm{C} = 61\,\mathrm{K}$ [141]. The ferromagnetic order is axial, with the easy magnetisation axis oriented along the crystallographic *c*-axis, that is, perpendicular to the hexagonal *ab*-planes [141].

[1] For reasons of conciseness, the ensuing discussion is restricted to CrI_3, although a number of the observations apply also to the other chromium trihalides.

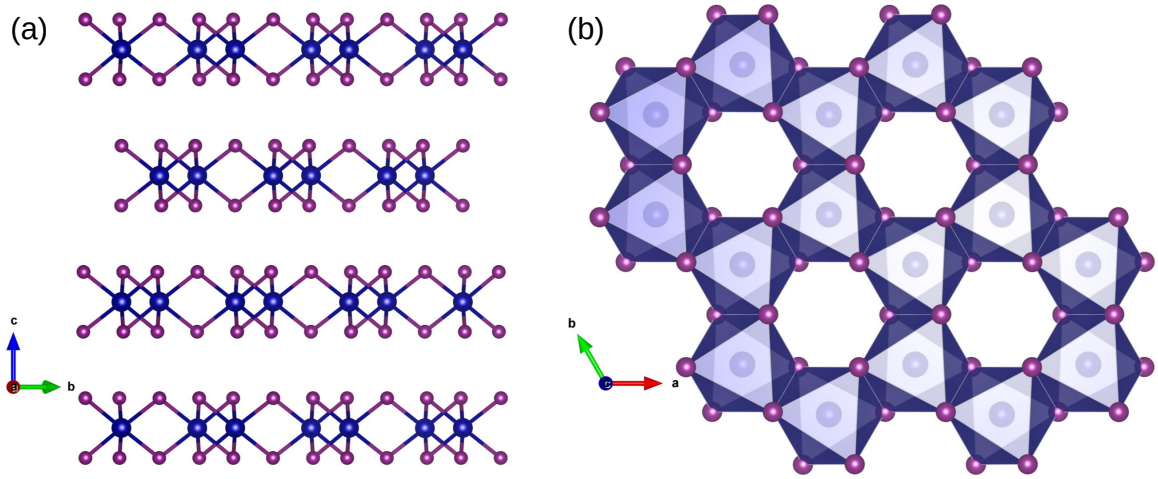

Figure 6.1.: Low-temperature, orthorhombic crystal structure of CrI_3 (a) in the *bc*-plane, (b) in the *ab*-plane. Blue spheres depict Cr^{3+} ions, purple I^- ions. Crystallographic data taken from [141], visualisation performed in VESTA [56].

6.1.2. Exchange Constants

Continuing with the above crystallographic considerations, it is found that three of the chromium-chromium nearest neighbours lie in the *ab*-planes and three perpendicular to the *ab*-planes. Designating the corresponding exchange coupling constants as J_1–J_3 for the intralayer nearest-neighbour exchange, and J_{c1}–J_{c3} for interlayer nearest-neighbour exchange, Fig. 6.2 visualises the various exchange constants.[2] Their quantitative values were determined by inelastic neutron scattering [144] and are listed together with the corresponding lengths and number of neighbours in Table 6.1. Using $J^{\text{eff}} = \sum_i (n_i J_i)$, $J_{ab}^{\text{eff}} = 3 \cdot J_1 + 6 \cdot J_2 + 3 \cdot J_3 \approx 77.7\,\text{K}$ for the effective in-plane exchange coupling, and $J_c^{\text{eff}} = 1 \cdot J_{c1} + 6 \cdot J_{c2} + 3 \cdot J_{c3} \approx 6.8\,\text{K}$ for the effective out-of-plane exchange coupling are found. This results in the ratio $J_c^{\text{eff}}/J_{ab}^{\text{eff}} \approx 0.09$, highlighting the dominance of the intralayer over the interlayer coupling.

6.1.3. Chromium Ion in CrI_3

Based on valence considerations in a purely ionic picture, the oxidation state of chromium in CrI_3 may be taken to be 3+, resulting in the electronic configuration [Ar]$3d^3$. Hund's rules predict for an isolated Cr3+ ion: $S = 3/2$; $L = 3$, and; $J = 3/2$ (see also Section 2.2.3). In an ideal octahedral coordination, crystal-field theory predicts a splitting of the 3d-orbital shell into lower-lying threefold degenerate t_{2g} orbital manifold and higher-lying twofold degenerate e_g orbital manifold [18] (see Section 2.2.1). Under the assumption of a complete quenching of the orbital moment, the ground state is predicted to be an orbital singlet Γ_2, and the g-factor to

[2] Unlike in Chapters 2, 4, and 5, a positive value of J in the present chapter implies ferromagnetic exchange coupling.

intralayer coupling				interlayer coupling			
	length [Å]	N	strength [K]		length [Å]	N	strength [K]
J_1	3.965	3	24.49	J_{c1}	6.589	1	-0.56
J_2	6.867	6	1.28	J_{c2}	7.701	6	0.82
J_3	7.929	3	-1.16	J_{c3}	7.713	3	0.82
J_{ab}^{eff}			77.7	J_c^{eff}			6.8

Table 6.1.: Bond lengths, the number of neighbours, N, connected via the respective bond length, and the corresponding intra- and interlayer coupling constants in CrI_3. J_{ab}^{eff} (J_c^{eff}) corresponds to the effective intralayer (interlayer) exchange constant. Positive value of J_i refers to ferromagnetic coupling. Crystallographic information from [141], coupling constants from [144].

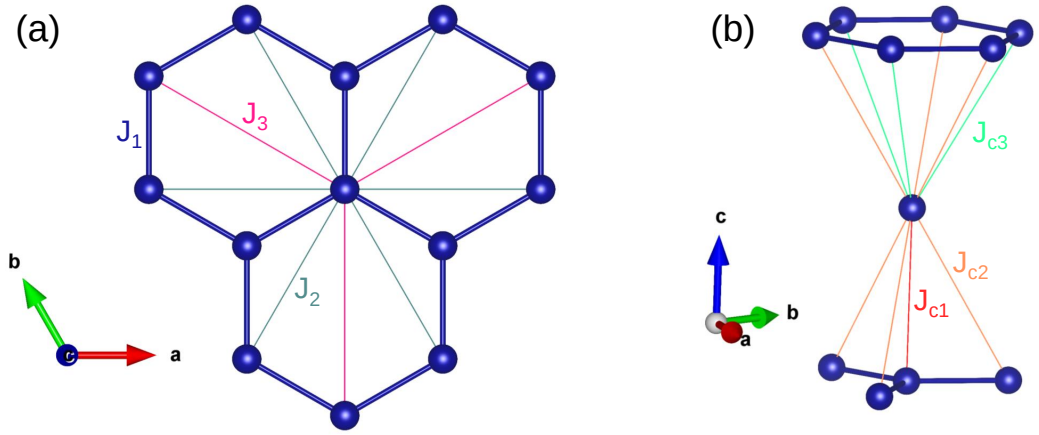

Figure 6.2.: Visualisation of the chromium-chromium coupling constants J_i in CrI_3 up to six nearest neighbours, (a) three of which, J_1–J_3, lie in the *ab*-plane, and; (b) three of which, J_{c1}–J_{c3}, lie perpendicular to the *ab*-plane. Crystallographic data taken from [141], visualisation performed in VESTA [56].

be isotropic and equal to the free-electron value [18]. However, small spin-orbit coupling typically restores a finite orbital moment by admixing higher-lying states of the Γ_5 orbital triplet into the ground state [18]. Based on Eq. 2.10, the g-factor is then expected to be lowered with respect to its free-electron value by $|8\lambda/\Delta_{CF}|$, where λ is the spin-orbit coupling constant and Δ_{CF} the crystal-field splitting [18].

With typical values of λ for paramagnetic Cr^{3+} of $\lambda \approx 10\,\text{meV}$ [18] and with $\Delta_{CF} \approx 0.5\,\text{eV}$–$1\,\text{eV}$ in CrI_3 [145, 146], the paramagnetic g-factor of Cr^{3+} in CrI_3 is expected to amount to $g \approx 1.84$–1.92. Moreover, due to the minimal distortion of the Cr^{3+} octahedra in the high-temperature $C2/m$ and low-temperature $R\bar{3}$ phases, the g-factor is expected to be isotropic.

Room-temperature X-band ESR on CrI_3 detected $g = 1.986$, albeit with no information on the sample orientation [147]. Furthermore, X-ray magnetic circular

dichroism (XMCD) studies at $T = 20\,\mathrm{K}$ found small but finite orbital moments $L_\mathrm{c} = -0.059$ and $L_\mathrm{ab} = -0.059$, resulting in vanishing orbital moment anisotropy $\Delta L = L_\mathrm{c} - L_\mathrm{ab} \lesssim 0.001$ [146]. The latter observation confirms the almost complete quenching of the orbital moment as well as the expectation based on the negligible distortion of the chromium octahedra in the low-temperature phase of CrI_3. The sizeable discrepancy in the g-factor values between, on the one hand, the predictions from crystal-field theory and, on the other hand, the observation from X-band ESR can be understood by taking into account covalent-bonding effects which simple crystal-field considerations with a perfect ionic bonding neglect. Covalent bonding tends to reduce the spin-orbit coupling constant λ, leading to a less pronounced reduction $8\lambda/\Delta_\mathrm{CF}$ of the free-electron g-factor [18]. Indeed, covalent bonding between the 3d orbitals of the chromium ions and the 5p orbitals of the iodine ions is argued to be significant in CrI_3 [146]. This point is briefly revisited in the next section.

6.1.4. Sources of Anisotropy in CrI_3

Fascinatingly, CrI_3 preserves its long-range order all the way to atomically thin samples [148]. In particular, monolayer CrI_3 was observed to order ferromagnetically at $T_\mathrm{C} = 45\,\mathrm{K}$ [148]. Moreover, a sizeable zero-field excitation gap of almost $0.4\,\mathrm{meV}$ ($\approx 90\,\mathrm{GHz}$) at the Brillouin zone centre in inelastic neutron scattering [143] and ferromagnetic resonance experiments [149, 150] on the one hand, and considerable magnetic anisotropy field of approximately $2.8\,\mathrm{T}$ in isothermal magnetisation measurements [141, 151] on the other hand, were observed in bulk samples. Since a purely two-dimensional system of Heisenberg spins and long-range interactions is prevented from developing long-range order [152], the detection of long-range ferromagnetic order in a monolayer – and indeed in a quasi-two-dimensional bulk – of CrI_3 raises the question about the mechanism through which the spin-rotation invariance is broken and anisotropy introduced in this van-der-Waals system.

It is generally accepted that neither shape nor dipolar anisotropy can account for the observed behaviour [145, 146]. In layered structures, such as van-der-Waals materials, shape anisotropy favours in-plane arrangement of the spins [145], and, as such, it contradicts the observed easy-axis anisotropy oriented along the crystallographic c-axis. Dipolar magnetic anisotropy in CrI_3 too favours in-plane spin orientation and is rather weak [146]. Following Eq. 2.12, its energy may be estimated as $E_\mathrm{dipole} \approx 0.016\,\mathrm{meV}$, corresponding to about $0.09\,\mathrm{T}$. This is more than 30 times smaller than the actually-observed anisotropy field $B_\mathrm{anis} \approx 2.8\,\mathrm{T}$ [141, 149, 151]. Furthermore, it is also generally accepted that neither can single-ion anisotropy of the chromium ions satisfactorily account for the large anisotropy field [143, 145]. This is due to the already-mentioned almost completely quenched orbital angular moment which couples the spin and crystalline lattice degrees of freedom.

On the other hand, both symmetric and antisymmetric exchange interactions were proposed as potential causes of the anisotropy behaviour in CrI_3. In particular, it was shown by means of density functional theory modelling that spin-orbit coupling on the iodine ions can give rise to a sufficiently large anisotropic symmetric superexchange [145]. Along a similar line of argument, a combination of theoretical modelling and experimental XMCD observations were used to highlight the crucial role of p–d covalence between the neighbouring iodine's p orbital and chromium's d orbital in determining the anisotropy in layered van-der-Waals ferromagnets with Cr^{3+} ions [146]. Moreover, antisymmetric Dzyaloshinskii-Moriya (DM) interactions were invoked as a necessary addition to the usual Heisenberg Hamiltonian for establishing of the observed anisotropy [153], in spite of early theoretical arguments to the contrary [145]. Still further, a Kitaev Hamiltonian with an anisotropy-inducing off-diagonal term Γ was proposed as an appropriate model to describe the magnetic interactions in CrI_3 [150]. Lastly, it was shown that the hitherto-obtained neutron scattering data do not allow for a univocal discrimination between the applicability of the Heisenberg-Dzyaloshinskii-Moriya model and of the Kitaev model to CrI_3 [143]. In summary, whereas several candidates have been ruled out as being responsible for the magnetocrystalline anisotropy in CrI_3, no unified agreement appears to exist about the dominant anisotropy-inducing mechanism.

6.1.5. Long-Range Magnetic Order in Thin Layers of CrI_3

Another fascinating feature pertaining to the magnetism in CrI_3 is the complex evolution of a long-range magnetic order in atomically-thin samples. As already alluded to, in its exfoliated monolayer rendition, CrI_3 is a long-range-ordered ferromagnet [148]. Samples with thickness up to at least ten atomic layers were observed to preserve the same in-plane ferromagnetic arrangement of the spins as the monolayer while exhibiting out-of-plane antiferromagnetic arrangements of the spins [13, 148, 154, 155]. Consequently, CrI_3 with thickness of 2–10 layers is a long-range-ordered layered, A-type antiferromagnet. Lastly, this antiferromagnetic order was found to evolve at $T^* = 45\,\mathrm{K}$ also in thin surface regions, approximately 13 nm in thickness, of otherwise ferromagnetically-long-range-ordered bulk CrI_3 [156, 157].

It was shown by means of first-principles calculations that the stacking order of the hexagonal layers in CrI_3 determines the interlayer magnetic coupling, with rhombohedral, ideal ABC-like stacking favouring ferromagnetic coupling and monoclinic, imperfect ABC-like stacking favouring antiferromagnetic coupling between the adjacent layers [158]. It was subsequently shown by means of Raman scattering that thin multilayers and surface layers of bulk CrI_3 do not undergo a structural phase transition upon cooling, but that they instead remain in the high-temperature monoclinic phase while cooling through the bulk ferromagnetic transition at 61 K and all the way down

to at least 5 K [159]. Therefore, it may be concluded that it is due to the alleviation of the structural phase transition in thin multilayers and in the surface layers of bulk CrI_3 that these structures exhibit long-range antiferromagnetism [157, 159].

Lastly, a number of imaging techniques unveiled the presence of magnetic domains in CrI_3. They were first observed by electron microscopy which allowed to set a minimal value for the domain width as 70 nm [160]. Subsequently, the presence of domains was inferred from magneto-optical Kerr effect measurements on thin multilayers and the domain width was estimated to lie in the micrometre regime [148]. Single-spin magnetometry based on diamond nitrogen-vacancy centres was used to view domains in CrI_3 and even to confirm the interlayer antiferromagnetic coupling in atomically-thin samples of the material [161]. Moreover, a recent ferromagnetic resonance (FMR) study invoked the presence of domains in order to account for the observed field dependence of the detected resonances [162].

Note that all the available information on magnetic domains in CrI_3 stems from studies which mapped the magnetisation orientation, and hence the spatial extension of magnetic domains, solely in the lateral, *ab*-plane of the sample. As such, no information is available on the distribution of the magnetisation along the *c*-axis. In other words, the size of the domains along the *c*-axis of CrI_3 is not known. It may be speculated that for samples whose thickness amounts to the lateral size of the domains, i.e. with thickness on the order of few micrometers [148], a single magnetic domain extends across all the layers. For bulk samples, such as measured in the present study, the situation is more complicated and no simple prediction about the spatial extension of the domains along the *c*-axis is possible.

However, the measurements performed in the frame of this work are – similarly to all the reported literature – sensitive solely to the effects which the presence of domains cause in the *ab*-plane of the sample and they remain unaffected by the possibly-varying spatial extension of the domains along the *c*-axis. Correspondingly, the ensuing discussion concerns itself solely with the presence, shape, and dynamics of *lateral* domains, that is of domains as they appear in a single *ab*-layer.

6.2. Sample and Experimental Details

The measurements on CrI_3 presented in this chapter were performed on several thin single-crystal samples obtained from HQ Graphene [163]. All the samples originated from the same batch. High-frequency electron spin resonance (HF-ESR) measurements were performed on an approximately rectangularly-shaped thin sample of dimensions 2.2(1) mm x 1.4(1) mm x 0.095(15) mm. Under the approximation of a perfectly rectangular sample, the corresponding demagnetisation factors can be calculated as $N_x = 0.049(8)$, $N_y = 0.079(14)$, and $N_z = 0.871(21)$. DC and AC susceptibility mea-

surements were performed on further similarly-shaped samples. The crystallographic a-, b-, and c-axes are taken to lie along the spatial x-, y-, and z-coordinates, respectively.

Due to the known air- and light sensitivity of CrI_3 [163, 164], the samples were stored in a dark vacuum-sealing container in an argon-filled glove box. The various measurements were also prepared in the glove box and exposure to air and light minimised during transport from the glove box to the respective measurement device. Owing to the very small sample thickness, different sample holders had to be utilised in the magnetisation measurements for the application of the magnetic field within the ab-plane and along the c-axis, respectively. The former allowed for the utilisation of a quartz sample holder with a low magnetic background, whereas the latter necessitated the usage of a standard brass sample holder. In each case, the sample was attached with Kapton tape.

For HF-ESR measurements, the sample was fixed by Kapton tape to the inside walls ($B||ab$-plane) or the bottom ($B||c$-axis) of a PEEK sample holder (c.f. Fig. 3.2c). The lid's sealing capabilities were enhanced by wrapping several layers of teflon tape around the lid's windings.

6.3. Experimental Results

6.3.1. DC Magnetisation

6.3.1.1. Static Magnetic Susceptibility

Axis-dependent static magnetic susceptibility, $\chi = M/B$, and low-temperature isothermal magnetisation measurements were performed in order to characterise the commercially-obtained samples of CrI_3. The former measurement was performed in an applied field of 0.1 T in a zero-field-cooled mode, and the obtained static susceptibility curves are presented in Fig. 6.3a. As may be seen therein, χ_{ab} and χ_c are similar, though not identical, in the high-temperature region. The discrepancy between the curves has two likely origins: firstly, the two different sample holders utilised for the two respective orientations of the magnetic field possess a different (diamagnetic) background; secondly, the mechanical manipulation of the sample during weighing and installation may lead to exfolation of a small number of the weakly, van-der-Waals-bonded surface layers, resulting in the utilisation of incorrect sample mass in the analysis (c.f. Section 6.2).

As the temperature is decreased to around 75 K, both curves shoot up, signalling the onset of the long-range ferromagnetic order. The c-axis exhibits approximately five times larger static susceptibility than the ab-plane in the ordered phase, confirming that the c-axis is the easy magnetisation axis. Interestingly, once the long-range ferro-

magnetic order is established, χ_{ab} shows a sizeable downturn, untypical for a ferromagnet. The downturn may be attributed to domain effects, detectable as a consequence of measuring the static magnetic susceptibility in a zero-field-cooled regime, and to the antiferromagnetic ordering of the surface layers, the existence of which in bulk samples was inferred from Raman scattering [165]. The phase transition temperatures may be determined by considering the minimum in the derivative of the c-axis static susceptibility: the ferromagnetic phase transition occurs[3] at $T_C = 61.0(5)\,\mathrm{K}$ and the weaker structural phase transition from the high-temperature monoclinic $C2/m$ to the low-temperature rhombohedral $R\bar{3}$ phase at $T_S = 212.5(20)\,\mathrm{K}$ (c.f. upper and lower inset in Fig. 6.3a). Both values show good correspondence with previously-reported magnetisation [141, 168] and specific heat studies [169, 170]. For the rest of the analysis and discussion of CrI_3 presented in this chapter, the ferromagnetic ordering temperature shall be fixed to the hereby-obtained value. It shall be seen in Section 6.3.3 that the analysis of AC susceptibility measurements, which enable the calculation of the true ferromagnetic phase transition temperature (i.e. $T_C(B \to 0\,\mathrm{T})$), yields $T_C = 61.06\,\mathrm{K} \pm 0.04\,\mathrm{K(stat)} \pm 0.5\,\mathrm{K(sys)}$.

In order to analyse the static magnetic susceptibility further, Curie-Weiss analysis was performed on χ_c in temperature regions $150\,\mathrm{K} \leq T \leq 200\,\mathrm{K}$ and $250\,\mathrm{K} \leq T \leq 300\,\mathrm{K}$, that is, below and above T_S. The fitting was carried out simultaneously in both temperature regions under the constraint of minimising the absolute difference in the optimised values of χ_0 and μ_{eff} stemming from the two fitting regions. That is, simultaneous minimisation of $|\chi_0(T < T_S) - \chi_0(T > T_S)|$ and of $|\mu_{eff}(T < T_S) - \mu_{eff}(T > T_S)|$ was sought. The former constraint reflects the expected unique constant background for the entire temperature region. The latter constraint derives from the expectation that the structural phase transition does not significantly affect the crystalline environment of an individual magnetic ion. This is, inter alia, suggested by the minimal change in the Cr^{3+}–I^- separation between the crystal phases (c.f. Section 6.1.3). On the other hand, the Weiss temperature θ was left as a free parameter throughout the fitting, as the structural changes at T_S are known to influence the magnetic coupling between in-plane and out-of-plane neighbours. Concretely, the antiferromagnetically-ordered surface layers exhibit the high-temperature $C2/m$ phase, whereas the ferromagnetically-ordered bulk exhibits the low-temperature $R\bar{3}$ phase [159] (see also 6.1.5).

The fitting procedure yielded $\mu_{eff} = 3.4(3)$ and $\theta = 81(15)\,\mathrm{K}$ for the low-temperature fitting region, and $\mu_{eff} = 3.4(5)$ and $\theta = 60(30)\,\mathrm{K}$ for the high-temperature fitting region, with a diamagnetic constant background term $\chi_0 = -0.022(2)\,\mathrm{erg G^{-2} mol^{-1}}$.[4]

[3] Strictly speaking, a ferromagnetic phase transition with a corresponding transition temperature T_C is defined in case of a ferromagnet only for vanishing external static magnetic field, $B = 0\,\mathrm{T}$. Hence, the presently-obtained value is only an approximation, though – as brief literature survey reveals – not an unusual one [141, 166, 167].

[4] Such a large value of the diamagnetic constant term likely originates from the dominant diamagnetic

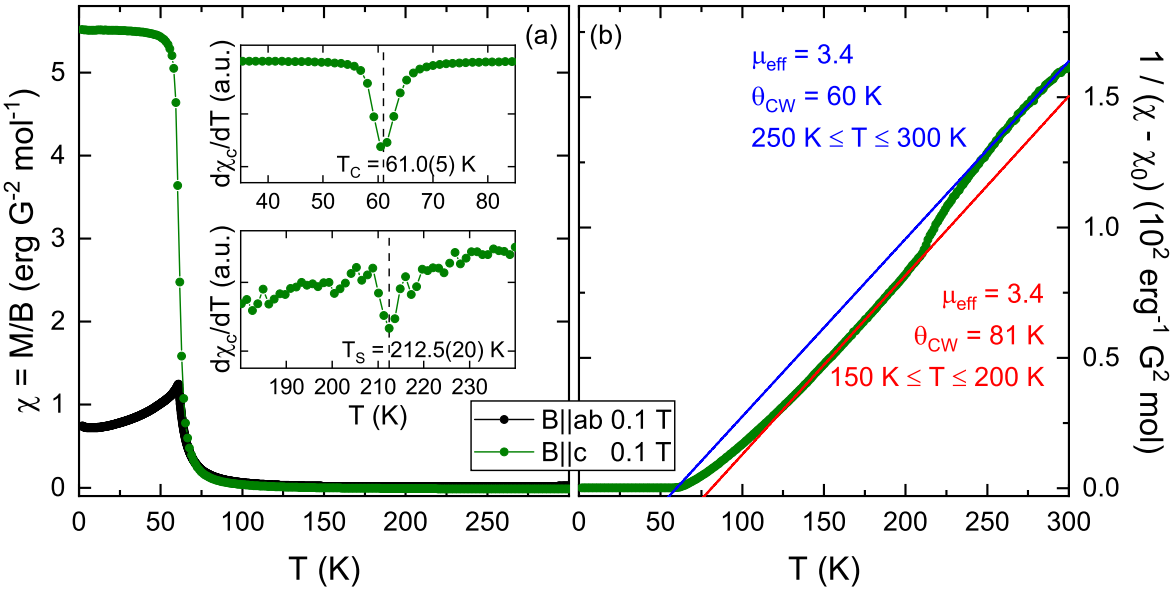

Figure 6.3.: (a) Static magnetic susceptibility of CrI_3 as a function of temperature obtained at 0.1 T in a zero-field-cooled mode for $B||ab$-plane (black circles) and $B||c$-axis (green circles). The insets shows the derivative of the c-axis susceptibility, with the dashed lines marking the various phase transitions (see text for details and note that the upper inset has a three-orders-of-magnitude larger ordinate scale than the lower inset). (b) Inverse of the static magnetic susceptibility for $B||c$-axis where the susceptibility has been accounted for a diamagnetic background. Red (blue) straight line depicts a Curie-Weiss fit in the temperature region $150\,\mathrm{K} \leq T \leq 200\,\mathrm{K}$ ($250\,\mathrm{K} \leq T \leq 300\,\mathrm{K}$). Optimised fitting parameters are displayed in the graph.

Fig. 6.3b depicts the Curie-Weiss curves based on these optimised parameters. It may be seen that for $T \lesssim 130\,\mathrm{K}$, the static susceptibility data start to deviate from the lower of the two Curie-Weiss fits (red solid line in Fig. 6.3b).

Utilising the room-temperature g-factor obtained from X-band electron paramagnetic resonance $g = 1.986$ [147], the total magnetic moment may be calculated from the effective moments as $J = 1.3(2)$ for the low-temperature, and $J = 1.3(3)$ for the high-temperature region. The uncertainty in the above-obtained fitting parameters was estimated by relaxing the two fitting constraints. The large uncertainty associated with the high-temperature fitting region may be owing to the dominating effect of the diamagnetic background over the sample signal, resulting in small signal-to-noise ratio.

The expected value based on the above-discussed XMCD measurements $J = L + S = 1.559$ [146] lies higher than, but just outside the respective error bars of the presently-obtained values of the total magnetic moment. The Weiss temperature's proximity to the actual ferromagnetic ordering temperature implies that fluctuations are not significant in the evolution of long-range order in CrI_3. Note that relaxing the constraints in the low-temperature fitting region results in $\mu_{\mathrm{eff}} = 3.76(45)$ (corresponding

background due to the sample holder and the Kapton tape used in attaching the sample.

to $J = 1.46(30)$) and $\theta = 72(12)\,\mathrm{K}$, which corroborates previous literature results on the material very well [141]. Overall, it may be concluded that the commercially-obtained samples utilised in the present study show comparable magnetic behaviour to the state-of-the-art samples reported in literature.

6.3.1.2. Isothermal Magnetisation at 2 K

Isothermal magnetisation performed at $T = 2\,\mathrm{K}$ and displayed in Fig. 6.4 shows – similarly to the low-temperature static magnetic susceptibility – strongly anisotropic behaviour. The considerably more abrupt magnetisation increase when $B||c$-axis compared to $B||ab$-plane confirms the c-axis as the easy magnetisation axis. The more gradual magnetisation growth observed along the ab-plane is associated with the re-orientation of the magnetisation away from the easy-axis and into the ab-plane. The effective anisotropy field may be estimated as the difference between the respective axis-dependent saturation field values, $B_\mathrm{A} = B_\mathrm{ab}^\mathrm{sat} - B_\mathrm{c}^\mathrm{sat}$. The saturation fields can be read off graphically from Fig. 6.4 as: $B_\mathrm{ab}^\mathrm{sat} = 2.86(5)\,\mathrm{T}$ and $B_\mathrm{c}^\mathrm{sat} = 0.20(9)\,\mathrm{T}$, resulting in $B_\mathrm{A} = 2.66(10)\,\mathrm{T}$. Similarly, the saturation magnetisation may be read off from the same figure $M_\mathrm{ab}^\mathrm{sat} = 2.85(16)\,\mu_\mathrm{B}$/f.u. and $M_\mathrm{c}^\mathrm{sat} = 3.04(10)\,\mu_\mathrm{B}$/f.u., thereby confirming within the respective error-bar limits the expectation for a quasi-spin-only $3d^3$ magnetic ion and the previous literature observations [141, 148, 151, 171]. Note that owing to the small sample mass ($m = 0.91(3)\,\mathrm{mg}$), a small uncertainty in the mass determination ($\Delta m \approx 0.03\,\mathrm{mg}$) results in a sizeable uncertainty in the measured magnetisation, including the saturation value. Consequently, it is not possible to argue with definiteness on the basis of Fig. 6.4 whether or not the observed difference in the saturation magnetisation between the two crystallographic orientations is significant. A measurement of the magnetisation as a function of the sample's rotation in the magnetic field would be able to settle the current ambiguity. As $M^\mathrm{sat} = \mu_\mathrm{B} g_\mathrm{J} J$, axis-dependent saturation values would indicate anisotropy either in the g-factors or in the total magnetic moment. Although g-factor anisotropy is not expected owing to the negligible distortion of the chromium octahedra [141], it shall be seen in Section 6.3.2 that the low-temperature ferromagnetic magnon branches are more satisfactorily described by anisotropic g-factors, with $g_\mathrm{ab} > g_\mathrm{c}$.

Considering the isothermal magnetisation in Fig. 6.4 in more detail, a series of small jumps in the up-sweep direction for $B||c$-axis starting at $B = 0.2\,\mathrm{T}$ and culminating at $B = 2.1\,\mathrm{T}$ may be observed, accompanied by pronounced hysteresis in this field regime. On the other hand, no jumps and no hysteresis are observed in the isothermal magnetisation for $B||ab$-plane. As already discussed in Section 6.1, it is known from magnetic force microscopy that surface layers of bulk CrI_3 develop long-range A-type antiferromagnetic order with a spin flip at $B = 2.1\,\mathrm{T}$ [157]. Although the present magnetisation data reveal a set of jumps, their interpretation as flipping of the anti-

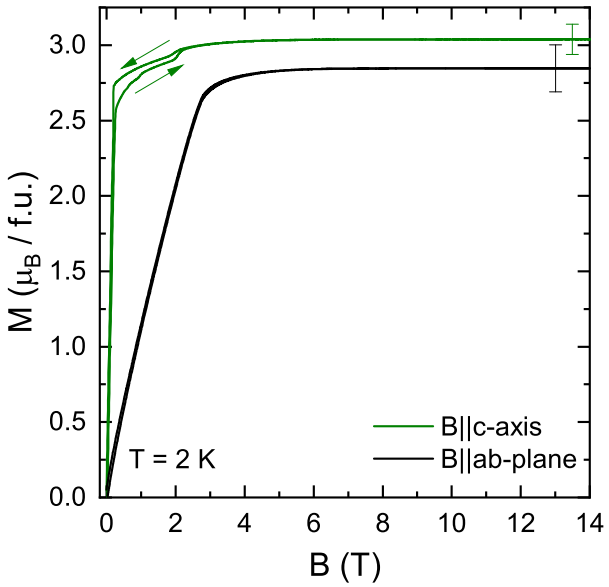

Figure 6.4.: Isothermal magnetisation of CrI_3 for $B||c$-axis (green) and $B||ab$-plane (black) at $T = 2\,\mathrm{K}$. Both curves depict a full measurement cycle $0\,\mathrm{T} \rightarrow 14\,\mathrm{T} \rightarrow 0\,\mathrm{T}$.

ferromagnetic surface layers appears plausible. A possible explanation for the cascade of jumps may be a more complex surface structure in the presently-studied sample compared to the originally-reported measurements. The complexity may be a result of a partial deterioration of the sample's surface, perhaps due to the surface's reaction with atmospheric oxygen and nitrogen during the sample installation. Importantly for the present study, the antiferromagnetically-ordered surface seems to have protected the bulk from contamination, since the main features of the static magnetic susceptibility in Fig. 6.3 and of the isothermal magnetisation in Fig. 6.4 appear unaffected, as the good correspondence with the literature data bears witness to. Furthermore, the focal point of the present chapter are high-frequency electron spin resonance studies, for which the sample was protected from exposure to air at all times.

6.3.2. High-Frequency Electron Spin Resonance

6.3.2.1. Ground-State Ferromagnetic Resonance

A selection of spectra obtained in the ferromagnetically-ordered phase of CrI_3 with the external field applied along the c-axis (at $T = 2\,\mathrm{K}$ or $T = 4\,\mathrm{K}$) and within the ab-plane (at $T = 2\,\mathrm{K}$) are displayed in Fig. 6.5. Several spectra in both crystallographic directions show a small amount of wave-phase mixing, resulting in asymmetric Lorentzian absorption features. Moreover, ab-plane spectra obtained at $\nu \gtrsim 150\,\mathrm{GHz}$ show an increased level of background noise. However, careful comparison of the spectra obtained in the up- and down-sweep directions allows for an unambiguous assignment of all the resonance features (marked by coloured symbols in Fig. 6.5). Whereas no reso-

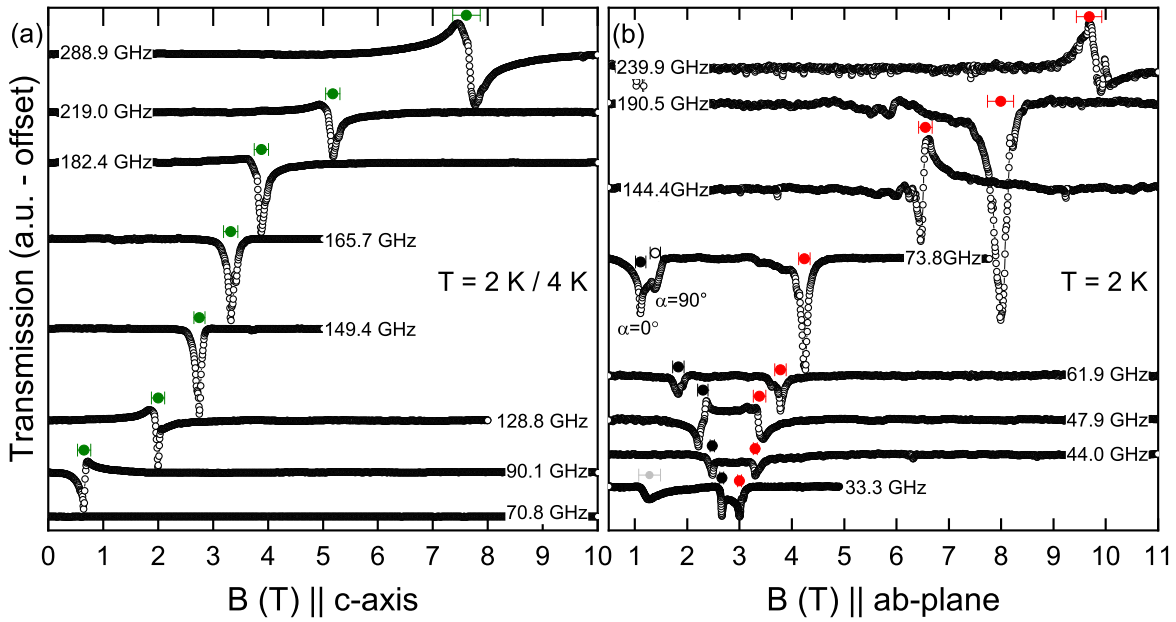

Figure 6.5.: Selected spectra of CrI_3 at various frequencies deep in the ferromagnetically-ordered phase for (a) $B||c$-axis, and; (b) $B||ab$-plane. Coloured symbols mark the positions of the resonance features.

nances have been detected below 80 GHz in the c-axis orientation of the applied field, a single c-axis resonance feature has been observed at all frequencies above 80 GHz. In the ab-plane, on the other hand, at least two distinct features have been found for $\nu < 80\,\mathrm{GHz}$. Moreover, for $60\,\mathrm{GHz} < \nu < 90\,\mathrm{GHz}$ the ab-plane resonance feature lying lower in field splits into two distinct features, with possible spectral weight also in between, as demonstrated by the closed and open circles in the spectrograph at $\nu = 73.8\,\mathrm{GHz}$ in Fig. 6.5b. In a ferromagnetic resonance model with lateral domains, the two thus-arisen features may be assigned to two extremal orientations of the domain walls with respect to the applied magnetic field: the more intense, left-hand-side feature corresponds to the parallel alignment of the domain walls with the magnetic field, $\alpha = 0°$; the weaker, right-hand-side feature to the perpendicular alignment, $\alpha = 90°$ (see also the subsequent discussion on the form of the lateral-domain structure)

Beyond the dominant features, a small number of spectra stemming from both orientations exhibit resonances which broadly follow a gapless, paramagnetic behaviour with g-factor of $g = 2.00$ (for illustration see the ab-plane low-field feature at $\nu = 33.3\,\mathrm{GHz}$ in Fig. 6.5b marked by a grey circle). While a domain-wall mode in a related compound $CrSiTe_3$ was found to exhibit vanishing zero-field excitation gap, akin to the present observation, the mode showed right bending at finite frequency [167], contrary to the present frequency dependence. Although no univocal determination of the observed features' origin is possible in the present case, since the features appear only in a small number of spectra, they shall not be discussed further in the ensuing.

All the low-temperature resonances are summarised in the resonance-frequency–magnetic-field diagram presented in Fig. 6.6. As may be seen, good correspondence exists between the present data and previously published FMR data along the *c*-axis at 1.5 K (purple squares in Fig. 6.6) [149], as well as between the present data and angle-dependent FMR measurements at 5 K (blue squares) [150]. Previous *ab*-plane FMR measurements in a narrow frequency window from 20 GHz to 40 GHz at 10 K also show reasonable correspondence (orange squares) [162]. A small shift of the saturation field in the ten-Kelvin data with respect to the here-presented two-Kelvin data towards lower fields is observed, confirming that with increasing temperature the anisotropy field weakens, leading to a lower saturation field.

To model the observed ferromagnetic resonance behaviour in CrI_3, the magnetocrystalline anisotropy is taken to lie along the *c*-axis and the presence of lateral domains is recalled. Under the given constraints and for Faraday configuration, appropriate for the experimental setup in this study, the ferromagnetic resonance behaviour is quantified by the following domain-based model [167, 172]:

$$\left(\frac{\nu_1}{\gamma_{\mathrm{ab}}}\right)^2 = (B_{\mathrm{A}} + N_x M_{\mathrm{S}})(B_{\mathrm{A}} + M_{\mathrm{S}}\sin^2\alpha) - \frac{(B_{\mathrm{A}} + M_{\mathrm{S}}\sin^2\alpha - N_z M_{\mathrm{S}})(B_{\mathrm{A}} + N_x M_{\mathrm{S}})}{(B_{\mathrm{A}} + N_y M_{\mathrm{S}})^2} B^2 \tag{6.1}$$

for the external magnetic field $B \leq B_{\mathrm{A}} + N_y M_{\mathrm{S}}$ applied along the *b*-axis (i.e within the *ab*-plane);

$$\left(\frac{\nu_2}{\gamma_{\mathrm{ab}}}\right)^2 = \{B - [B_{\mathrm{A}} - (N_z - N_y)M_{\mathrm{S}}]\}\{B - (N_y - N_x)M_{\mathrm{S}}\} \tag{6.2}$$

for $B \geq B_{\mathrm{A}} + N_y M_{\mathrm{S}}$ applied along the *b*-axis, and;

$$\frac{\nu_3}{\gamma_{\mathrm{c}}} = B + B_{\mathrm{A}} - N_z M_{\mathrm{S}} \tag{6.3}$$

for B applied along the easy *c*-axis. In the above, $\gamma_{\mathrm{ab,c}} = g_{\mathrm{ab,c}} \cdot 13.996\,[\mathrm{GHz/T}]$ is the axis-dependent gyromagnetic ratio with the corresponding *g*-factor; B_{A} is the effective anisotropy field; M_{S} is the saturation magnetisation; and N_x, N_y, and N_z is the demagnetisation factor along the crystallographic *a*-, *b*-, and *c*-axis, respectively.[5] α corresponds to the angle which the applied magnetic field B encloses with a particular domain wall.[6]

To perform the fitting of the resonance features, a least-squares minimisation routine

[5] For external field applied within the *ab*-plane along the *a*-axis, the demagnetisation factors N_x and N_y in Eqs. 6.1 and 6.2 are exchanged.

[6] Due to the lateral structure of the domains, the angle α lies solely in the *ab*-plane.

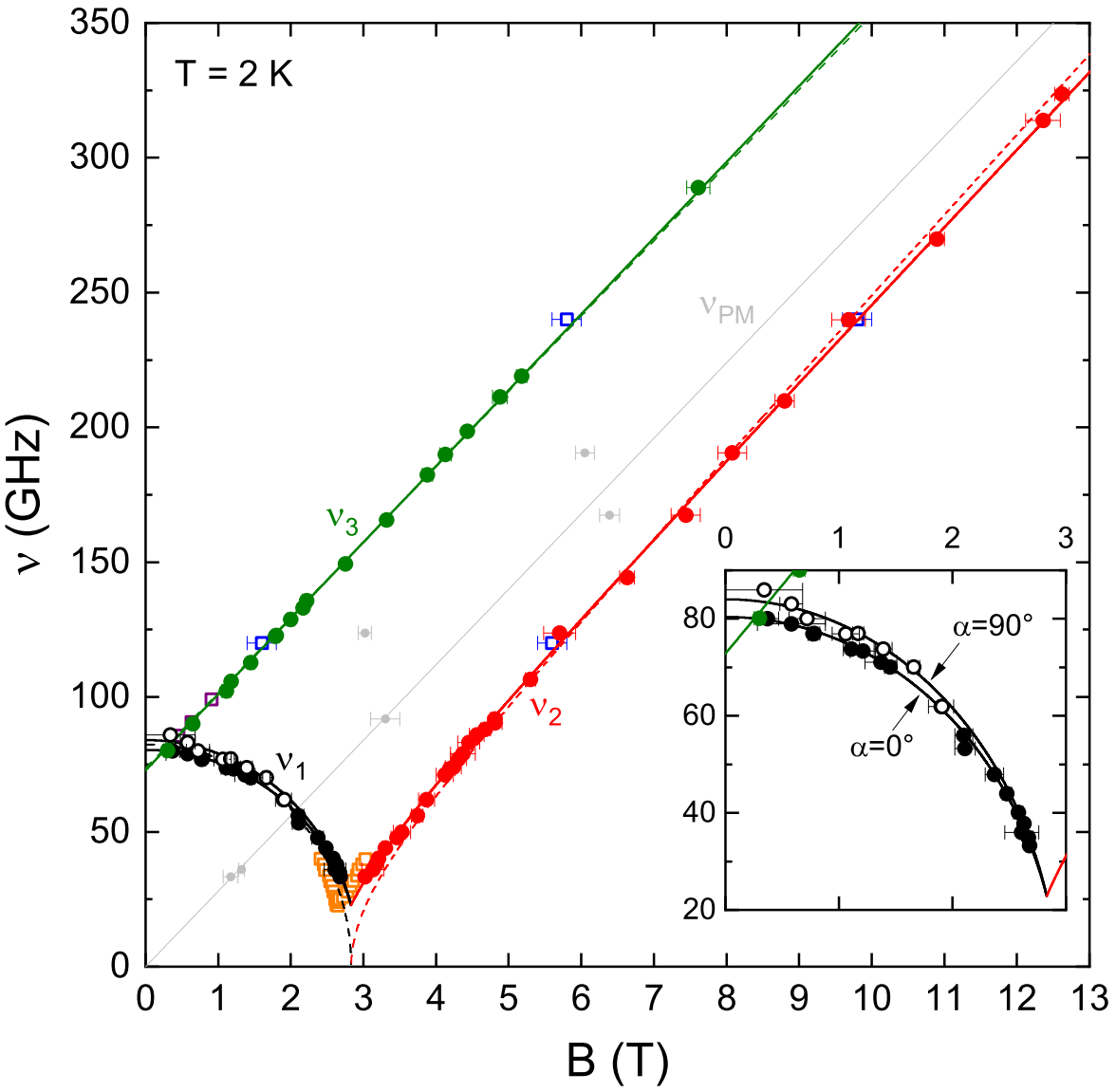

Figure 6.6.: Resonance-frequency–magnetic-field diagram of CrI_3 at 2 K. Black and red circles were obtained with the external magnetic field applied within the *ab*-plane, green circles along the *c*-axis. Closed circles for $B||ab$ correspond to $\alpha = 0°$; open circles to $\alpha = 90°$ (see text for details). Orange open squares are data points at 10 K digitised from [162], blue open squares at 5 K from [150], and purple open squares at 1.5 K from [149]. Solid lines display the fitting results based on the domain-based FMR model (Eqs. 6.1, 6.2, and 6.3), dashed lines on the domain-free FMR model (see text for details). Light-grey solid line depicts a paramagnetic line with $g = 2.00$. The inset zooms in on the low-frequency, low-field region of the main plot.

was implemented simultaneously on all resonance features in Fig. 6.6 such that the various branches were fitted by the respective equation. In particular, Eq. 6.1 was applied to the two *ab*-plane low-field branches (closed and open black data in Fig. 6.6) with two fixed values of the angle between the external field and the domain wall: $\alpha = 0°$ and $\alpha = 90°$, respectively. The optimised parameters resulting from such domain-based model are: $g_c = 2.01(1)$; $g_{ab} = 2.04(4)$; $B_A = 2.81(10)\,\mathrm{T}$, and; $M_S = 0.26(10)\,\mathrm{T}$; and the optimised curves are displayed in Fig. 6.6 as solid lines. The obtained anisotropy field compares well with its determination from magnetisation measurements [141, 151]. With the unit cell volume $134.8\,\text{Å}^3$ [141], the saturation magnetisation obtained from the fitting amounts to $M_S = 3.0(10)\,\mu_B$/f.u., lying in an excellent agreement with the theoretical expectations and previous magnetisation measurements [141, 151]. Using $B_S = B_A + N_y M_S$, the saturation field is calculated to be $B_S = 2.83(1)\,\mathrm{T}$.

Upon inspection of Eqs. 6.1–6.3, it may be noted that only the low-field planar excitations, quantified by Eq. 6.1, have explicit domain dependence via the angle α. In fact, a uniaxial domain-free FMR model differs from its domain-based counterpart only in the low-field planar regime [20, 167]. To describe the low-field *ab*-plane spin-wave excitations by means of a domain-free model, Eq. 6.1 is substituted with [20, 167]:

$$\left(\frac{\nu_1}{\gamma_{ab}}\right)^2 = \left\{[B_A + (N_y - N_z)M_S]^2 - B^2\right\} \cdot \frac{B_A + (N_x - N_z)M_S}{B_A + (N_y - N_z)M_S} \tag{6.1b}$$

For comparative purposes, Fig. 6.6 includes also the fitting results from a tentative attempt to describe the resonance features in CrI_3 by means of the domain-free FMR model (dashed lines, Eqs. 6.1b, 6.2, and 6.3). As is apparent, a better fitting quality, with a seven-times smaller residual-squares sum, is obtained in the framework of the domain-based model than within the domain-free picture. The difference between the two models is especially evident when considering the branch ν_1: firstly, whereas the domain-based model predicts the splitting of ν_1, the domain-free model makes no such prediction; secondly, whereas the domain-free model predicts the softening of ν_1 all the way to $\nu_{min} = 0\,\mathrm{GHz}$, the domain-based model predicts the softening to terminate at finite frequency $\nu_{min} = \gamma_{ab}\sqrt{N_z M_S (B_A + N_x M_S)}$. The observed splitting of ν_1 and its termination at $\nu_{min} \approx 23\,\mathrm{GHz}$ strongly suggest that the correct model to describe the low-temperature magnetic resonance behaviour in CrI_3 is the domain-based model given in Eqs. 6.1–6.3. This corroborates the previous observation of domains in CrI_3 by means of microscopic methods [148, 160, 161].

Note that the form of the low-field double resonance feature for $B||ab$-plane (c.f. Fig. 6.5a) which is associated with the two extremal orientations of the domain magnetisation with respect to the magnetic field does not allow for a definitive discrimination between (i) a statistically-random arrangement of the lateral domains with

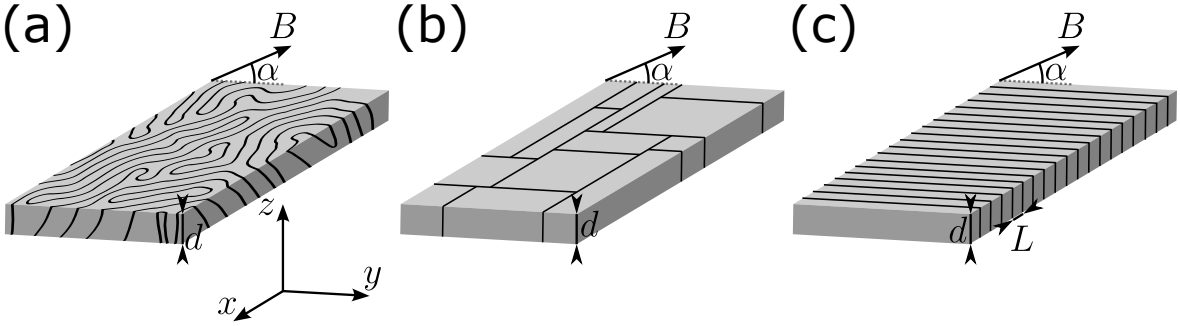

Figure 6.7.: A schematic visualisation of three types of envisaged ground-state lateral-domain structures in CrI_3: (a) domains are randomly-shaped and randomly-oriented with respect to each other; (b) domains consist of rectangular prisms but are randomly-oriented, and; (c) domains consist of equally-shaped rectangular prisms and arranged in periodic stripes with width L. d is the sample thickness, α the angle between a particular domain wall and the external magnetic field B, whereby α lies solely in the xy-plane, i.e. in the sample's ab-plane.

respect to each other and (ii) an orthogonal arrangement of the lateral domains with respect to each other. The two scenarios are illustrated in Fig. 6.7. Whereas the former case implies for the ground state a continuum of angles $0° \leq \alpha \leq 90°$ (Fig. 6.7a), the latter case permits only two orientations: $\alpha = 0°$; $\alpha = 90°$ (Fig. 6.7b). Although some spectrographs exhibit two clearly defined features with negligible spectral weight in between, other spectrographs may be pointing to a resonance continuum between the two extremal orientations. For reasons of simplicity and without introducing significant inaccuracy, the above fitting routine assumed the case of orthogonally-oriented domains (Fig. 6.7b).

A yet further extension to the envisaged microscopic picture of the lateral domains is possible. While the domains in Figs. 6.7a and 6.7b are randomly oriented with respect to each other, the domain arrangement may, in principle, occur in a periodic stripe fashion [173, 174]. This was previously observed on the related ferromagnetic semiconductor $CrBr_3$ [160] and on the metal Fe_3GeTe_2 [175].[7] Fig. 6.7c presents an example of such a periodic stripe fashion. Unlike the random arrangement of orthogonally-shaped domains (Fig. 6.7b), the effect of periodicity alters the resonance matrix and hence the field dependence of the resonance frequencies. However, for systems in which the sample thickness, d, is much greater than the domain width, L, such that the aspect ratio L/d vanishes, the stripe-domain model reduces to the presently-utilised simple-domain model. With the estimated domain width in CrI_3 on the order of $1\,\mu$m [160] and with the sample thickness in the range of 50–100 μm, the present FMR is not measurably affected by the additional complexity due to the stripe-domain behaviour. Moreover, micromagnetic simulations based on the stripe-domain model did not con-

[7] In these two cases, no information about the spatial extension of the lateral domains along the c-axis was available either.

firm the presence of stripe domains in CrI_3 [162]. Therefore, the simple domain-based model defined in Eqs. 6.1–6.3 appears to be justified as a description of the ferromagnetic resonance in CrI_3. High-resolution electron microscope studies are required to verify the potential presence of stripe domains, and resonance studies on samples with thickness comparable to the domain width are required to elucidate the effect of stripe domains on ferromagnetic resonance behaviour in CrI_3.

Beyond the resonance behaviour due to ferromagnetic spin waves in the bulk, two further magnetic-resonance phenomena are, in principle, expected to occur in CrI_3. Firstly, earlier polarised Raman scattering experiments detected Raman modes which could be interpreted as antiferromagnetic resonance associated with the antiferromagnetically-ordered surface layers [165]. Whereas the Raman study identified two linear gapped modes with $\Delta_1 \approx 100\,\mathrm{GHz}$ and a negative slope, and with $\Delta_2 \approx 120\,\mathrm{GHz}$ and a positive slope [165], these modes have not been found in the present study. This may be owing to the utilisation of unpolarised microwave radiation, or owing to the weak signal expected from the surface of an already-small sample.

Secondly, a collective resonance of the domain walls is also expected within the domain-based model [162, 167]. Although domain-wall modes were previously observed in a related ferromagnetic van-der-Waals semiconductor $CrSiTe_3$ using a coplanar waveguide sample rod [167], no definitive signature thereof has been detected in the present study. This may be owing to the low transmission power in the low-frequency regime, in which the domain wall mode is expected for CrI_3, of the presently-utilised setup. As already alluded to above, the resonance features which have been detected in a small number of spectra but cannot be accounted for by the model in Eqs. 6.1–6.3 do not warrant a conclusive argument about their origin as domain-wall resonance (c.f. grey data points in Figs. 6.5 and 6.6). A comparable FMR study on CrI_3 makes no mention of a domain wall mode [162].

Upon inspecting Eqs. 6.1 and 6.3 it becomes clear that the domain-based model of ferromagnetic resonance predicts the *observation* of unequal zero-field excitation gaps corresponding to the two main crystallographic orientations, and, moreover, the *observation* of two different values of the *ab*-plane gap corresponding to the two extremal orientations of the external magnetic field with respect to the domain wall, $\alpha = 0°$ and $\alpha = 90°$. Labelling the gaps determined from $B||c$ as $\tilde{\Delta}_\mathrm{c}$ and from $B||ab$ as $\tilde{\Delta}_\mathrm{ab}$, the various values, as determined by the above fitting procedure at 2 K, are: $\tilde{\Delta}_\mathrm{c}(T = 2\,\mathrm{K}) = 72.8(2)\,\mathrm{GHz}$; $\tilde{\Delta}_\mathrm{ab}(T = 2\,\mathrm{K}, \alpha = 0°) = 80.4(2)\,\mathrm{GHz}$, and; $\tilde{\Delta}_\mathrm{ab}(T = 2\,\mathrm{K}, \alpha = 90°) = 84.0(2)\,\mathrm{GHz}$. The variedness of the values comes from the presence of lateral domains and from finite demagnetisation effects acting within the ferromagnetic sample. The *true* zero-field splitting, quantifying the magnetic anisotropy of the system, remains thereby unique; in a domain-free scenario and in the limit of vanishing demagnetisation, the prediction of the excitation gap as deduced from Eqs. 6.1

and 6.3 reduces to the expected unique value $\Delta = \gamma B_A$. Accounting for these effects in the fitting results, $\Delta_c(T = 2\,\mathrm{K}) = 79.2(16)\,\mathrm{GHz}$ and $\Delta_{ab}(T = 2\,\mathrm{K}) = 80.2(10)\,\mathrm{GHz}$ are found, thus confirming within the error bar limits the expected presence of a unique anisotropy gap: $\Delta = 80(1)\,\mathrm{GHz}$. Previous ferromagnetic resonance measurements determined the zero-field splitting to be $\Delta = 82.9\,\mathrm{GHz}$ [149] and $\Delta = 72.5\,\mathrm{GHz}$ [150], but utilising thereby only a limited number of data points (former), or an indirect, rotation-dependent measurement (latter). More coarsely energy-resolved inelastic neutron scattering found $\Delta = 90\,\mathrm{GHz}$ [143].

6.3.2.2. Temperature Dependence of the Ferromagnetic Resonance

Temperature Dependence of the Linewidth

Spectra obtained at various temperatures along both principal crystallographic orientations at various fixed frequencies are displayed in Fig. 6.8. The spectra obtained with $B||c$-axis at $\nu = 102.1\,\mathrm{GHz}$ (Fig. 6.8a) exhibit a symmetric Lorentzian feature which broadens and shifts to higher resonance fields with increasing temperature. A very similar behaviour all the way up to 120 K is found along the c-axis also at $\nu = 135.7\,\mathrm{GHz}$ (data not shown). At $\nu = 135.7\,\mathrm{GHz}$ and $T = 140\,\mathrm{K}$, the Lorentzian feature becomes so broad that it can no longer be resolved. On the other hand, the resonance feature stemming from $B||ab$-plane at $\nu = 73.8\,\mathrm{GHz}$ (Fig. 6.8b) continuously shifts to lower resonance fields with increasing temperature. At low temperatures, the feature is asymmetric due to its being split into two distinct absorption peaks, as noted above. Only for $\gtrsim 28\,\mathrm{K}$ is a single symmetric Lorentzian peak observed.

Fitting the temperature-dependent spectra in Figs. 6.8a and 6.8b by means of a Lorentzian function, the temperature dependence of the linewidth, quantified as the function's full width at half maximum, may be studied. Designating the linewidth obtained from spectra with $B||c$-axis ($B||ab$-plane) as ΔB_c (ΔB_{ab}), it may be seen in Figs. 6.8c and 6.8d that both, ΔB_c and ΔB_{ab}, show two regions of distinct temperature dependence, demarcated by the ferromagnetic ordering temperature. Whereas ΔB_c continuously increases, ΔB_{ab} shows weak negative temperature dependence upon approaching T_C from below and strong positive dependence for $T > T_C$.

The weak temperature dependence of the linewidth in the ferromagnetically-ordered phase suggests that magnetisation relaxation in this temperature region is dominated by a spin-spin relaxation process [176]. At the lowest temperatures, $\Delta B \approx 100$–$150\,\mathrm{mT}$. Based on $\tau = \hbar/(g\mu_B(\Delta B))$ [91], this amounts to the relaxation time $\tau \approx 10^{-10}$–$10^{-11}\,\mathrm{s}$, typical for spin-spin relaxation processes in long-range-ordered ferromagnets [177, 178].

Much more pronounced, approximately linear temperature dependence is observed for $T > T_C$. The distinct increase of the linewidth for $T > T_C$ indicates gradual prevalence of a spin-phonon relaxation mechanism in this temperature regime [179]. In partic-

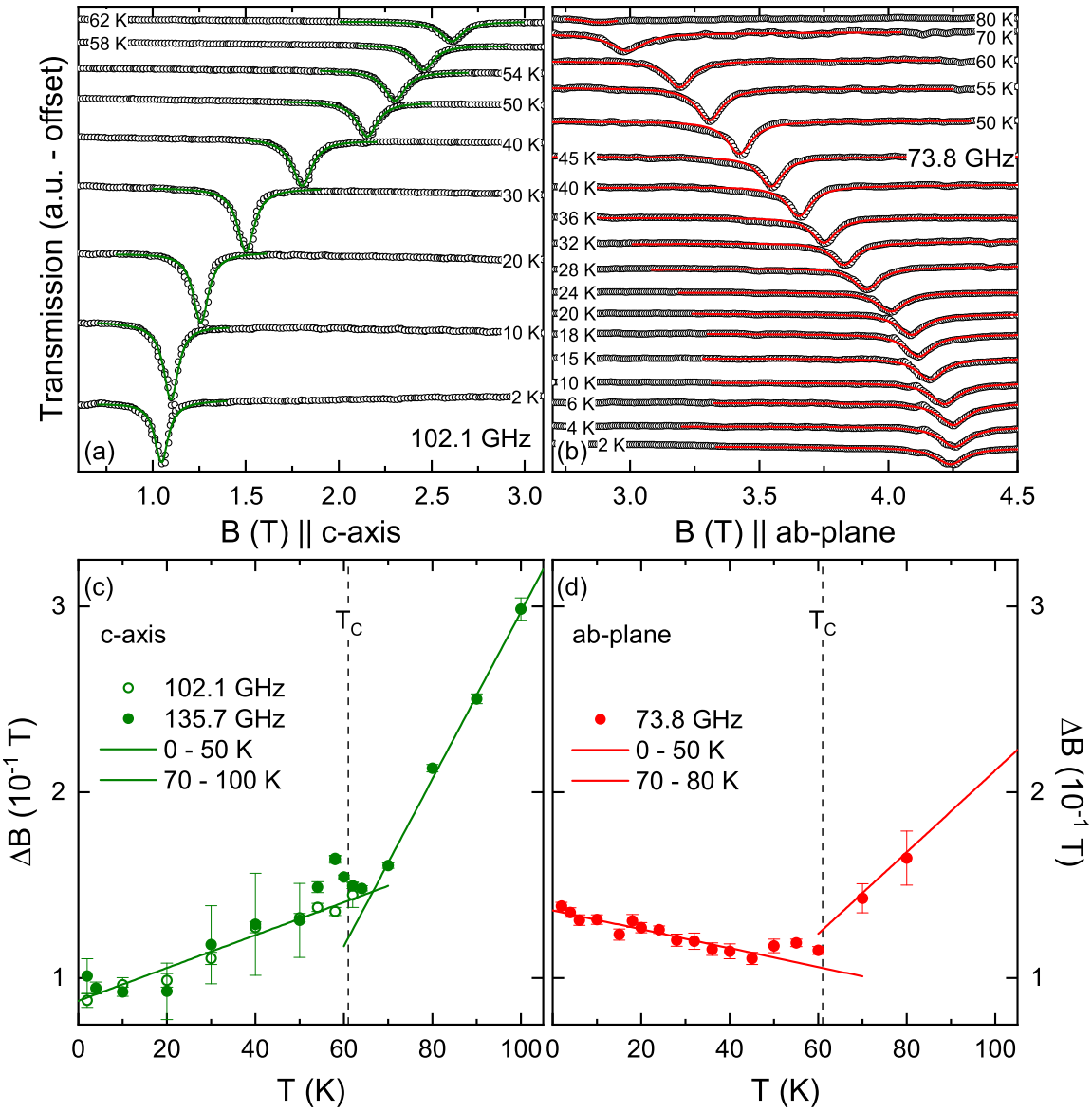

Figure 6.8.: Spectra at various temperatures obtained with (a) $B||c$-axis at $\nu = 102.1\,\mathrm{GHz}$, and; (b) $B||ab$-plane at $\nu = 73.8\,\mathrm{GHz}$. Green and red solid lines in (a) and (b) show fits to the spectra by means of a Lorentzian function. Temperature dependence of the corresponding linewidth, ΔB, obtained from spectra with (c) $B||c$-axis at $\nu = 102.1\,\mathrm{GHz}$ and at $\nu = 135.7\,\mathrm{GHz}$, and; (d) $B||ab$-plane at $\nu = 73.8\,\mathrm{GHz}$. Lines in (c) and (d) show linear fits to the data as a guide for the eye. Vertical dashed lines in (c) and (d) mark the ferromagnetic ordering temperature at $B = 0\,\mathrm{T}$.

ular, it was previously argued that an increase in ΔB for $T \gg T_C$ may be due to a temperature-dependent phonon modulation either of the antisymmetric exchange interaction or of the crystalline field [179]. Whereas a phonon modulation of the crystalline field was argued as the appropriate relaxation avenue in the related van-der-Waals feromagnetic semiconductor $CrBr_3$ [179], both of the above scenarios are possible in CrI_3. On the one hand, the antisymmetric, Dzyaloshinskii-Moriya exchange interactions were seen in several studies as essential for opening of the topological Dirac gap [144, 153, 180], but alternative accounts were also proposed [145, 150, 181]. On the other hand, the relatively low value of the crystal-field energy $\Delta_{CF} \approx 0.5$–$1.0\,\mathrm{eV}$ [145, 146] when compared to other cases of Cr^{3+} in an octahedral environment (c.f. Section 2.2.1), combined with the proposed sizeable p–d covalence between neighbouring iodine and chromium ions [146] may result in appreciable modulation of the crystalline field as the temperature is increased.

Moreover, as the data in Figs. 6.8c and 6.8d reveal, $\Delta B_c > \Delta B_{ab}$ at all temperatures above T_C, amounting to, e.g., $\Delta B_c \simeq 1.4 \Delta B_{ab}$ at 80 K. Since the effective intralayer coupling $J_{\mathrm{eff}}^{\mathrm{intra}}$ is predicted to be one [182] or even two [142, 183] orders of magnitude larger than the effective interlayer coupling $J_{\mathrm{eff}}^{\mathrm{inter}}$, and, moreover, since inelastic neutron scattering found $J_{\mathrm{eff}}^{\mathrm{intra}} \approx 77.7\,\mathrm{K}$ and $J_{\mathrm{eff}}^{\mathrm{inter}} \approx 6.8\,\mathrm{K}$ [144] (c.f. Section 6.1), a considerable amount of exchange narrowing may be expected to affect the resonance features for $B||ab$-plane, leading to a decrease in the intrinsic paramagnetic linewidth [91]. Although the observed difference between ΔB_c and ΔB_{ab} is not large, the expected line broadening arising from spin-phonon coupling must be taken into account. Due to the strong covalent bonding in the *ab*-plane as compared to the weak van-der-Waals bonding along the *c*-axis of bulk CrI_3, it may be expected that spin-phonon coupling is considerably larger in the *ab*-plane than along the *c*-axis. Consequently, resonance line broadening due to spin-phonon coupling via a preferred relaxation path in the *ab*-plane likely masks the true extent of exchange narrowing in the *ab*-plane.

Lastly, the linewidth of a ferromagnet at small resonance frequency $\nu_{\mathrm{res}} \ll \nu_E$, where ν_E is the effective exchange frequency, is expected to diverge as $\Delta B \propto \xi^{3/2}$ for $T \to T_C^+$, where ξ is the correlation length [184]. The exchange frequency may be estimated from $(2\pi\nu_E)^2 = (2/3)S(S+1)\sum_i n_i (J_i)^2$, where n_i is the coordination number of the i^{th} nearest neighbour coupled with the exchange constant J_i [184]. Using the fitting parameters from inelastic neutron scattering [144] and evaluating the above sum to the first three nearest neighbours, the effective exchange frequency amounts to $\nu_E \approx 257\,\mathrm{GHz}$. As this is at most only three-and-a-half-times larger than the resonance frequency at which the linewidth displayed in Figs. 6.8a and 6.8b was obtained, the above condition for observing linewidth broadening as $T \to T_C^+$ is not satisfied. This explains the merely linear temperature dependence of ΔB in the entire temperature region above T_C and the lack of critical broadening in the vicinity of T_C.

Temperature Dependence of the Zero-Field Excitation Gap

In order to map the temperature evolution of $\tilde{\Delta}_c$, and the c-axis g-factor, g_c, frequency–magnetic-field diagrams at various temperatures in the low-temperature, ferromagnetically-ordered phase and at elevated temperatures above T_C have been constructed (see Fig. 6.9). The field dependence of the resonance features has been fitted by means of Eq. 6.3, with $\tilde{\Delta}_c = \gamma_c(B_A - N_z M_S)$ and $g_c = \gamma_c/(13.996\,[\mathrm{GHz/T}])$ following from the fits (the fitted curves are shown in Fig. 6.9 as solid lines).

Moreover, the temperature evolution of $\tilde{\Delta}_{ab}$ has been estimated by following the gradual shift towards lower resonance fields and eventual disappearance of the low-field resonance features obtained for $B||ab$ as a function of increasing frequency and temperature (c.f. Fig. 6.10). To illustrate the procedure, consider the set of spectra at $T = 10\,\mathrm{K}$ in Fig. 6.10a: following the evolution of the double resonance feature (corresponding to $\alpha = 0°$ and $\alpha = 90°$), it is found that while the two features can still be observed at $\nu = 80.0\,\mathrm{GHz}$ (as marked by the closed and open circles in the corresponding spectrograph), the features are no longer visible at $\nu = 83.2\,\mathrm{GHz}$. This indicates that at $T = 10\,\mathrm{K}$, the zero-field splitting satisfies $80.0\,\mathrm{GHz} < \tilde{\Delta}_{ab} < 83.2\,\mathrm{GHz}$. $\tilde{\Delta}_{ab}$ is then estimated as the middle point between the two concerned spectrograms: $\tilde{\Delta}_{ab}(T = 10\,\mathrm{K}) = 81.6(32)\,\mathrm{GHz}$, with the uncertainty reflecting the frequency difference between the two spectrograms.[8]

The thus-obtained temperature dependence of $\tilde{\Delta}_c$ and $\tilde{\Delta}_{ab}$ is depicted in Fig. 6.11a. Note that since these gap values have not been accounted for domain and demagnetisation effects, the same finite difference between $\tilde{\Delta}_{ab}$ and $\tilde{\Delta}_c$ already discussed above in relation to the two-Kelvin data can also be observed at elevated temperatures before vanishing at about 50 K. Since saturation magnetisation in a ferromagnet shows a decreasing tendency for increasing temperature [6], leading to weaker demagnetising fields, and since with weaker demagnetising fields the number of domains is expected to decrease, the difference in the observed gap values, $\tilde{\Delta}_{ab} - \tilde{\Delta}_c$, is too expected to show a decreasing tendency, an effect observed also in Fig. 6.11a.

To obtain the actual zero-field excitation gap Δ from $\tilde{\Delta}_c$ and $\tilde{\Delta}_{ab}$, demagnetisation corrections are applied to these values, similarly to as has already been applied to the two-Kelvin data above. The resulting temperature dependence of Δ is presented in Fig. 6.11b, confirming again that within error bars, a unique zero-field excitation gap is observed. Interestingly, at 62 K (i.e., just above T_C) $\Delta = 19.8(7)\,\mathrm{GHz}$ (approximately 25% of its value at 2 K) and vanishes only above $T_\Delta \approx 80\,\mathrm{K}$, i.e. for $T \gtrsim 1.30 T_C$. The resonance-frequency–magnetic-field diagram obtained at 100 K indicates a paramagnetic, gapless excitation spectrum (c.f. bottom right graph in Fig. 6.9). The present

[8] For completeness, note that the resonance features marked by red circles in the spectra at 50 K (Fig. 6.10d) belong to ν_2 of the resonance-frequency–magnetic-field diagram and are not of interest in the present discussion, as the branch is not characterised by zero-field splitting (c.f. Fig. 6.6)

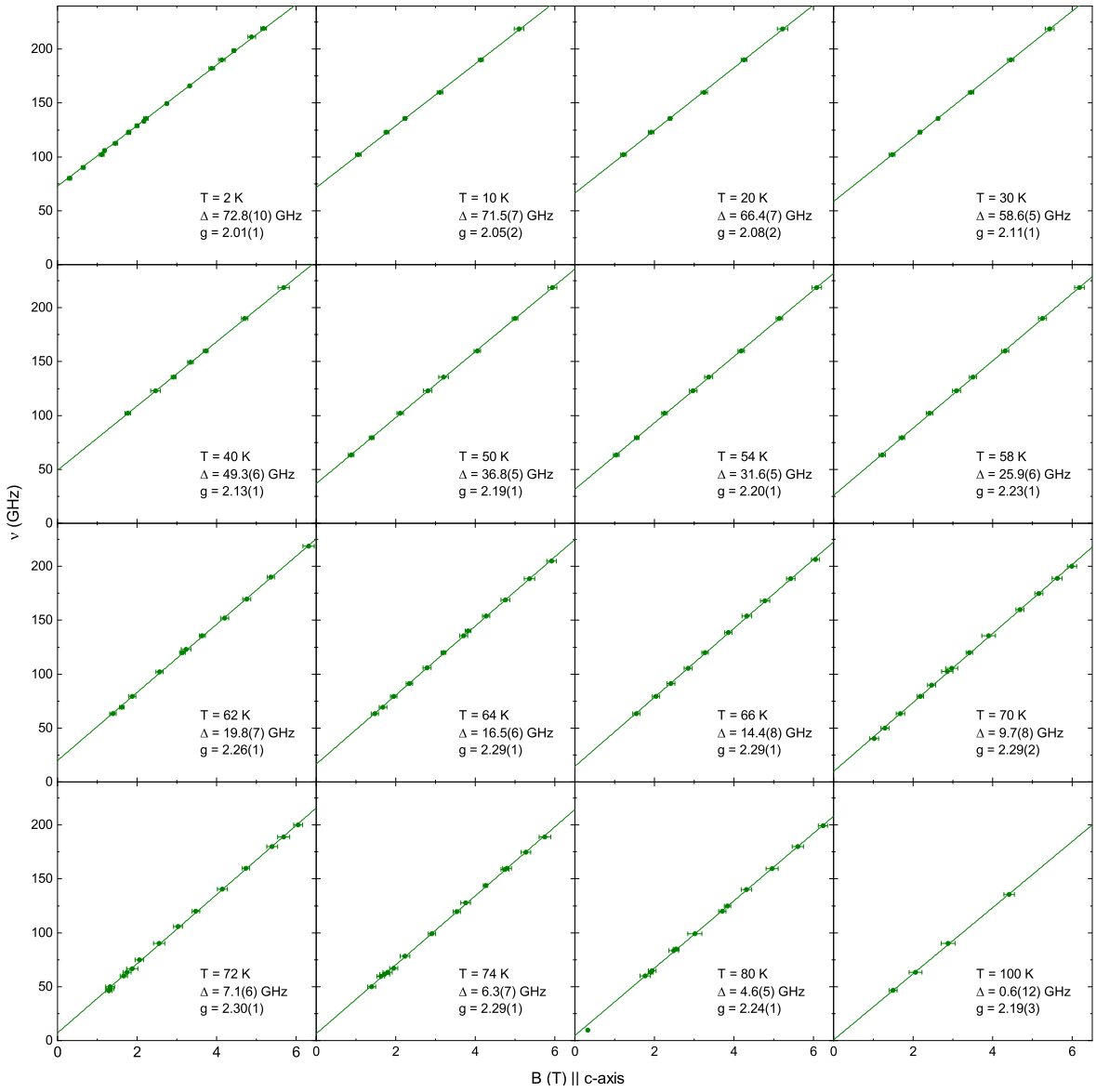

Figure 6.9.: Frequency–magnetic-field diagrams along the *c*-axis at various temperatures. Solid lines are least-squares fits according to Eq. 6.3. The fitting parameters are displayed in the individual plots.

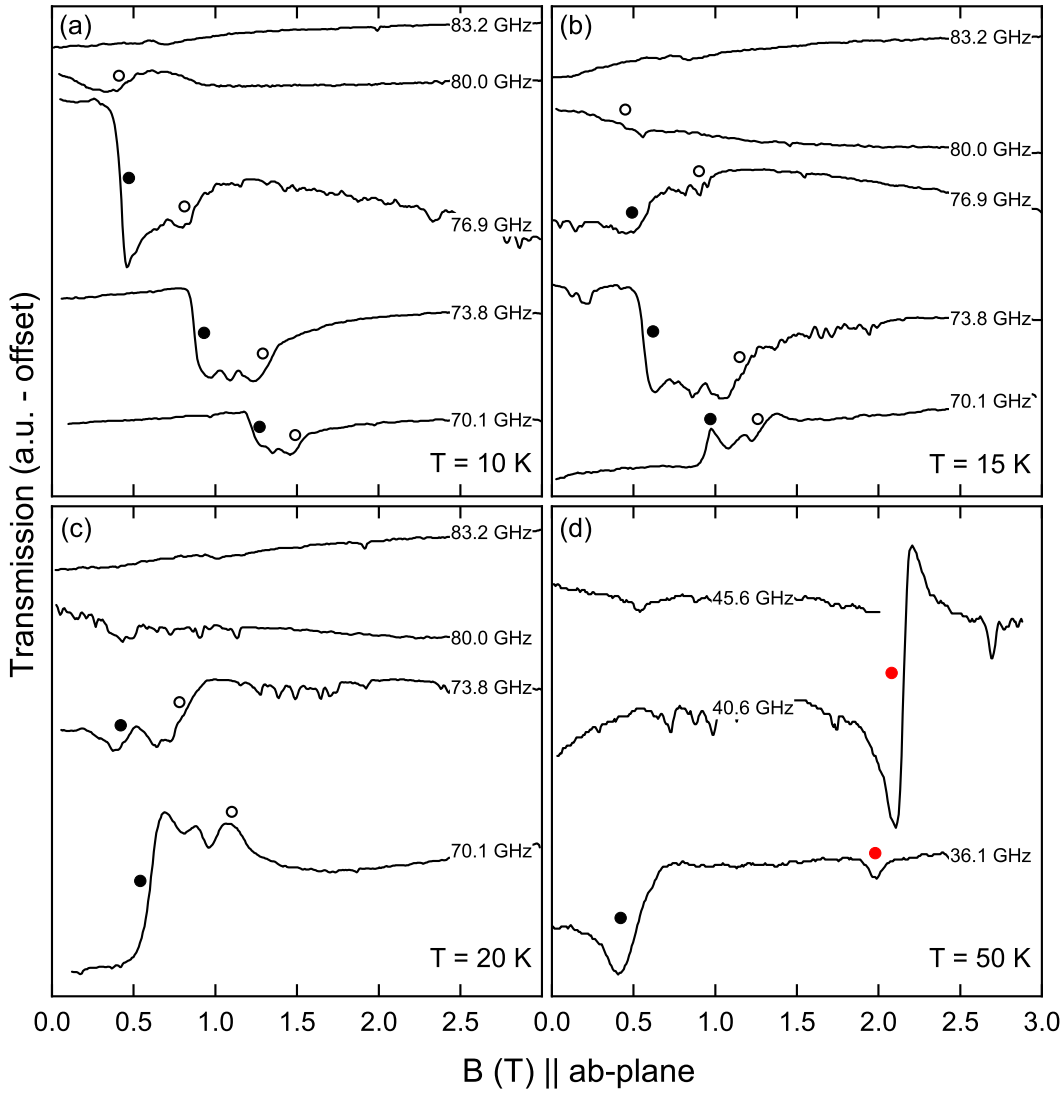

Figure 6.10.: Low-field *ab*-plane spectra at selected temperatures used to estimate the *ab*-plane zero-field splitting, $\tilde{\Delta}_{\mathrm{ab}}$ (see text for details). Coloured symbols mark resonance features positions.

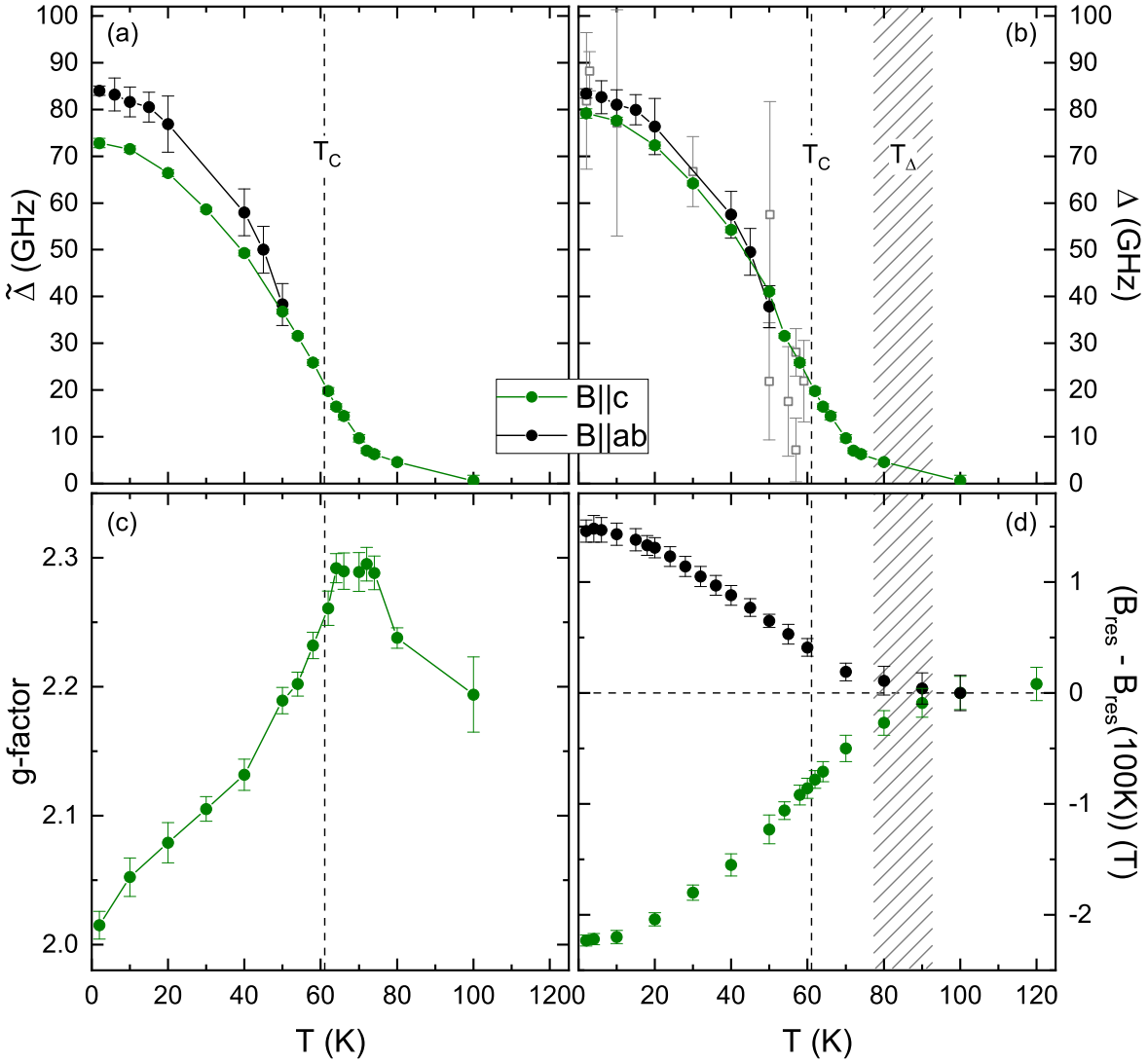

Figure 6.11.: Temperature dependence of the zero-field excitation gap stemming from spectra obtained with $B||c$ (green data points) and with $B||ab$ (black data points) (a) prior to demagnetisation corrections (designated $\tilde{\Delta}$), and; (b) after demagnetisation corrections (designated Δ). Furthermore, temperature dependence of (c) the effective c-axis g-factor, and; (d) of the difference of resonance fields at $\nu = 135.7\,\mathrm{GHz}$ ($B||c$, green data points) and $\nu = 73.8\,\mathrm{GHz}$ ($B||ab$, black data points) from their respective value at 100 K. Open grey squares in (b) are INS data from [143]. Vertical dashed lines mark T_C, horizontal dashed line in (d) the position of zero resonance-field shift, and shaded area shows the region around T_Δ (see text for details).

results qualify earlier inelastic neutron scattering observations which saw the complete closing of the anisotropy gap already at T_C [143, 153]. In the cited neutron scattering experiments, however, the weak inelastically-scattering peak due to a finite gap at T_C may have been overshadowed by the dominant elastically-scattering peak in its vicinity.

The fitting of the resonance spectra in Fig. 6.9 provides information also on the effective g-factor via the relation $\gamma_i = (g_i \mu_B)/h$. The temperature dependence of the optimised value of g_c is displayed in Fig. 6.11c. Therein, three distinct regions may be observed. In the long-range-ordered temperature region $T \leq T_C$, g_c continuously increases, before reaching a plateau-like maximum with a peak value of 2.30(2) for $64\,\mathrm{K} \leq T \leq 74\,\mathrm{K}$. Finally, g_c decreases for $T > 74\,\mathrm{K}$, amounting to $g_c = 2.19(3)$ at $T = 100\,\mathrm{K}$. Room-temperature X-band electron paramagnetic resonance measurements on an unoriented single crystal of CrI_3 found $g = 1.986$ [147]. The deviation of the c-axis g-factor at 100 K from $g = 1.986$ obtained here indicates that local magnetic fields still evolve at this temperature and points to the presence of short-range order. Interestingly, similar analysis of the effective g-factor obtained from high-temperature HF-ESR was previously performed on $CrGeTe_3$ [167, 185] and $CrSiTe_3$ [167]. In each case, comparable increase in the g-factor for the field applied along the easy magnetisation axis ($B||c$-axis) was observed up to T_C. Moreover, [167] followed the evolution of the g-factor for $T > T_C$ and found a decrease of g_c, albeit with no plateaux regime as seen in the present case in Fig. 6.11c. It was argued that on-site as well as off-site spin-orbit coupling [185], or anisotropic symmetric exchange and single-ion anisotropy [167], respectively, were responsible for the observed temperature dependence of the g-factor.

Extracting the resonance field positions from the spectra in Figs. 6.8a and 6.8b, the effect of temperature on the resonance field may be studied. Approximating the paramagnetic resonance field by its value at 100 K, above which no resonance signal was detected, Fig. 6.11d depicts the temperature-dependent shift in the resonance field position, $B_{res} - B_{res}(100\,\mathrm{K})$, from this paramagnetic value. Such a shift signals the evolution of anisotropic local magnetic fields [186]. As may be seen in Fig. 6.11d, below 80 K, which corresponds to the temperature T_Δ, the resonance positions are shifted towards higher values in the case of $B||ab$, while opposite trend appears for $B||c$. These observations imply the presence of anisotropic local magnetic fields, quasi-static on the timescale of the HF-ESR experiment (i.e. $1/\nu \approx 10^{-11}\,\mathrm{s}$). This demonstrates the presence of anisotropic short-range magnetic order in the temperature regime $T_C \leq T \leq T_\Delta$. The anisotropic nature of the observed resonance shift correlates with the observation of a finite anisotropy gap in this temperature regime. The sign of the shift opposes the findings in $CrCl_3$ which exhibits planar anisotropy [186] and is similar to what is found in $Cr_2Ge_2Te_6$ [187]. The data show that the effective magnetic easy axis is oriented parallel to the crystallographic c-axis, as also suggested by the low-temperature magnon field dependence and static magnetisation measurements presented above.

As seen in the gradual decrease of g_c with increasing temperature above T_C (Fig. 6.11c), the system tends to its paramagnetic value, $g = 1.986$, as expected. However, as indicated by the deviation of the g-factor at 100 K from its room-temperature value ($g_c(100\,\mathrm{K}) = 2.19(3)$; $g(300\,\mathrm{K}) = 1.986$) (see the above discussion), the system is not truly paramagnetic at 100 K. It is in light of this observation that the shifts in the axis-dependent resonance fields depicted in Fig. 6.11d are to be understood. The lack of difference in the shift of B_{res} between the c-axis and the ab-plane which sets in at T_Δ does not imply that the system is truly paramagnetic at this temperature. Instead, it implies that the shift in the resonance fields for $T \leq T_\Delta$ is isotropic. In other words, the data in Figs. 6.11c and 6.11d imply that short-range order is anisotropic for $T \leq T_\Delta$, and isotropic for $T \geq T_\Delta$.

6.3.3. AC Susceptibility

The thus-far presented DC magnetisation and high-frequency electron spin resonance results on CrI_3 have been complemented by AC magnetisation studies. With a broad range of applications, ranging from establishing the presence and nature of long-range order, through building-up of a magnetic phase diagram, to studying relaxation phenomena in, e.g., superparamagnetic particles or single-molecule magnets, AC susceptibility measurements provide a powerful and versatile technique in the study of magnetic materials. In the present case, the aim of AC susceptibility measurements was to obtain the true, external-magnetic-field-independent ferromagnetic ordering temperature, to perform a critical-exponent analysis of the ferromagnetic phase transition, and to quantify the relaxation mechanism of the ferromagnetically-long-range-ordered phase in CrI_3.

6.3.3.1. DC-Field-Dependent AC Susceptibility

Fig. 6.12 presents the results of AC susceptibility measurements performed in various static DC fields applied parallel to the easy magnetisation c-axis, that is, for $B_{DC}||c$-axis. Coming from high temperature of Curie-Weiss-like behaviour (data not shown), χ' obtained at $B_{DC} = 0\,\mathrm{T}$ exhibits a significant increase as the ferromagnetic ordering temperature is approached. At $T \simeq T_C$, $\chi'(B_{DC} = 0\,\mathrm{T})$ reaches its maximal value and remains approximately constant for all temperatures below T_C. For $B_{DC} > 0\,\mathrm{T}$, the monotonous increase of χ' upon cooling and subsequent approximately temperature-independent behaviour for $T < T_C$ is replaced with a gradual evolution of a peak-like structure as the ferromagnetic ordering temperature is approached from above. For an increasing value of B_{DC}, the peak-like structure broadens, becomes weaker, and shifts to higher temperatures. Moreover, for $0\,\mathrm{T} < B_{DC} \leq 0.2\,\mathrm{T}$, the peak-like structure is followed by a gradual increase of χ' towards the lowest temperatures. No such increase is observed for $B_{DC} > 0.2\,\mathrm{T}$; instead, χ' assumes a vanishing value.

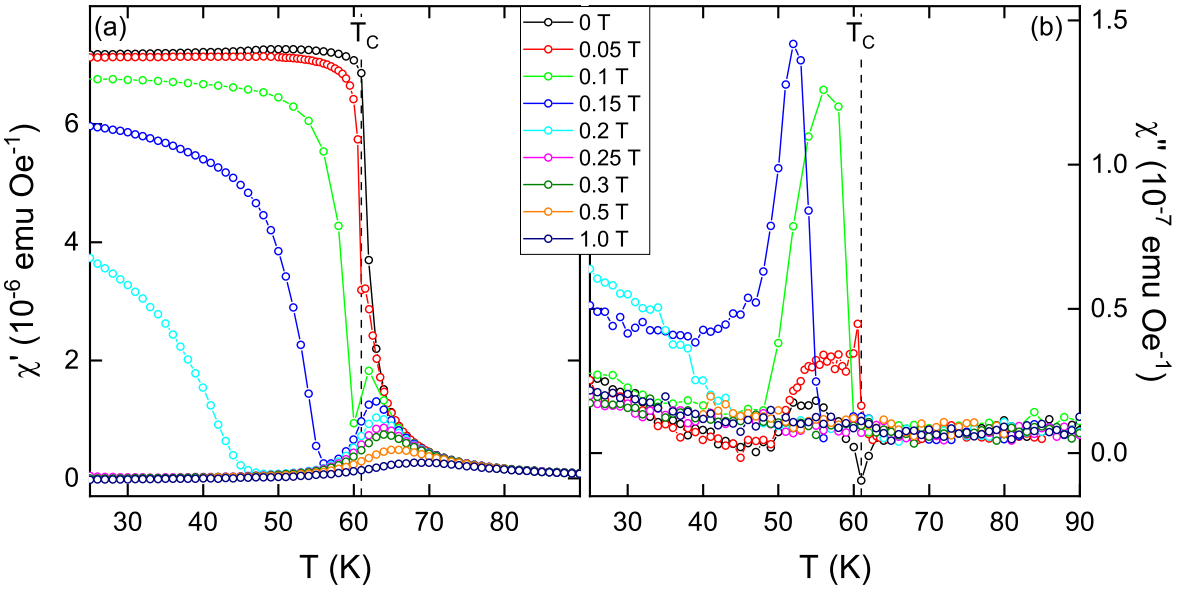

Figure 6.12.: AC susceptibility of CrI_3 obtained with AC-field excitation amplitude $B_{AC} = 5\,\text{Oe}$ and excitation frequency $f_{AC} = 500\,\text{Hz}$ in various DC fields $0\,\text{T} \leq B_{DC} \leq 1\,\text{T}$: (a) real part, χ'; (b) imaginary part, χ''.

Furthermore and as may be seen in Fig. 6.12b, χ'' is finite with a complex structure for DC fields $0\,\text{T} \leq B_{DC} \leq 0.2\,\text{T}$ for all temperatures below T_C. On the other hand, χ'' assumes a more-or-less featureless character for $B_{DC} > 0.2\,\text{T}$ at all temperatures.

It is possible to account for the above observations in a phenomenological sense by considering the evolution of the static magnetisation in the various temperature and DC-field regimes. In particular, isothermal magnetisation in the long-range-ordered phase for $B||c$-axis exhibits a typical behaviour of a ferromagnet along the easy axis with an almost instantaneous increase towards the spontaneous magnetisation, followed by an approximately constant, fully-saturated regime (see Fig. 6.4 for $T = 2\,\text{K}$, and Ref. [169] for elevated temperatures). Recalling that $B_c^{sat}(T = 2\,\text{K}) = 0.2\,\text{T}$ and focusing firstly on the low-temperature behaviour of the in-phase component of the AC susceptibility, χ' is found to respond to the driving field B_{AC} only for $B \leq B_c^{sat}$, i.e. in the region of finite slope of the isothermal static magnetisation. Once the magnetic moments have been saturated by the DC field and the slope of the isothermal static magnetisation becomes (approximately) zero, χ' too vanishes. In the temperature region around T_C, the behaviour of χ' is determined by the evolution of the long-range ferromagnetic order and can be used for a critical-exponent analysis (to be returned to presently). Lastly, the high-temperature in-phase component of the AC susceptibility tends to zero as the temperature is increased above T_C, mimicking a paramagnet's Curie-Weiss-like behaviour.

The evolution of the out-of-phase component of the AC susceptibility, χ'', indicates that in the DC-field region in which the magnetic moments are not completely saturated,

dissipative losses occur at all temperatures below T_C.

In order to provide a deeper quantitative insight into the way in which long-range ferromagnetic order develops in bulk CrI_3, the static-magnetic-field-dependent χ' data presented in Fig. 6.12a can be analysed by means of the static scaling theory [188–190]. For a second-order paramagnet-ferromagnet (PM-FM) phase transition, the static scaling theory predicts $T_{max} \propto B_{DC}^{\epsilon}$, where T_{max} can be equated with the temperature at which the peak-like structure in χ' reaches its maximum value χ'_{max} (c.f. Fig. 6.12a), and where ϵ is a dummy exponent.[9] By seeking an appropriate value of ϵ, it is possible to linearise the dependence of T_{max} on B_{DC}^{ϵ}. An implementation of a least-squares-minimisation routine yields $\epsilon = 0.79$. Correspondingly, fitting a linear equation to $T_{max} \propto B_{DC}^{0.79}$ of the form $T_{max} = a \cdot B_{DC}^{0.79} + T_C$ enables the extraction of the ferromagnetic phase transition temperature as the y-axis intercept. The thus-obtained T_C provides a true value of the ferromagnetic ordering temperature, as it is obtained for vanishing external DC field. The procedure yields $T_C = 61.06\,K \pm 0.04\,K(stat) \pm 0.5\,K(sys)$, lying in good agreement with the approximated value of T_C from DC-magnetisation measurements in Sec. 6.3.1, and from other thermodynamic studies [170, 171, 183].[10] The resulting linearised dependence of T_{max} on $B_{DC}^{0.79}$ and the corresponding linearised fit are displayed in Fig. 6.13a.

Equipped with the true ferromagnetic ordering temperature, the quantitative analysis of the present AC-susceptibility results may be further elaborated. The static scaling theory postulates that the reduced magnetisation $m = M/M_S$ satisfies [188, 190, 191]:

$$m(b,t) \propto t^{\beta} F_{\pm}\left(\frac{b}{t^{\beta+\gamma}}\right) \tag{6.4}$$

where F is Helmholtz free energy, with $t = (T - T_C)/T_C$ and $b = B_{DC}/T_C$ being the reduced temperature and field, respectively, and where β and γ refer to critical exponents with their usual meaning. Exploiting the definition of AC susceptibility as the derivative of the magnetisation with respect to the applied magnetic field, it follows from Eq. 6.4 that [190]:

$$\chi(b,t) = \frac{\partial m}{\partial b} \propto t^{-\gamma} F_{\pm}\left(\frac{b}{t^{\beta+\gamma}}\right) = b^{\frac{1}{\delta}-1} G\left(\frac{b}{t^{\beta+\gamma}}\right) \tag{6.5}$$

where G is Gibbs free energy. Defining the reduced temperature associated with the maximum in the peak-like structure in χ' as $t_{max} = (T_{max} - T_C)/T_C$, the following

[9] The nature of the PM-FM phase transition in bulk CrI_3 remains disputed. Most recent inelastic neutron scattering analysis suggests that the phase transition may possess a weak first-order character [144].

[10] The utilisation of a number of individual data points to determine T_C reduces the corresponding statistical error. In such a way, the precision of the determined value of T_C is improved compared to the above DC-susceptibility determination. The systematic error, originating predominately from the thermometer calibration, remains thereby unchanged.

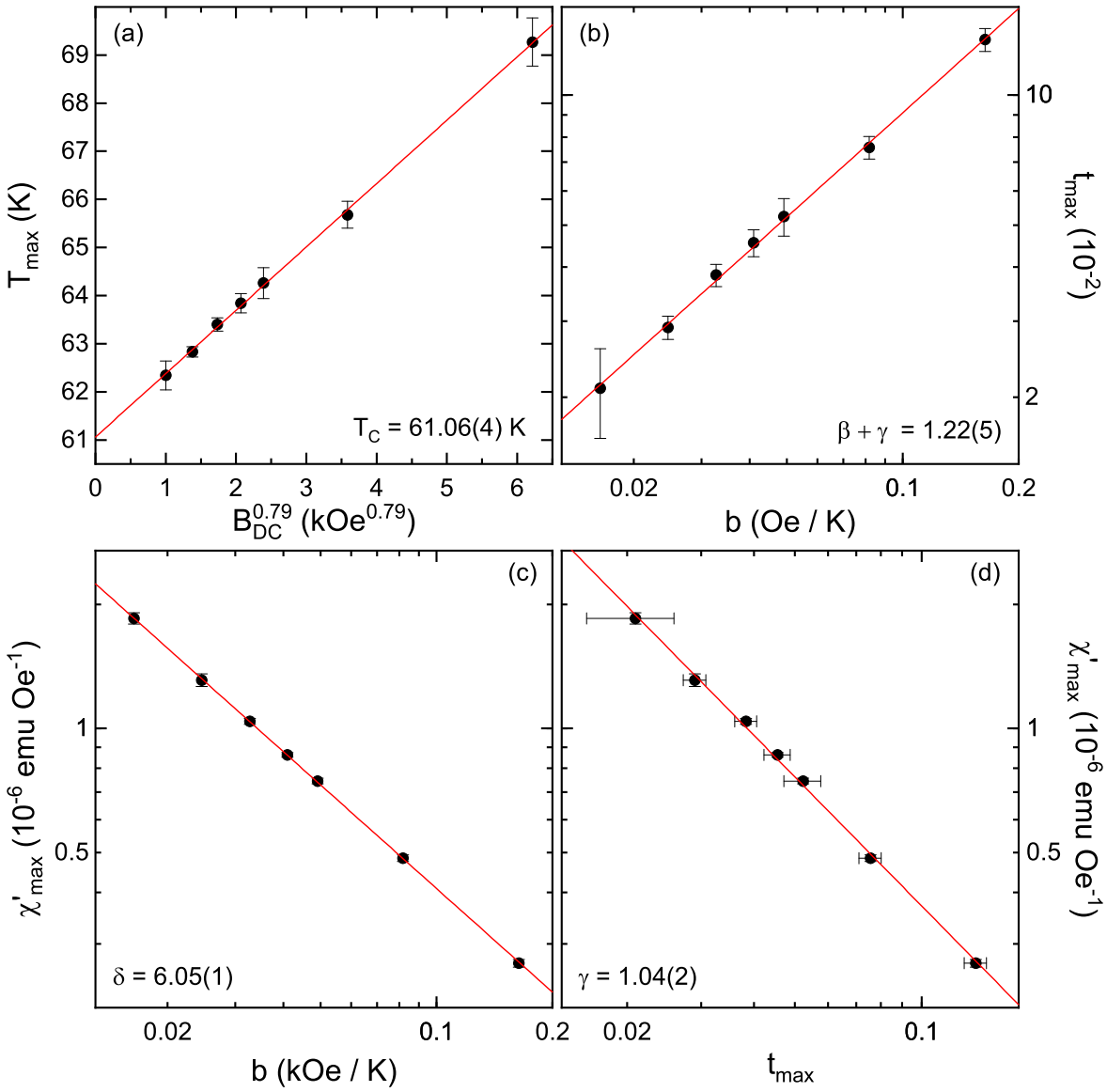

Figure 6.13.: (a) Linearised dependence of the temperature $T_{\max}$ of the peak-like maximum in χ' on the applied static field B_{DC}; (b)–(d) log-log plots of the scaling relations in Eqs. 6.6a–c between the reduced magnetic field, b, temperature, $T_{\max}$, and the peak-like maximum, $\chi'_{\max}$ (see text for details). All data points were extracted from Fig. 6.12a. Red solid lines are fits to the data. The individual plots display the parameter of interest obtained from the respective fit.

scaling relations can be derived from Eq. 6.5 [188, 190]:

$$\begin{aligned} t_{\max} &\propto b^{1/(\beta+\gamma)} \\ \chi'_{\max} &\propto b^{(1/\delta)-1} \\ \chi'_{\max} &\propto t_{\max}^{-\gamma} \end{aligned} \tag{6.6}$$

where δ is a further critical exponent and where the static-magnetic-field-dependent values of $\chi'_{\max}$ are, similarly to $T_{\max}$, extracted from the data in Fig. 6.12a. Utilising the above-obtained value $T_C = 61.06\,K$, Eq. 6.6 can be used to obtain the values of the various critical exponents. Least-squares-minimisation routines applied to the logarithmic counterparts of Eq. 6.6 yield: $\beta + \gamma = 1.22(5)$; $\delta = 6.05(1)$, and; $\gamma = 1.04(2)$. The various scaling relations together with the resulting fits are displayed in Figs. 6.13b–d in log-log plots, exhibiting good correspondence between the experimental AC-susceptibility data and the fitted curves.

The value of the exponent β can be calculated from the above results as $\beta = 0.21(4)$. Moreover, the Widom relation, given by $\gamma = \beta(\delta - 1)$, can be used to perform a self-consistency check of the obtained critical exponents, obtaining $\gamma = 1.05(2)$. This compares well with the value of γ obtained directly by analysing the AC susceptibility data by means of Eq. 6.6, indicating good self-consistency of the present results.

Although the presently determined critical exponents are self-consistent, a caution should be exercised when associating their values with any particular model system. This is, firstly, because of the finite temperature step size utilised in the AC-susceptibility measurements presented in Fig. 6.12 and the finite magnetisation resolution of the device, and, secondly, because of the lack of a priori knowledge about the region around the ferromagnetic phase transition in which the critical behaviour is manifested and hence in which the scaling analysis is applicable. Whereas the first of these limiting factors could, in principle, be reduced by utilising smaller temperature step size, the exponential dependence of the scaling relations in Eq. 6.6 necessarily leads to an inherent amplification of the error associated with the temperature, magnetisation, and DC-field reading. The second of these limiting factors is something of a chicken-and-egg problem, as the critical region can be experimentally determined only after performing the critical-scaling analysis, though it is precisely the information about the extent of the critical region which is required as an input for performing the analysis. Without prior knowledge from numerical modelling of the critical phenomena, the interpretation of the critical scaling remains limited. Nevertheless, it has been applied to the analysis of the ordering phenomena in several members of the family of the chromium-based van-der-Waals semiconducting ferromagnets, such as $CrGeTe_3$ [167, 190], $CrSiTe_3$ [167, 192, 193], $CrBr_3$ [194], and not last CrI_3 [168, 171].

The presently-obtained values of the various critical exponents do not allow for a univo-

cal association with any one particular model system for which theoretical predictions exist [188, 191, 195]. The rather low value $\beta = 0.21(4)$ may signal a departure from the three-dimensional models for which the value ranging from $\beta = 0.325$ (3D Ising model) to $\beta = 0.365$ (3D Heisenberg model) is predicted [195]. In particular, the observation appears to rule out a possibility of a mean-field model for which $\beta = 0.5$ is predicted [188]. Indeed, a detailed analysis of a large number of two-dimensional magnetic systems derived a phenomenological observation that $0.1 \lesssim \beta \leq 0.25$ holds for two-dimensional systems [196]. Based on this observation, the obtained value $\beta = 0.21(4)$ would suggest a reduced dimensionality of the dominant magnetic interactions in CrI_3. A similar supposition may be warranted also on the basis of the determined value $\delta = 6.05(1)$. With predictions for δ ranging from $\delta = 4.78$ for the 3D Ising system to $\delta = 5$ for the mean-field system [195], the presently-determined value of δ too demonstrates a departure from the three-dimensional models and indicates a gradual shift towards 2D Ising system ($\delta = 15$) [195]. On the other hand, the value $\gamma = 1.04(2)$ lies in the vicinity of the prediction for the mean-field model and some distance away from models with reduced dimensions (e.g. 2D Ising $\gamma = 1.75$ [195]).

Previous analyses of scaling relations in CrI_3 relied on DC-magnetisation technique and obtained critical exponents which were argued to point to a crossover from a mean-field behaviour towards a 3D Ising model [168, 171]. In particular, it was concluded that the interlayer coupling plays an essential role in establishing three-dimensional long-range order in bulk CrI_3 [168, 171, 197]. However, as shall be argued later, the current HF-ESR and isothermal magnetisation data point rather to the significance of magnetocrystalline anisotropy as the driving force behind long-range ferromagnetic order in bulk CrI_3.

6.3.3.2. AC Susceptibility at Various Excitation Frequencies

In order to obtain information about relaxation processes and to quantify relaxation times in the long-range-ordered ferromagnetic phase of CrI_3, studies of AC susceptibility's dependence on the frequency of the excitation AC field, f_{AC}, have been performed in static DC field $B_{DC} = 0\,T$.[11] The advantage of such measurements over the earlier performed analysis of HF-ESR (c.f. Section 6.3.2.2) is the possibility of studying magnetisation relaxation in a DC-field-free environment. This is particularly interesting for CrI_3 where, as seen earlier, DC fields of approximately 0.2 T along the c-axis, and of 3 T along the ab-plane lead to the magnetisation saturation.

The obtained AC susceptibility curves in the complete available range of excitation frequencies $0.5\,kHz \leq f_{AC} \leq 10\,kHz$ are displayed in Fig. 6.14. As may be seen in Fig. 6.14a, the in-phase component χ' shows negligible dependence on f_{AC} and the

[11] In order to study relaxation in the paramagnetic phase above T_C, excitation-frequency-dependent AC susceptibility would have to be measured in a range of static DC fields $B_{DC} > 0\,T$ [198]. This, however, was not subject of the present study.

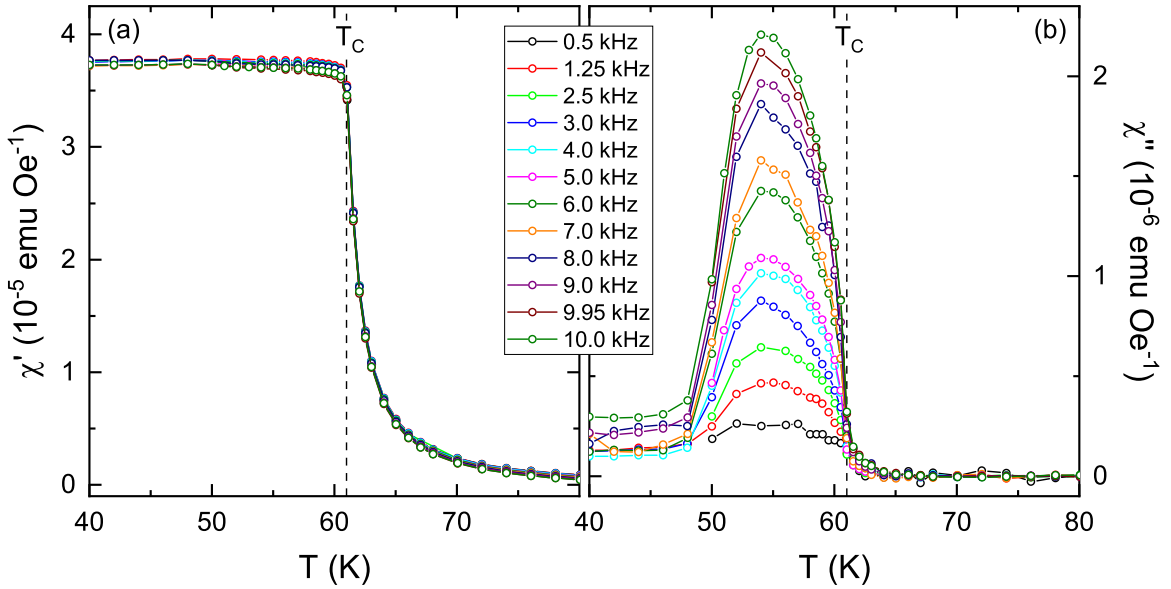

Figure 6.14.: AC susceptibility of CrI_3 obtained with AC-field excitation amplitude $B_{AC} = 2\,\mathrm{Oe}$ at various excitation frequencies $0.5\,\mathrm{kHz} \leq f_{AC} \leq 10\,\mathrm{kHz}$ and for $B_{DC} = 0\,\mathrm{T}$: (a) real part, χ'; (b) imaginary part, χ''.

curves resemble the static DC susceptibility presented in Fig. 6.3a. On the other hand, χ'' exhibits significant dependence on f_{AC} in the temperature region $48\,\mathrm{K} \lesssim T \lesssim 61\,\mathrm{K}$, with a peak-like structure developing in this temperature region and growing in size with the increasing value of f_{AC}. Interestingly, as f_{AC}, the peak in χ'' remains approximately symmetric about its middle point of around 54 K and does not move to lower temperatures, thereby lying in contrast with earlier comparable studies on the ferromagnet Fe_3O_4 [199]. The finite value of χ'' indicates the occurrence of a dissipation, that is, of a relaxation process [200]. The termination of the peak at around 48 K and the onset of low, approximately constant temperature dependence of χ'' suggests prevalence of a different relaxation process with a considerably longer relaxation time at this temperature.

Extracting the excitation-frequency-dependent values of χ' and χ'' at particular temperatures, the so-called Cole-Cole diagram may be constructed by plotting χ' on the abscissa and χ'' on the ordinate [200]. In case of a unique relaxation process, such a diagram describes a single semicircle, with each data point on the semicircle corresponding to a particular value of f_{AC} [198]. The apex of the semicircle, denoted here as $f_{AC}^{max}(T)$, corresponds to the relaxation time characteristic of the relaxation process in question at that particular temperature via the relation $\tau(T) = 1/(2\pi f_{AC}^{max}(T))$ [198]. Fig. 6.15a presents the Cole-Cole diagrams for $T = 54\,\mathrm{K}$ and $T = 56\,\mathrm{K}$ obtained from the data in Fig. 6.14. As may be seen, despite lying on an arc of a semicircle, the data points do not encompass a full semicircle and, in particular, do not reach the presumed apex. Therefore, the data are insufficient to establish univocally whether a unique re-

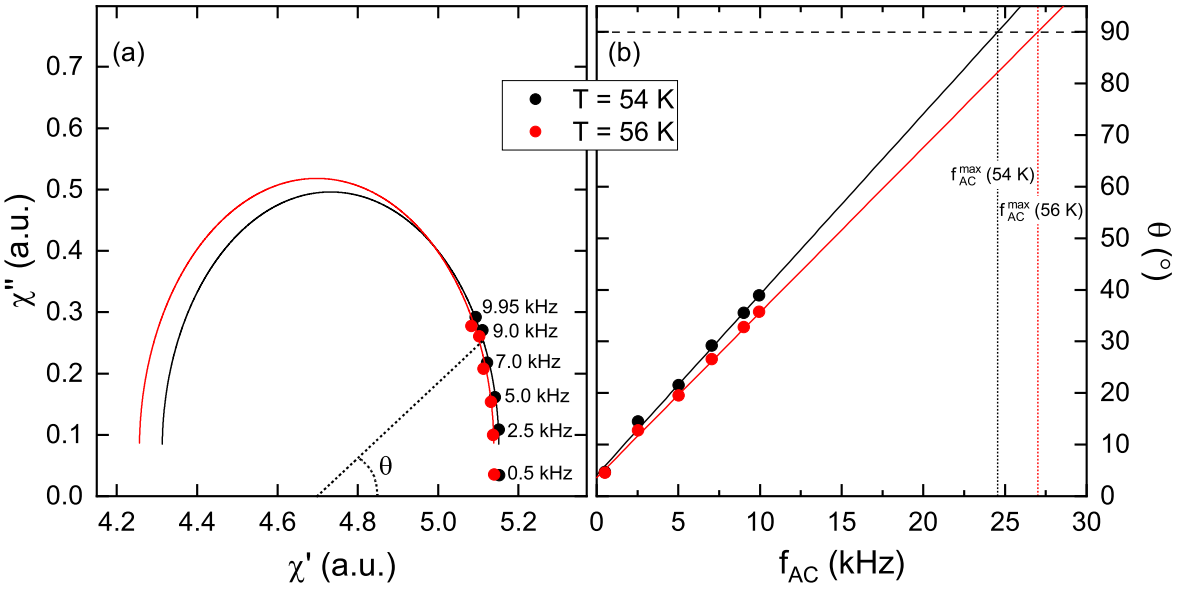

Figure 6.15.: (a) Cole-Cole diagrams stemming from AC susceptibility measurements presented in Fig. 6.14 at 54 K (black) and 56 K (red), fitted by the equation of a circle (black and red solid lines). θ designates the angle which an individual data point encloses with the graph's abscissa; (b) dependence of θ on the AC excitation frequency, f_{AC}, as derived from (a). Black and red solid lines are linear fits to the data. Horizontal dashed line marks $\theta = 90°$, corresponding to the apex of the semicircle in (a). Vertical dashed lines mark the corresponding $f_{\mathrm{AC}}^{\mathrm{max}}$.

laxation mechanism (corresponding to a single regular semicircle in the Cole-Cole plot) or several relaxation mechanisms (corresponding to a flattened single semicircle or to a series of semicircles) are at play at the respective temperatures [198]. In order to remove these uncertainties, measurements with a set of higher AC excitation frequencies are required.

In order to provide an estimate of the relaxation times nonetheless, it is assumed that the datasets at the respective temperature do lie on a unique circle. Hence, each dataset is fitted in the first step by the equation of a circle (black and red solid lines in Fig. 6.15a). The individual data points are then treated as enclosing an angle θ with the abscissa of the graph, as illustrated by the black dotted line in Fig. 6.15a. From trigonometric considerations, the dependence of θ on the AC excitation frequency is obtained. This is depicted in Fig. 6.15b and exhibits linear dependence. By fitting a straight line to these data, an estimate can be made for f_{AC} when $\theta = 90°$, i.e. for the frequency corresponding to the apex of the semicircle in Fig. 6.15a. One finds: $f_{\mathrm{AC}}^{\mathrm{max}}(54\,\mathrm{K}) \approx 24.5\,\mathrm{kHz}$, corresponding to $\tau(54\,\mathrm{K}) \approx 6.5 \times 10^{-6}\,\mathrm{s}$, and; $f_{\mathrm{AC}}^{\mathrm{max}}(56\,\mathrm{K}) \approx 27\,\mathrm{kHz}$, corresponding to $\tau(56\,\mathrm{K}) \approx 5.9 \times 10^{-6}\,\mathrm{s}$ (see Fig. 6.15b).

Since the actual Cole-Cole diagrams may extend significantly higher than estimated by the fitted semicircles in Fig. 6.15a, the obtained values of $f_{\mathrm{AC}}^{\mathrm{max}}$ provide merely a lower limit of the actual relaxation frequencies, and thus the actual relaxation times may be

considerably shorter. Still, with the time scale of a typical spin-spin relaxation process of the domain magnetisation lying several orders of magnitude lower ($\tau_{S-S} \approx 10^{-10}$–$10^{-11}$ s [176]), it may be speculated that the mechanism responsible for the peak-like structure in Fig. 6.14b is of a different nature. Indeed, relaxation phenomena in ferromagnets are expected to be dominated by the domain walls, as the walls' delicate balance between exchange energy and anisotropy energy can be easily destroyed by an exciting AC field, leading to dissipation of magnetisation [198]. Moreover, typical relaxation times associated with domain-wall effects lie in the order of 10^{-5}–10^{-8} s [201–203], matching with the presently-estimated relaxation time. Therefore, it is argued that the relaxation effect leading to the peak-like structure in χ'' seen in Fig. 6.14b originates in domain-wall effects, such as moving or reshaping of the domain walls. The possibility of observing domain-wall effects in the present case is made plausible also by the fact that the AC susceptibility in Fig. 6.14 was measured upon heating with $B_{DC} = 0$ T, whereby the cooling to the lowest temperatures was also performed in zero DC field.[12]

6.3.4. High-Temperature Isothermal Magnetisation

6.3.4.1. Anisotropy Effects in Isothermal Magnetisation

Fig. 6.16a depicts axis-dependent isothermal magnetisation curves obtained at selected temperatures above the ferromagnetic ordering temperature. These curves expand on earlier measurements performed in the temperature range $2\,\mathrm{K} < T < T_C$, available elsewhere [197]. Starting from temperatures $T = 64$ K, i.e. just above T_C, the magnetisation shows a pronounced discrepancy between the two orientations in the entirety of the measured field regime. This is reminiscent of the isothermal magnetisation at 2 K, depicted in Fig. 6.4. As discussed in reference to Fig. 6.4, the discrepancy in the detected magnetisation at 14 T may be a result of a small error in the sample mass determination, or of anisotropy in the values of the g-factors or of the total magnetic moment (see Section 6.3.1). Interestingly, the size of the discrepancy between the two axes decreases with increasing temperature, becoming vanishingly small for $T \gtrsim 160$ K. The latter observation indicates that the error in the sample mass determination cannot explain the observed anisotropic behaviour. An earlier report of isothermal magnetisation of CrI_3 too detected anisotropic effects up to 6 T at selected temperatures in the vicinity of T_C ($T = 50$ K and $T = 75$ K), though no explicit discussion thereof was given [141].

[12] Based on the presently-estimated relaxation time of 10^{-5}–10^{-6} s, spin-phonon relaxation of the domain magnetisation, with typical relaxation times of 10^{-4}–10^{-7} s [176], could also be responsible for the current observation [176]. Definitive differentiation between phonon-mediated relaxation of the domain magnetisation and domain-wall effects could be achieved by repeating the AC susceptibility measurements in Fig. 6.14 with having saturated the ferromagnetic domains by cooling to the lowest temperatures with $B_{DC} > B_{sat}$. If domain walls are responsible for the observed effect, then in a saturated, domain-free scenario, a vanishing χ'' response can be expected.

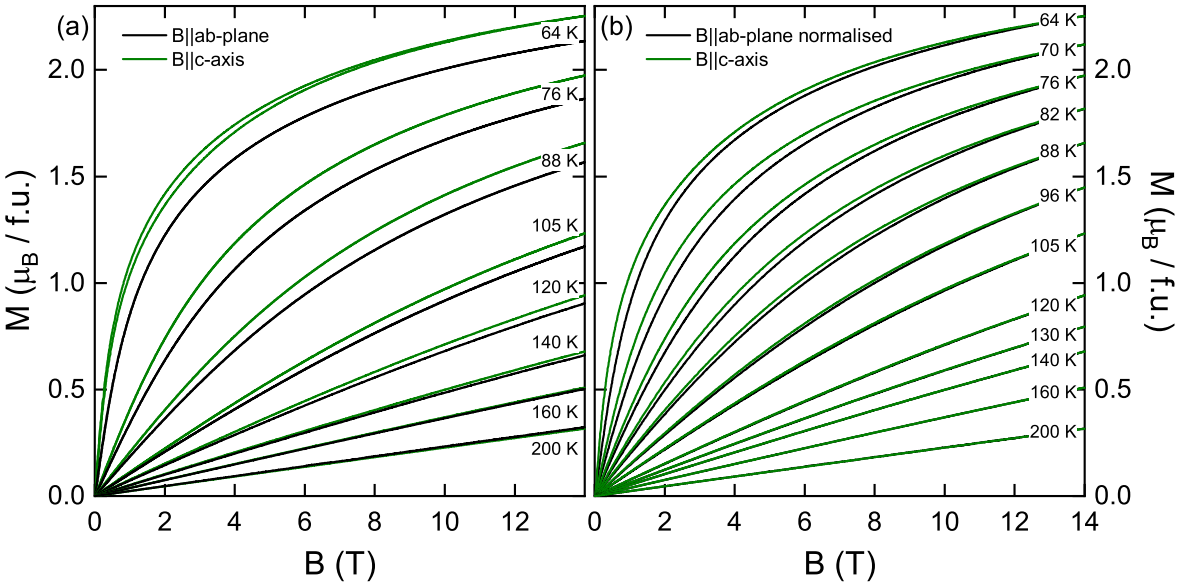

Figure 6.16.: (a) Isothermal magnetisation at selected temperatures as a function of applied magnetic field along the *ab*-plane (black) and c-axis (green); (b) the same magnetisation curves as in (a) together with magnetisation curves at additional temperatures with each *ab*-plane curve scaled to the *c*-axis magnetisation at 14 T at the respective temperature. The curves in (a) depict a full measurement cycle $0\,\mathrm{T} \rightarrow 14\,\mathrm{T} \rightarrow 0\,\mathrm{T}$, the curves in (b) only the up-sweep $0\,\mathrm{T} \rightarrow 14\,\mathrm{T}$.

In order to account for the potential anisotropy in the g-factors or total magnetic moment, each *ab*-plane magnetisation curve in Fig. 6.16a has been scaled to the *c*-axis magnetisation value at 14 T at the respective temperature. The resulting curves are plotted in Fig. 6.16b. It may be seen that even after accounting for the above effects, the isothermal magnetisation at temperatures close enough to T_C exhibits anisotropic behaviour. To be concrete, starting at 64 K, the two magnetisation curves show different bending in the magnetic field, with *c*-axis bending in a more pronounced way. With increasing temperature, the difference in the bending weakens and the two curves align ever better with each other. Finally, the two curves fall perfectly onto each other for $T \gtrsim 105\,\mathrm{K}$, such that the magnetisation for $B||ab$ is hidden underneath the curves for $B||c$ in Fig. 6.16b. Such different bending points to non-vanishing magnetocrystalline anisotropy in this temperature region. Indeed, the observed behaviour above T_C is a precursor of the low-temperature behaviour in which the *c*-axis is the easy magnetisation axis. Moreover, the present observation corroborates the detection of a finite zero-field excitation gap and anisotropic shift in the resonance fields for $T \leq T_\Delta$ observed in HF-ESR measurements (c.f. Section 6.3.2.2).

Furthermore, starting from 64 K, the magnetisation curves depicted in Fig. 6.16b exhibit finite right bending in the magnetic field. Its extent weakens with increasing temperature, although a close inspection of the curves reveals that even at 200 K, a small right curvature is present. Especially interesting is the observation that the right

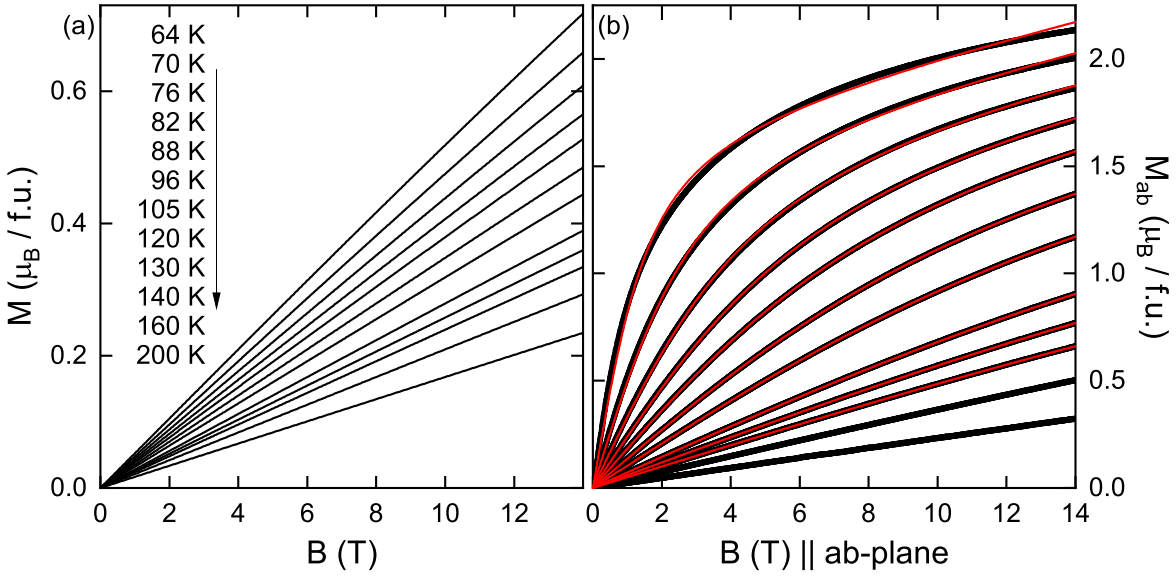

Figure 6.17.: (a) Simulation of isothermal magnetisation by means of a Brillouin function with $S = 3/2$, $L = 0$, $g = 2$, and $M_S = 3\,\mu_B$/f.u. at the same selected temperatures as displayed in Fig. 6.16b; (b) isothermal magnetisation at the same selected temperatures along the *ab*-plane (black), fitted by means of a modified Brillouin function (Eq. 6.7, red), see text for details.

bending clearly persists for $T \gtrsim 105\,\mathrm{K}$, i.e. for temperatures for which no anisotropic behaviour in the scaled magnetisation curves in Fig. 6.16b is visible. The right bending may be an indication of underlying short-range ferromagnetic correlations. To be sure, the observed right bending is likely enhanced by the applied magnetic field, such that without appropriate theoretical underpinning, it may not be possible to disentangle the two contributions. The enhancement due to the applied magnetic field is likely to become especially significant as $T \to T_C^+$.

That short-range ferromagnetic correlations may at least partially be responsible for the curvature of the magnetisation curves can be seen when predictions for an ideal paramagnetic Cr^{3+} ion are considered. Assuming $S = 3/2$, $L = 0$, $g = 2$, and $M_S = 3\,\mu_B$/f.u., Fig. 6.17a shows such predictions on the basis of a usual Brillouin function [6] for the various temperatures shown in Fig. 6.16b. Although the real saturation magnetisation will decrease with increasing temperature, this will not affect the curvature but merely the absolute value of the simulated magnetisation. As is evident from Fig. 6.17a, a pure Cr^{3+} paramagnet in the studied temperature and magnetic-field regime would exhibit a perfectly linear magnetisation field dependence, contrary to the present observations.[13]

Using the isothermal magnetisation in Fig. 6.16, an attempt may be made at quantifying the ensemble size of the short-range ferromagnetically-correlated magnetic moments

[13]For completion, the magnetisation curve of an antiferromagnet would, depending on the strength and orientation of the external magnetic field with respect to the magnetocrystalline anisotropy, display either no field dependence, left bending in the field, or at most linear field dependence [6].

above T_C.[14] To do so and focusing henceforth only on the unscaled isothermal magnetisation for $B||ab$-plane, the magnetisation curves may be fitted by means of the following function [6, 204]:

$$M = M_S \cdot \left[\left(\frac{2\tilde{S}+1}{2\tilde{S}} \right) \cdot \coth\left((2\tilde{S}+1)\frac{y}{2} \right) - \left(\frac{1}{2\tilde{S}} \right) \cdot \coth\left(\frac{y}{2} \right) \right] + \chi_0 B \qquad (6.7)$$

with M_S, $\tilde{S}$, and χ_0 being free fitting parameters, and where M_S denotes the saturation magnetisation, χ_0 a field-independent term, and $y = (g\mu_B B)/(k_B T)$. The term in the square brackets is a modified Brillouin function. Herein the individual ion's spin S is substituted by $\tilde{S}$ to denote the sum of the spins of ions participating in a short-range ferromagnetically-correlated ensemble, $\tilde{S} = \sum_i S_i$, where i runs over all members of the correlated ensemble. It follows from these considerations that the correlated ensembles can be projected back into the usual Brillouin function by taking them to correspond to individual magnetic ions completely uncorrelated from all neighbouring ions, just as would be the case for paramagnetic centres. Note that including the linear term in Eq. 6.7 is necessary in order to describe the data well for $T \lesssim 82\,\mathrm{K}$. Furthermore, note that the small curvature prevents reliable fitting for $160\,\mathrm{K} \leq T \leq 200\,\mathrm{K}$.

The fitting results of this procedure at selected temperatures are depicted in Fig. 6.17b as red solid lines. Despite successful convergence of all the fits up to 140 K, it may be seen that upon approaching the ferromagnetic ordering temperature, the quality of the fitting is reduced. This indicates the breaking-down of the above-assumed simple correlation model. This is likely, on the one hand, owing to the negligence of the field-induced contributions to the correlations, and, on the other hand, owing to treating the correlation between two magnetic ions as a linear binary effect whereby correlations grow linearly with decreasing temperature and individual ions are either perfectly correlated or completely uncorrelated.

Still, it may be seen that for $T \gtrsim 82\,\mathrm{K}$, Eq. 6.7 describes the magnetisation curves well. That is, the magnetisation data above this temperature may be described by a single value of $\tilde{S}$ which is obtained directly from the fits. This may indicate that the applied field does not significantly change the size of the short-range ferromagnetically-correlated ensemble. The approximate number of spins in such ensemble can be estimated as $\tilde{n} = \tilde{S}/S$, where $S = 3/2$. The resulting temperature dependence of $\tilde{n}$ is displayed in Fig. 6.18a. For illustrative purposes, the figure includes the obtained value of $\tilde{n}$ also for $T \lesssim 82\,\mathrm{K}$. The grey marked area in the figure emphasises that the simple correlation model is insufficient in quantifying the magnetisation in this temperature region and the obtained values of $\tilde{n}$ are hence to be taken as providing

[14] The impetus for the ensuing analysis was provided by a discussion in the framework of a bachelor student supervision. Correspondingly, elements of the ensuing analysis were previously published in Ref. [197].

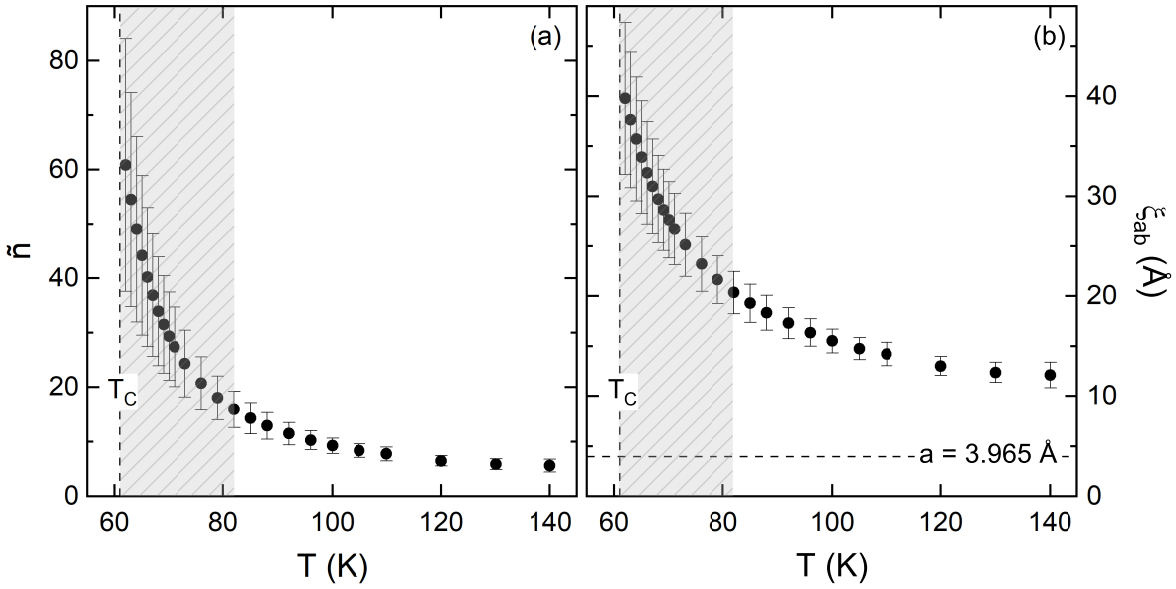

Figure 6.18.: Temperature dependence of (a) the number of ferromagnetically-correlated moments, $\tilde{n}$, and; (b) the *ab*-plane correlation length, ξ_{ab}. Shaded regions mark temperatures for which the simple correlation model likely breaks down, see text for details. Vertical dashed lines mark the ferromagnetic ordering temperature, and horizontal dashed line in (b) marks the in-plane Cr–Cr nearest-neighbour separation, taken from [141].

merely a very crude approximation. As seen in Fig. 6.18a, $\tilde{n}$ is found to decrease upon heating, indicating the gradual splitting of the ferromagnetically-correlated ensembles due to thermal fluctuations.

6.3.4.2. Correlation Length Estimation

Using the values of $\tilde{n}$, it is possible to provide a rough estimate of the in-plane ferromagnetic correlation length ξ_{ab}. To do so, an assumption is made that the ferromagnetic short-range correlations above T_C extend solely in the *ab*-planes, such that the *c*-axis correlation length, ξ_c, vanishes. Such an assumption is justified based, firstly, on earlier numerical calculations on bulk CrI_3 which predict that intralayer coupling is one [182] or even two [142, 183] orders of magnitude stronger than interlayer coupling, and, secondly, on inelastic neutron scattering results which show that $J_{\text{eff}}^{\text{intra}} \approx 77.7\,\text{K}$ and $J_{\text{eff}}^{\text{inter}} \approx 6.8\,\text{K}$ [144] (see Section 6.1). Moreover, inelastic neutron scattering on a related van-der-Waals ferromagnet $CrSiTe_3$ found the persistence of in-plane correlations well above T_C and all the way up to room temperature with vanishing out-of-plane correlations [205]. Assuming further that the correlated ensembles form circles with a diameter equalling the correlation length ξ_{ab}, it is possible to express the correlation length as:

$$\xi_{\mathrm{ab}} = \sqrt{\frac{2\sqrt{3}}{\pi} \cdot a^2 \cdot \tilde{S}} \tag{6.8}$$

where $a = 3.965\,\text{Å}$ is the in-plane nearest-neighbour Cr–Cr separation [141]. The thus-estimated temperature dependence of the correlation length is depicted in Fig. 6.18b, where the grey area emphasises again the crudeness of the approximation in the marked temperature region. Given that inelastic neutron scattering revealed $\xi_{\mathrm{ab}} = 220\,\text{Å}$ at $10\,\text{K}$ [143], i.e. in the long-range-ordered phase, the presently-obtained values of the correlation length of several tens of Angstroms appear reasonable. Especially interesting is the observation that at $140\,\text{K}$, i.e. the highest temperature for which the fitting by means of Eq. 6.7 was still possible, ξ_{ab} still lies about three times higher than the in-plane nearest-neighbour Cr–Cr separation (c.f. dashed horizontal line in Fig. 6.18b). This points to significant robustness of the in-plane short-range correlations and is reminiscent of the above-cited case of $CrSiTe_3$. However, it ought to be stressed that inelastic neutron scattering is required in order to provide accurate quantification of the correlation lengths.

6.3.4.3. Critical Scaling of DC-Field Isothermal Magnetisation

Isothermal magnetisation obtained at elevated temperatures, some of which has been presented in the previous section, may be also used to perform a critical-scaling analysis (see [188, 191, 195] for theoretical approaches to such an analysis). In the current case, the aim is to complement the above-presented and discussed critical-scaling analysis on the basis of AC-susceptibility measurements (see Section 6.3.3).

Fig. 6.19 depicts the critical isotherm of CrI_3, i.e. the isothermal magnetisation obtained at the ferromagnetic ordering temperature, for $B||ab$-plane. With the ferromagnetic ordering temperature determined in the above AC susceptibility analysis $T_{\mathrm{C}} = 61.06\,\text{K}$, the critical isotherm was measured at $T = 61\,\text{K}$. It can be shown that for the magnetisation of a critical isotherm it holds that [188]:

$$M(T = T_{\mathrm{C}}) = a \cdot B^{(1/\delta)} \tag{6.9}$$

where δ is the critical exponent, obtained already in the above AC susceptibility analysis, and a is a scaling constant. Applying a least-squares-minimisation routine to the logarithmic form of Eq. 6.9, $\delta = 6.22(10)$ is found for the fitting region $10\,\text{T} \leq B \leq 14\,\text{T}$. The fitted curve is displayed in Fig. 6.19 as a red solid line. The value of δ obtained from the present analysis of the DC magnetisation lies above its determination from the AC susceptibility: $\delta_{\mathrm{DC}} = 6.22(10)$; $\delta_{\mathrm{AC}} = 6.05(1)$. Nevertheless, the close proximity of the two values to each other justifies the upholding of the original interpretation of δ as indicating a departure from three-dimensional models

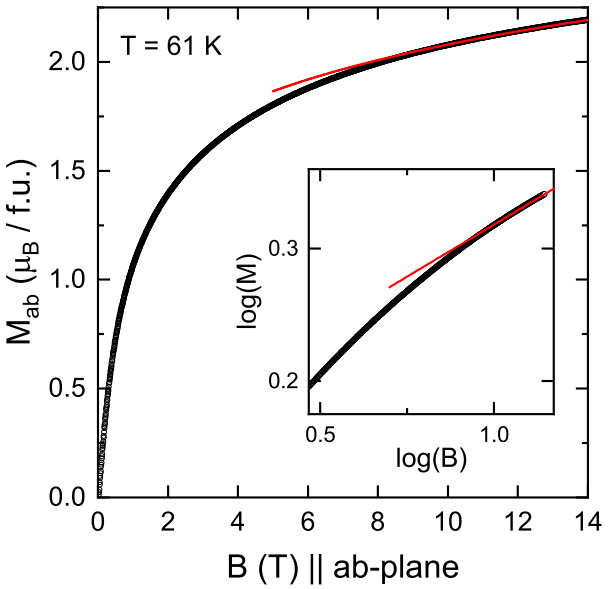

Figure 6.19.: Critical magnetisation isotherm ($T = T_C = 61\,K$) of CrI_3 obtained for $B||ab$-plane. Red solid line is a fit to the field regime $10\,T \leq B \leq 14\,T$ by means of Eq. 6.9. The inset depicts the main plot on a log-log scale.

and towards two-dimensional Ising system (see Section 6.3.3).

Furthermore, the value of the critical exponents β and δ obtained in the above AC susceptibility analysis can be verified on the basis of DC magnetisation measurements. Starting from Eq. 6.6, it can be shown that for true critical exponents, the renormalised magnetisation curves given by $M|t|^{-\beta}$ as a function of the renormalised field given by $B|t|^{-(\beta+\gamma)}$ for different temperatures below and above T_C fall onto each other [188, 206]. More specifically, one renormalised curve $M|t|^{-\beta}$ vs. $B|t|^{-(\beta+\gamma)}$ is expected for $T < T_C$, and another for $T > T_C$.

Using the above-obtained values $\beta_{AC} = 0.21(4)$ and $\gamma = 1.04(2)$, it is found that the isothermal magnetisation curves obtained for $B||ab$-plane collapse onto each other very well for all temperatures $T \geq 70\,K$. Fig. 6.20a demonstrates this for selected temperatures $70\,K \leq T \leq 100\,K$. As the temperature is decreased from 70 K towards the ferromagnetic ordering temperature, the overlap becomes progressively less satisfactory (data not shown). A similar effect is observed also for isothermal magnetisation below T_C: in the temperature region $44\,K \leq T \leq 53\,K$, a good overlap of the various curves is found (Fig. 6.20a). However, as the temperature is increased from 53 K towards T_C, the overlap becomes progressively less satisfactory (data not shown).

Using $\beta = 0.21(4)$ and $\gamma = 1.04(2)$, no satisfactory overlap of the renormalised magnetisation curves above T_C for $B||c$-axis can be found (data not shown). However, using adjusted values of $\beta = 0.18$ and $\gamma = 1.13$, a very good overlap is achieved for the renormalised curves at all temperatures $T \geq 70\,K$ (see Fig. 6.20b). Similarly to above,

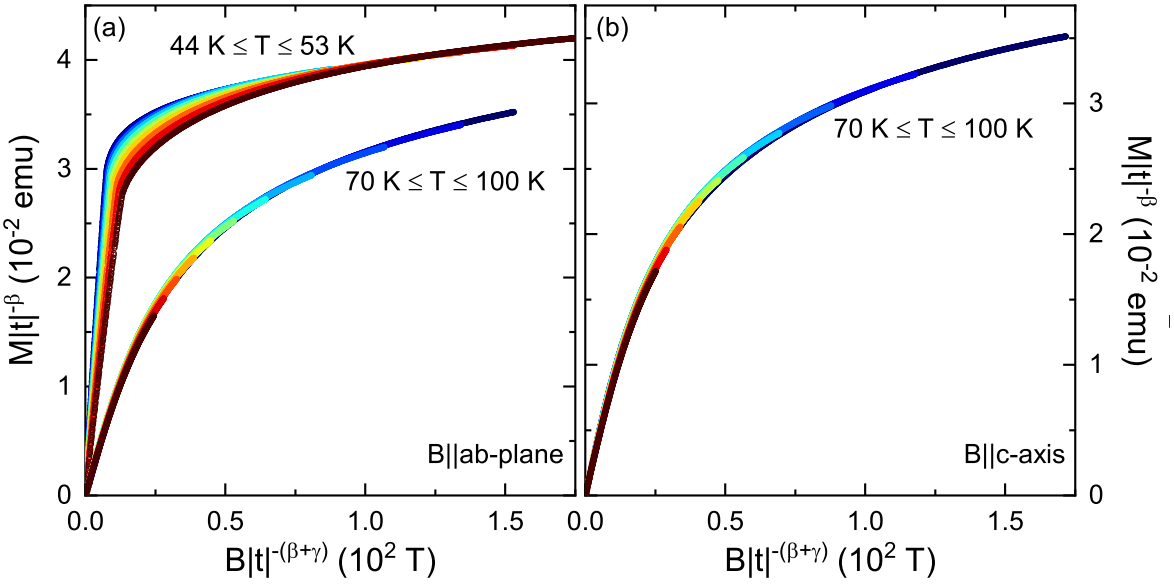

Figure 6.20.: Renormalised isothermal magnetisation as a function of renormalised magnetic field of CrI_3 at selected temperatures (a) for $B||ab$-plane below and above the ferromagnetic ordering temperature, and; (b) for $B||c$-axis above the ferromagnetic ordering temperature.

as the temperature is decreased from 70 K towards T_C, the overlap becomes gradually worse. No isothermal magnetisation was performed below the ferromagnetic ordering temperature for $B||c$-axis.

The adjusted value of β for $B||c$-axis lies within the error bar of its originally-determined value and, as such, requires no re-interpretation. In particular and as noted above, empirical investigations found that for two-dimensional magnets, β satisfies: $0.1 \lesssim \beta \leq 0.25$ [196]. As $\beta = 0.18 < 0.25$ for $B||c$-axis, CrI_3 may be classified as a predominantly two-dimensional magnet also on the basis of the renormalised magnetisation for $B||c$-axis. On the other hand, the value of γ for $B||c$-axis lies outside of the error bars of its value determined from AC susceptibility. Nevertheless, the close proximity of the two values to each other may be a good indication that the real value of γ falls in the region $1.04 \lesssim \gamma \lesssim 1.13$. Although such a determination has a limited precision, it does allow to uphold the original interpretation that γ lies in the vicinity of the prediction for the mean-field-model.

Lastly, it may be remarked that the renormalised magnetisation curves in Fig. 6.20 show a similarly-good [168] or even superior [171] overlap than previous literature reports.

6.4. Discussion and Summary

In a wide frequency and magnetic-field regime, ferromagnetic magnon excitations in CrI_3 are exactly captured by a domain-based model in Eqs. 6.1–6.3. The analysis by means of the model provides microscopic parameters from which the magnetisation easy axis is determined to lie along the crystallographic c-axis, the axis-dependent g-factors with $g_c = 2.01(1)$ and $g_{ab} = 2.04(4)$, and the zero-field excitation gap $\Delta(T = 2\,\mathrm{K}) = 80(1)\,\mathrm{GHz}$ are obtained. Whereas the low-temperature magnon field dependence univocally points to the existence of domains in bulk CrI_3, the domains' exact shape could not be ascertained on the basis of the present magnetic resonance experiments.

The obtained low-temperature value of the excitation gap as well as the gap's temperature dependence in the ferromagnetically-ordered phase are corroborated by earlier studies [143, 149, 150]. However, whereas previous inelastic neutron scattering found the vanishing of Δ at T_C [143], the present study is, thanks to its high energy resolution, able to follow the gap's temperature evolution also above T_C (c.f. Fig. 6.11b). Concretely, at 62 K (i.e. just above T_C), Δ is found to amount to 19.8(7) GHz (approximately 25 % of its value at 2 K) and to vanish only for $T \gtrsim 80\,\mathrm{K}$, i.e. for $T = T_\Delta \gtrsim 1.3 T_C$. Furthermore, anisotropic shift in the resonance field is also observed to emerge below $T \simeq T_\Delta$ (c.f. Fig. 6.11d). At the same time, isothermal magnetisation at temperatures above T_C reveals a difference in the right bending between $B||c$ and $B||ab$ even after presumed effects due to anisotropic g-factor and total magnetic moment have been accounted for (c.f. Fig. 6.16b).

On the other hand, a deviation from Curie-Weiss-like behaviour is found to set in approximately below 130 K (c.f. Fig. 6.3b), while finite right bending in isothermal magnetisation is detected for temperature as high as $T = 200\,\mathrm{K}$ (c.f. Fig. 6.16b). Lastly, fitting of the resonance-frequency–magnetic-field diagram at temperatures above T_C found a deviation from the high-temperature paramagnetic value of the g-factor; in particular, $g = 2.19(3)$ was observed at $T = 100\,\mathrm{K}$ (c.f. Fig. 6.11c). Although not measured in this work, specific heat measurements found magnetically-driven entropy changes below about 150 K [170, 171].

Synthesising these observations into a self-contained picture of evolution of ferromagnetic order in CrI_3, four regimes of magnetic interactions may be identified:

- a high-temperature, purely paramagnetic regime above T_{PM};
- a regime of short-range ferromagnetic correlations which is split by the onset of magnetocrystalline anisotropy to:
  - a higher-temperature, isotropic short-range correlations regime at temperatures $T_\Delta \leq T_{SRO}^{iso} \leq T_{PM}$;
  - a lower-temperature, anisotropic short-range correlations at temperatures

$T_{\mathrm{C}} \leq T_{\mathrm{SRO}}^{\mathrm{aniso}} \leq T_{\Delta}$, and;

- a ferromagnetically-long-range-ordered phase for $T \leq T_{\mathrm{C}}$.

Whereas the experimental evidence presented in this chapter points univocally to the existence of the different temperature regimes, the designation of the various temperature boundaries is influenced by the sensitivity of the various experimental methods used to determine them. Correspondingly, T_{PM} may be identified to lie at $T_{\mathrm{PM}} \approx 130\,\mathrm{K}$ by the analysis of static magnetic susceptibility, at $T_{\mathrm{PM}} \approx 150\,\mathrm{K}$ by the analysis of specific heat, and at $T_{\mathrm{PM}} \gtrsim 200\,\mathrm{K}$ based on right bending of the isothermal magnetisation. In a similar vein, T_{Δ} may be identified to be $T_{\Delta} \approx 80\,\mathrm{K}$–$90\,\mathrm{K}$ by HF-ESR and to be $T_{\Delta} \approx 105\,\mathrm{K}$ by isothermal magnetisation. The ferromagnetic ordering temperature is found to be $T_{\mathrm{C}} = 61.0(5)\,\mathrm{K}$ and $T_{\mathrm{C}} = 61.06\,\mathrm{K} \pm 0.04\,\mathrm{K(stat)} \pm 0.5\,\mathrm{K(sys)}$ by DC- and AC-field susceptibility, respectively.

These observations point to a scenario of a purely two-dimensional (i.e. in-plane) and Heisenberg-like (i.e. isotropic) short-range order at $T_{\Delta} \leq T \leq T_{\mathrm{PM}}$. This develops an anisotropic character below T_{Δ}; that is, for $T \leq T_{\Delta}$, the magnetic moments start to experience a preferred magnetisation direction which lies along the c-axis.[15] These findings imply that long-range order in CrI_3 does not primarily evolve from a purely Heisenberg-like short-range-ordered regime through increasing in-plane correlations in the presence of small but finite interlayer coupling as observed, e.g., in the paradigmatic 2D Heisenberg system La_2CuO_4 [6]. Instead, the onset of anisotropic effects well above T_{C} indicates that long-range ferromagnetic order in CrI_3 is at least partially driven by magnetocrystalline anisotropy, as also suggested previously by theoretical studies [145, 182].

Additionally, the critical exponents obtained from AC susceptibility (Fig. 6.13), and corroborated by analysis of DC magnetisation (Figs. 6.19 and 6.20) provide at least partial further evidence that interlayer interactions do not dominate the ferromagnetic ordering in CrI_3. Concretely, $\beta = 0.21(4)$ and $\delta = 6.05(1)$ suggest that at T_{C} the appropriate model to characterise the magnetic interactions in CrI_3 is of reduced dimensionality (most likely exhibiting 2D character). The small departure of the critical exponent γ from $\gamma = 1$, which may be implied by the combined critical scaling analysis from AC and DC-field susceptibility, and its value $1.04 \lesssim \gamma \lesssim 1.13$ corroborates the supposition that at T_{C}, the magnetic interactions are predominantly two-dimensional.

The conclusion that long-range ordering in CrI_3 is at least partially anisotropy-driven

[15] Although the magnetic moments remain predominantly Heisenberg-like in the entire short-range regime, it could be asserted that at T_{Δ} they start to develop a weak Ising-like character. However, the usage of the term "Ising" in this context should not be equated with implying terahertz-regime single-ion anisotropies typically known for 4f magnetic ions, such as gadolinium or dysprosium. In the present context, Ising-like character is intended to differentiate the truly Heisenberg behaviour of the magnetic moments in the *ab*-planes above T_{Δ} from the moments' tendency to orient along a preferred magnetisation axis below T_{Δ}.

and that dominant magnetic interactions may be two-dimensional is also corroborated, firstly, by the detection of long-range ferromagnetic order in a monolayer of CrI_3 [148] which, trivially, cannot be driven by growing out-of-plane correlations, and, secondly, by the small reduction of T_C from 61 K to 45 K as the sample's thickness is reduced from bulk to monolayer which indicates that interlayer interactions do not dominate the ferromagnetic ordering in CrI_3 [148]. It is natural to extend the arguments advanced for a single layer of CrI_3 also to the case when the monolayer is expanded to a bulk and thus to provide a uniform account of the decisive mechanism by which Mermin-Wagner theorem is circumvented and long-range order established in this system with dominant Heisenberg interactions operating on a two-dimensional lattice.

Relaxation times on the order of 10^{-10}–10^{-11} s were detected in the long-range-ordered phase at the lowest temperatures by high-frequency electron spin resonance. These could be attributed to a spin-spin relaxation mechanism. At the same time, an upper limit of $\approx 10^{-6}$ s on the relaxation time in the long-range-ordered phase but in the vicinity of T_C was provided by the analysis of the AC susceptibility data. The order of this relaxation time could be reconciled with the dynamics of domain-wall motion or reshaping. However, higher frequencies of the exciting AC field are required to quantify the relaxation time more precisely.

7. Overall Summary and Conclusion

This work is devoted to the experimental investigation of long-range-ordered magnets: the magnetoelectric antiferromagnets $MnTiO_3$ and $LiMnPO_4$, and the ferromagnetic van-der-Waals material CrI_3. The principal experimental method is high-frequency electron spin resonance. The employed setup utilises a millimetre vector network analyser in combination with Schottky diodes to generate excitation frequencies in the range $30\,\mathrm{GHz} \lesssim \nu \lesssim 1000\,\mathrm{GHz}$. In combination with a superconducting magnet and liquid-helium cooling, the materials can be investigated in magnetic fields up to 18 T and temperatures $1.8\,\mathrm{K} \lesssim T \lesssim 270\,\mathrm{K}$. The main experimental method is complemented by electron spin resonance in the X-band frequency range using a cavity setup, and by magnetisation measurements in static and oscillating magnetic fields.

$MnTiO_3$ belongs to the class of ilmenite titanates which exhibit a layered honeycomb crystal structure. The material features Mn^{2+} ions, leading to $S = 5/2$, $L = 0$ in the ground state, and enters G-type long-range antiferromagnetic order at $64.0(5)\,\mathrm{K}$ with c-axis as the easy magnetisation axis. The resonance-frequency–magnetic-field diagram at $T = 2\,\mathrm{K}$ can be exhaustively described by the model of a two-sublattice antiferromagnet with uniaxial anisotropy. The quantitative analysis yields the zero-field excitation gap $\Delta = 166(1)\,\mathrm{GHz}$ and effective g-factors $g_\parallel = 1.98(1)$ and $g_\perp = 2.00(1)$. The subsequent analysis finds the effective exchange field $B_\mathrm{E} = 107(6)\,\mathrm{T}$ and effective anisotropy field $B_\mathrm{A} = 0.17(1)\,\mathrm{T}$, implying $B_\mathrm{A} \ll B_\mathrm{E}$. The anisotropy is argued to originate predominantly from magnetic dipole-dipole interactions. The zero-field excitation gap exhibits an order-parameter-like temperature dependence and closes completely at T_N. Above T_N, a shift of the resonance field with increasing temperature up to $T \approx 200\,\mathrm{K}$ indicates a pronounced region of short-range order.

$LiMnPO_4$ is a member of the olivine-structured orthophosphates class which exhibit complex ground-state properties, including exceptionally large magnetoelectric tensors, weak ferromagnetism, and incommensurate magnetic phases. Similarly to the studied titanate, $LiMnPO_4$ too features Mn^{2+} ions. The antiferromagnetic order forms at $33.5(2)\,\mathrm{K}$ with an easy magnetisation axis along the a-axis. Isothermal magnetisation along the hard magnetisation b-axis reveals a spin flip at $B_\mathrm{C2} = 4.9(2)\,\mathrm{T}$ and $T = 2\,\mathrm{K}$. With increasing temperature, B_C2 shifts weakly to higher fields, before disappearing as $T \to T_\mathrm{N}^-$, confirming it to be an inherent property of the ground state. It is argued that the feature signals a canting of the magnetic moment in the ground state by 0.16° from the easy towards the hard magnetisation axis. Symmetry analysis reveals a lack

of inversion centre between the nearest magnetic neighbours, which lie in the *bc*-plane. This leads to the speculation that Dzyaloshinskii-Moriya interactions give rise to the spin canting. The field dependence of the low-energy magnon excitations reveals two zero-field excitation gaps, $\Delta_1 = 112.4(2)\,\mathrm{GHz}$ and $\Delta_2 = 179.9(2)\,\mathrm{GHz}$, and an isotropic effective g-factor $g_{\mathrm{easy}} = g_{\mathrm{im}} = g_{\mathrm{hard}} = 2.00(1)$. The complete field dependence of the magnon branches, including an anomalous branch above the spin-flop field, can be accounted for within a model of a two-sublattice antiferromagnet with orthorhombic anisotropy and a rotation of the anisotropy axis by 6.5° towards the hard axis at the spin-flop field. Analysis of the temperature-dependent resonance indicates, firstly, that the system preserves its orthorhombic anisotropy at least up to $\approx 0.9T_{\mathrm{N}}$ with complete closure of Δ_1 and Δ_2 as $T \to T_{\mathrm{N}}^{-}$, and secondly, that no detectable short-range order develops above T_{N}.

CrI_3 consists of weakly, van-der-Waals-coupled honeycomb layers which easily undergo exfoliation. The material develops long-range ferromagnetic order at 61 K. Ferromagnetic resonance in the ground state reveals a large zero-field excitation gap $\Delta = 80(1)\,\mathrm{GHz}$ and a pair of anisotropic g-factors, $g_{\mathrm{c}} = 2.01(1)$ and $g_{\mathrm{ab}} = 2.04(4)$. The magnon excitations univocally indicate the presence of ferromagnetic domains, although the domains' exact structure cannot be ascertained by ferromagnetic resonance alone. The excitation gap Δ preserves a finite value at T_{C} and completely closes only at $T_\Delta \approx 1.3T_{\mathrm{C}}$. Up to about the same temperature, anisotropic shifts in the resonance field and anisotropic isothermal magnetisation are detected. These observations are interpreted as indicating the evolution of magnetocrystalline anisotropy already above T_{C}, which provides the necessary condition for circumvention of the Mermin-Wagner theorem and evolution of long-range ferromagnetic order in the monolayer. Isothermal magnetisation implies isotropic short-range order at least up to $\approx 200\,\mathrm{K}$. Critical-scaling analysis, derived from AC susceptibility and DC magnetisation, yields $T_{\mathrm{C}} = 61.06\,\mathrm{K} \pm 0.04\,\mathrm{K(stat)} \pm 0.5\,\mathrm{K(sys)}$, and the critical exponents $\beta = 0.21(4)$, $\gamma = 1.05(2)$, and $\delta = 6.05(1)$. The latter indicate a predominantly two-dimensional nature of the magnetic interactions at T_{C}, in line with theoretical simulations and inelastic neutron scattering observations. Relaxation times on the order of 10^{-10}–$10^{-11}\,\mathrm{s}$ are detected at the lowest temperatures by high-frequency electron spin resonance, and of $\approx 10^{-6}\,\mathrm{s}$ in the vicinity of T_{C} by AC susceptibility. The former are attributed to a spin-spin relaxation mechanism, whereas the latter can be reconciled with domain-wall motion or reshaping.

Jointly, these observations demonstrate the indispensable insights which high-frequency electron spin resonance delivers in a laboratory-scale setup, thus avoiding the necessity for large-scale neutron-reactor- or synchrotron-based experiments; insights which are valuable for fundamental research as well as for future applications. Especially noteworthy is the highly precise determination of the zero-field excitation gap, thanks to

which the crucial role of magnetocrystalline anisotropy in formation of long-range ferromagnetic order in bulk CrI_3 could be determined, and thanks to which materials can be designed for a stable spin-current transport in spintronic-based devices. Also of great value is the precise mapping of the field dependence of the low-energy magnon excitations in a large range of magnetic fields thanks to which the rotation of the anisotropy axis at the spin-flop field of $LiMnPO_4$ was inferred, and thanks to which the interplay between exchange coupling and anisotropy in magnetic heterostructures can be studied. As this work bears witness to, these are but a few examples of how high-frequency electron spin resonance can be combined with other experimental techniques to study complex magnetic materials.

A. List of Publications

1. W. Hergett,†, **M. Jonak**,† J. Werner, F. Billert, S. Sauerland, C. Koo, C. Neef, R. Klingeler: *Synthesis and Magnetism of a Li_2FeSiO_4 Single Crystal.*
   Journal of Magnetism and Magnetic Materials **477**, 1–3 (2019).

2. Anirudha Ghosh, H. Johan M. Jönsson, D. J. Mukkattukavil, Y. Kvashnin, D. Phuyal, M. Agåker, Alessandro Nicolaou, **M. Jonak**, R. Klingeler, M. V. Kamalakar, Håkan Rensmo, Tapati Sarkar, Alexander N. Vasiliev, Sergei Butorin, J.-E. Rubensson, Olle Eriksson, and Mahmoud Abdel-Hafiez: *Intra-Atomic and Local Exchange Fields in the Van der Waals Magnet CrI_3*
   arXiv:2201.04400 [cond-mat.str-el] (submitted to Physical Review Letters (2022)).

3. Anirudha Ghosh, D. Singh, T. Aramaki, Qingge Mu, V. Borisov, Y. Kvashnin, G. Haider, **M. Jonak**, D. Chareev, S. A. Medvedev, R. Klingeler, M. Mito, E. H. Abdul-Hafidh, J. Vejpravova, M. Kalbáč, R. Ahuja, Olle Eriksson, and Mahmoud Abdel-Hafiez: *Exotic magnetic and electronic properties of layered CrI_3 single crystals under high pressure*
   Phys. Rev. B **105**, L081104 (2022).

4. J. Arneth, **M. Jonak**, S. Spachmann, M. Abdel-Hafiez, Y.O. Kvashnin, R. Klingeler: *Uniaxial pressure effects in the two-dimensional van-der-Waals ferromagnet CrI_3*
   Phys. Rev. B **105**, L060404 (2022).

5. **M. Jonak**, E. Walendy, M. Abdel-Hafiez, R. Klingeler: *Low-energy magnon excitations and the emerging anisotropic nature of short-range order in CrI_3*
   (submitted to Physical Review B (2022)).

6. L. Gries,† **M. Jonak**,† A. Elghandour, K. Dey, R. Klingeler: *The role of magnetoelastic coupling and magnetic anisotropy in $MnTiO_3$*
   arXiv:2207.14750 [cond-mat.str-el] (submitted to Physical Review B (2022)).

† Both authors contributed equally to this work

B. Bibliography

[1] Press release: The Nobel Prize in Physics 2021.

[2] G. Parisi, Phys. Rev. Lett. **43**, 1754–1756 (1979).

[3] G Parisi, Journal of Physics A: Mathematical and General **13**, L115–L121 (1980).

[4] M. Mézard and A. Montanari, *Information, Physics, and Computation* (Oxford University Press, Oxford, 2009).

[5] H. Nishimori, *Statistical Physics of Spin Glasses and Information Processing* (Oxford University Press, Oxford, 2001).

[6] S. J. Blundell, *Magnetism in Condensed Matter*, Oxford Master Series in Condensed Matter Physics (Oxford University Press, Oxford, 2001).

[7] D. I. Khomskii, *Basic Aspects of the Quantum Theory of Solids* (Cambridge University Press, Cambridge, 2010).

[8] P. Fazekas, *Lecture Notes on Electron Correlation and Magnetism*, Vol. 5, Series in Modern Condensed Matter Physics (World Scientific Publishing, Singapore, 1999).

[9] S. M. Rezende, R. L. Rodríguez-Suárez, and A. Azevedo, Phys. Rev. B **93**, 054412 (2016).

[10] R. E. Camley and R. L. Stamps, Journal of Physics: Condensed Matter **5**, 3727–3786 (1993).

[11] B. Heinrich and J. A. C. Bland, *Ultrathin Magnetic Structures II* (Springer Berlin, Heidelberg, 1994).

[12] M. Farle, Reports on Progress in Physics **61**, 755–826 (1998).

[13] D. R. Klein, D. MacNeill, J. L. Lado, D. Soriano, E. Navarro-Moratalla, K. Watanabe, T. Taniguchi, S. Manni, P. Canfield, J. Fernández-Rossier, and P. Jarillo-Herrero, Science **360**, 1218–1222 (2018).

[14] D. Ghazaryan, M. T. Greenaway, Z. Wang, V. H. Guarochico-Moreira, I. J. Vera-Marun, J. Yin, Y. Liao, S. V. Morozov, O. Kristanovski, A. I. Lichtenstein, M. I. Katsnelson, F. Withers, A. Mishchenko, L. Eaves, A. K. Geim, K. S. Novoselov, and A. Misra, Nature Electronics **1**, 344–349 (2018).

[15] Y. Tserkovnyak, A. Brataas, and G. E. W. Bauer, Phys. Rev. B **66**, 224403 (2002).

[16] E. Saitoh, M. Ueda, H. Miyajima, and G. Tatara, Applied Physics Letters **88**, 182509 (2006).

[17] D. I. Khomskii, *Transition Metal Compounds* (Cambridge University Press, Cambridge, 2014).

[18] A. Abragam and B. Bleaney, *Electron Paramagnetic Resonance of Transition Ions* (Oxford University Press, Oxford, 2012).

[19] S. Rezende, *Fundamentals of Magnonics* (Springer, Heidelberg, 2020).

[20] S.V. Vonsovskii, *ed.*, *Ferromagnetic Resonance*, Translated from Russian by Z. Lerman (Israel Program for Scientific Translations, Jerusalem, 1964).

[21] G. Rado and H. Suhl, *Magnetism*, Vol. 1 (Academic Press, New York and London, 1963).

[22] E. A. Turov, *Physical Properties of Magnetically Ordered Crystals* (Academic Press, New York, 1965).

[23] J. Tjepkema, *How to Plot Hydrogen Orbitals.* MATLAB Central File Exchange, retrieved on 15/08/2022.

[24] J. M. D. Coey, *Magnetism and Magnetic Materials* (Cambridge University Press, Cambridge, 2009).

[25] J. Werner, *Experimentelle Untersuchungen der Magnetisierung und der Elektronenspinresonanz an Übergangsmetallverbindungen mit konkurrierenden Wechselwirkungen*, PhD Thesis, 2019.

[26] N. W. Ashcroft and N. D. Mermin, *Solid State Physics* (Harcourt College Publishers, Orlando, 1976).

[27] B. Weber, *Koordinationschemie: Grundlagen und aktuelle Trends* (Springer Spektrum Berlin, Heidelberg, 2014).

[28] T. Holstein and H. Primakoff, Phys. Rev. **58**, 1098–1113 (1940).

[29] J. H. Van Vleck, Phys. Rev. **78**, 266–274 (1950).

[30] F. Keffer and C. Kittel, Phys. Rev. **85**, 329–337 (1952).

[31] T. Nagamiya, K. Yosida, and R. Kubo, Advances in Physics **4**, 1–112 (1955).

[32] S. J. Blundell and K. M. Blundell, *Concepts in Thermal Physics* (Oxford University Press, Oxford, 2006).

[33] A. F. Andreev and V. I. Marchenko, Soviet Physics Uspekhi **23**, 21–34 (1980).

[34] V. Glazkov, T. Soldatov, and Y. Krasnikova, Applied Magnetic Resonance **47**, 1069–1080 (2016).

[35] H. Tanaka, S. Teraoka, E. Kakehashi, K. Iio, and K. Nagata, Journal of the Physical Society of Japan **57**, 3979–4003 (1988).

[36] M. Lakshmanan, Philosophical Transactions of the Royal Society A: Mathematical, Physical and Engineering Sciences **369**, 1280–1300 (2011).

[37] C. Kittel, Phys. Rev. **73**, 155–161 (1948).

[38] C. Kittel, Phys. Rev. **82**, 565–565 (1951).

[39] www.abmillimetre.com.

[40] C. P. Poole, *Electron Spin Resonance* (Interscience Publishers, New York, 1967).

[41] G. Feher and A. F. Kip, Phys. Rev. **98**, 337–348 (1955).

[42] M. Linzer, Journal of Applied Physics **40**, 372–376 (1969).

[43] G. E. Pake and E. M. Purcell, Phys. Rev. **74**, 1184–1188 (1948).

[44] B. Chesca, R. Kleiner, and D. Koelle, *The SQUID Handbook* (John Wiley and Sons, Ltd, 2004).

[45] R. L. Fagaly, Review of Scientific Instruments **77**, 101101 (2006).

[46] M. Buchner, K. Höfler, B. Henne, V. Ney, and A. Ney, Journal of Applied Physics **124**, 161101 (2018).

[47] S. Foner, Review of Scientific Instruments **30**, 548–557 (1959).

[48] Magnetic Property Measurement System: SQUID VSM AC Option User's Manual. Part Number 1505-400, A1. Quantum Design, 2010.

[49] Physical Property Measurement System: AC Measurement System (ACMS II) Option User's Manual. Part Number 1084-800, Rev. A2. Quantum Design, 2017.

[50] O. J. Schumann, *The Cologne Laue Indexation Program.* Gnu general public license (2008).

[51] L. Gries, M. Jonak, A Elghandour, K. Dey, and R. Klingeler, *The role of magnetoelastic coupling and magnetic anisotropy in $MnTiO_3$* (arXiv:2207.14750 [cond-mat.str-el], 2022).

[52] Y. Syono, S.-I. Akimoto, Y. Ishikawa, and Y. Endoh, Journal of Physics and Chemistry of Solids **30**, 1665–1672 (1969).

[53] Y. Ishikawa and S.-i. Akimoto, Journal of the Physical Society of Japan **13**, 1298–1310 (1958).

[54] J. J. Stickler, S. Kern, A. Wold, and G. S. Heller, Phys. Rev. **164**, 765–767 (1967).

[55] K. Dey, *Single-crystal growth, Magnetic and Thermodynamic Investigations of lmenite Titanates and Lanthanum Nickelates*, PhD Thesis, 2021.

[56] K. Momma and F. Izumi, Journal of Applied Crystallography **44**, 1272–1276 (2011).

[57] T. F. W. Barth and E. Posnjak, Zeitschrift für Kristallographie **88**, 265–270 (1934).

[58] T. F. W. Barth and E. Posnjak, Zeitschrift für Kristallographie **88**, 271–280 (1934).

[59] J. B. Goodenough and J. J. Stickler, Physical Review **164**, 768–778 (1967).

[60] Y. Todate, Y. Ishikawa, K. Tajima, S. Tomiyoshi, and H. Takei, Journal of the Physical Society of Japan **55**, 4464–4476 (1986).

[61] I. Y. Hwang, K. H. Lee, J.-H. Chung, K. Ikeuchi, V. O. Garlea, H. Yamauchi, M. Akatsu, and S.-i. Shamoto, Journal of the Physical Society of Japan **90**, 064708 (2021).

[62] G. Shirane, S. J. Pickart, and Y. Ishikawa, Journal of the Physical Society of Japan **14**, 1352–1360 (1959).

[63] Y. Yamaguchi, H. Kato, H. Takei, A. Goldman, and G. Shirane, Solid State Communications **59**, 865–868 (1986).

[64] R. E. Newnham, J. H. Fang, and R. P. Santoro, Acta Crystallographica **17**, 240–242 (1964).

[65] C. C. Stephenson and D. Smith, The Journal of Chemical Physics **49**, 1814–1818 (1968).

[66] L. Gries, *Experimentelle Untersuchung der Ilmenit-Titanate* $MnTiO_3$ *und* $Mn_{0.75}Ni_{0.25}TiO_3$ *mittels hochauflösender Kapazitätsdilatometrie*, Master Thesis, 2021.

[67] H. Yamauchi, H. Hiroyoshi, M. Yamada, H. Watanabe, and H. Takei, Journal of Magnetism and Magnetic Materials **31-34**, 1071–1072 (1983).

[68] H. Kato, M. Yamada, H. Yamauchi, H. Hiroyoshi, H. Takei, and H. Watanabe, Journal of the Physical Society of Japan **51**, 1769–1777 (1982).

[69] H. Watanabe, H. Yamauchi, and H. Takei, Journal of Magnetism and Magnetic Materials **15-18**, 549–550 (1980).

[70] J. Akimitsu, Y. Ishikawa, and Y. Endoh, Solid State Communications **8**, 87–90 (1970).

[71] J. Darriet and L. Regnault, Solid State Communications **86**, 409–412 (1993).

[72] J. Akimitsu and Y. Ishikawa, Journal of the Physical Society of Japan **42**, 462–469 (1977).

[73] N. Mufti, G. R. Blake, M. Mostovoy, S. Riyadi, A. A. Nugroho, and T. T. M. Palstra, Phys. Rev. B **83**, 104416 (2011).

[74] M. Fiebig, Journal of Physics D: Applied Physics **38**, R123–R152 (2005).

[75] H. Toyosaki, M. Kawasaki, and Y. Tokura, Applied Physics Letters **93**, 072507 (2008).

[76] J. G. Cherian, T. D. Tokumoto, H. Zhou, E. S. Choi, and S. A. McGill, Phys. Rev. B **87**, 214411 (2013).

[77] A. Ito, H. Kawano, H. Yoshizawa, and K. Motoya, Journal of Magnetism and Magnetic Materials **104-107**, 1637–1638 (1992).

[78] Y. Yamaguchi, T. Nakano, Y. Nozue, and T. Kimura, Phys. Rev. Lett. **108**, 057203 (2012).

[79] Y. Yamaguchi and T. Kimura, Nature Communications **4**, 2063 (2013).

[80] J. J. Stickler and G. S. Heller, Journal of Applied Physics **33**, 1302–1303 (1962).

[81] J. Akimitsu and H. Yamazaki, Physics Letters A **55**, 177–178 (1975).

[82] L. R. Walker, Phys. Rev. **105**, 390–399 (1957).

[83] F. M. Johnson and A. H. Nethercot, Phys. Rev. **114**, 705–716 (1959).

[84] N. I. Gordon, A. M. Kadigrobov, and M. A. Savchenko, Soviet Physics JETP **21**, 576–579 (1965).

[85] K. Dey, private correspondence, 2019.

[86] S. Foner, Phys. Rev. **130**, 183–197 (1963).

[87] T. Nagamiya, Progress of Theoretical Physics **11**, 309–327 (1954).

[88] J. Werner, C. Neef, C. Koo, A. Ponomaryov, S. Zvyagin, and R. Klingeler, Phys. Rev. B **103**, 174406 (2021).

[89] A. Elghandour, private correspondence, 2022.

[90] J. Krzystek, A. Ozarowski, and J. Telser, Coordination Chemistry Reviews **250**, 20th International Conference on Coordination and Bioinorganic Chemistry, 2308–2324 (2006).

[91] P. W. Anderson and P. R. Weiss, Rev. Mod. Phys. **25**, 269–276 (1953).

[92] J. Barak, V. Jaccarino, and S. M. Rezende, Journal of Magnetism and Magnetic Materials **9**, 323–332 (1978).

[93] A. Fukaya, A. Ito, H. Aruga Katori, and T. Goto, Journal of the Physical Society of Japan **69**, 3027–3039 (2000).

[94] F. L. A. Machado, P. R. T. Ribeiro, J. Holanda, R. L. Rodríguez-Suárez, A. Azevedo, and S. M. Rezende, Phys. Rev. B **95**, 104418 (2017).

[95] S. M. Rezende, A. R. King, R. M. White, and J. P. Timbie, Phys. Rev. B **16**, 1126–1131 (1977).

[96] M. Hagiwara, K. Katsumata, H. Yamaguchi, M. Tokunaga, I. Yamada, M. Gross, and P. Goy, International Journal of Infrared and Millimeter Waves **20**, 617–622 (1999).

[97] A. K. Padhi, K. S. Nanjundaswamy, and J. B. Goodenough, Journal of The Electrochemical Society **144**, 1188–1194 (1997).

[98] P. S. Herle, B. Ellis, N. Coombs, and L. F. Nazar, Nature Materials **3**, 147–152 (2004).

[99] A. Yamada, Y. Takei, H. Koizumi, N. Sonoyama, R. Kanno, K. Itoh, M. Yonemura, and T. Kamiyama, Chem. Mater. **18**, 804–813 (2006).

[100] T. A. Wani and G. Suresh, Journal of Energy Storage **44**, 103307 (2021).

[101] J.-P. Rivera, Ferroelectrics **161**, 147–164 (1994).

[102] D. Vaknin, J. L. Zarestky, J.-P. Rivera, and H. Schmid, Phys. Rev. Lett. **92**, 207201 (2004).

[103] R. Toft-Petersen, M. Reehuis, T. B. S. Jensen, N. H. Andersen, J. Li, M. D. Le, M. Laver, C. Niedermayer, B. Klemke, K. Lefmann, and D. Vaknin, Phys. Rev. B **92**, 024404 (2015).

[104] M. Fiebig, Journal of Physics D: Applied Physics **38**, R123–R152 (2005).

[105] M. Bibes and A. Barthélémy, Nature Materials **7**, 425–426 (2008).

[106] A. P. Pyatakov and A. K. Zvezdin, Physics-Uspekhi **55**, 557–581 (2012).

[107] Y. N. Kharchenko, N. F. Kharcheno, M. Baran, and R. Szymczak, Low Temperature Physics **29**, 579–583 (2003).

[108] R. Toft-Petersen, J. Jensen, T. B. S. Jensen, N. H. Andersen, N. B. Christensen, C. Niedermayer, M. Kenzelmann, M. Skoulatos, M. D. Le, K. Lefmann, S. R. Hansen, J. Li, J. L. Zarestky, and D. Vaknin, Phys. Rev. B **84**, 054408 (2011).

[109] N. A. Spaldin, M. Fiebig, and M. Mostovoy, Journal of Physics: Condensed Matter **20**, 434203 (2008).

[110] B. B. Van Aken, J.-P. Rivera, H. Schmid, and M. Fiebig, Nature **449**, 702–705 (2007).

[111] Y. Yiu, M. D. Le, R. Toft-Petersen, G. Ehlers, R. J. McQueeney, and D. Vaknin, Phys. Rev. B **95**, 104409 (2017).

[112] J. Werner, C. Neef, C. Koo, A. Ponomaryov, S. Zvyagin, and R. Klingeler, Phys. Rev. B **103**, 174406 (2021).

[113] C. Neef, H. Wadepohl, H.-P. Meyer, and R. Klingeler, Journal of Crystal Growth **462**, 50–59 (2017).

[114] J. Li, W. Tian, Y. Chen, J. L. Zarestky, J. W. Lynn, and D. Vaknin, Phys. Rev. B **79**, 144410 (2009).

[115] N. F. Kharchenko, V. A. Desnenko, Y. N. Kharchenko, R. Szymczak, and M. Baran, Low Temperature Physics **28**, 646–652 (2002).

[116] D. Vaknin, J. L. Zarestky, L. L. Miller, J.-P. Rivera, and H. Schmid, Phys. Rev. B **65**, 224414 (2002).

[117] W. Tian, J. Li, J. W. Lynn, J. L. Zarestky, and D. Vaknin, Phys. Rev. B **78**, 184429 (2008).

[118] T. B. S. Jensen, N. B. Christensen, M. Kenzelmann, H. M. Rønnow, C. Niedermayer, N. H. Andersen, K. Lefmann, J. Schefer, M. v. Zimmermann, J. Li, J. L. Zarestky, and D. Vaknin, Phys. Rev. B **79**, 092412 (2009).

[119] E. Fogh, O. Zaharko, J. Schefer, C. Niedermayer, S. Holm-Dahlin, M. K. Sørensen, A. B. Kristensen, N. H. Andersen, D. Vaknin, N. B. Christensen, and R. Toft-Petersen, Phys. Rev. B **99**, 104421 (2019).

[120] T. J. Diethrich, S. Gnewuch, K. G. Dold, K. M. Taddei, and E. E. Rodriguez, Chem. Mater. **34**, 5039–5053 (2022).

[121] I. Kornev, M. Bichurin, J.-P. Rivera, S. Gentil, H. Schmid, A. G. M. Jansen, and P. Wyder, Phys. Rev. B **62**, 12247–12253 (2000).

[122] S. Geller and J. L. Durand, Acta Crystallographica **13**, 325–331 (1960).

[123] R. Toft-Petersen, N. H. Andersen, H. Li, J. Li, W. Tian, S. L. Bud'ko, T. B. S. Jensen, C. Niedermayer, M. Laver, O. Zaharko, J. W. Lynn, and D. Vaknin, Phys. Rev. B **85**, 224415 (2012).

[124] J. M. Mays, Phys. Rev. **131**, 38–53 (1963).

[125] R. P. Santoro and R. E. Newnham, Acta Crystallographica **22**, 344–347 (1967).

[126] C. Neef, *Züchtung und Untersuchung von $LiMPO_4$ M = (Mn, Fe, Co) Mikro- und Makrokristallen*, PhD Thesis, 2016.

[127] R. M. Bozoroth and V. Kramer, J. Phys. Radium **20**, 393–401 (1959).

[128] S. Spachmann, private correspondence, 2022.

[129] J. Werner, C. Neef, C. Koo, S. Zvyagin, A. Ponomaryov, and R. Klingeler, Phys. Rev. Materials **4**, 115403 (2020).

[130] D. Arčon, A. Zorko, P. Cevc, R. Dominko, M. Bele, J. Jamnik, Z. Jagličić, and I. Golosovsky, Journal of Physics and Chemistry of Solids **65**, 1773–1777 (2004).

[131] D. Arčon, A. Zorko, R. Dominko, and Z. Jagličić, Journal of Physics: Condensed Matter **16**, 5531–5548 (2004).

[132] G. Srinivasan and M. S. Seehra, Phys. Rev. B **28**, 1–7 (1983).

[133] M. Hase, M. Hagiwara, and K. Katsumata, Phys. Rev. B **54**, R3722–R3725 (1996).

[134] M. Hagiwara, M. Ikeda, Y. Idutsu, S. Kimura, and Z. Honda, Journal of the Korean Physical Society **62**, 2046–2049 (2013).

[135] S. Shinozaki, A. Okutani, D. Yoshizawa, T. Kida, T. Takeuchi, S. Yamamoto, O. N. Risset, D. R. Talham, M. W. Meisel, and M. Hagiwara, Phys. Rev. B **93**, 014407 (2016).

[136] J. Werner, S. Sauerland, C. Koo, C. Neef, A. Pollithy, Y. Skourski, and R. Klingeler, Phys. Rev. B **99**, 214432 (2019).

[137] M. Abdel-Hafiez, private correspondence, 2022.

[138] P. Pincus, Phys. Rev. Lett. **5**, 13–15 (1960).

[139] A. G. Gurevich, V. A. Sanina, E. I. Golovenchits, and S. S. Starobinets, Journal of Applied Physics **40**, 1512–1517 (1969).

[140] G. E. Fanucci, J. Krzystek, M. W. Meisel, L.-C. Brunel, and D. R. Talham, Journal of the American Chemical Society **120**, 5469–5479 (1998).

[141] M. A. McGuire, H. Dixit, V. R. Cooper, and B. C. Sales, Chemistry of Materials **27**, 612–620 (2015).

[142] S. Feldkemper and W. Weber, Phys. Rev. B **57**, 7755–7766 (1998).

[143] L. Chen, J.-H. Chung, T. Chen, C. Duan, A. Schneidewind, I. Radelytskyi, D. J. Voneshen, R. A. Ewings, M. B. Stone, A. I. Kolesnikov, B. Winn, S. Chi, R. A. Mole, D. H. Yu, B. Gao, and P. Dai, Phys. Rev. B **101**, 134418 (2020).

[144] L. Chen, J.-H. Chung, M. B. Stone, A. I. Kolesnikov, B. Winn, V. O. Garlea, D. L. Abernathy, B. Gao, M. Augustin, E. J. G. Santos, and P. Dai, Phys. Rev. X **11**, 031047 (2021).

[145] J. L. Lado and J Fernández-Rossier, 2D Materials **4**, 035002 (2017).

[146] D.-H. Kim, K. Kim, K.-T. Ko, J. Seo, J. S. Kim, T.-H. Jang, Y. Kim, J.-Y. Kim, S.-W. Cheong, and J.-H. Park, Phys. Rev. Lett. **122**, 207201 (2019).

[147] C. L. Saiz, M. A. McGuire, S. R. J. Hennadige, J. van Tol, and S. R. Singamaneni, MRS Advances **4**, 2169–2175 (2019).

[148] B. Huang, G. Clark, E. Navarro-Moratalla, D. R. Klein, R. Cheng, K. L. Seyler, D. Zhong, E. Schmidgall, M. A. McGuire, D. H. Cobden, W. Yao, D. Xiao, P. Jarillo-Herrero, and X. Xu, Nature **546**, 270–273 (2017).

[149] J. F. Dillon and C. E. Olson, Journal of Applied Physics **36**, 1259–1260 (1965).

[150] I. Lee, F. G. Utermohlen, D. Weber, K. Hwang, C. Zhang, J. van Tol, J. E. Goldberger, N. Trivedi, and P. C. Hammel, Phys. Rev. Lett. **124**, 017201 (2020).

[151] N. Richter, D. Weber, F. Martin, N. Singh, U. Schwingenschlögl, B. V. Lotsch, and M. Kläui, Phys. Rev. Materials **2**, 024004 (2018).

[152] N. D. Mermin and H. Wagner, Phys. Rev. Lett. **17**, 1133–1136 (1966).

[153] L. Chen, J.-H. Chung, B. Gao, T. Chen, M. B. Stone, A. I. Kolesnikov, Q. Huang, and P. Dai, Phys. Rev. X **8**, 041028 (2018).

[154] T. Song, X. Cai, M. W.-Y. Tu, X. Zhang, B. Huang, N. P. Wilson, K. L. Seyler, L. Zhu, T. Taniguchi, K. Watanabe, M. A. McGuire, D. H. Cobden, D. Xiao, W. Yao, and X. Xu, Science **360**, 1214–1218 (2018).

[155] H. H. Kim, B. Yang, T. Patel, F. Sfigakis, C. Li, S. Tian, H. Lei, and A. W. Tsen, Nano Letters **18**, 4885–4890 (2018).

[156] Y. Liu, L. Wu, X. Tong, J. Li, J. Tao, Y. Zhu, and C. Petrovic, Scientific Reports **9**, 13599 (2019).

[157] B. Niu, T. Su, B. A. Francisco, S. Ghosh, F. Kargar, X. Huang, M. Lohmann, J. Li, Y. Xu, T. Taniguchi, K. Watanabe, D. Wu, A. Balandin, J. Shi, and Y.-T. Cui, Nano Letters **20**, 553–558 (2020).

[158] N. Sivadas, S. Okamoto, X. Xu, C. J. Fennie, and D. Xiao, Nano Letters **18**, 7658–7664 (2018).

[159] N. Ubrig, Z. Wang, J. Teyssier, T. Taniguchi, K. Watanabe, E. Giannini, A. F. Morpurgo, and M. Gibertini, 2D Materials **7**, 015007 (2019).

[160] O. Bostanjoglo and W. Vieweger, physica status solidi (b) **32**, 311–321 (1969).

[161] L. Thiel, Z. Wang, M. A. Tschudin, D. Rohner, I. Gutiérrez-Lezama, N. Ubrig, M. Gibertini, E. Giannini, A. F. Morpurgo, and P. Maletinsky, Science **364**, 973–976 (2019).

[162] X. Shen, H. Chen, Y. Li, H. Xia, F. Zeng, J. Xu, H. Y. Kwon, Y. Ji, C. Won, W. Zhang, and Y. Wu, Journal of Magnetism and Magnetic Materials **528**, 167772 (2021).

[163] www.hqgraphene.com.

[164] D. Shcherbakov, P. Stepanov, D. Weber, Y. Wang, J. Hu, Y. Zhu, K. Watanabe, T. Taniguchi, Z. Mao, W. Windl, J. Goldberger, M. Bockrath, and C. N. Lau, Nano Letters **18**, 4214–4219 (2018).

[165] S. Li, Z. Ye, X. Luo, G. Ye, H. H. Kim, B. Yang, S. Tian, C. Li, H. Lei, A. W. Tsen, K. Sun, R. He, and L. Zhao, Phys. Rev. X **10**, 011075 (2020).

[166] X. Zhang, Y. Zhao, Q. Song, S. Jia, J. Shi, and W. Han, Japanese Journal of Applied Physics **55**, 033001 (2016).

[167] Z. Li, D.-H. Xu, X. Li, H.-J. Liao, X. Xi, Y.-C. Yu, and W. Wang, *Abnormal Critical Fluctuations Revealed by Magnetic Resonance in the Two-Dimensional Ferromagnetic Insulators* (arXiv:2101.02440 [cond-mat.mes-hall], 2021).

[168] Y. Liu and C. Petrovic, Phys. Rev. B **97**, 014420 (2018).

[169] Y. Liu and C. Petrovic, Phys. Rev. B **97**, 174418 (2018).

[170] K. Spurgeon, G. Kozlowski, M. A. Susner, Z. Turgut, and J. Boeckl, SCIREA Journal of Electric Engineering **5**, 141–162 (2020).

[171] G. T. Lin, X. Luo, F. C. Chen, J. Yan, J. J. Gao, Y. Sun, W. Tong, P. Tong, W. J. Lu, Z. G. Sheng, W. H. Song, X. B. Zhu, and Y. P. Sun, Applied Physics Letters **112**, 072405 (2018).

[172] J. Smit and H. Beljers, Philips Res. Rep. **R263**, 113–130 (1955).

[173] J. O. Artman and S. H. Charap, Journal of Applied Physics **49**, 1587–1589 (1978).

[174] F. J. Rachford, P. Lubitz, and C. Vittoria, Journal of Applied Physics **53**, 8940–8951 (1982).

[175] Q. Li, M. Yang, C. Gong, R. V. Chopdekar, A. T. N'Diaye, J. Turner, G. Chen, A. Scholl, P. Shafer, E. Arenholz, A. K. Schmid, S. Wang, K. Liu, N. Gao, A. S. Admasu, S.-W. Cheong, C. Hwang, J. Li, F. Wang, X. Zhang, and Z. Qiu, Nano Letters **18**, 5974–5980 (2018).

[176] C. Kittel and E. Abrahams, Rev. Mod. Phys. **25**, 233–238 (1953).

[177] A. F. Kip and R. D. Arnold, Phys. Rev. **75**, 1556–1560 (1949).

[178] D. W. Healy, Phys. Rev. **86**, 1009–1013 (1952).

[179] D. Huber and M. Seehra, Journal of Physics and Chemistry of Solids **36**, 723–725 (1975).

[180] Y. O. Kvashnin, A. Bergman, A. I. Lichtenstein, and M. I. Katsnelson, Phys. Rev. B **102**, 115162 (2020).

[181] L. Ke and M. I. Katsnelson, npj Computational Materials **7** (2021).

[182] O. Besbes, S. Nikolaev, N. Meskini, and I. Solovyev, Phys. Rev. B **99**, 104432 (2019).

[183] J. Arneth, M. Jonak, S. Spachmann, M. Abdel-Hafiez, Y. O. Kvashnin, and R. Klingeler, Phys. Rev. B **105**, L060404 (2022).

[184] K. Kawasaki, Progress of Theoretical Physics **39**, 285–311 (1968).

[185] S. Khan, C. W. Zollitsch, D. M. Arroo, H. Cheng, I. Verzhbitskiy, A. Sud, Y. P. Feng, G. Eda, and H. Kurebayashi, Phys. Rev. B **100**, 134437 (2019).

[186] J. Zeisner, K. Mehlawat, A. Alfonsov, M. Roslova, T. Doert, A. Isaeva, B. Büchner, and V. Kataev, Phys. Rev. Materials **4**, 064406 (2020).

[187] J. Zeisner, A. Alfonsov, S. Selter, S. Aswartham, M. P. Ghimire, M. Richter, J. van den Brink, B. Büchner, and V. Kataev, Phys. Rev. B **99**, 165109 (2019).

[188] H. E. Stanley, *Introduction to Phase Transitions and Critical Phenomena*, The International Series of Monographs on Physics (Oxford University Press, London, 1971).

[189] S. Kaul, Journal of Magnetism and Magnetic Materials **53**, 5–53 (1985).

[190] Y. Sun, W. Tong, and X. Luo, Phys. Chem. Chem. Phys. **21**, 25220–25225 (2019).

[191] M. E. Fisher, Reports on Progress in Physics **30**, 615–730 (1967).

[192] V. Carteaux, F. Moussa, and M. Spiesser, Europhysics Letters (EPL) **29**, 251–256 (1995).

[193] B. Liu, Y. Zou, L. Zhang, S. Zhou, Z. Wang, W. Wang, Z. Qu, and Y. Zhang, Scientific Reports **6**, 33873 (2016).

[194] J. T. Ho and J. D. Litster, Journal of Applied Physics **40**, 1270–1271 (1969).

[195] M. F. Collins, *Magnetic Critical Scattering*, Oxford Series on Neutron Scattering in Condensed Matter (Oxford University Press, New York, 1989).

[196] A. Taroni, S. T. Bramwell, and P. C. W. Holdsworth, Journal of Physics: Condensed Matter **20**, 275233 (2008).

[197] E. Walendy, *Untersuchungen der magnetischen Eigenschaften des Van-der-Waals-Materials CrI_3*, Bachelor Thesis, 2021.

[198] M. Balanda, Acta Physica Polonica A **124**, 964–976 (2013).

[199] V. Skumryev, H. Blythe, J. Cullen, and J. Coey, Journal of Magnetism and Magnetic Materials **196-197**, 515–517 (1999).

[200] W. Haase and S. Wróbel, *Relaxation Phenomena* (Springer, Heidelberg, 2003).

[201] W. P. Mason, Phys. Rev. **83**, 683–684 (1951).

[202] J. K. Galt, Phys. Rev. **85**, 664–669 (1952).

[203] C. M. Srivastava, S. N. Shringi, R. G. Srivastava, and N. G. Nanadikar, Phys. Rev. B **14**, 2032–2040 (1976).

[204] R. Klingeler, B. Büchner, S.-W. Cheong, and M. Hücker, Phys. Rev. B **72**, 104424 (2005).

[205] T. J. Williams, A. A. Aczel, M. D. Lumsden, S. E. Nagler, M. B. Stone, J.-Q. Yan, and D. Mandrus, Phys. Rev. B **92**, 144404 (2015).

[206] N. Khan, A. Midya, K. Mydeen, P. Mandal, A. Loidl, and D. Prabhakaran, Phys. Rev. B **82**, 064422 (2010).

Note of Gratitude

It falls upon with a sense of deep gratitude to thank those without whom this enterprise would not have been possible.

First and foremost, I would like to thank my supervisor, Prof. Dr. Rüdiger Klingeler, for having granted me the opportunity to undertake this research project under his supervision and in his research group. I thank him for his warmness, generosity, and around-the-clock support. Furthermore, I thank him for creating a very pleasant working environment in which each and everyone can feel welcome and appreciated.

Second of all, I would like to thank Prof. Dr. Maurits W. Haverkort for having kindly agreed to act as a second referee to this work. I thank him for his flexibility, ease of communication, and readiness to discuss scientific questions.

Third of all, I would like to thank my day-to-day supervisor, Dr. Changhyun Koo, for introducing me to the HF-ESR measurement technique, for supporting me in performing the experiments, for providing exhaustive maintenance of the experiment, and for willingly and patiently answering all my questions.

I would also like to thank Rudi Eitel for his continued technical support thanks to which our experiments operate smoothly. His expertise and concrete practical support has helped me on many an occasion. Equally, I would like to thank Dr. Marion Kerscher for her technical support in conducting the X-band measurements. I also thank Dr. Simon Müller for assisting me in preparing the pictorial visualisations in this text.

A very special and humble thanks goes to Rahel for carefully proof-reading the manuscript, and to Johannes, Lena, and Kaustav for so willingly and patiently sharing their expertise with me.

I would like to thank each and every member, past and present, of the F25 group for their kindness and friendliness, making it a pleasure and a delight to be counted among the group members. A special mention deserves my officemate Ahmed who is a great friend to me – patient, self-sacrificing, a role model. A further humble thanks goes to Jan and to Lukas for their friendship, and for always being good-spirited, understanding, and greatly supportive. Equally do I thank Sven for his friendship, his sincerity, and inspiration.

I wish also to thank my dearest friends outside of the university. My deep appreciation and felt joy to Simon and to Christian for being so wonderful, as well as to Graham and to Samko for being who you are.

Nakoniec sa v bázni a s láskou obraciam aj na mojich rodičov, ktorí pre moje duchovné, duševné a materiálne dobro obetovali všetko. Im patrí moja vďaka aj táto práca.

Glory be to the Father, and to the Son, and to the Holy Spirit. As it was in the beginning, is now, and ever shall be, world without end. Amen.